

<http://researchcommons.waikato.ac.nz/>

Research Commons at the University of Waikato

Copyright Statement:

The digital copy of this thesis is protected by the Copyright Act 1994 (New Zealand).

The thesis may be consulted by you, provided you comply with the provisions of the Act and the following conditions of use:

- Any use you make of these documents or images must be for research or private study purposes only, and you may not make them available to any other person.
- Authors control the copyright of their thesis. You will recognise the author's right to be identified as the author of the thesis, and due acknowledgement will be made to the author where appropriate.
- You will obtain the author's permission before publishing any material from the thesis.

***Preparation of mesoporous solids containing
encapsulated metal species of technological interest***

A thesis submitted in fulfilment
of the requirements for the degree of

Doctor of Philosophy

in

Chemistry

at

The University of Waikato

by

Sheng Xu



THE UNIVERSITY OF
WAIKATO
Te Whare Wānanga o Waikato

Abstract

The advent of mesoporous silicas such as MCM-41 has provided new opportunities for research into supported metal catalysis. The loading of metals into framework structures and particularly into the pores of porous molecular sieves, has long been of interest because of their potential catalytic activity. The larger pore sizes of mesoporous silicas allow for the possibility of preparing dispersions of metal/metal oxide particles within the pores while still allowing access by reagent molecule. In standard fabrication processes, metal particle size is not well controlled. Most studies of metal/metal oxide loaded mesoporous silicas report metal/metal oxide particles larger than the pore diameter. In the present work, new methods of preparing metal loaded systems have been developed to facilitate a more even dispersion of the metal. The metals were loaded as readily decomposed organometallic complexes so the chemistry involved in forming the metal/metal oxide particles minimized possible sintering effects. New synthetic routes were developed to facilitate loading into the pores or the framework of the silica matrix.

An optimised acid synthetic route for preparing MCM-41 was used throughout. The acid concentration, surfactant concentration, reaction time and stirring rate, all of which have strong influence on the morphology and structure of the mesoporous materials under acidic synthetic conditions, were optimised to give systems of maximum surface area while exhibiting regular pore structures and good stability. The refined reaction conditions of high stirring speeds, low surfactant concentration, high acid concentrations and short reactions times developed in the present work represent important improvements in synthetic methodology giving stable, well ordered, small pore, thick walled and high surface area products.

Single metal and mixed metal organometallic complexes were loaded into the preformed mesoporous supports by a modified imbibing method and then

decomposed to prepare metal and mixed metal nanoparticles within the structures. However, loading by this method caused disordering and destruction of the MCM-41 porous supports, the broadening of the XRD diffraction lines, and the significant reduction of pore size, pore volume and specific surface area.

A major contribution of the current work has been the development of two methods for controlling the loading of metals into the structures during synthesis. These methods offer the significant advantages of loading without structural effects and yielding producing systems where surface area increased rather than decreased with loading. By the M method, a hydrophobic organometallic complex was incorporated within the micelle system formed by the surfactant, cetyltrimethylammonium bromide. This micelle system containing the organometallic complex forms the template for the pores during the sol-gel formation of the mesoporous solids. Incorporation of the metal within the micelle facilitates the dispersion of the metal throughout the surfactant phase filling the pores of final precursor material. Calcining to remove the organic material favours leaving the metal or metal oxide in the form of small particles widely and uniformly dispersed in the mesoporous channels. By the T method, organometallic molecules are dissolved in the $\text{Si}(\text{OEt})_4$ of the synthesis mixture. Calcining the organic material from the resulting precursor favours leaving the metal or metal oxide in a widely and uniformly dispersed state in the walls of mesopores.

The synthetic methods developed were extended to prepare mixed metal nanoparticles of defined composition using single-source mixed metal organometallic compounds. In this way novel mixed metal (Mo/Fe and Mo/Co) phases with compositions determined by the stoichiometry of the initial mixed metal complex were produced and characterised.

The nature of the metal/metal oxide particles was studied by XRD and TEM. At the

metal loadings obtained (ranging up to 4%) crystalline metal and metal oxide particles should be readily detected. The absence of well defined XRD peaks characteristic of the metal or metal oxides in any of the samples provided evidence that the metals after calcining were well dispersed, with particles sizes less than a few nm and too small to give diffraction signals. TEM studies revealed a clearly defined hexagonal pore structure with pore diameters of approximately 2 nm but gave no evidence of metal particles larger than the resolving power of the instrument (approximately 1 nm).

Acknowledgments

I would like to take the opportunity to thank the people who have helped or assisted me during my studies.

Firstly, I would like to extend my sincere thanks to my supervisor, Alan Langdon for his guidance and support over the course of my studies. His knowledge and advice have been invaluable, without which I couldn't have accomplished all my experiments and this thesis

I am grateful to Professor Brian for his patience in teaching me and for his guidance and support. His professionalism and expertise in chemistry have been precious to me in this long and hard journey.

The academic and technical staff from Chemistry Department, were always helpful. In particular, I would like to thank Wendy for AA, Helan for SEM and TEM, Lisa for BET, Inda and Yuanji for XRD.

I would like to acknowledge the financial support from New Zealand Postgraduate Study Abroad Awards (NZPSAA) for their support to my attendance of the international conference.

Of course, none of this would have been possible without the support and encouragement of my family and for this I am forever grateful.

***Preparation of mesoporous solids containing encapsulated
metal species of technological interest***

Abstract

Acknowledgments

Content

Abbreviation

Chapter 1 Introduction and literature survey

1.1 General introduction	1
1.2 Literature review	2
1.2.1 Porous structures	2
1.2.2 Proposed mechanisms for mesostructure formation	4
Liquid crystal templating (LCT)	5
Silicate Layer Puckering	7
Silicate rod assembly in alkaline systems	8
Silica rod assembly in acid solutions	8
1.2.3 Synthetic pathways for producing mesoporous silica	9
1.2.4 Electrostatic assembly pathways	10
Synthesis of M41S (basic conditions)	10
Synthesis of SAB (acid conditions)	11
1.2.5 Neutral assembly pathways	11
Synthesis of HMS	11
Synthesis of MSU	13

1.2.6 Innovations in synthesis methodology	14
1.2.7 Pore size control	15
Choice of templates (surfactant)	16
Addition of auxiliary organic chemicals	16
Variation of reaction parameters	17
Post-modification	18
1.2.8 Morphology control	19
1.2.9 Hydrothermal stability	20
1.2.10 Calcining	21
1.2.11 Encapsulation of metal particles	22
Encapsulation of iron nanoparticles	24
Encapsulation of gold nanoparticles	24
Encapsulation of molybdenum nanoparticles	26
Encapsulation of mixed metal and metal/metal oxide nanoparticles	27
1.2.12 Methods of loading	28
(1) Incorporation of metal into the silica structure during the synthesis	30
(2) Adsorption from aqueous solution	32
Lattice ion exchange	32
Template ion exchange	32
(3) Aqueous solution impregnation and vaporisation	33
(4) Chemical vapour deposition	34
(5) Adsorption or impregnation using organic solutions	

of organometallic complexes and preformed MCM-41	34
(6) Encapsulation of organometallic compounds during synthesis	35
1.2.13 Comparison of activity of structural and non structural iron in Fe-MCM-41	36
1.2.14 Characterisation of metal loaded mesoporous silica	37
Characterisation of the lattice	37
Characterisation of the encapsulated metal	38
1.2.15 Application of organometallic compounds to catalytic systems	39
1.3 Specific objectives of the present research	39
1.4 Outline to thesis	42
1.5 References for Chapter 1	43

Chapter 2 Materials and Methods

2.1 Chemicals	51
2.2 Preparation of substituted ferrocenes	51
2.2.1 Preparation of acetyl-ferrocene (Fac):	52
2.2.2 Preparation of di-Acetylferrocene (Fd)	53
2.2.3 Preparation of Butyrylferrocene (Ft).	53
2.2.4 Preparation of Benzoylferrocene (Fb)	53
2.3 Preparation of mixed metal compound	54
2.3.1 Preparation of the mixed Mo-Fe complex, Cp(CO) ₃ MoFe(CO) ₂ Cp	54
2.3.2 Preparation of the mixed Mo-Co complex, [Cp(CO) ₂ Mo] ₂ Co(CO) ₃ CMe and Cp(CO) ₂ Mo[Co(CO) ₃] ₂ CMe	55
2.4 Preparation of pure silica mesoporous MCM-41 material	56

2.5. Encapsulation of metal particles by mesoporous MCM-41 materials	57
2.5.1 Micelle method (I Method)	57
2.5.2 TEOS method (M Method)	57
2.5.3 Imbibing method (T Method)	58
2.6 Characterisation of Mesoporous Silicas	59
2.6.1 Powder X-ray Diffraction (XRD)	59
2.6.2 Nitrogen adsorption	64
2.6.3 Electron microscopy	68
2.6.4 Fourier Transform Infra-Red Spectroscopy	70
2.6.5 ICP/OES chemical analysis	70
2.7 References for Chapter 2	75

*Chapter 3 Optimisation of the synthesis of MCM-41
under acid conditions*

3.1 Introduction	76
3.2 Effect of acid concentration on mesoporous	77
3.2.1 XRD characterisation of MCM-41 phases from at different acid concentrations	78
3.2.2 N ₂ adsorption–desorption isotherm of MCM-41	83
3.2.3 Effect of acid concentration on Si yield	86
3.2.4 Effect of Acid concentration on the Si/CTAEBBr ratio in MCM-41 precursor	87
3.3 The effect of reactant concentration	87
3.3.1 Effect of reactant concentration on mesoporous structures	88
3.3.2 N ₂ adsorption–desorption isotherm of MCM-41	92
3.3.3 Effect of reactant concentration on Si yield	86
3.4 The effect of reaction time	96
3.4.1 Effect of reaction time on mesoporous structures	97

3.4.2 N ₂ adsorption–desorption isotherm of MCM-41	101
3.4.3 Effect of reaction time on Si yield	103
3.5 The effect of stirring rate	104
3.5.1 Introduction	104
3.5.2 Experimental	104
3.5.3 Effect of stirring rate on induction times	104
3.5.4 Effect of stirring rate on structural features	105
3.5.5 Effect of stirring speed on particle morphology	110
3.5.6 Effect of stirring speed on N ₂ adsorption-desorption characteristics	115
3.5.7 Effect of stirring rate on Si yield	120
3.5.8 Conclusion	121
3.6 Studies of product stability	122
3.6.1 Effect of aging	122
3.6.2 The thermal stability of calcined product	125
3.6.3 The effect of acid and base on product stability	126
3.6.4 The effect of the stirring rate on the age stability	129
3.6.5 The hydrothermal stability	130
3.7 Mechanism of MCM-41 precursor formation	133
3.8 References for Chapter 3	136

Chapter 4 Preparation of metal loaded MCM-41 by immersion treatment of preformed phases

4.1 Introduction	137
4.2 The effect of solvent immersion on the preformed MCM-41 structure	137
4.2.1 Effect of solvent on mesoporous structure	138
4.2.2 Effect of solvent on nitrogen adsorption	140
4.2.3 Discussion of solvent effects on the MCM-41 structure	145

4.2.4 Summary	147
4.3 The loading of Fc and substituted Fc (S-Fc) complexes into MCM-41 by the I method	148
4.3.1 The effect of Fc and S-Fc concentration on the metal loading	149
4.3.2 Effect of loading S-Fc on mesoporous structures	151
4.3.3 Effect of loading S-Fc on N ₂ adsorption-desorption Characteristics	152
4.3.4 Kinetic effects during loading	153
4.3.5 Effect of immersion time loading on mesoporous structure	155
4.3.6 Summary	158
4.4 The calcination of S-Fc loaded MCM-41 (I method)	159
4.4.1 The effect of calcination time on S-Fc MCM-41 (I method)	159
4.4.2 Effect of calcining time on nitrogen adsorption of S-Fc loaded MCM-41	160
4.4.3 Thermal studies of the calcinations of S-Fc MCM-41	162
4.4.4 XRD evidence for the formation of iron oxide in the calcined S-Fc MCM-41	163
4.4.5 Summary	164
4.5 The loading of other organometallic complexes into MCM-41 by I Method	164
4.5.1 Results for the loading with other organometallic complexes into MCM-41	165
4.5.2 The effect of loading other organometallic complexes into MCM-41 on XRD	166
4.5.3 The effect of loading other organometallic complexes into MCM-41 on nitrogen adsorption	167
4.5.4 The infrared spectrum	167
4.6 References for Chapter 4	171

Chapter 5 The loading of MCM-41 by organometallic compounds

during synthesis by the M and T Methods

5.1 Introduction: Loading of metals in MCM-41 during synthesis	172
5.2 The effect of react conditions on the Fc-MCM-41	172
5.2.1 The effect of reaction time on loading and structural properties of Fc-MCM-41	172
5.2.2 The effect of acid concentration on Fc loading and MCM-41 mesoporous structures	177
5.3 Preparation and properties of metal loaded MCM-41 by the M and T methods using ferrocene	178
5.3.1 Determination of ferrocene content	179
5.3.2 Effect of Fc loading on structural features	179
5.3.3 Effect of Fc loading on N₂ adsorption-desorption characteristics	184
5.4 Preparation and properties of metal loaded MCM-41 by the M and T methods using substituted ferrocenes	187
5.4.1 Determination of organometallic content	188
5.4.2 Effect of S-Fc loading on structural features	191
5.4.3 Effect of S-Fc loading on N₂ adsorption-desorption characteristics	196
5.5 The loading of other organometallic compounds into MCM-41 by T and M Method	199
5.5.1 Determination of metal content	200
5.5.2 Effect of organometallic complexes loading on structural features	200
5.5.3 The effect of loading with organometallic complexes on nitrogen adsorption	204
5.6 Summary	208

***Chapter 6 The loading of mixed metal and bimetallic complexes into
mesoporous solids by the M, T and I Methods***

6.1 Introduction	208
6.2 Determination of metal content	209
6.3 Effect of mixed metal and bimetallic complexes loading on structural features	210
6.4 The effect of loading mixed metal complexes on nitrogen adsorption	214
6.5 The infrared spectrum	216
6.6 TEM	221
6.7 XRD evidence for the absence of crystalline iron oxide in the calcined iron loaded phases	221
6.8 Discussion and conclusions	223
6.9 Reference for Chapter 6	225

Chapter 7 Discussion

7.1 Optimisation of the acid route for the preparation of stable MCM-41	227
7.2 Loading of Preformed Calcined MCM-41 with transition metals by imbibing organometallic complexes (I method)	230
7.3 Loading during synthesis	233
7.4 Preparation of MCM-41 with encapsulated mixed metal phases	237
7.5 Catalysis by MCM-41 with encapsulated mixed metal nanoparticles	238
7.6 Reference for Chapter 7	240

Chapter 8 Conclusion and further work

8.1 Summary and conclusions	242
8.2 Suggestions for further work	244
8.2.1 Characterisation of encapsulated nanoparticles	244
8.2.2 Chemistry of encapsulated complexes	244
8.3.3 Catalysts based upon Co/Mo MCM-41 systems	245
8.2.4 Catalysts based upon mixed metal Au MCM-41 systems	245
8.2.5 Further improvements of synthetic conditions	245
8.3 Reference for Chapter 8	247

Chapter 1 Introduction and literature survey

1.1 General Introduction

Porous materials have found widespread applications as adsorbents, ion exchangers, molecular sieves and catalysts in a range of technologies including industrial processing, water treatment and environmental protection. They are of two types: microporous (pores ≤ 20 Å) and mesoporous (pores ~ 20 – 500 Å). The utility of these materials is manifested in their micro-/meso-structures, which allow molecules access to large internal surfaces and cavities that enhance catalytic activity and adsorptive capacity. Microporous materials are exemplified by the large family of aluminosilicates, known as zeolites in which the pores are regular arrays of uniformly-sized cages and channels [1, 2]. Microporous zeolites are some of the most widely used commercial catalysts in industry, finding applications as catalysts for oil refining and organic synthesis, particularly when dealing with molecules having kinetic diameters less than 10 Å.

Despite these desirable catalytic properties of zeolites, they become inadequate when reactants with sizes greater than the dimensions of the pores have to be processed. Also, because of their strong acidic nature, H-zeolites are rapidly deactivated due to coke and side product formation intrinsically limiting their applications. In addition, the narrow pores and cavities of zeolites are too small to accommodate the metal, mixed metal and metal/metal oxide nanoparticles that have shown much recent promise in low temperature heterogeneous catalysis. Therefore, much effort has been focussed on the preparation of zeolite-type materials with pore diameters larger than those of the traditional zeolites. One of the most exciting discoveries in the field of materials synthesis in recent years has been the discovery of mesoporous molecular sieves. This family of materials, generically called M41S, have large channels from 1.5 to 10 nm ordered in hexagonal (*M*obil *C*omposition of *M*atter-41 i.e. MCM-41), cubic (MCM-48), and laminar (MCM-50)

arrays. MCM-41, one member of this family [3] exhibiting a regular hexagonal array of uniform pore openings, high surface area and tuneable pore size which has attracted great attention as a support for creating novel heterogeneous catalysts [4]. The porous silicas themselves are not very active as catalysts due to their neutral frameworks. The incorporation of trivalent cations like Al, Cr, V, Ti and B into the MCM-41 framework generates additional moderate-to-strong acidity and hence enhanced catalytic activity [5-7].

Perhaps even more importantly, the advent of MCM-41 type materials has opened up new possibilities for preparing catalysts with uniform pores in the mesoporous region, which allow access to the relatively large molecules present in, for example, crude oils and in the production of fine chemicals. These large pores can also accommodate metal and mixed metal nanoparticles and still allow access of smaller molecules. Whenever a new type of material such MCM-41 is discovered, there is an explosion of scientific interest to investigate novel aspects of its nature, synthesis procedures and mechanisms, modification and commercial applications. However, in spite of such interest and the outstanding progress made in producing large pore molecular sieves, few of the materials so far synthesized have found commercial application in current catalytic processes [8].

The work described in this thesis was directed towards the general aim of developing techniques for producing MCM-41 phases with metal, mixed metal and metal/metal oxide nanoparticles of defined composition, oxidation state and particle size deposited in the pores. It was postulated that in this way, mesoporous catalytic phases containing tailored mono-disperse particles of controllable size and with resistance to sintering might be prepared.

1.2 Literature Review

1.2.1 Porous structures

According to the International Union of Pure and Applied Chemistry (IUPAC) rules, porous materials are divided into three classes: microporous (<2 nm), mesoporous (2–50 nm) and macroporous (>50 nm). Well-known members of the microporous class are the zeolites, which are the most widely used catalysts in industry due to their catalytic, adsorptive and shape selective properties, but their applications are intrinsically limited by their small channel diameters. Hence, there has been an ever growing interest in expanding the pore sizes of zeolite-type materials from the microporous region to mesoporous region to meet the increasing demands in both industrial and fundamental studies. It was not until 1982 [9] that success was achieved by changing the synthesis gel compositions when the first so-called ultra large pore molecular sieve, AIPO4-8 [10], containing 14-membered rings, was discovered. Indeed, this not only broke the deadlock of the traditional viewpoint that zeolite molecular sieves could not be constructed with more than 12-membered rings, but also stimulated further investigations on other ultra large pore molecular sieves, such as VPI-5 [11], cloverite [12], and JDF-20 [13]. However up to now, these materials, as with the case of the mesoporous silicas, have not found any significant applications because of either their inherently poor stability or their weak acidity. As a consequence, they are inferior compared to pillared layered clays [14].

In 1990, Yanagisawa et al. [15] reported the synthesis of mesoporous materials by intercalation of long-chain (typically C₁₆) alkyltrimethylammonium cations into the layered silicate kanemite followed by calcining to remove the organic species. Unfortunately, Yanagisawa et al.'s materials were not well characterised and their results were largely ignored.

In 1992 Mobil researchers [3] reported the discovery of a novel family of silica-based mesoporous molecular sieves, M41S, of which MCM-41 is an important member. Since

then there has been a growing interest in synthesizing these materials with large internal surface area, pore uniformity and easily controllable pore sizes. The M41S family contains hexagonal MCM-41, cubic MCM-48 and unstable lamellar MCM-50 phases. MCM-41 has a hexagonal arrangement of unidirectional pores; while MCM-48 has a highly interwoven and branched pore structure. MCM-41 and MCM-48 have attracted attention because they may find applications in catalysis, adsorption and guest-host chemistry. Other types of mesoporous silicas have now been prepared and include for example the “acid prepared mesostructures” materials (APM), that have been given the class term SBA and are which discussed in more detail in Section 1.2.4.

1.2.2 Proposed mechanisms for mesostructure formation

There have been a number of models proposed to explain the formation of mesoporous materials and to provide a rational basis for the various synthesis routes. Two typical mechanisms have been proposed so far [3], accompanied by other modified routes [16, 17]. These models are predicated upon the role of surfactants guiding the formation of the inorganic mesostructures from the dissolved inorganic precursors. Surfactants contain a hydrophilic head group and a long hydrophobic tail group within the same molecule and will self-organize in such a way as to minimize contact between the incompatible ends. How the inorganic precursor interacts with the surfactant is the issue whereby models diverge; the type of interaction between the surfactant and the inorganic precursor will be seen as a significant difference occurring in the various synthesis routes, the formation models, and the resulting classes of mesoporous materials.

Patarin et al. [18] recently concluded that the interaction between the inorganic precursor and the organic template is the key factor in controlling mesoporous silica formation, but noted that the mechanism appears to depend much on the experimental conditions of synthesis. They found further that none of the proposed mechanisms provides an

exclusive and definite answer.

From the literature it is obvious that the mechanisms involved in the formation of ordered mesoporous materials depend not only on parameters related to the specific chemistry and chemical interactions involved for any given system studied, but also on the physical conditions employed. At least the following factors are of general importance: type of inorganic material (metal, metal oxide or other) and its propensity to crystallise in the walls; type of precursors used (alkoxides or salts) and the kinetics of their hydrolysis and condensation; type of surface active molecules (cat-, an-, or non-ionic); the respective and relative concentrations of surfactant (micellar or liquid crystal) and inorganic species; pH (acidic or alkaline), temperature (low temperature or hydrothermal) and synthesis time; additives (inorganic salts and organic molecules); order of mixing; type of solvent (aqueous or non-aqueous) and solvent composition; types of synthesis (evaporation induced self-assembly or precipitation); physical shape of product formed (monolith, film, fibre or powder) [19]. Of these variables, pH has a dominant effect on the possible mechanisms. For alkaline pH, liquid crystal templating, silicate layer puckering and silicate rod assembly models have been proposed. The rod mechanism for acid solutions differs from that proposed for alkaline conditions in that it is proposed that silica layers are formed on the interior as well as exterior surface of the rods (see Figure 1.4).

Liquid crystal templating (LCT)

The liquid crystal templating (LCT) mechanism proposed by the Mobil researchers [3], was based on the idea that surfactant liquid crystal structures serve as organic templates for the formation of these materials. In support of this templating mechanism, the structure and pore dimensions of MCM-41 materials are intimately linked to the properties of the surfactant, including surfactant chain length and solution chemistry. The whole process may be via two possible mechanistic pathways as schematically shown in

Figure 1.1

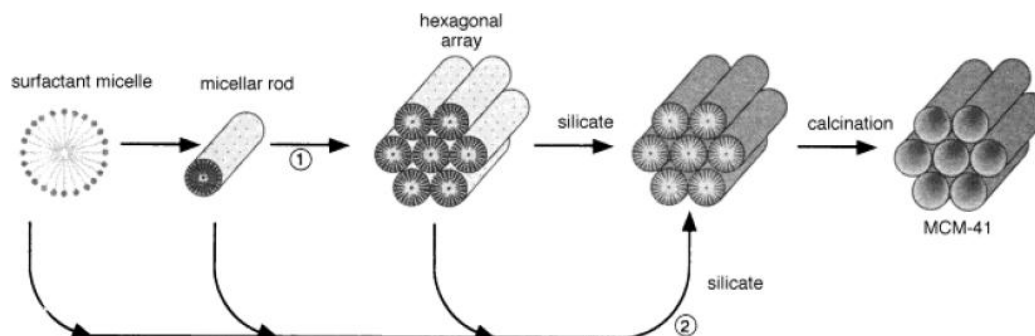


Figure 1.1 Two possible LCT mechanistic pathways for the formation of MCM-41: (1) liquid crystal phase initiated and (2) silicate anion initiated [3].

(1) The silicate precursor species occupy the space between a pre-existing hexagonal lyotropic liquid crystal (LC) phase and deposit on the micellar rods of the LC phase.

2) The inorganics mediate, in some manner, the ordering of the surfactants into the hexagonal arrangement.

In either case, the inorganic components (which are negatively charged at the high pH values used) preferentially interact with the positively charged ammonium head groups of the surfactants and condense into a solid, continuous framework. The resulting organic-inorganic mesostructure could be alternatively viewed as a hexagonal array of surfactant micellar rods embedded in a silica matrix; removal of the surfactants produces the open, mesoporous MCM-41 framework. It is now known that first mechanistic pathway did not take place in early work because the surfactant concentrations used were far below the critical micelle concentration (CMC) required for hexagonal LC formation [20]. This mechanistic pathway may be possible under higher surfactant concentrations.

The second mechanistic pathway of LCT was postulated as a cooperative self-assembly of the ammonium surfactant and the silicate precursor species below the CMC. No

preformed LC phase is necessary for MCM-41 formation but, to date, the actual details of MCM-41 formation have not yet been fully agreed upon. Several mechanistic models have now been advanced which share the basic idea that the silicate species promote LC phase formation below the CMC.

Silicate Layer Puckering

A formation mechanism proposed by Firouzi et al. [21] is the transformation from a lamellar to hexagonal phase. The central tenet of their conclusion is that the mesophase formed is governed by charge density, coordination state, and steric requirements of the inorganic and organic species at the interface and not necessarily by a preformed liquid crystal structure. In contrast, a micellar assembly of organic molecules will be broken up and rearranged upon addition of inorganic species to form a new phase often with lamellar morphologies. The lamellar phase was isolated in the reaction period between 1 and 20 min at 75°C. After 20 min the hexagonal mesostructures were detected. They propose that when the lamellar phase was hydrothermally treated at 100°C, it was converted to the hexagonal phase over 10 days according to Figure 1.2.

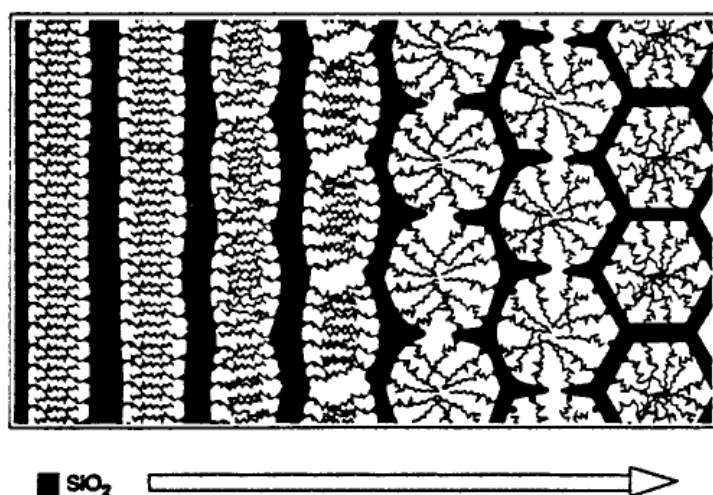


Figure 1.2 Curvature induced by charge density matching. The arrow indicates the reaction coordinate [21].

Silicate rod assembly in alkaline systems

This is essentially a special case of path 2 of the LCT mechanism (see Figure 1.1). Chen and co-workers [22] found, using in situ ^{14}N NMR spectroscopy, that the hexagonal LC phase did not develop during MCM-41 synthesis. They proposed that, under the synthesis conditions reported by Mobil, the formation of MCM-41 began with the deposition of two to three monolayers of silicate precursor onto isolated surfactant micellar rods (Scheme 3). The silicate-encapsulated rods were randomly ordered, eventually packing into a hexagonal mesostructure. Heating and aging then completed the condensation of the silicates into the as-synthesized MCM-41 mesostructure.

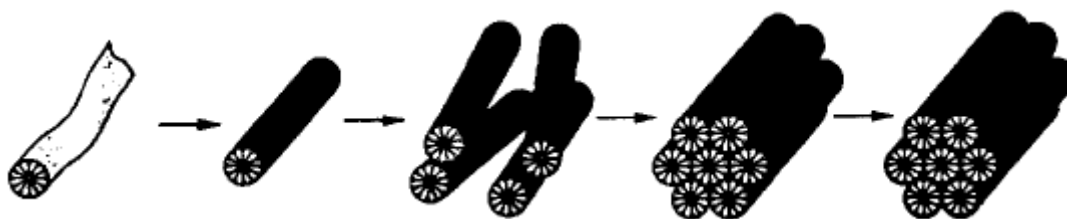


Figure 1.3 Assembly of silicate-encapsulated rods [22].

Silica rod assembly in acid solutions

Mesa and co-workers [23] proposed that the initial hydrochloric solution of cetyltrimethylammonium bromide (CTAB) surfactant is a colloidal system containing micelles of surfactant. The addition of Tetraethyl orthosilicate (TEOS), which is adsorbed and hydrolyzed into siliceous species in the palisade layer of the micelles (Figure 1.3), and polycondensation inside and outside of the palisade layer, which lead to increase of the micelle size and the stiffness of the wormlike micelles (rodlike micelles). The micelles are bound together by hydrogen bonds between silanol groups and water, which corresponds to the transformation into the solid state.

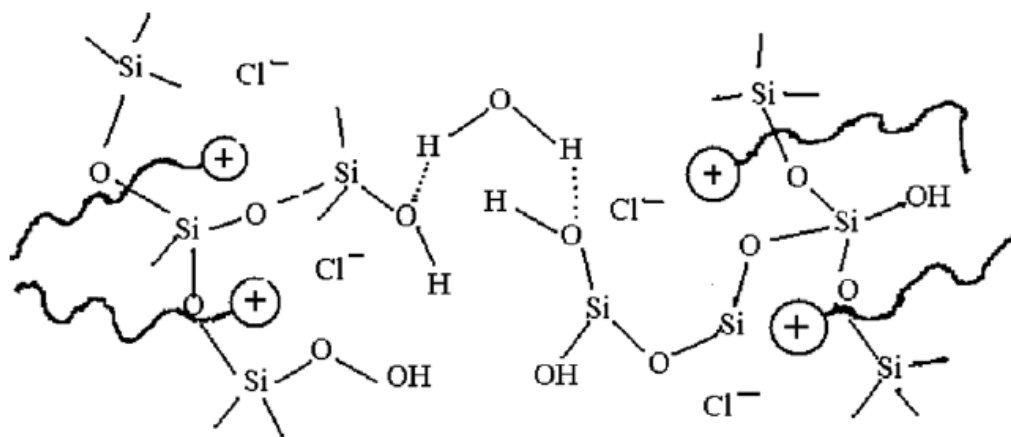


Figure 1.4 Schematic representation of cross section of micellar rod illustrating build up of silica at both interior and exterior surfaces generating micron size particles of SBA-3 (Santa Barbara No. 3) type silica [24].

1.2.3 Synthetic pathways for producing mesoporous silica

By 1999, only seven years after the discovery of the mesoporous silica, more than 4000 studies concerning their formation and properties had been published [26]. Their synthesis is based on the use of surfactant micelles which act as templates for the silica poly-condensation. Mesoporous molecular sieves normally are prepared by one of four possible assembly pathways (Figure 1.5). A generalized mechanism of formation based on the specific type of electrostatic interaction between a given inorganic precursor I and surfactant head group S was proposed by Huo and co-workers [24]. The S^+I^- pathway originally utilized by Mobil researchers involves electrostatic interactions and charge matching between positively charged assemblies of rod-like micelles of quaternary ammonium surfactants (S^+) and anionic silicate species (I^-). The second pathway proposes that cooperative interactions between inorganic and organic species based on charge interaction can also be achieved by using reverse charge matching (S^-I^+). The third and fourth, so-called counterion-mediated pathways, are further extensions of the first and second pathways, mediated by combinations of cationic or anionic surfactants and corresponding inorganic species ($S^+X^-I^+$, X^- = halides; or $S^-M^+I^-$, M^+ = alkali metal ion)

(see Figure 1.5).

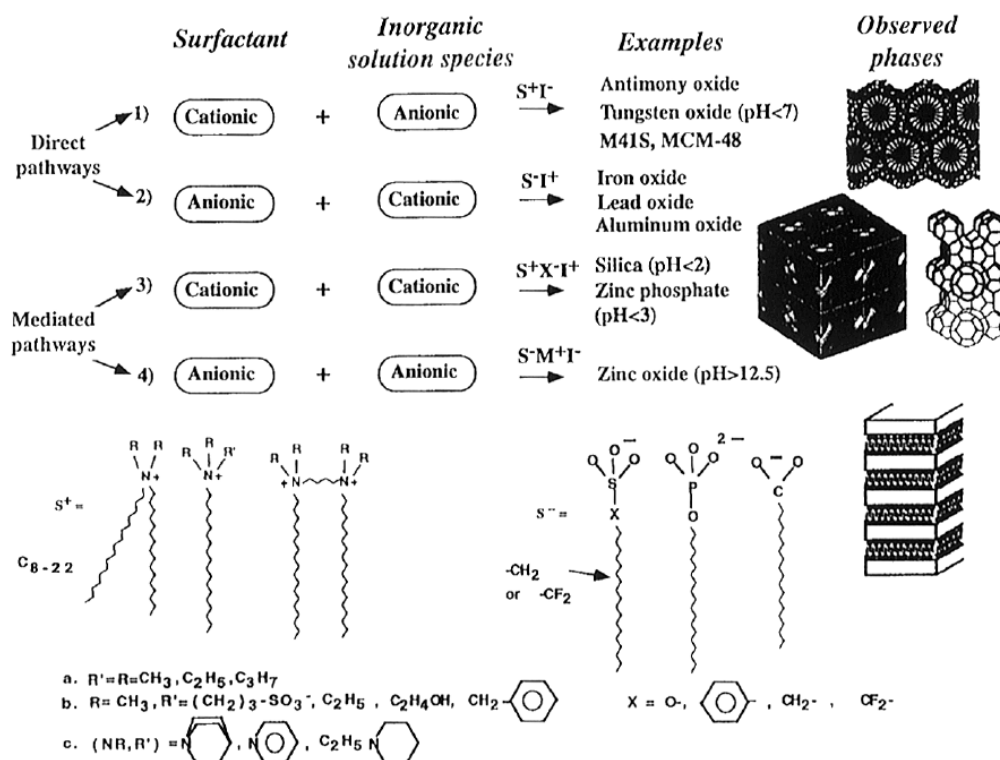


Figure 1.5 A general scheme for the self-assembly reaction of different surfactant and inorganic species: electrostatic: (1) S^+I^- , (2) S^-I^+ , (3) $S^+X^+I^+$, and (4) $S^-M^+I^-$. [25]

1.2.4 Electrostatic assembly pathways

Synthesis of M41S (basic conditions)

Reactions can be carried out either under hydrothermal conditions (above 100°C) or at room temperature (up to 100°C). The methods at different temperatures differ in the pressure and pH of the reaction mixture and in the reaction time [26]. The so-called room temperature procedure differs from the hydrothermal procedure in that a stainless steel autoclave is not required but only organic silica (TEOS) can be employed for the silica source. Normally the concentration of surfactant is above 1 wt%. Cai et al. [27] described a synthesis route where the concentration of the surfactant was much less than previously

reported (between 0.5–0.1 wt %). With this method, MCM-41 samples with both highly ordered nanometer-scale periodicity and micrometer-scale defined morphologies were obtained. Silicate surfactant rod-like micelles were packed hexagonally. Slow reaction rates were observed. This is an example of a kinetically controlled route rather than the previously reported thermodynamically controlled route and more long-range order was obtained.

Synthesis of SBA (acid conditions)

According to Huo et al. [24], the synthesis of siliceous mesophases from TEOS under strongly acidic conditions can be performed at lower temperatures, within shorter synthesis times and with lower surfactant concentrations than are needed for the basic high-temperature synthesis. The resulting “acid prepared mesostructures” materials (APM), have been given the class term SBA [28]. SBA-1 is cubic [29, 30], but unlike MCM-48 is not bicontinuous (i.e. have parallel non intersecting pores), SBA-3 is the APM mesostructural analogue of MCM-41. These acidic SBA products had smaller pore diameters and thicker walls than the MCM-41 products hydrothermally synthesized in basic media. Although high-quality hexagonal mesophases can be obtained from extremely acidic to basic ($0 < \text{pH} < 11$) conditions, the superiority of extremely acidic synthesis ($\text{pH} < 1$) has been shown to give mesoporous silica materials with higher surface areas and larger mesopore volumes [31].

The acid synthesis route is an important development because the synthesis is very simple and the morphology is easy to control, compared to the basic synthesis route. The materials have good structural (well ordered) and textural (narrow pore size distribution) properties.

1.2.5 Neutral assembly pathways

Synthesis of HMS

Tanev and co-workers [32] have demonstrated a neutral templating route for preparing the mesoporous molecular sieve, HMS (*Hexagonal Mesoporous Silica*), which is formed by hydrogen bonding interactions and self-assembly involving neutral amine surfactants (S^0) and neutral inorganic precursors (I^0). The electrically neutral (S^0I^0) assembly pathway is complementary to the electrostatic pathways. There are significant structural differences between MCM-41 and HMS silica materials. MCM-41 derivatives typically exhibit three or more X-ray diffraction lines, indicative of long-range hexagonal channel packing. In contrast, HMS silicas show one or, at most, two broad X-ray peaks as a consequence of a small crystallite domain size and/or a much lower degree of channel packing order. These materials had higher amounts of interparticle mesoporosity than MCM-41. Although they are distinguishable with regard to structural ordering, MCM-41 and HMS molecular sieves both exhibit a sharp step in their nitrogen adsorption isotherms, corresponding to the presence of a regular mesoporous framework. Hence, it is thought that HMS silicas are special members of the MCM-41 class [33]. The neutral templating route can be expected to have advantages in loading the materials with metals during synthesis because metal in the form of neutral complexes should be taken up by the neutral micellar templates. The hydrogen-bonded route produces ordered mesoporous material with thicker framework walls than the electrostatic LCT-derived silicates. The thicker pore walls improve the thermal and hydrothermal stability of the mesoporous framework. The silicate framework in the resulting mesophase was neutrally charged, so the surfactants could be removed by simple solvent extraction, which can avoid some degradation of the mesoporous framework caused by high temperature calcining [34-36].

Tanev and Pinnavaia [32] further exploited the S^0I^0 route by the use of double-headed

alkylamines (α , Ω -dialkylamine) to create porous lamellar mesostructures.

Synthesis of MSU

In 1995, after the discovery of MCM-41 and HMS silica mesoporous materials, a new mesoporous silica family, MSU-X (*Michigan State University-X*) was reported by Bagshaw [33]. The hydrogen-bonding synthesis route used surfactants with a polyethylene oxide head group.

Because the lengths of the head and tail groups could be adjusted, pores could be synthesized without the use of swelling agents. The polyethylene oxide head group is nonionic (N^0), unlike the amine head group (S^0) which while uncharged, can be ionized. The nonionic route (N^0T^0) seemed to provide greater pore ordering than the neutral route (S^0T^0), but still lacked long-range hexagonal packing order. The pores were more “wormlike” than rodlike cylinders.

MSU-X has attracted considerable attention because the polyethylene oxide templates are low cost, non-toxic, biodegradable and the products possess thicker framework walls and thus improved thermal stability compared with MCM41 and HMS. Silica sources for MSU-X are alkoxy silanes and sodium silicate solutions. The latter is inexpensive, and makes large-scale preparation possible. However, synthesis of MSU-X using sodium silicate solution as silica source has not been widely reported [23]. MSU-X is usually prepared in neutral solution.

Boissière and co-workers [37] reported production of MSU-X by a two-step synthesis, giving very good reproducibility and high reaction yields. This reaction involved an initial assembly step between silica oligomers and nonionic micelles, followed by a

condensation step induced by the addition of sodium fluoride as catalyst.

1.2.6 Innovations in synthesis methodology

Mokaya and co-workers [38] reported that the preparation of large crystals MCM-41 could be achieved by using calcined small crystallites of MCM-41 as seeds in a multistage synthesis method. They noted that the method should be useful for making high quality thin films of mesoporous materials.

Park and co-workers [39] reported that MCM-41 was obtained by microwave treatment of precursor gel at 100–120 °C for 1 h or less, a very short period of time compared with the hydrothermal method. In addition, microwave radiation provided a way to control product crystallinity and morphology. The addition of a small amount of ethylene glycol in synthetic mixture contributed to improving crystallinity, forming particles of MCM-41 that were homogeneous in shape with reduced particle size.

Khushalani and co-workers [40] demonstrated that the mesoporous silica materials can be synthesized by using a mixture of two surfactants: cetylpyridinium chloride (CPCl) and cetyltrimethylammonium chloride (CTACl). It is believed that increased cooperative interactions between the pyridinium headgroup of the CPCl surfactant and silica building blocks gives materials that display an enhanced degree of order of the mesopores relative to those formed using CTACl alone.

Blin and co-workers [41] reported that well-ordered spherical mesoporous materials with a hexagonal arrangement of channels, analogous to MCM-41, have been directly synthesized by varying the weight percentage of decaoxyethylene cetyl ether [C₁₆(EO)₁₀] in aqueous solution. They proposed that the interactions of the silica source with

hydrophilic chain heads of surfactant molecules should disturb the preformed hexagonal micelle array to give disordered wormhole mesostructured materials, analogous to MSU.

Gruen and co-workers [42] reported that the use of ammonia as a catalyst and tetra-alkoxysilanes as silica sources provided a fast and convenient method for the preparation of high-quality MCM-41. They also reported the addition of an alcohol (e.g. ethanol or isopropanol) leads to a homogeneous system which allows the formation of spherical MCM-41 particles. These spherical MCM-41 particles can be used as a starting material for spray drying to larger agglomerates. The main advantage of the method is short reaction times, excellent reproducibility and easy preparation of large batches.

Mokaya and co-workers [38] reported that when the calcined MCM-41 crystallites were used as seeds during the secondary synthesis, the template molecules attach themselves at the mouth of the pore channels of the primary MCM-41 and encourage crystal growth parallel to the channels and, consequently, growth of larger crystals becomes possible. This method can be applied in future preparation of large single crystals and high quality thin films of MCM-41.

1.2.7 Pore size control

Following the discovery of the M41S family of ordered silica materials, considerable attention has been focused on tailoring their pore structures. For example, the diameter of the hexagonally packed, one-dimensional channels in MCM-41 can be tailored from 15 to over 100 Å by a variety of methods [43-45].

Four ways have been demonstrated to tailor the pore sizes effectively. One has involved increasing the length of the alkyl chain of the surfactant molecule which leads to a larger

diameter of templating micelles. Another involves adding auxiliary organic molecules to the synthesis mixture. Additives such as 1,3,5-trimethylbenzene dissolved in the hydrophobic region of the micelles causing their swelling which leads to larger pore sizes of the final products. The third technique involves changes in reaction conditions such as the restructuring of the mesoporous under mild aqueous conditions, e.g. the pH of the reaction mixture, the reaction temperature, and the reaction time. Finally the channel diameter may be slightly modified post-synthesis by cation exchange, adsorption and chemical treatments such as silanation, boronation and treatment with inorganic acids [46].

(i) Choice of templates (surfactant)

The surfactant plays an extremely important role in the synthesis due to a self-assembly process to form the precursor materials. Namba et al. [47] have succeeded in the hydrothermal synthesis of highly ordered silica MCM-41 using n-cetyltrimethylammonium bromide ($C_{16}TMABr$) or nocosyltrimethylammonium chloride ($C_{22}TMACl$) as templates by reducing the pH (pH=9) at the beginning of reaction. Moreover, the pore size of MCM-41 has been finely controlled by using a mixture of $C_{16}TMABr/C_{22}TMACl$ template. In this case, the pore size obtained was from 1.8 to 4.2 nm.

(ii) Addition of auxiliary organic chemicals

MCM-41 with various pore sizes was synthesized using different type of organic auxiliary chemical. The auxiliary organic species added to the reaction gel can be solubilized inside the hydrophobic regions of micelle, causing an increase in micelle diameter so as to increase the pore size of MCM-41. Depending on the type and the amount of organic auxiliary chemical, the pore diameter of mesoporous material can be enlarged and the size

uniformity of the pores can be improved. Sayari and co-workers [45] have demonstrated that careful addition of long chain primary alcohols during the synthesis of MCM-41 is an excellent method for synthesizing and adjusting both the mesostructure and morphology of mesoporous silicates produced from cationic surfactant (CnTMAX) silicate systems.

Variation of reaction parameters

Textural restructuring of MCM-41 can be achieved by providing longer crystallisation times [44, 45] or via post-synthesis thermal treatments [46].

Cheng and co-workers [48] reported that highly crystalline MCM-41 with a very narrow pore-size distribution, high surface area, large grain size and thick channel walls was prepared in alkali-free media. The properties of the product depended on the source and concentration of the reactants, the gel aging time, the temperature and the duration of the synthesis.

Corma and co-workers [44] emphasized that swollen, uniform and well-crystallized mesoporous MCM-41 type materials can be directly obtained without addition of auxiliary organics by adjusting the surfactant CTAB concentration in the presence of small cations such as TMA^+ , TEA^+ , or Na^+ and controlling the crystallization variables. These results not only have an important impact on the preparation of larger pore mesoporous materials, but also open new insights into the mechanism of formation of these materials.

Sayari and co-workers [45] reported that the periodic mesoporous silicates could be synthesized using cetyltrimethylammonium bromide by a typical preparation procedure and tailored by post-synthesis hydrothermal treatment method to give

large-pore MCM-41 samples with a high degree of structural ordering. This confirmed previous findings that the hydrothermal restructuring method is a convenient way to synthesize high quality MCM-41 silicates with tailored pore sizes, but only up to 6.5 nm.

Kruk and co-workers [49] reported that the MCM-41 mesoporous molecular sieves could be synthesized at low temperature in the presence of cetyltrimethylammonium bromide and then subjected to post-synthesis hydrothermal treatment at elevated temperatures (413 K and 423 K) to give good quality, large pore MCM-41 with hydrothermal stability comparable with that for the most stable MCM-41 materials reported in the literature.

It was also shown that the hydrothermal treatment in water at 423 K led to initial improvement of the ordering, but the pore size increase was relatively small (ca. 10%). Extended treatments afforded materials with significantly enlarged unit cells, but with lower degree of pore structure ordering.

Post-synthesis modification

Surface-modified mesoporous materials with various active sites have been extensively investigated in recent years, because functional modification permits tailoring of the surface properties for numerous potential applications in the fields of heterogeneous catalysis and adsorption–separation. Generally, the modification of mesoporous materials typically employs two approaches: (1) the direct synthesis wherein a silane containing the desired functional group is added to the synthesis mixture and the functional group is incorporated during synthesis, and (2) post-synthetic grafting, i.e. the functional group is incorporated after the surfactant/polymer template is removed from the mesopores [50].

The second method is post-treatment (e.g., grafting or silylation) of pore wall of the preformed mesoporous molecular sieves. This method has flexibility to finely tune the pore size of any kind of the pre-formed mesoporous molecular sieves. It has been demonstrated in the case of MCM-41 by chemical vapour deposition (CVD) of tetraalkoxysilanes. However, the CVD process appears to be self-limited, most likely due to pore-blocking [51, 52].

Chen and co-workers [53] reported that SBA-3 with pore sizes of 22–25 Å has been successfully prepared by TEOS liquid phase deposition on the pristine SBA-3 with a pore size of ca. 27 Å. After the first TEOS modification, the resulting sample shows obvious changes in textural properties. Compared to SBA-3, the modified SBA-3 sample has negligible micropores. The presence of ethoxysilyl groups on modified SBA-3 sample is supported by FT-IR and carbon content measurement, and their loading amount is estimated to be ca. 5.7 wt% by TGA. The second TEOS modification is less efficient to change the textural properties of SBA-3 owing to its lower loading (ca. 1.3 wt %).

1.2.8 Morphology control

Fabrication of mesoporous materials with controlled morphologies has been one of the main subjects in this rapidly developing research field. It is important to design the morphology of mesoporous materials as well as the mesostructure for desired applications where discrimination between molecules is required. It is therefore theoretically and practically important to study in detail how these particles are grown from solutions [43].

Mesoporous silica can be synthesized by either an alkaline route or an acidic route. It has been reported that the morphology is easier to control under acidic conditions because the

interaction between surfactant and silica framework is weaker than the alkaline route. Mesoporous silica films, hollow tubular, fibers, spiral and gyroid shapes have been synthesized under acidic conditions [55-58].

Yang and co-workers [59] reported that a gyroid-to-sphere shape transition could be performed in the growth of mesoporous silica morphologies that are synthesized under quiescent acidic aqueous conditions. It appears that the gyroid shapes materials could be obtained under high acidity condition. By contrast, low acidity circumstances favour a spherical shape formation. And a synthesize 1–10 mm diameter mesoporous silica spheres with a narrow sphere size and pore size distribution portends a myriad of applications in large molecule catalysis, chromatographic separations and nanocomposites.

Jin and co-workers [60] reported that the highly ordered SBA-15-type mesoporous silicas with various morphologies have been synthesized under different conditions, and their 2D hexagonal mesostructures were confirmed by the XRD patterns and the TEM images. For the materials synthesized through the one-step route, their morphologies are dependent on the reaction temperatures, the concentration of inorganic salt and the acid species. The short column-shaped particles, the finely defined hexagonal platelets and the spheres can be obtained by means of adjusting these synthetic parameters. The morphologies of the mesoporous materials synthesized through the two-step route can be controlled by the acidity of the solution.

1.2.9 Hydrothermal stability

In spite of the generally satisfactory thermal stability of ordered mesoporous materials, their hydrothermal stability is usually quite poor, both in steam at high temperatures and in hot water. This deficiency is one of the major factors that hinder prospective applications of mesoporous materials in petrochemical processing. Over the last several

years, much research has been devoted to the identification of conditions suitable for the direct synthesis of hydrothermally stable mesoporous materials and to the development of methods for an effective post-synthesis stabilization of mesoporous materials.

The relatively low hydrothermal stability can be attributed to the amorphous nature of the mesoporous walls. However, there are a number of examples of mesoporous materials that have reasonably good hydrothermal stabilities. [61] In general, acidic synthetic conditions produce more hydrothermally stable products than alkaline conditions.

Cheng and co-workers [48] described a straightforward method of controlling the channel diameter of the mesoporous molecular sieve MCM-41 in the 26.1-36.5 Å range and the wall thickness in the 13.4-26.8 Å range while using a single gel mixture. Samples synthesized at higher temperatures have higher thermal stability. The thick channel wall leads to a greatly increased thermal stability of the product. The thickest-walled material can withstand calcining at 900 °C with little structural damage. The internal surface area of the sample depends on its channel diameter and channel wall thickness. Because samples of the same d spacing with thicker walls have smaller channel diameters, they have lower surface areas.

1.2.10 Calcining

While variety of methods of template removal such as ion exchange [61], solvent extraction [62] or chemical decomposition [63] have been demonstrated for different systems, calcining remains the current best practice for removing templates from most mesostructures and zeolites.

Calcining serves not only to remove water and the organic template from inside the

porous network via high temperature oxidation, but also to consolidate the silicate framework via thermal condensation. During calcining the organic template is oxidized to CO₂ and H₂O thereby leaving the void space formed by the template micelles empty. Simultaneously, thermal condensation of the silica structure causes bond rearrangements through dehydration, dehydroxylation and siloxane bridge formation that lead to a more condensed form of silica and a contraction of the mesostructure repeat unit. The calcining of all mesoporous materials, such as MCM-41, SBA-15, and MSU-X, at high temperatures continues to be a vital step in the synthesis of these types of materials. However, it is a part of the synthesis process that has been the subject of limited study, which has tended to focus on template decomposition pathways [64, 65] rather than improving the process itself. In fact, early in the development of mesostructured materials synthesis, most workers observed that low heating rates were required in order to avoid collapse of the porous network [66]. However, long calcinations times at high temperatures can result in pore structure collapse if the mesoporous silica sample is poorly ordered. The use of slow heating rates became part of standard mesostructure (M41S, HMS, MSU-X, SBA-15, etc.) calcining procedures.

Bagshaw co-workers [67] reported that rapid calcining of high quality silicate mesostructures is possible at rates at least up to 100°C min⁻¹. Some ‘fine-tuning’ of the mesopore structure is possible by controlling the rate of heating during the calcining process and lower temperatures might be used to calcine the non-ionically templated SBA-15 and MSU-X materials. Rapid calcining of mesoporous silica and silicate materials is possible with generally minimal effect on the porous structure of siliceous materials.

1.2.11 Encapsulation of metal particles

A major drawback of M41S-type materials lack of Al lies in their inherent low acidity and

consequent inert nature toward various organic transformations. Surface modifications are necessary to make them more active, especially in the field of catalysis. The incorporation of transition metals into the mesoporous framework by direct hydrothermal synthesis provides a technique for introducing active metal sites [68]. The advantages of M41S type mesoporous materials (relative to microporous materials) for catalysed reactions result from the narrow controlled pore size distribution and large regular pores openings, which allow the diffusion of reactants into, as well as the fast diffusion of the products from the pores [69, 70].

Because of the larger pore sizes available in mesoporous solids, one of their attractions is the possibility of carrying out reactions involving molecules too large to penetrate the pores of microporous materials. Reactions can take a number of forms. They may be simple surface reactions that are facilitated by the large surface area provided. Further it is possible to modify the surfaces by introducing acid species, by doping with trivalent atoms (Al, Fe, or Ga) into the walls of the mesoporous silica which creates Brønsted acid sites and allows preparation of materials of various acidity, catalytic and adsorptive properties [71]. On these sites, ion exchange can take place and the acidity or basicity of the material can be controlled. It is also possible to introduce molecular catalytic species, which may be tethered to the mesopore, to carry out reactions in confined environments. Another avenue for catalytic functionalisation is the deposition of metal particles within the pores. In the latter two approaches, it is necessary to perform the mesoporous solid and then to introduce the catalyst. More recently, it has been shown possible to introduce transition metal-based species into the pores during synthesis [72].

The incorporation of transition metals into the framework structures and particularly into the pores of mesoporous molecular sieves is of interest because of their potential catalytic activity and the fact that the well defined pores can accommodate only nanoparticles of the metal as pure metals or mixed metals, as their oxides or other chemical forms [73]. Finding new ways for loading metals and mixtures of metal in to mesoporous phases in a

controlled way is thus of continuing interest.

Encapsulation of iron nanoparticles

Iron (III)-incorporation into MCM-41 has received much attention because of its redox properties and thus its potential application in many oxidation processes [74], the selective catalytic reduction of NO_x with hydrocarbons [75] and in alkylation reactions. It is understood that the reducibility of active iron species plays a key role in the oxidation processes. Moreover, the use of iron as catalytically active species is attractive because iron-containing compounds generally show low toxicity [76] and are readily available.

Although the trivalent iron-substituted mesoporous silica molecular sieves show much promise for large molecules, they have the same disadvantages as the microporous materials. A major problem with both microporous and mesoporous iron substituted molecular materials is the instability of trivalent tetrahedral (framework) iron during heat treatment. This problem is well documented in the literature and, hence the application of iron-substituted molecular sieves has been limited, in contrast to many other transition metal-containing molecular sieves [77].

Loading of immobilized metal chloride after synthesis provides an alternative way of adding iron but has the disadvantages of either partially or fully blocking the pores thereby reducing the specific surface area, pore volume, and pore diameter; loss by leaching; obstructing the active sites and catalyst poisoning by the chloride [78].

Encapsulation of gold nanoparticles

An example of this application is provided by the loading of gold nanoparticles into MCM-41 and MCM-48. Prior to the early 1990's, gold surfaces had been regarded as being essentially inert and having little catalytic activity. Experimental observation of a lack of dissociative activity during adsorption of hydrogen by the smooth surface of Au was supported by theoretical calculation [79]. Since Haruta's [80] discovery of the catalytic activity of supported Au nanoparticles, this field has attracted rapidly growing interest due to the potential applicability to various reactions of industrial and environmental significance [81-85]. It has become clear that the catalytic system is complex and is dependent upon catalyst preparation, pre-treatment method, nature of support material, gold particle size and gold loading. The key requirement is to have well-dispersed gold particles. The reasons for the unique behaviour of finely dispersed gold, especially when compared to other noble metals, are still under debate [86-88].

Particle size and support material are also important. The optimum particle size of the Au nanocatalyst seems to be around 3 nm and activity is reduced by sintering. Moisture may also be important [89].

Encapsulation of preformed Au nanoparticles provides a possible way of protecting the particles from sintering. For example, Tiemann and co-workers [90] used the strong confinement of the uniform ordered pore system of mesoporous silica to restrict the mobility of species that lead to thermal sintering. The particles are contained within the pores and while accessible to gas phase reactants are protected from poisons larger than the pore size. However, for gold/metal oxide catalytic systems, it is generally believed that silica is a poor support, its use resulting in low catalytic activity [91]. It is not clear whether the reason is because the size of Au nanoparticles tends to be bigger on a silica surface or because the catalyst/support interaction is poor. It is not easy to separate these roles in catalytic reactions in systems of gold nanoparticles supported on metal oxides. Recently, K nyam and co-workers [92] proposed a simple but very promising method for synthesizing mesoporous materials containing controlled size and shape Au nanoparticles.

They reported the results obtained for post synthesis insertion of gold nanoparticles into mesoporous silica materials MCM-41 and MCM-48 by an imbibing method where the preformed phase was treated with aqueous suspension of the gold particles. They claim that two- and five-nanometer gold particles were encapsulated in both materials. However when 20-nm gold particles were used, they were too large to be inserted into the pores.

Encapsulation of molybdenum nanoparticles

Oxidation is a core technology for converting petroleum-based materials to useful chemicals of higher oxidation states. Catalytic olefin epoxidation in the liquid phase is an important topic for the synthesis of fine chemicals, because epoxides are chemical compounds of great importance as intermediate products in the preparation of a wide variety of chemical products ranging from petrochemical compounds to fine chemicals [93].

The generally good catalytic activities of several molybdenum complexes are applied as versatile catalysts for the oxidation of organic substrates and therefore of significant current interest. Molybdenum based catalysts are applied for the industrial epoxidation of propylene with t-butyl hydroperoxide since the late 1960s. Thus, considerable efforts were dedicated in the following decades to the understanding of the involved catalytic reactions in order to reach even better yields and selectivities [94].

Barrio and co-workers reported that molybdenum-containing catalysts were prepared by anchoring Mo(VI) groups onto different aminofunctionalized silica surfaces and then tested in the epoxidation reaction of 1-octene with ethylbenzene hydroperoxide (EBHP) as an oxidant. Catalytic performance with selectivities as high as 80% could be obtained at EBHP conversions of about 80% when the Mo complexes were immobilized on a silica substrate functionalized with a diamino-containing moiety [93].

Xie and co-workers introduced Mo into MCM-41 and used the Mo-MCM-41 mesoporous molecular sieve as catalyst in the cracking of polypropylene [95].

Huong and co-workers prepared silicomolybdic acid supported on mesoporous MCM-41 catalyst by impregnation and found interesting partial oxidation of methane to formaldehyde by molecular oxygen [96].

Mingjun and co-workers used two different mesoporous materials, Si-MCM-41 and Al-MCM-41, to anchor catalytically active oxodiperoxo molybdenum sites via the silylated ligand acetamide. Further surface silylation with Me_3SiCl by a post synthetic procedure improved the catalytic properties by changing the surface properties [97].

Mo-incorporated SBA-1 mesoporous molecular sieves, synthesized under acidic condition using MoCl_2 and cetyltriethylammonium bromide, have been used as catalysts for partial oxidation of methane with oxygen as an oxidant. It was found that the catalytic performance of Mo-SBA-1 materials directly synthesized from the Mo-containing gel were superior to those of Mo-impregnated pure siliceous SBA-1 and amorphous silica [98].

Encapsulation of mixed metal and metal/metal oxide nanoparticles

The encapsulation of mixed metal and metal/metal oxide systems provides further options for catalyst design. The catalytic properties of these systems is likely to be influenced by the metal/metal and/or metal/metal oxide particle sizes due to changes in electronic structure and the increased percentage of surface atoms as particle sizes decrease. Chemisorption bond strength between the metal surface and the substrate also change with particle size, leading to the appearance of strong metal support interactions. The addition of a second metal can be used to control the metal/metal oxide dispersion due to the formation of a mixed oxide phase or oxide interface between the support and the

active metal. For example, in copper–iron-based materials the formation of alloys has been established. The presence of Fe and Cu in the catalyst significantly influences the sintering and carbidization and, improves catalytic activity and stability in the reverse water gas shift reaction.

Significant progress towards catalyst design was made by Claus et al [99] who investigated the requirements for an optimum ammonia synthesis catalyst. They showed that a rational catalyst development strategy could be used to construct active sites with the desired intermediate nitrogen interaction energy by combining two metals: one with a high adsorption energy and one with a low adsorption energy. A combination of Mo (which binds N too strongly) with Co (which binds N too weakly) allowed a catalyst to be developed using this principle which had a low pressure ammonia synthesis activity much better than that of that of the individual constituents. They determined that a 1:1 mixed metal cobalt/molybdenum compound provided catalytic activity comparable to the much more expensive rhodium and much better than the iron catalyst used industrially. The possibility exists that iron/molybdenum nano particles encapsulated in MCM-41 would provide an effective ammonia synthesis catalyst.

Murid and co-workers reported that the sulphided Co-Mo-based catalysts have been extensively used in industry for hydrodesulfurization reactions. Over the past few decades, several different models have been proposed to explain the promotional effect of Co. The addition of a small amount of Co to Mo/Al₂O₃ dramatically improves the hydrodesulfurization activity of Mo [100].

Carlos and co-workers reported that Fe was combined with Ni as promoters using Mo/MCM-41-type mesoporous support. The replacement of 35% of the atomic Ni in the catalyst by Fe induces an increase in the hydrodesulfurization activity, indicating the Fe is acting as an effective promoter. Possibly, Bronsted acidity induced by Fe incorporation is playing an important role for this promotion [101].

1.2.12 Methods of loading

Several methods have been developed for introducing metals, metal ions, metal oxides or metal complexes into MCM-41 and other mesoporous materials. It can be expected that different synthetic methods will lead to different locations and coordination environments of metal species and thus different catalytic properties. The elucidation of the relationship between the coordination structure and the catalytic property, viz., the structure–property relationship of the metal species introduced into MCM-41 is crucial for the catalytic applications of these materials. [102].

Metal species can be incorporated into mesoporous silicas by substitution into the skeleton or insertion into the channels outside the skeleton. Incorporation strategies include: (1) incorporation of metal into the silica structure during the synthesis, (2) adsorption from aqueous solution, (3) aqueous solution impregnation and vaporisation, (4) chemical vapour deposition (CVD), and (5) adsorption or impregnation using organic solutions of organometallic complexes. These procedures can be divided into two groups: a direct synthesis method (procedure 1) and a post-synthesis method (procedures 2, 3, 4, 5). The post-synthesis methods have the following advantages: **(a)** The structure of the resultant mesoporous materials remains is ordered after incorporation of the metal; **(b)** high flexibility in choice of metal to be loaded, **(c)** the materials obtained generally have undiminished or even enhanced thermal and hydrothermal stability [103,104]. Compared with post-synthesis incorporation methods, the direct synthesis method uses a two-step synthesis procedure, which allows preparation of nanoporous organic–inorganic hybrid materials in shorter times. However, the resultant materials usually show less structural ordering, and the organosilane precursor must be chosen carefully to avoid phase separation during both synthesis and the surfactant removal process.

For both loading methods, the physical properties of the supported components may be changed after loading due to the quantum size confinement effect of the ordered nanopores in the host [105].

(1) Incorporation of metal into the silica structure during the synthesis

A wide variety of metal ions can be readily introduced directly during synthesis. This is the most extensively studied method. By using the direct synthesis method, atomically isolated metal species can be substituted isomorphously for silicon atoms into the MCM-41 framework where they can act as catalytically active centres. Transition metals such as Ti, Cr, Fe and Cu have been successfully incorporated into MCM-41 skeletons, achieving high catalytic activity and selectivity for various oxidation reactions [106].

A typical procedure is illustrated by the preparation of Fe-MCM-41. The iron source (ferric nitrate) was added into the synthesis gel containing the silica source (tetraethyl orthosilicate) and the template (hexadecyltrimethylammonium bromide) before hydrothermal synthesis. After hydrothermal synthesis at 393 K for 96 h, the resultant solid was filtered, washed, dried, and finally calcined at 823 K in air for 6 h. Iron species directly introduced into the synthesis of Si-MCM-41 have been used in the benzylation of benzene [71]. The use of silatrane together with other metal atranes allows harmonization of the hydrolysis rates of metals and silicon, which allows mixing at atomic level from the very beginning of the reaction. Highly-doped new materials are attainable through atrane chemistry [107].

Gu and co-workers [108] reported that highly dispersed and uniform Fe₂O₃ and palladium nanoparticles can be incorporated into the pore channels of mesoporous thin films (MTFs) through a newly developed strategy in which a molecular assembly template was used as

a carrier to provide the compatible environment for the hydrophobic compounds. The guest nanoparticles were strictly confined inside the pore channels of host MTFs due to the molecular level dissolution of the precursor compounds into the hydrophobic core of the surfactant template micelles. Since this method is a one-pot, one-step method, the orientations of pores have no effect on the access of guest materials to the channels of MTFs [109, 110]. The synthesized composite films may find applications in a variety of fields such as nonlinear optics.

Ozin and co-workers [111] have successfully employed a liquid crystalline phase composed of metal precursor and surfactant as a supermolecular template to synthesize mesostructured silica films functionalized by noble metal nanoparticles. However, the metallic nanoparticles seemed to have a broad size distribution.

The incorporation of metal ions into the framework of SBA-15 is very difficult because of the strongly acidic synthesis conditions [109]. Several studies have dealt with incorporation of metal ions into SBA-15 using solely post-synthetic grafting methods. During preparation of the materials by these methods metal oxides are often formed in the channels and this may reduce the specific surface area, pore volume, and pore diameter or have a negative effect on the catalysis [110].

Vinu and co-workers [112] have proposed to incorporate iron atoms into SBA-15 materials by a simple adjustment of the pH of gel mixtures above the isoelectric point of silica ($\text{pH} < 2$) so that negatively charged silica species can easily interact with the positively charged iron hydroxo complexes $[\text{Fe}(\text{OH})^{2+}]$, resulting in incorporation of larger quantities of Fe into the SBA-15 mesoporous silica matrix. They also found that the pore diameter of the corresponding Al-SBA-15 materials can be easily controlled by variation of the synthesis temperature.

(2) Adsorption from aqueous solution

Ion exchange

In this method, metal ions are generated adjacent to the ion exchange positions of the framework and these ions subsequently form metal or metal oxide clusters while moving toward the outer surface. As long as the size of the cluster is smaller than the pore, it may be encapsulated in the pore system. However, the distribution of particles is generally not uniform and the metal component can be found both inside the pores and on the outer surface. The advantage of this method is that the amount of metal ions can be regulated up to the ion exchange capacity of the silicate.

A typical synthesis method was performed by stirring solid MCM-41 in an aqueous solution of $\text{Fe}(\text{NO}_3)_3$ at 323 K. After this treatment, the samples were filtered, washed, dried at 393 K, and calcined at 773 K.

The metals introduced via cation exchange procedure can be relatively easy incorporated into the walls of MCM-41 and therefore can occupy both framework and extra framework positions as was reported by Grubert et al. [113].

Template ion exchange

Unlike aluminosilicate zeolites, the purely silicious mesoporous materials do not possess ion exchange ability. However, the cationic surfactants in the as-synthesized MCM-41 can be replaced by other cations such as VO^{2+} , Mn^{2+} , Fe^{3+} , $[\text{Co}(\text{en})_2\text{Cl}_2]^+$ and other positively charged complexes [102]. For example, Mokaya et al. [38] prepared Fe-MCM-41 by the exchange of the template cations with the Fe^{3+} ions in the ethanolic solution), followed by

filtration, washing, drying, and calcining at 823 K.

(3) Aqueous solution impregnation and vaporisation

Wet preparation techniques such as incipient wetness and impregnation are generally used for the preparation of supported metal catalysts. However, these methods only rarely (and often accidentally) give uniform distributions of metal particles. This lack of control ensures that the production of metal particles exclusively within the pores of a support material is unlikely.

In a typical synthesis outgased silica or mesoporous material (673 K, 3 h in oven) was saturated with an aqueous solution of iron (III) nitrate and rotated with heating at 353 K for 1 h in an evaporation flask. The impregnated powder was dried at 393 K for 12 h and then calcined at 823 K for 4 h in oven [114].

Various Lewis acidic catalysts (AlCl_3 , ZnCl_2 , FeCl_3 , GaCl_3 and InCl_3) [115] and metal oxides (Ga_2O_3 , In_2O_3 , Tl_2O_3 and Fe_2O_3) [116] have been introduced into ordered mesoporous Si-MCM-41 by incipient wetness technique. These studies indicated that mesoporous materials containing iron species exhibited outstanding catalytic activity. In the case of Fe-MCM-41 the one-dimensional pore structure might introduce a less than optimal diffusion to and from the active centers. For Fe-MCM-41, the nature of the active site could also be an issue, since completely isolated Fe-ions may not be the most favourable site. Indeed, nano-sized Fe_2O_3 clusters could prove much more reactive due to their high degree of coordinative instauration.

Fröba et al. [117] have reported a series of researches on the synthesis of Fe_2O_3 nanoparticles formed in the channels of the mesoporous materials by a wet impregnation

technique followed by drying and calcining.

(4) Chemical vapour deposition

Chemical vapour deposition (CVD) can be used for both ion-exchanger and non-ion-exchanger porous materials and has been used to deposit metal particles in and on zeolites and mesoporous materials. Metal particles are formed by the attachment of the metal precursor (generally a metal complex such as a carbonyl) to the surfaces of the support material, where it subsequently decomposes. The amount of metal that can be introduced by this procedure is limited by the pore volume of the support material. For these catalysts, the metal particles are attached to both the interior and exterior surfaces of the matrix.

The method is illustrated by the work of Decyk et al. [118]. FeCl_3 was sublimed onto SiO_2 or mesoporous molecular sieves under anaerobic conditions at 603 K for 3 h. The treated material was washed with distilled water to reduce the amount of chloride ions. Finally, the catalyst was dried and calcined at 823 K in air flow for 4 h.

Oldroyd et al. have proposed that organometallic complexes can be grafted onto the surface of mesoporous silica through surface silanol groups as anchor sites by chemical vapour deposition under anhydrous conditions [119].

(5) Adsorption or impregnation using organic solutions of organometallic complexes and preformed MCM-41

Transition metal complexes and organometallic compounds can be encapsulated in the mesoporous MCM-41 supports by physical adsorption or covalent linkage. Sinclair [120]

loaded the mesopores of MCM-41 microspheres with toluene solutions of iron acetylacetonate as the iron sources. The hybrid microspheres were then calcined to obtain iron-containing MCM-41 spheres. More recently the loading of metalloporphyrins in the pores of MCM-41 has been achieved [121].

In a similar way, Decyk et al. introduced ferroceneacetic acid (FAA) by immersing the solid material (1 g of silica or hydrogen form of mesoporous material) in 100 cm³ of a FAA solution in toluene. The mixture was stirred at room temperature for 6 h, separated from the solution by filtration, washed with 200 cm³ of toluene and finally dried at 353 K for 10 h [122].

Thermal stability of ferrocene species immobilised on the solid surface is not significantly influenced by the nature and composition of the matrix contrary to leaching behaviour. The feature of these solids as catalysts has been estimated in the hydroxylation/polymerisation of phenol and decomposition of isopropanol. In the latter reaction the redox properties are slightly pointed out. All FAA modified solids exhibit very high activity in the polymerisation of phenol, which dominates over the hydroxylation activity. The nature of polymers formed is strongly dependent on the type and composition of the matrix applied for FAA immobilization [123].

(6) Encapsulation of organometallic compounds during synthesis.

Grosshans and co-workers [124] describe the use of a simple long chain metal soap to co-direct the synthesis of a metal-modified mesoporous material. It is expected with such molecules, that mixed micelles can be formed between the soap and the surfactant due to strong lipophilic interactions between the long alkyl chains of each component. The procedure presented establishes a new route for the incorporation of transition metals into MCM-41 together with a mechanism for tuning the porous structure.

An alternative and potentially more general novel approach to loading metals into MCM-41 has been reported by Michitaka [125] who added ferrocene to the synthetic mixture and produced Fe loaded MCM-41. It can be reasoned that if the templating micellar assemblies in the synthesis mixture incorporate another (secondary) substance within their cores, they will carry the secondary substance selectively into the channels of the resulting mesoporous structure. This procedure offers the interesting possibility of incorporating a variety of metals and mixed metal compounds using their ferrocene or other organometallic derivatives. The use of different ferrocene or organic moieties also allows the possibility of modifying the pore structure of the final MCM-41 product.

1.2.13 Comparison of activity of structural and non structural iron in Fe-MCM-41

A wide variety of metal ions can be readily introduced by the direct hydrothermal (DHT) and the template ion exchange (TIE) methods. In the case of Fe-MCM-41, Qinghong and co-workers [106] have found that the DHT method results in iron atoms mainly in tetrahedral coordination and isolated from each other in the framework of MCM-41, whereas, aggregated iron oxides with iron in octahedral coordination are mainly observed in TIE samples. Especially, by using the DHT methods, atomically isolated metal species can be substituted isomorphously for silicon atoms into the MCM-41 framework and act as catalytically active centers. Up to now, some transition metals of Ti, V, Cr, Fe, Cu, and have been successfully incorporated into MCM-41 skeletons, achieving high catalytic activity and selectivity for various types of oxidation reactions. Fe-MCM-41 prepared by the DHT method exhibited higher catalytic activity for the epoxidation of styrene with H_2O_2 than observed for the material prepared by the TIE method.

1.2.14 Characterisation of metal loaded mesoporous silica

A variety of methods is available for the characterization of the lattice and the metal particles loaded into it.

Characterisation of the lattice

Adsorptive methods can be used to determine specific surface areas. The BET model for the determination of specific surface areas should be applied only for type II and IV isotherms; with other isotherm types the BET data should be treated with great care.

Micro- and mesopores can be determined from nitrogen or argon adsorption isotherms, whereas meso- and macropores can be characterized by mercury porosimetry. In amorphous porous solids, pores either are in the particles (micropores or mesopores) or are the result of the structure of connected nanoparticles (meso- to macropores). In the latter, the interparticle voids represent the pores, and the void size is a direct function of particle sizes and shapes. In materials of extreme low density, one has to consider that pore volume and diameter, may change during the measurement due to compression of the network. Mesopores, especially those that are ordered or uniform, are often identified by hysteresis between the adsorption and desorption isotherm, in which the form of the hysteresis loop provides information about the pore shape.

For the pore size distribution of mesopores, the BJH model is commonly applied. Micropores in the range of 1–2 nm have to be interpreted with great care because the BJH model is based on the Kelvin equation, which is valid only for pore sizes from larger than 2.5 nm to approximately 100 nm [126].

It has been pointed out by Ghosh [127] that micropores cannot be identified reliably by a type I isotherm; a reliable assignment of the presence of micropores is only possible if there is a point of inflection in the low-pressure range ($p/p_0 < 10^{-1}$) of high-resolution adsorption isotherms with argon as carrier gas.

Characterisation of the encapsulated metal

Depending on the metal and the level of loading, a number of physical techniques may be used to provide indirect information on aspects such as particle size and location and valence state. These methods include TEM, SEM, XRF, XRD, XANES/EXAFS, EPR, Mössbauer and FTIR spectroscopy. Some of these techniques are not readily available and research on such aspects is still insufficient to define even the location and the coordination structure of the metal. In many cases, the content of metal atoms introduced is very low and many characterization techniques cannot provide useful information. X-ray absorption spectroscopy (XANES/EXAFS) is becoming a powerful technique to determine the local structure around the excited atom. A few researchers have applied this technique to study the coordination structure of hetero-atoms introduced to MCM-41 and other mesoporous materials [102]. The use of electron microscopy has been far less extensive. For iron loaded MCM-41, the use of bright field TEM has been used to infer the presence of iron nanoparticles from changes in the contrast of the images [128]. Limitations in the application of the technique to MCM sieves mean that while it has been suggested that these nanoparticles are embedded inside the mesopores (vastly increasing the active surface area of the catalyst), there has been no direct evidence given that the nanoparticles were indeed incorporated into the pore structure [129].

The colour of the metal-containing samples synthesized is often a simple indication of whether the bulk oxide of the metal exists.

1.2.15 Application of organometallic compounds to catalytic systems

Organometallic complexes are of catalytic interest in their own right. As homogeneous catalysts they can efficiently and selectively catalyze many reactions and are widely applied in industrial processes. In terms of industrial applications, the heterogenization of

homogeneous catalysts is of significant interest. A major drawback of homogeneous catalysts is the difficulty of separating the products from the reaction solution and recovering and recycling the catalyst. Mesoporous silicas offer the possibility to provide support systems with tailored pores sizes for the heterogenization of small molecule homogeneous catalysts [130].

Another useful feature of organometallic compounds in the context of heterogeneous catalysts, is that in many cases they can be relatively easily decomposed, leaving only the metal as a non volatile product. Thus they allow pure metal atoms to be introduced into a catalytic system without the accompanying anion atoms that often act as catalytic poisons.

Supported transition metal catalysts continue to provide improved routes for a wide range of industrial chemical processes. Metal and mixed metal/metal oxide feature strongly in recent developments in this area. Mesoporous silicas provide ideal porous support materials for such catalytic systems. They offer the advantages of easy access of reactant gasses to the catalytic sites and by their restricted pore sizes, inhibit sintering effects that potentially lead to loss of catalytic activity. The preparation of mesoporous silicas containing metal and mixed metal species introduced via organometallic complexes, principally various metal ferrocenes, will be the main focus of the present study.

1.3 Specific objectives of the present research

The motivation of the present investigation was the idea that MCM mesoporous silica phases should provide ideal porous supports for catalytically active metal, mixed metal and mixed metal metal/metal oxide nanoparticles. The pore sizes of M41S silicas are ideal for the easy access of reagents and egress of products and highly dispersed nanoparticles on the large internal surface areas of the pores should be protected against sintering by the their separation, low mobility and the geometric restriction of the pore diameters. Further it was postulated that if the metal species were added during the synthesis step, then

uniform dispersion and monodispersity was more likely to be achieved. Thus we sought to prepare systems of metal, mixed metal and metal/metal oxide nanoparticles of controllable size and with resistance to sintering. Systems prepared with metal and metal oxides known to be catalytically active may lead to the development of useful heterogeneous catalysts.

Specific research questions we wished to address during the research include the following:

1. Which of the numerous methods that have been reported in the literature, is most likely to produce mesoporous silicas compatible for use as catalysts? Will such a method also provide a route for loading with metals? The literature review has identified the acid route as being the most likely candidate. This needs to be confirmed and the method optimised.
2. Can absorption/decomposition of appropriate organometallic compounds be used to prepare metal and mixed metal nanoparticles of controllable composition encapsulated within preformed mesoporous supports? Studies with a variety of single metals (Mo, Co and Fe) and mixed metals (Mo and Fe, Mo and Co) organometallic compounds are envisaged. The compounds need to be chosen to have low decomposition temperatures and be free of elements that are known to act as catalytic poisons. We believe that such compounds will allow us to produce porous materials containing very small metallic particles that, because of low temperature preparation will have undergone minimal sintering.

This work uses pre-formed mesoporous phases, such as M41S silica compounds. And solutions of organometallic iron compounds such as ferrocene and molybdenum compounds such as $\text{Mo}_2(\text{C}_5\text{H}_5)_2(\text{CO})_6$ (with differing sizes, stabilities, polarities etc) will be used to load the solids with the molecular compounds. Rapid evaporation of the solvents followed by calcining should deposit metal or metal oxide within the

pores of the solids as the organometallic molecules decompose.

3. Is it possible to develop a general method for loading mesoporous silicas with metal nanoparticles by incorporating the metal in the form of an organometallic compound into the structures during the synthesis step? One method could involve the loading of the micellar phases of the reaction mixture with appropriate organometallic compounds prior to the synthesis reaction. Important variables are likely to be the size and shape of the organic moiety, the organometallic compound concentration in the micellar phase, the surfactant employed and the synthetic route used. The proposed method will make use of the surfactant-templated synthesis of mesoporous solids [3]. Hydrophobic organometallic molecules (e.g. ferrocene, $\text{Mo}_2(\text{C}_5\text{H}_5)_2(\text{CO})_6$ and its analogues) will be encapsulated within the micelle system formed by a suitable surfactant (e.g. cetyltrimethylammonium bromide). This micelle system will be used as a template for the sol-gel formation of mesoporous solids which should give rise to isolated molecules dispersed throughout the surfactant phase filling the pores. Careful calcining, should remove all the organic material and leave the metal or metal oxide in the form of small particles widely and uniformly dispersed. To our knowledge, this approach to metal-loading of porous materials has been reported only once and could find very wide application if the technique proves to be successful.
4. As an alternative to loading the micelle, it is proposed to dissolve the organometallic complex in the TEOS silica source. This may introduce the metal into different sites within the silica. To our knowledge, this approach to metal-loading of porous materials has been not reported and could find very wide application if the technique proves to be successful.
5. Can we extend these synthetic methods to prepare mixed metal nanoparticles of defined composition by using single-source mixed metal (e.g. Mo-Fe and Mo-Co) organometallic compounds. The single-source precursors could be $\text{Cp}(\text{CO})_3\text{MoFe}(\text{CO})_2\text{Cp}$, or $[\text{Cp}(\text{CO})_2\text{Mo}]_2\text{Co}(\text{CO})_3\text{CMe}$. This procedure could give rise to novel mixed metal phases which could reveal synergistic catalytic effects.

1.4 Outline of the thesis

The thesis is presented in 8 chapters. Chapter 1 is a general introduction and literature review and sets out the objectives for the research. Chapter 2 describes the materials and methods used in the work. Chapter 3 is concerned with the optimisation of the synthesis of MCM-41 under the acid conditions that were judged to be most compatible to loading during synthesis. Chapter 4 describes the preparation of metal loaded MCM-41 using conventional immersion treatments, I method, of preformed phases in organometallic complex solutions. In Chapter 5, novel methods for loading MCM-41 with organometallic compounds during synthesis are developed. In the M method the complexes are encapsulated in the micelles of the synthesis solution while in the T Method the complexes are dissolved in the TEOS. Chapter 6 describes the loading of mixtures of metal complexes and bimetallic complexes into mesoporous solids by the M, T and I Methods to give mixed metal systems. A general discussion of the results given in Chapter 7 and Chapter 8 summarises conclusions and makes suggestions for further work.

1.5 References for Chapter 1

1. Breck, D.W. *Zeolite Molecular Sieves: Structure Chemistry and Use*, Wiley, New York, **1974**.
2. Dyer, A. *An Introduction to Zeolite Molecular Sieves*, Wiley, New York, **1988**.
3. Kresge, C.T.; Leonowicz, M.E.; Roth, W.J.; Vartuli, J.C.; Beck, J.S.; *Nature* 359, **1992**, 710.
4. Corma, A. *Chem. Rev.* 97, **1997**, 2373.
5. Ryoo, R.; Kim, J.M. *J. Chem. Soc., Chem. Commun.*, **1995**, 711.
6. Luan, Z.; Cheng, C.F.; He, H.; Klinowski, J. *J. Phys. Chem.* 99, **1995**, 10590.
7. Inui, T.; Kim, J.B.; Seno, M. *Catal. Lett.* 29, **1994**, 271
8. Avelino, C. *Chem. Rev.*, 97, **1997**, 2373-2419
9. Wilson, S. T.; Lok, B. M.; Messina, C. A.; Cannan, T. R.; Flanigen, E. M. *Am. Chem. Soc.* 104, **1982**, 1146-1147.
10. Dessau, R. M.; Schlenker, J. L.; Higgins, J. B. *Zeolites*, 10, **1990**, 522-527.
11. Davis, M. E.; Saldarriaga, C.; Montes, C.; Garces, J.; Crowder, C. *Nature*, 331, **1988**, 698-702.
12. Estermann, M.; Mccusker, L. B.; Baerlocher, Ch.; Merrouche, A.; Kessler, H. A. *Nature*, 352, **1991**, 320-323.
13. Jones, R. H.; Thomas, J. M.; Chen, J.; Xu, R.; Huo, Q.; Li, S.; Ma, Z.; Chippindale, A. M. *J. Solid State Chem.*, 102, **1993**, 204-208.
14. Zhao, X.S.; Lu, G.Q.; Millar, G.J. *Ind. Eng. Chem. Res.* 35, **1996**, 2075-2090
15. Yanagisawa, T.; Schimizu, T.; Kiroda, K.; Kato, C. *Bull. Chem. Soc. Jpn.*, 63, **1990**, 988-992.
16. Inagaki, S.; Fukushima, Y.; Kuroda, K. *Stud. Surf. Sci. Catal.* 84, **1994**, 125-132.
17. Steel, A.; Carr, S. W.; Anderson, M. W. *J. Chem. Soc., Chem. Commun.*, **1994**,

- 1571-1572.
18. Patarin, J; Lebeau, B; Zana, R. *Curr. Opin. Col.l Interface Sci.*, 7, **2002**, 107 –15
19. Anders, E.C; Palmqvist. *Curr. Opin. Col.l Interface Sci.*, 8, **2003**, 145-155
20. Vartuli, J. C; Kresge, C. T; Leonowicz, M. E; Chu, A. S; McCullen, S. B; Johnson, I. D; Sheppard, E. W. *Chem. Mater.*, **1994**, 6, 2070-2077
21. Firouzi, A; Atef, F; Oertli, A.G; Stucky, G.D; Chmelka, B.F. *J. Am. Chem. Soc.* 119, **1997**, 3596.
22. Chen, C.-Y; Burkett, S. L; Li, H.X; Davis, M. E. *Microporous Mater.* **1993**, 2, 27-34.
23. Mesa, M; Sierra, L; Guth, J.L. *Microporous and Mesoporous Materials*. 102, **2007**, 70–79.
24. Huo, Q; Leon, R; Petroff, P.M; Stucky, G.D. *Science*. 268, **1995**, 1324.
25. Zhao, D.; Huo, Q.; Feng, J.; Chmelka, B. F.; Stucky, G. D. *J. Am. Chem. Soc.* 120, **1998**, 6024.
26. Chatterjee, M.; Iwasaki, T.; Hayashi, H.; Onodera, Y.; Ebina, T.; Nagase, T. *Catalysis Letters*. 52, **1998**, 21–23
27. Cai, Qiang.; Lin, Wen-Yong.; Xiao, Feng-Shou.; Pang, Wen-Qin.; Chen, Xi-Hua.; Zou, Ben-San. *Microporous and Mesoporous Materials*, 15, **1999**, 1-15
28. Huo, Q.; Margolese, D. I.; Stucky, G. D. *Chem. Mater.* 8, **1996**, 1147-1160.
29. Huo, Q.; Margolese, D. I.; Ciesla, U.; Feng, P.; Gier, T. E; Sieger, P.; Leon, R.; Petroff, P. M.; Sch üth, F.; Stucky, G. D. *Nature*, 368,**1994**, 317-321;
30. Huo, Q.; Margolese, D. I.; Ciesla, U; Demuth, D. G.; Feng, P; Gier, T. E.; Sieger, P; Firouzi, A.; Chmelka, B. F; Sch üth, F.; Stucky, G. D. *Chem. Mater.* **1994**, 6, 1176-1191.
31. Yukakom. S.; Yasutake, T.; Isamu, M.; Shuichi, K. *Journal of Porous Materials* 4, **1997**, 129–134

32. Tanev, P.T. and Pinnavaia, T.J. *Science*. 267, **1995**, 865-867.
33. Bagshaw, S. A.; Pinnavaia, T. J. *Angew. Chem., Int. Ed. Engl.* 35, **1996**, 1102.
34. Prouzet, E.; Pinnavaia, T. J. *Angew. Chem., Int. Ed. Engl.* 36, **1997**, 516.
35. Zhang, W.; Pauly, T. R.; Pinnavaia, T. J. *Chem. Mater.*, 9 (11), **1997**, 2491 -2498.
36. Pauly, T. R.; Pinnavaia, T. J. *Chem. Mater.*, 13 (3), **2001**, 987 -993.
37. Boissière, C.; Larbot, A.; Bourgaux, C.; Prouzet, E.; Bunton, C. A. *Chem. Mater.* 13, **2001**, 3580-3586.
38. Mokaya, R.; Zhou, W.; Jones, W. *Chem. Commun.*, **1999**, 51–52.
39. Park, S.E.; Kim, D. S.; Chang, J.S.; Kim, W. Y. *Catalysis Today* 30 September **1998**, 301-308.
40. Khushalani, D.; Kuperman, A.; Coombs, N.; Ozin, G. A. *Chemistry of materials* 8 (8), **1996**, 2188-2193.
41. Blin, J. L.; Le ónard, A.; Su, B. L. *J. Phys. Chem. B*, **2001**, 105, 6070-6079.
42. Gruen, M; Unger, K; Matsumoto, A; Tsutumi, K. *Micropor. Mesopor. Mater.* 27, **1999**, 207.
43. Cheng, C.F.; Zhou, W.; Klinowski, J. *Chem. Phys. Lett.* 263, **1996**, 247.
44. Corma, A; Kan, Q.; Navarro, M.T.; Perez, P. J.; Rey, F. *Chem. Mater.* 9, **1997**, 2123.
45. Sayari, A.; Liu, P.; Kruk, M.; Jaroniec, M. *Chem. Mater.* 9, **1997**, 2499
46. Vansant, E.F. *Pore Size Engineering in Zeolites* (John Wiley, Chichester, **1990**).
47. Namba, S.; Mochizuki, A.; Kito, M. *Stud. Surf. Sci. Catal.* 117, **1998**, 257.
48. Cheng, C.F.; Park, D.H.; Klinowski, J. *J. Chem. Soc., Faraday Trans.* 93, **1997**, 193.
49. Kruk, M.; Jaroniec, M.; Sayari, A. *Micropor. Mesopor. Mater.* 27, **1999**, 217.
50. Chen, Y.; Han, J.; Zhang, H. *Applied Surface Science* 253, **2007**, 9400–9406

51. Zhao, X.S.; Lu, G.Q.; Hu, X. *Chem. Commun.* **1999**, 1391.
52. Fodor, K.; Bitter, J.H.; De Jong, K.P. *Microporous Mesoporous Mater.* **56**, **2002**, 101.
53. Chen, F.; Shen, S.; Xu, X.J.; Xu, R.; Kooli, F. *Microporous and Mesoporous Materials* **79**, **2005**, 85–91
54. Haruta, M.; Dat éM. *Applied Catalysis A: General* **222**, **2001**, 427–437
55. Ryoo, R.; Ko, C.H.; Cho, S.J.; Kim, M.J. *J. Phys. Chem. B* **101**, **1997**, 10610.
56. Lin, H.P.; Cheng, S.; Mou, C.Y. *Chem. Mater.* **10**, **1998**, 581.
57. Lin, H.P.; Kao, C.P.; Mou, C.Y.; Liu, S.B. *J. Phys. Chem. B* **104**, **2000**, 7885.
58. Lin, H.P.; Cheng, Y.R.; Mou, C.Y. *Chem. Mater.* **10**, **1998**, 3772.
59. Yang, H.; Vovk, G.; Coombs, N.; Sokolov, I.; Ozin, G.A. *J. Mater. Chem.*, **8**(3), **1998**, 743–750.
60. Jin, Z.W.; Wang, X. D.; Cui, X.G. *Colloids and Surfaces A: Physicochem. Eng. Aspects*, **316**, **2008**, 27–36.
61. Lang, N.; Tuel, A. *Chem. Mater.* **16**, **2004**, 1961.
62. Tanev, P.T.; Pinnavaia, T.J.; *Chem. Mater.* **8**, **1996**, 2068.
63. Xia, Y.D.; Mokaya, R. *J. Phys. Chem.B.* **110**, **2006**, 9122.
64. Glibert, K.H.; Baldwin, R.M.; Way, J.D. *Ind. Eng. Chem. Res.* **40**, **2001**, 4844.
65. Chen, C-Y.; Li, H-X; Davis, M.E. *Microporous Mater.* **2**, **1993**, 17.
66. Kleitz, F.; Schmidt, W.; Sch üh, F. *Micro. Meso. Mater.* **44**, **2001**, 95.
67. Bagshaw, S.A.; Bruce, I.J. *Micro. Meso. Mater.* **109**, **2008**, 199–209.
68. Sheldon, R.A.; Arends, I.W.C.E.; Lempers, H.E.B. *Catal. Today* **41**, **1998**, 387.
69. Decyk, P.; Trejda, M.; Ziolek, M. *C. R. Chimie* **8**, **2005**, 635–654
70. Udayakumar, S.; Ajaikumar, S.; Pandurangan, A. *Applied Catalysis A: General* **307**, **2006**, 245–256

71. He, N.; Bao, S.; Xu, Q. *Appl. Catal., A*, 169, **1998**, 29
72. Parvulescu, V.; Su, B.L. *Catalysis Today*. 69, **2001**, 315–322
73. Yuan, Z.Y.; Ma, H.T.; Luo, Q.; Zhou, W.Z.; *Materials Chemistry and Physics* 77, **2002**, 299–303
74. Wang, Y.; Zhang, Q.; Shishido, T.; Takehira, K. *J. Catal.* 209, **2002**, 186.
75. Decyk, P.; Trejda, M.; Lewandowska, A.; Ziolk, M. *J. Pol. Environ. Stud.* 10, **2001**, 50.
76. Sax, N.I. *Dangerous Properties of Industrial Materials, sixth ed*, Van Nostrand Reinhold Company Inc., New York, **1984**.
77. Trong, O.D.; Desplantier, G.D.; Danumah, C.; Kaliaguine, S. *Applied Catalysis A: General* 253 (2), **2003**, 545–602.
78. Alvarez, A.M.; Bengoa, J.F.; Cagnoli, M.V.; Gallegos, N.G.; Yeramian, A. A.; Marchetti, S.G. *Surface Science and Catalysis Part A and B* 142, **2002**, 1339–1346.
79. Hammer, B.; Norskov, J.K. *Nature*. 376, **1995**, 238.
80. Haruta, M.; Yamada, N.; Kobayashi, T.; Iijima, S. *J. Catalysis*, 115, **1989**, 301.
81. Haruta, M. *Studies Surf. Sci. Catalysis.*, 145, **2003**, 31;
82. Idakiev, V.; Tabakova, T.; Naydenov, A.; Yuan, Z.Y.; Su, B.L. *Applied Catalysis B: Environmental*. 63, **2006**, 178–186
83. Haruta, M.; Date, M. *Appl. Catalysis*, A222, **2001**, 427.
84. Valden, M.; Lai, X.; Goodman, D. W. *Science*, 281, **1998**, 1647.
85. Daniel, M.C.; Astruc, D. *Chem. Rev.*, 104, **2004**, 293.
86. Boccuzzi, F.; Chiorino, A.; Manzoli, M. *Surf. Sci.* 442, **2000**, 454.
87. Meier, D. C.; Goodman, D. W. *J. Am. Chem. Soc.*, 126, **2004**, 1892.
88. Yuan, Y.; Kozlova, A. P.; Asakura, K.; Wan, H.; Tsai, K.; Iwasawa, Y. *J. Catalysis*, 170, **1997**, 191.
89. Date, M.; Okumura, M.; Tsubota, S.; Haruta, M. *Angew. Chem., Int. Ed.*, 43, **2004**, 2129.

90. Tiemann, M.; Froba, M. *Chem. Mater.* 13, **2001**, 3211.
91. Schubert, M.M.; Hackenberg, S.; Veen, A.C.; Muhler, M.; Plazak, V.; Behm, R.J.; *J. Catal.* 197, **2001**, 113.
92. Kònyam, Z.; Puentes, V. F.; Kiricsi, I.; Zhu, J.; Alivisatos, A. P.; Somorjai, G. A. *Catal. Lett.* **2002**, 81, 137.
- 93 Barrio, L.; Campos-Mart ín, J.M.; Pilar de Frutos, M.; Fierro, J.L.G. *Ind. Eng. Chem. Res.* 47, **2008**, 8016–8024
- 94 Saraiva, M.S.; Filho, D.L.N.; Nunes, C.D.; Vaz, P.D.; Nunes, T.G.; Calhorda, M.J. *Microporous and Mesoporous Materials.* 117, **2009**, 670–677
95. Xie, C.X.; Liu, F.S.; Yu, S.T.; Xie, F.F.; Li, L.; Zhang, S.F.; Yang, J.Z. *Catalysis Communications* 10, **2008**, 79–82
96. Huong, T.M.; Fukushima, K.; Ohkita, H.; Mizushima, T.; Kakuta, N. *Catalysis Communications.* 7, **2006**, 127–131.
97. Jia, M.; Seifert, A.; Berger, M.; Giegengack, H.; Schulze, S.; Thiel. W.R. *Chem. Mater.* 16, **2004**, 877-882
98. Dai, L.X.; Teng, Y.H.; Tabata, K.; Suzuki, E.; Tatsumi, T. *Microporous and Mesoporous Materials.* 44-45, **2001**, 573-580
99. Claus J.H. *J.Am.Chem.Soc.* 123, **2001**, 8404-8405.
100. Hussain, M.; Song, S.K.; Lee, J.H.; Ihm. S.K.; *Ind. Eng. Chem. Res.* 45, **2006**, 536-543
101. Linares, C.F.; Am èzqueta, P.; Scott, C. *Fuel.* 87, **2008**, 2817–2823
102. Zhang, Q.H.; Yang, W.; Wang, X.X.; Wang, Y.; Shishido, T.; Takehira, K.; *Microporous and Mesoporous Materials.* 77, **2005**, 223–234
103. Shylesh, S.; Singh, A.P. *Journal of Catalysis.* 244, **2006**, 52–64
104. He, N.; Cao, J.; Bao, S.; Xu, Q. *Mater. Lett.* 31, **1997**, 133.
105. Liu, S.; Cool, P.; Lu, L.C.; Beyers, E.; Van der Voort, P.; Vansant, E. F.; Jiang, M. *Microporous and Mesoporous Materials* 79, **2005**, 299–305
106. Kawabata, T.; Ohishi, Y.; Itsuki, S.; Fujisaki, N.; Shishido, T.; Takaki, K.; Zhang,

- Q.H.; Wang, Y.; Takehira, K. *Journal of Molecular Catalysis A: Chemical*. 236, **2005**, 99–106
107. Haskouria, J. E.; Cabrerab, S.; Calde śc, M.; Alamo, J.; A. Portera, B; Marcosa, M.D.; Amoro śa, P.; Porter, D. B. *International Journal of Inorganic Materials* 3, **2001**, 1157 –1163
108. Gu, J.L.; Shi, J.L.; Xiong, L.M.; Chen, H.R.; Ruan, M. *Microporous and Mesoporous Materials*. 74, **2004**, 199–204
109. Plyuto, Y.; Berquier, J.M.; Jacquiod, C.; Ricolleau, C. *Chem. Commun.*, **1999**, 1653
110. Besson, S.; Gacoin, T.; Ricolleau, C.; Boilot, J.P. *Chem. Commun.*, **2003**, 360
111. Ozin, Dag.; Samarskaya, O.; Coombs, N.; Ozin, G.A. *J. Mater. Chem.* 13, **2003**, 328.
112. Vinu, A.; Sawant, D.P.; Ariga, K.; Hossain, K. Z.; Halligudi, S. B.; Hartmann, M.; Nomura, M. *Chem. Mater.* 17, **2005**, 5339-5345
113. Grubert, G.; Hudson, M.J.; Joyner, R.W.; Stockenhuber, M. *J. Catal.* 196, **2000**, 126.
114. Decyk, P.; Trejda, M.; Ziolk, M.; Glaszczka, K.; Bettahar, M.; Monteverdi, S.; Mercy, M. *J. Catal.* 219, **2003**, 146.
115. Choudhary, V.R.; Jana, S.K.; Kiran, B.P. *Catal. Lett.* 64, **2000**, 223.
116. Sun, Y; Walspurger, S.; Tessonnier, J.P.; Louis, B.; Sommer, J. *Applied Catalysis A: General*. 300, **2006**, 1–7
117. Fröba, M.; Köhn, R.; Bouffaud, G. *Chem. Mater.* 11, **1999**, 2858.
118. Decyk, P.; Trejda, M.; Ziolk, M.; Lewandowska, A. *Stud. Surf. Sci. Catal.* 142, **2002**, 1785.
119. Oldroyd, R.D.; Thomas, J.M.; Maschmeyer, T. P.; MacFaul, A.; Snelgrove, D.W.; Ingold, K.U.; Wayner, D.D.M. *Angew. Chem. Int. Ed.* 35, **1996**, 2787.

120. Sinclair, B.; *The Scientist*. 12, **1998**, 17.
121. Hadi, N.; Helda, H.; Salasiah, E.; Halimaton, H.; Zainab, R. *Materials Chemistry and Physics*. 96, **2006**, 337–342
122. Decyk, P.; Trejda, M.; Ziolk, M. *C. R. Chimie*. 8, **2005**, 635–654
123. Zhou, B.; Hermans, S.; Somorjai, G.A. *Nanotechnology in Catalysis, vol. 1*, Kluwer Academic/Plenum Publishers, New York, **2004**, 313.
124. Grosshans, V.S.; Tihay, S.F.; Rabu, P.; Paillaud, J.L.; Braunstein, P.; Lebeau, B.; Estournès, C.; Guille, J.L.; Rueff, J.M. *Microporous and Mesoporous Materials* 106, **2007**, 17–27
125. Ohtaki, M.; Inata, K.; Eguchi, K. *Chem. Mater.* **1998**, 2582–2584.
126. Okumura, M.; Tsubota, S.; Iwamoto, M.; Haruta, M.; *Chem. Lett.*, **1998**, 315.
127. Ghosh, A.; Patra, C.R.; Mukherjee, P.; Kumar, R.; Sastry, M. *Micropor. Mesopor. Mater.* 58, **2003**, 201.
128. Zhu, H.; Lee, B.; Dai, S.; Overbury, S.H. *Langmuir* 19, **2003**, 3974.
129. Haruta, M. *Studies Surf. Sci. Catalysis.*, 145, **2003**, 31.
- 130 Gimenez, J.; Nunes, C. D.; Vaz, P.D.; Valente, A.A.; Ferreira, P.; Calhorda, M.J.; *Journal of Molecular Catalysis A: Chemical* 256, **2006**, 90–98.

Chapter 2 Materials and Methods

2.1 Chemicals

Speciality chemicals used during the project along with their suppliers, are listed below:

Tetraethyl orthosilicate (TEOS) was used for the silica source in all syntheses. It was supplied as a pure liquid by BDH Chemicals Ltd., Poole, England.

The cationic surfactant cetyltrimethylammonium bromide (CTAB) and hexadecylpyridinium chloride (PD) were used as the structure directing agents and were supplied by Sigma-Aldrich, Steinheim, Germany.

Ferrocene (Fc) was supplied by BDH Chemicals Ltd, Poole, England.

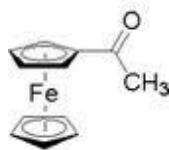
Cyclopentadienyl iron dicarbonyl dimer (Fy) and cyclopentadienyl molybdenum tricarbonyl dimer (O-Mo) supplied by Strem Chemicals, Newburyport, U.S.A.

Other organometallic complexes were prepared as required from readily available laboratory chemicals

2.2 Preparation of substituted ferrocenes

Four substituted ferrocene compounds were successfully synthesised by the Friedel Crafts reaction following the procedure of Main [1, 2]. The same mole ratios were used throughout, except for di-acetyl ferrocene where the acid chloride and aluminium chloride were doubled. All the compounds were red brown solids, except butyl ferrocene, which formed an oily product. Percentage yields were all about 50%. Acid chlorides were used in the reactions. Special care was taken to avoid contact of the acid chloride with H₂O. Glassware was oven dried, degreased with dichloromethane and dried under vacuum. The synthetic work was carried out by Gourdie as part of a related research programme [3]. Details of the syntheses are given below.

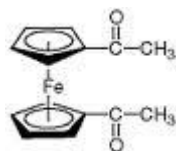
2.2.1 Preparation of acetyl-ferrocene (Fac)



The preparation instructions in section 2.2.1 to 2.2.4 are taken directly from the work of Gourdie [3]. Acetyl chloride (4.3 g, 0.055 mol) was added to ferrocene (9.3 g, 0.05 mol) and dry dichloromethane (40 mL) in a three necked, round bottomed flask (500 mL). The flask was equipped with a drying tube and a large magnetic stirrer bar. The flask was immersed into an ice bath. Anhydrous aluminum chloride (6.7 g, 0.05 mol) was then added in 10 portions with ≈ 1 minute between each addition. A watch glass was kept over the beaker containing the AlCl_3 between additions to prevent air from reacting with the AlCl_3 . The solution went from red brown to a deep wine red after the first few additions. The mixture was then stirred in an ice bath for 2 hours until the ice melted and the temperature rose to room temperature. The solution was returned to an ice bath and hydrolyzed by gradual addition of water (10 mL). Further water (10-15 mL) was then added more rapidly. The ice bath was removed and 10% aqueous $\text{Na}_2\text{S}_2\text{O}_4$ solution (prepared and used on the same day) was added drop wise with stirring until the upper layer turned from brown to a cream yellow. The solution was left to stir for 10-20 minutes until the strong odour of sulfur dioxide was no longer detectable. The reaction mixture was placed in a separation funnel and the lower (organic phase) was separated. The remaining aqueous layer was extracted 3 times with dichloromethane (30 mL) and the organic extracts were combined and washed first with 5% NaOH (10 mL) and then saturated NaCl (10 mL). The solution was dried over CaCl_2 and the solvent evaporated by two thirds. The solution was placed in a freezer (6°C) over night and allowed to crystallise. The supernatant was decanted from the crystals into a dry, clean round bottomed flask which was put back into the freezer for a further 24 hours. The first batch of red brown powder like crystals of Fac were collected and dried on a rotary evaporator and the yield determined (3.26 g). A second fraction of Fac crystals was collected and dried (0.56 g). The liquid was put back into the freezer to produce a third fraction of crystals

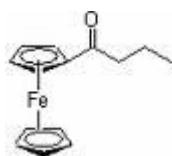
(0.72 g). An overall yield of 35.7% was obtained.

2.2.2 Preparation of di-Acetylferrocene (Fd)



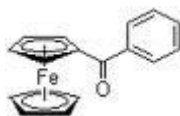
Di-acetyl ferrocene was prepared using the method described above for acetyl ferrocene. The quantities were: Acetyl chloride (8.6 g, 0.11 mol), ferrocene (9.3 g, 0.055 mol), dry dichloromethane (40 mL), anhydrous aluminium chloride (13.4 g, 0.1 mol), and water (10 mL). The first batch of brown powder like crystals was collected and dried on the rotary evaporator (4.31 g). The liquid that was put back into the freezer crystallized out over night and the second batch of crystals was collected and dried on the rotary evaporator (4.07 g). An overall yield of 57.0% was obtained.

2.2.3 Preparation of Butyrylferrocene (Ft)



Butyryl ferrocene was prepared using the acetyl ferrocene method. The reagents used were: Butyryl chloride (5.86 g, 0.055 mol), ferrocene (9.3 g, 0.055 mol), dry dichloromethane (40 mL), anhydrous aluminium chloride (6.7 g, 0.05 mol) and water (10 mL). Since no crystals were formed, even after prolonged cooling in the freezer, the solution was dried over CaCl₂ and the solvent evaporated off. This left the product Ft as a red brown gel-like material. The purity of the material was unknown and no yield was determined.

2.2.4 Preparation of Benzoylferrocene (Fb)



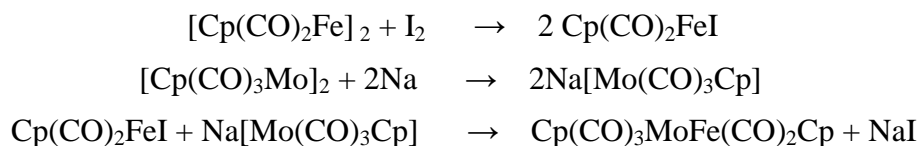
Benzoylferrocene was prepared in the same way as acetyl ferrocene. The quantities

were: benzoyl chloride (7.73 g, 0.055 mol), ferrocene (9.3 g, 0.055 mol), dry dichloromethane (40 mL), anhydrous aluminium chloride (6.7 g, 0.05 mol), and water (10 mL). The solution went from red brown to an intense purple after the first addition of AlCl_3 . The first batch of brown powder like crystals was collected and dried on the rotary evaporator (7.88 g). The liquid that was put back into the freezer crystallized out over night and the second batch of Fb crystals was collected and dried on the rotary evaporator (0.09 g). An overall yield of 52.7% was obtained.

2.3 Preparation of mixed metal complexes

2.3.1 Preparation of mixed Mo-Fe complex, $\text{Cp}(\text{CO})_3\text{MoFe}(\text{CO})_2\text{Cp}$

The compound was prepared by a two step reaction. Firstly $\text{Cp}(\text{CO})_2\text{FeI}$ was prepared and then this was reacted with $\text{Na}[\text{Mo}(\text{CO})_3\text{Cp}]$. The reactions are as follows;



Preparation of $\text{Fe}(\text{CO})_2\text{CpI}$ [2]

$\text{Fe}(\text{CO})_2\text{CpI}$ was prepared in a nitrogen-flushed Schlenk flask to which was added $[\text{Cp}(\text{CO})_2\text{Fe}]_2$ (4.00g, 10 mmol), I_2 (3.0g, 12 mmol) and CHCl_3 (50mL), the solution was refluxed for at least 30 minutes and left to cool. After evaporation of the solvent on the rotary evaporator and drying the residue on the vacuum line, the product (5.9 g) was a black powder, with carbonyl absorption bands $\nu(\text{CO})$ 2041 and 1996cm^{-1} (CH_2Cl_2 solution) c.f. lit. [2] 2044, 2000cm^{-1} (Hexane) indicating that the preparation had been successful.

Preparation of $\text{Cp}(\text{CO})_3\text{MoFe}(\text{CO})_2\text{Cp}$

A 1% sodium amalgam was prepared in a Schlenk flask from 140 g of Hg (10mL) and

about 1.4 g Na metal. 50 mL of THF was added and this was followed by purple $\text{Cp}(\text{CO})_3\text{Mo}$ (2.4 g, 5 mmol) and the mixture was stirred until complete conversion to the yellow $\text{Na}[\text{Mo}(\text{CO})_3\text{Cp}]$ reagent was achieved, (approximately 10 mmol). This solution was transferred by syringe under nitrogen to a solution of $\text{Fe}(\text{CO})_2\text{CpI}$ (3 g, 10 mmol) in THF (20 mL) in a N_2 -flushed Schlenk flask. The mixture was left to react for a couple of hours. The THF was removed under vacuum and the residue recrystallised from $\text{CH}_2\text{Cl}_2/\text{Et}_2\text{O}$. The powdered product was rinsed 5 times with $\text{CH}_2\text{Cl}_2/\text{Et}_2\text{O}$ by which time the rinsings were colourless.

2.3.2 Preparation of the mixed Mo-Co complex, $[\text{Cp}(\text{CO})_2\text{Mo}]_2\text{Co}(\text{CO})_3\text{CMe}$ and $\text{Cp}(\text{CO})_2\text{Mo}[\text{Co}(\text{CO})_3]_2\text{CMe}$

Preparation of $\text{MeCCo}_3(\text{CO})_9$

$\text{MeCCo}_3(\text{CO})_9$ was prepared in a nitrogen-flushed Schlenk flask to which was added $\text{Co}_2(\text{CO})_8$ (5.00 g, 15 mmol), MeCCl_3 (1.3 g, 10 mmol) and THF (50 mL). The solution was refluxed for at least 1-2 hours and left to cool. After evaporation of the solvent on the rotary evaporator and drying the residue on the vacuum line, the product was dissolved and recrystallised from petroleum spirits (60-80°C). The powdered product was rinsed 5 times with petroleum spirits by which time the rinsings were colourless and the product (1.7 g) was purple crystals. The reaction can be written as follows;

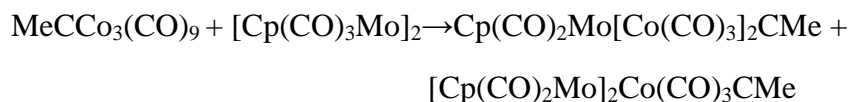


IR spectra (CH_2Cl_2 solution) 2102w, 2051vs, 2038vs, 2017m cm^{-1} . c.f. lit.[2] (hexane) 2109w, 2063vs, 2046vs, 2030m cm^{-1} .

Preparation of $[\text{Cp}(\text{CO})_2\text{Mo}]_2\text{Co}(\text{CO})_3\text{CMe}$ and $\text{Cp}(\text{CO})_2\text{Mo}[\text{Co}(\text{CO})_3]_2\text{CMe}$ [4]

The reaction of $\text{MeCCo}_3(\text{CO})_9$ with commercially available $[\text{Cp}(\text{CO})_3\text{Mo}]_2$, is

reported to yield two compounds, the relative amounts of each depending upon reaction conditions;



1.1g (2.4 mmol) $\text{MeCCo}_3(\text{CO})_9$, 0.8g (1.6 mmol) $[\text{Cp}(\text{CO})_3\text{Mo}]_2$ were dissolved in 50 mL benzene and refluxed under N_2 for about 4 days. The solvent was evaporated to dryness on a rotary evaporator and the product was leached out of the residue by rinsing with petroleum spirits until rinsings were no longer purple. The purple solution was chromatographed on a silica column and the eluant passed to waste. Product was then recovered using a petroleum spirits/benzene mixed solvent (5:1).to recover green $\text{Cp}(\text{CO})_2\text{Mo}[\text{Co}(\text{CO})_3]_2\text{CMe}$ and pure benzene to recover the $[\text{Cp}(\text{CO})_2\text{Mo}]_2\text{Co}(\text{CO})_3\text{CMe}$. Under the condition described above 0.25 g of $\text{Cp}(\text{CO})_2\text{Mo}[\text{Co}(\text{CO})_3]_2\text{CMe}$ was obtained and only traces of $[\text{Cp}(\text{CO})_2\text{Mo}]_2\text{Co}(\text{CO})_3\text{CMe}$. The purity of the products were confirmed by their IR spectra (CH_2Cl_2 solution) 2081vw, 2070m, 2051s, 2030vs, 2013m, 2002vs, 1950m, 1894sm cm^{-1} . c.f. lit. [2] (hexane) 2086vw, 2072m, 2043s, 2032vs, 2016m, 2003vs, 1948m, 1890sm cm^{-1} .

2.4 Preparation of pure silica mesoporous MCM-41 materials

Mesoporous silica was synthesized using CTEABr as the surfactant and TEOS as the silica source. 1.27 g of CTEABr was dissolved in 70 mL of 2.5 mol/L HCl in a 120mL beaker and 6.24 g TEOS was added with rapid stirring (1000 rpm, IKA[®] stirrer fitted with a 4.5 cm diameter propeller). After stirring for 8 hours at room temperature, the resultant white precipitate precursor phase was filtered, washed and dried at room temperature for several hours and then stored in a sealed vial. This material was calcined at 550°C to remove the template when required for loading by the I Method. The final samples of precursor phases and calcined materials were

characterized by low angle XRD and the calcined material was further characterized by BET surface area determination and BJH pore size measurements.

2.5. Loading mesoporous MCM-41 materials with organometallic complexes

2.5.1 Imbibing method (I Method)

The usual route to metal loaded MCM41 materials has been by post synthesis loading achieved by imbibing solutions of various metal compounds. This is sometimes called the incipient wetness method and will be abbreviated as the I Method. A general procedure for the I Method is as follows: 0.5 g of calcined mesoporous silica was added to 10 mL of the organometallic compound in toluene. In a departure from the normal imbibing procedure, the solution was stirred under partial vacuum for 24 h to ensure filling of all the pores with the complex solution. The vacuum was achieved by a water pump or a mechanical pump and was controlled to avoid excessive boiling and evaporation. Uncontrolled mechanical pumping led to the loss of the toluene solvent after approximately 15 min. The solid was filtered, washed until rinsings were colourless (generally this took 5x10 mL rinses with dichloroethane). This step was introduced to insure that all imbibed solution containing dissolved complex molecules not associated with the matrix was removed. In this way precipitation of complex aggregates when the solvent was evaporated was avoided. At the end of the rinsing period the product remained coloured. Prolonged further rinsing had no effect on the product colour indicating that the imbibed complex was not removed during prolonged rinsing. The sample was then dried at room temperature for 1 day.

2.5.2 Micelle method (M Method)

The micelle method (M method) was developed as a method to encapsulate the organometallic compound during synthesis. The compound (for example, ferrocene)

and the surfactant CTEABr were dissolved in a mixture of methanol (MeOH) and dichloromethane (CH_2Cl_2), from which the solvent was removed leaving an intimate mixture of the surfactant and the organometallic complex. The details of a typical preparation are summarised below.

Into a 50 mL round-bottom quickfit flask was added ferrocene (0.0575 g, 0.31 mol) and CTEABr (5.014 g, 0.138 mol), CH_2Cl_2 (6 mL) and MeOH (6 mL) and the flask was swirled until all solid had dissolved. Most of the solvent was removed on a rotary evaporator at 50°C . The remaining solvent was removed by connecting the flask to a water pump and pumping until the sample solidified. After one hour most of the product was recovered as a dry pale-yellow powder (4.51 g).

The dry pale-yellow powder prepared as described above was added into a 2.5 mol/L HCl solution to give a clear yellow solution. There was no evidence of insoluble ferrocene indicating that all the ferrocene had been solubilised in the CTEABr micelles, TEOS was slowly dropped in the rapidly stirred solution. After 24 hours, a yellow solid Metal-MCM-41 product and a pale blue supernatant containing oxidised iron was obtained. The product was filtered, washed and dried in air at room temperature, and then either stored in sealed vials or calcined for 4 h at 550°C .

2.5.3 TEOS method (T Method)

An alternative synthetic method for the preparation of metal loaded MCM-41 phases using organometallic compounds was achieved by dissolving the compound directly in the TEOS. This method is called the T Method. For example, Fc was dissolved in TEOS, and the doped TEOS was then added to acid as described above for the M-Method. The products were labelled as Metal-MCM-41. In cases where the complex was only poorly soluble in TEOS, 25% by weight of EtOH was added to the TEOS to enhance complex solubility. The EtOH had no effect on the MCM-41 when pure silica phases were prepared by the acid synthesis method. For those systems

where EtOH was necessary (Cp(CO)₃MoFe(CO)₂Cp (Mo-Fe) and Cp(CO)₂Mo[Co(CO)₃]₂CMe (Mo-Co), (see Section 6.1) for the T method, the same amount of EtOH in the TEOS was also used with the M method in order to allow direct comparisons to be made of the products from the two synthetic routes.

2.6 Characterisation of Mesoporous Silicas

Many different solid-state techniques can be used to characterise the mesoporous materials. Three broad categories are commonly used, diffraction, microscopic and spectroscopies techniques. These were used in the present work as described below.

2.6.1 Powder X-ray Diffraction (XRD)

Powder X-ray Diffraction (XRD) has been used for nearly a century and is an invaluable tool in solid state chemistry. It is primarily used for structure determination and the fingerprint characterisation of crystalline materials. X-rays are especially useful as the size of their wavelength is comparable to that of the distances between atoms in most crystals. This means that crystals can act as a diffraction grating, resulting in the scattered X-ray giving constructive and destructive interference patterns. The regular and repeating arrangement of atoms in a crystalline material create what is known as a Bragg angle when a crystal is subjected to X-rays, and then using Bragg Law:[7]

$$\sin\theta = n\lambda/2d \quad \text{-----(1)}$$

where n is an integer, λ is the wavelength considered, d is the inter-lattice spacing of the crystal, and θ is the angle of the incidence and of emergence of the radiation considered. The interplanar distance can be calculated from equation (1). As a result, highly crystalline materials generate XRD pattern with sharp and often distinct peaks or reflections, whereas non-crystalline materials show only broad features. By scanning through a series of incident angles, a diffraction trace can be obtained that is unique for the sample composition under analysis. Computerized data acquisition

allows the results to be compared with a library for rapid identification.

Crystalline materials are regularly analysed by X-ray diffraction, often with comparison to literature or the JCPDS database diffraction patterns as a means of identification. The JCPDS database contains over 60,000 entries, and many accumulated scans may be used in conjunction with this database to show the presence of small impurities. XRD can be very useful in the study of new materials as it may help to elicit important information such as crystallinity, it can provide information regarding the atomic constituents of the unit cell, and in some circumstances provide an estimate of the size of the particles present.

M41S materials are not crystalline with a regular lattice structure. The silica lattice is amorphous. However the regularity of the pore structure gives rise to diffraction effects. Thus XRD is especially useful in the study of these materials as it provides direct information about the arrangement of the pores. The order provided by the pores is short range so that there is generally only one strong diffraction peak corresponding to $n = 1$ in the Bragg equation. The d spacing corresponds to the diameter of the regularly arranged pores, typically giving a value of 2θ less than 10° . The combination of only these low angle reflections with no reflections in the higher region indicates an ordered pore structure surrounded by amorphous pore walls.

The structures of both the as-synthesized and calcined samples were characterised by small-angle powder XRD using a Philips X'PERT PW 3050/ θ - 2θ diffractometer. Samples were prepared by filling the sample holder with a slight excess compressing and leveling the sample with a microscope slide. While samples were not weighed care was taken to ensure that samples were of similar size so that peak intensities could be compared. Spectra were recorded using $\text{CuK}\alpha$ radiation and 2θ sampling technique. The voltage was set to 40 kV and the current to 40 mA. The scan was performed between 1.5 and 10° , with a step size of 0.02° . The time per step was set at 1.0 seconds. The diffraction patterns were analyzed using PC-APD diffraction

software.

Reproducibility of XRD results

The repeatability indicates the closeness of individual results obtained by the same method under the same conditions and over a small time range. Reproducibility is used to indicate the spreading of the results of replicate determinations; so a statement such as “results are highly (poorly) reproducible” means that the scatter of the results around the mean is low (high) so that a low (high) value of sample standard deviation (s) is expected.

The closeness of the replicate measurement in a set, i.e., the spread of the data about the central value (mean X) is defined as precision. The following measures of precision within a small set of n measurements are widely used:

Sample arithmetic mean	$X = \sum_i X_i / n$
Sample standard deviation	$s = [\sum_i (X_i - X)^2 / (n-1)]^{1/2}$
Relative standard deviation	$RSD = s/X$
Coefficient of variation (%)	$CV = (s/X) 100\%$

Experimentalists are aware that any measurement they make is affected by errors which can seriously affect the way the experimental results can be interpreted. The actions adopted to reduce these errors as much as possible will depend on the nature of the errors themselves and the use to which the information is intended to be put. A fundamental distinction can be made between random (statistical), and systematic (determinant) errors. In this research, random errors were estimated by carrying out replicate measurements. Systematic errors were checked for by periodically running selected samples as reference materials.

The reproducibility of the XRD results was assessed by taking about 3.0 g of uncalcined MCM-41-A pure silica (preparation 2.3) sample for XRD replicate measurement. About 0.3 g sample was taken from the bulk sample as a first testing.

After measuring, the tested sample was mixed with remaining bulk sample, and another 0.3 g sample was taken and measured. This process was repeated six times, and six results were obtained. The d_{100} spacing and intensity of all samples are shown in Table 2.1, where the sample mean (\bar{X}), sample standard deviation (s) and coefficient of variability (CV) are presented ($CV = (s/\bar{X}) 100\%$).

From the XRD patterns presented in Figure 2.1, it can be seen that the six XRD patterns for an uncalcined pure silica MCM-41 sample look very similar and have one sharp peak in the range of $2\theta = 2.5$ - 2.6° and two additional weak peaks in the range of 3.5 - 6° .

For the d_{100} spacing, the CV was 0.72%, indicating that the results are highly reproducible with low scatter of around the mean and a value of s of less than $0.02^\circ 2\theta$. However, for the intensity, the CV was 14.5% indicating that sample preparation, without weighing, can introduce significant errors to the intensity results. For most purposes it was felt that this reproducibility would be adequate.

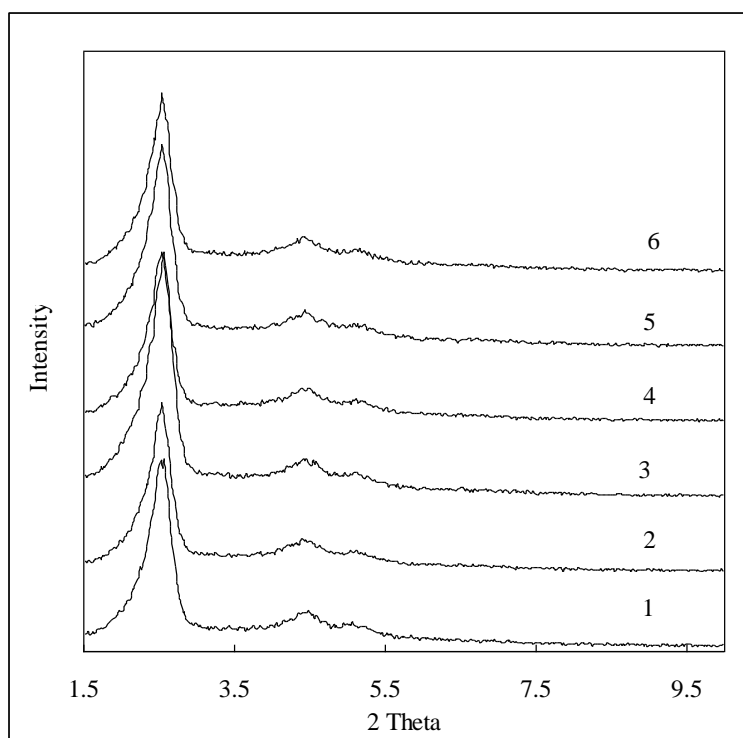


Figure 2.1 Replicate Powder XRD patterns of an as-synthesised MCM-41 sampled 6 times from a single batch of MCM-41.

Table 2.1 Data for XRD of the as synthesis samples with different time

Sample	1	2	3	4	5	6	X
2 Theta	2.57	2.54	2.58	2.53	2.54	2.54	2.55
d_{100} spacing	34.36	34.74	34.24	34.86	34.74	34.74	34.61
Intensity	2570	2321	3321	2315	2751	2447	2620

2 theta X = 2.55 s = 0.018 CV = 0.72%

d_{100} X = 34.61 s = 0.25 CV = 0.72%

Intensity X = 2620 s = 380 CV = 15%

Since no certified reference standard for MCM-41 has been made, the material used in this experiment was used as substitute reference standard. Data for XRD patterns of this sample measured over a period of 3 years are summarised in Figure 2.2 and Table 2.2. It can be seen from the five XRD patterns that while the d_{100} values are within ± 0.25 Å (0.72%), the intensities are much more variable than expected from the 15% CV obtained from replicates measured at the same time. In addition to intensity variation caused by sample preparation, we believe that further variation in samples run at different times resulted from variation in primary beam intensity of the XRD tube over the experimental period.

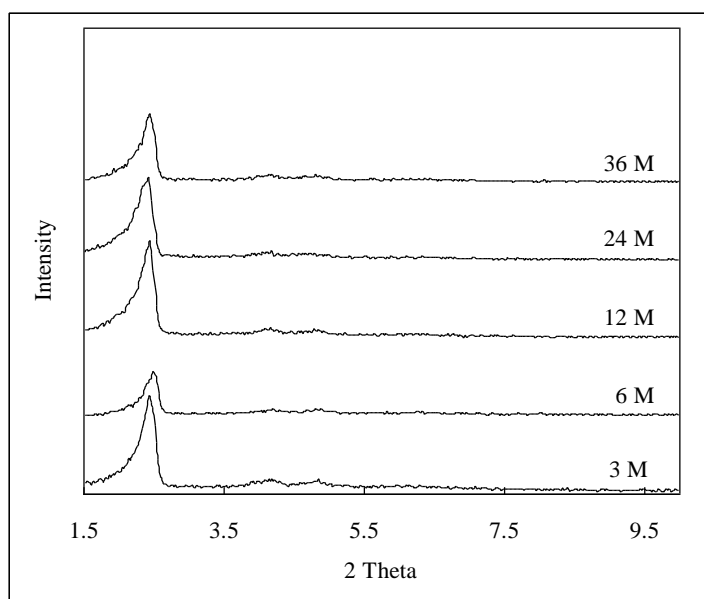


Figure 2.2 Powder of XRD patterns of the as-synthesis samples with different period

Table 2.2 Data for XRD of the as synthesised samples measured after various aging times

Age/months	3	6	12	24	36
2 Theta	2.44	2.47	2.45	2.44	2.45
d_{100} spacing (Å)	36.2	35.9	36.1	36.2	36.1
Intensity	12700	490	12600	10910	890

2.6.2 Nitrogen adsorption

Surface area (BET)

A well established method for determining the surface area of a powdered material is gas adsorption. The surface area is an important characteristic of a catalyst as it represents the amount of space on the material that is available for reaction. The high surface area of porous material results partly from both the external surface area of the particles but mainly the internal surface area of the pores. One of the more commonly used methods for measuring the total surface area of a material is the BET method, named after the developers Brunauer, Emmett Teller [5]. The most commonly used gas in gas adsorption is nitrogen. Many other gases, such as argon, oxygen, water, cyclopentane and benzene, have been used to characterise a variety of materials, but nitrogen remains as the most commonly used, and the technique has become much more widespread after the advent of user-friendly semi-automated commercial equipment and its associated software. The basic assumption of the method is that at the boiling point temperature of 77K, the amount of nitrogen that would be required to form a close-packed monolayer can be determined from the isotherm. The experimental method used to obtain the isotherm is generally a form of gas manometry where the amount of gas adsorbed is measured by a change in the gas pressure.

Pore size distribution

The distribution of pore volume with respect to pore size is called a pore size

distribution. It is generally accepted that the desorption isotherm is more appropriate than the adsorption isotherm for evaluating the pore size distribution of an adsorbent. The desorption branch of the isotherm, for the same volume of gas, exhibits a lower relative pressure, resulting in a lower free energy state. Thus, the desorption isotherm is closer to true thermodynamic stability. Since nitrogen has been used extensively in gas adsorption studies, it has been well-characterized and serves as the most common adsorbate for pore size distribution.

It is assumed that all pores emptied of their condensate during a relative pressure decrement have an average radius calculated from the Kelvin equation radii at the upper and lower values P/P_0 in the desorption step. The average capillary (core) radius is then used with the volume of gas desorbed over the pressure increment to determine the pore size distributions from the fraction of the pore volume that desorbs over the given pressure increment.

The equipment used was NOVA-1000 supplied by Quantachrome. An important feature of this instrument was that it allowed for the determination of a multipoint isotherm extending up to atmospheric pressure. The software provided allowed this information to be used to calculate porosity and pore size distribution according to the method proposed by Barrett, Joyner and Halenda (BJH) [6].

In order to determine the specific surface area and pore characteristics of a MCM-41 sample, approximately 0.1 to 0.2 g of the freshly calcined material was placed in the sample sample tube provided and the space filling rod was inserted into the neck of the tube. A 2.14-cm³ cell was used and was never filled more than to about one third of its volume to prevent sample loss during evacuation. It was confirmed by experiment that the degree of filling of the sample vessel did not affect final results. The sample was out-gassed at 120°C for 2 hours and then transferred to the measuring port. Depending upon sample weight the multipoint isotherm took between 30 minutes to 6 hours to run. Run time was the major reason why sample amounts had to

be limited, particularly when multipoint measurements were made.

The precision of the surface area/porosity measurements for MCM-41 samples was determined by taking about 3.0 g of freshly calcined MCM-41 and sampling about 0.1 g for testing. After the measurement the tested sample was mixed with the remainder of the sample and a second 0.1 g sample was measured. This process was repeated six times giving six replicate results. Data are summarised in Table 2.3 and Table 2.4.

Table 2.3 Data for replicate BET surface areas

Sample	1	2	3	4	5	6
Surface area (m ² /g)	1481	1582	1523	1377	1482	1436

Sample arithmetic mean $X = 1480 \text{ m}^2/\text{g}$

Sample standard deviation $s = 70 \text{ m}^2/\text{g}$

Relative standard deviation $RSD = 0.048$

Coefficient of variation (%) $CV = 4.8\%$

The data give a CV of 4.8%, and a sample standard deviation of $70 \text{ m}^2/\text{g}$.

The multipoint isotherm data was also used to determine the pore size distribution according to the BJH method. According to this method, the pore size distribution is divided into 10 pore size ranges and the surface area (or volume) associated with each pore size range is determined. From the pore size distribution presented in Figure 2.3, it can be seen that the six pore size distributions look very similar, with one sharp peak in the range of 2.3 nm, indicating that the pore size distributions were also highly repeatable.

Table 2.4 Data for pore area as a function of pore diameter (pore size distribution) for replicate samples of calcined MCM-41.

Pore size	1.33	1.57	1.83	2.07	2.30	2.55	2.98	3.68	4.63	6.11
-----------	------	------	------	------	------	------	------	------	------	------

1	346.2	262.6	222.2	312.5	491.0	280.9	66.78	16.4	8.88	4.74
2	330.5	299.7	185.5	325.2	504.3	288.2	70.39	16.9	8.82	4.84
3	359.1	284.4	206.0	322.9	479.9	327.9	73.77	15.8	9.22	5.13
4	404.9	267.0	191.5	331.7	466.8	338.9	73.25	18.2	9.65	5.24
5	386.1	264.5	221.3	314.4	450.8	332.8	63.58	16.4	9.02	4.94
6	377.0	293.2	203.3	353.0	493.1	272.7	73.42	16.3	8.94	4.95

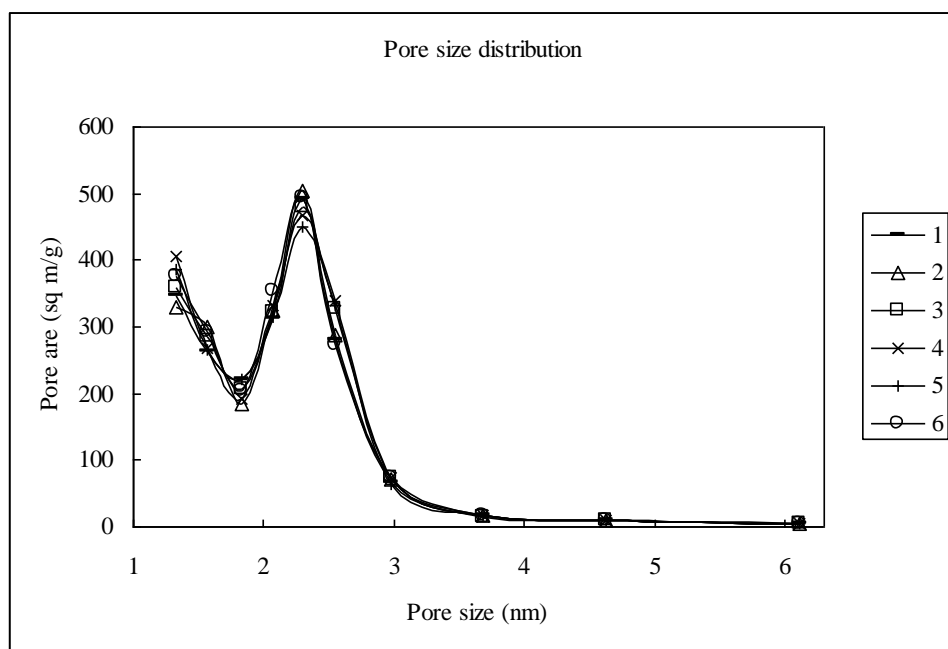


Figure 2.3 The pore size distribution of replicates of calcined MCM41

Calculation of wall thickness

In the case of MCM-41 with its hexagonally packed array of pores, wall thickness can be calculated from XRD and pore size data (Fig 2.4). The interplanar distance (unit cell) is the repeating unit, which in the case of MCM-41 is the distance across the half the face of the pore, the wall thickness and the other half of the face (see Figure 2.4). An approximate method for determining wall thickness is to use the pore size corresponding to the maximum in the pore size distribution determined by BJH method for P and the a_0 value determined from XRD. A more accurate measurement determination could be achieved by TEM.

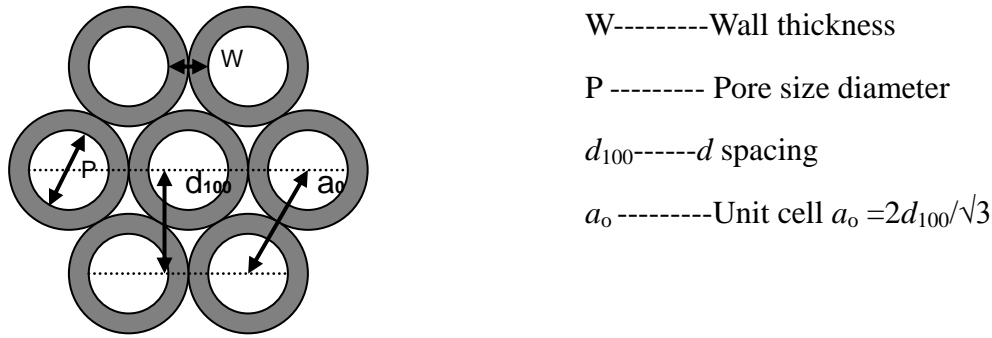


Figure 2.4 The geometric relationship between d spacing, unit cell or interplanar distance, pore size and wall thickness for MCM-41

From simple geometry it follows that;

$$W = a_o - P$$

2.6.3 Electron microscopy

Abbe's Law [8] dictates that the resolution of a microscope is:

$$d = 0.612\lambda/n \sin\theta$$

Where d is the resolution, λ wavelength of the radiation used to view the specimen, n refraction index of the medium through which the radiation travels, and θ is the aperture angle.

This means that the resolution is approximately equal to 1/2 the wavelength of the radiation used to view the specimen. The best possible resolution of an optical microscope using visible light is therefore ~200 nm. Electrons have a much shorter wavelength (~0.1nm) than light photons and are able to produce better resolution images. This allows much greater magnifications to be achieved than for optical systems.

Electron microscopy can be of two types: transmission electron microscopy (TEM) and scanning electron microscopy (SEM). TEM is similar to light microscopy in that the electrons pass through the sample. The sample has to be very thin to allow this. In

TEM, scattered electrons are used.

Scanning electron microscopy (SEM) is useful in the characterisation of the microscopic structure of materials with features of the order of 15 nm and above. Electrons are generated, accelerated by voltages between 1 and 30 kV and then directed towards a sample through the use of magnetic lenses. The primary beam of electrons scans the specimen and the backscattered, reflected and emitted secondary electrons are collected and focussed. As a result the technique is primarily used to study the surface, or near surface, of a specimen. In addition to revealing surface morphology, chemical analysis can be conducted by studying the X-ray fluorescence that occurs as a result of electron bombardment of the sample. SEM studies are of limited resolution and can also suffer from the fact that only a small percentage of the specimen is studied. SEM studies can be used in the characterisation of the M41S materials to determine surface properties and particle shape and morphology.

The instrument used for SEM was Hitachi S-4700. Dry powder samples were sprinkled onto brass stubs, excess material was removed with a gentle air stream from bellows and the sample was then coated with a carbon film to make it conducting. Representative micrographs were recorded electronically.

TEM images were collected from thin edges of the sample particles with a Phillips CM-30 electron microscope operating at 200 keV. TEM specimens were prepared by dipping a perforated carbon film supported on a copper grid into a suspension of mesoporous materials in ethanol that had been sonicated for 10 min and then left standing until the majority of the sample had settled. This ensured that only very small particles were captured onto the grid.

2.6.4 Fourier Transform Infra-Red Spectroscopy

Fourier Transform Infra-Red Spectroscopy (FT-IR spectroscopy) is a technique that is

commonly used for structure determination. It is a powerful tool for the characterization of specific function groups within a molecule (e.g. -OH, -COOH, -CH₂, -CH₃, groups etc). Infrared radiation can cause the atoms of molecules to vibrate. Each chemical bond in a molecule has a different strength and characteristic vibration frequency, therefore absorption of radiation occurs over a characteristic range of frequencies. Only a limited number of vibrational transitions are possible. The fundamental modes of vibration are stretching and bending. The absorption detected in an IR instrument gives rise to a spectrum that is unique for the specimen being analysed. The parameters used to describe a spectrum included the peak position (usually quoted as wave number of maximum absorption), and intensity (peak height or area).

FTIR was used to examine the MCM-41 phases that had been treated or prepared to incorporate organometallic complexes. The spectra obtained gave a quick indication of the presence of the compounds in the samples and whether any chemical change had occurred during encapsulation. For this work the instrument used was Spectrum 400 supplied by Perkin Elmer. Samples were prepared by KBr widow and scanning the appropriate wavelength range.

2.6.5 ICP/OES chemical analysis

Inductively coupled plasma/optical emission spectroscopy (ICP/OES) was used in initial studies of the metal content of the loaded samples. ICP/OES has revolutionized elemental analysis in the last two decades. The technique is based on classical atomic emission, except the atomization and excitation source is plasma. A plasma is an electrically neutral, highly ionized gas, which has a significantly higher temperature (5000-6000 K) and provides a less reactive chemical environment than a flame. The plasma gas is usually a stream of argon which is energized with high frequency electromagnetic field.

The major advantages of the ICP/OES technique is its ability to perform simultaneous multi-elemental analysis with a large linear dynamic range (determines a wide range of element concentrations without dilution), as well as minimal chemical interference and matrix effects. Spectral interference from complex samples may be overcome by selecting appropriate spectral line combinations.

Extraction and analysis of metals in the presence of Si matrix.

Initial experiments were performed on the ferrocene loaded precursor compounds. A 20-50 mg sample was dissolved in 2 mL 10% NaOH solution and heated to 40°C until the silica lattice had dissolved. Then 8 mL 40% HNO₃ was added to dissolve the ferrocene released. Initially a pale yellow solution suitable for analysis was formed. When the calcined samples were extracted, this way the iron oxide released upon dissolution of the silica matrix did not completely dissolve, even when heated to 60 to 80°C for prolonged periods. When 20% HCl was used in the acidification step, the iron oxide dissolved within 30 minutes. However, even when clear solutions were produced, the formation of a gel was observed after standing for more than 2 hours. This made analysis by ICP difficult because time delays between sample preparation and analysis were invariably greater than 2 hours. Initial results were variable and injection jet blockage was a major problem.

Atomic Absorption Spectroscopy

Atomic Absorption Spectroscopy (AAS) is based upon the absorption of radiation by free atoms, usually in the ground state. By selecting a wavelength for a given element that corresponds to an optical transition between atoms in the ground state and atoms in an excited level, the absorption of the radiation leads to a depopulation of the ground state. The value of the absorption is related to the concentration of the atoms in the ground state, and therefore, to the concentration of the element. By measuring the amount of radiation absorbed, a quantitative determination of the amount of

analyte can be made.

AAS is used routinely for quantitative elemental analyses. In brief the solution to be analysed is aspirated into the instrument where, it is drawn into the burner flame, undergoing a conversion from salt particles to an atomic vapour. A process of equilibrium between molecular, atomic and ionised atomic vapours then occurs. The position of this equilibrium depends on such factors as flame temperature, flame speed, solution composition and other factors.

The standard procedure for analysing samples generally involves the use of a standard of accurately known concentration of the element to be analysed (e.g. Fe). The solution with unknown concentration is then introduced and its concentration determined by interpolation by the AAS software using results for the previously determined standard. When the response is other than linear, it is necessary to plot a calibration curve using standards that cover the concentration range of interest.

While, as with ICP/OES methods, solid samples need to be dissolved completely in acid to yield homogeneous solution prior to analysis, AAS as an alternative to ICP/OE, had the advantage that access to the instrument was immediate so that samples could be analysed within 2 hours of their preparation. Thus the problem of gel formation could be avoided.

Metal analysis was performed on a GBC 919 atomic absorption spectrometer supplied by GBC Scientific Equipment Pty Ltd. For iron analysis, an iron lamp was used and operated conditions were: 341.5nm wavelength, 0.2 nm slit width, air-acetylene flame with flow rate set at 5.0.

Calibration curves for five Fe concentrations (from 10 to 50 mg/L) with matrices consisting of:

1. Standard prepared from $\text{Fe}(\text{NO}_3)_3$ in 20% HNO_3

2. Standard prepared from $\text{Fe}(\text{NO}_3)_3$ in 20% HNO_3 with 0.01 mg/L Si
3. Standard prepared from ferrocene in 20% HNO_3
4. Standard prepared from ferrocene in 20% HNO_3 with 0.01mg/L Si

Data are summarised in Figure 2.5 and 2.6. While absorbance for a given concentration of iron is systematically lower when the iron is in the form of ferrocene than when the iron is in the form of $\text{Fe}(\text{NO}_3)_3$, the presence of silica has a negligible effect.

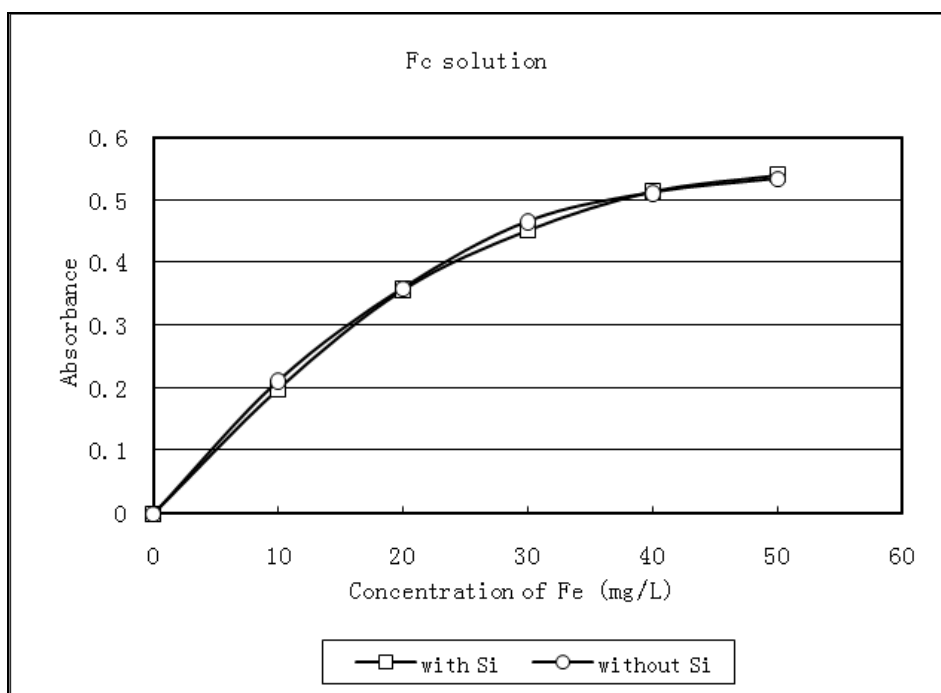


Figure 2.5 AA calibration curve for determination of iron with and without the presence of Si and using ferrocene solutions as standards.

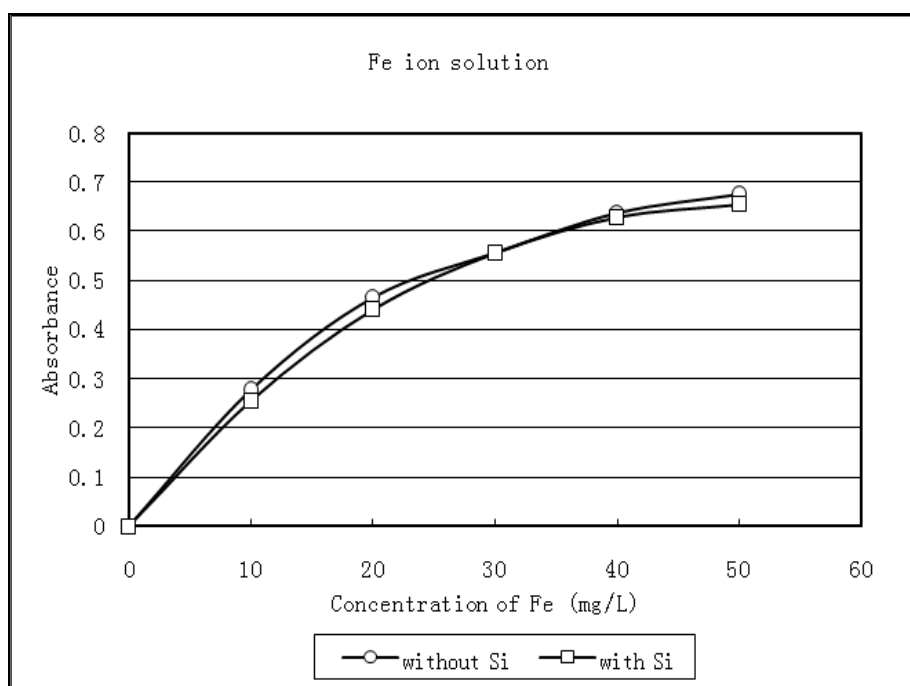


Figure 2.6 AA calibration curve for determination of iron with and without the presence of Si and using ferric nitrate solutions as standards.

2.7 References for Chapter 2

1. Main, L.; Nicholson, B. *Adv. Metal-Organic Chem.* 3, **1994**, 1, 4.
2. Adapted from R.B.King, *Organometallic Synthesis Vol 1*.
3. Gourdie, F. Undergraduate project report, University of Waikato, **2006**.
4. Thomas, J. M.; Thomas, W. J. *Principles and Practices of Heterogeneous Catalysis*, VCH, Weinheim, **1997**.
5. Brunauer, S.; Emmett, P.; Teller, E. *J. Amer Chem. Soc.*, 60, **1938**, 309
6. Barrett, E.P.; Jonyner, L.G.; Halenda, P.P. *J. Amer. Chem. Soc.*, 73, **1951**, 373
7. Sheppard, C.J.R. *Encyclopedia of Modern Optics*, **2005**, 61-69
8. Hayakawa, S.; Gohshi, Y. *Analytical Spectroscopy Library*. 7, **1996**, 171-206

Chapter 3 Optimisation of the synthesis of MCM-41 under acid conditions

3.1 Introduction

Mesoporous silica molecular sieves can be synthesized either in alkaline or acidic conditions [1]. The acid-derived materials have thicker pore walls, more ordered mesostructures, can be synthesized by less demanding conditions (room temperature and short reaction times) and, because the interaction between surfactant and silica framework is weaker, allow easier control over morphology [2]. Acidic products also have smaller pore diameters than the MCM-41 products hydrothermally synthesized in basic media. Although high-quality hexagonal mesophases can be obtained from extremely acidic to basic ($0 < \text{pH} < 11$) conditions, the superiority in terms of higher surface areas and larger mesopore volumes using extremely acidic synthesis conditions ($\text{pH} < 1$) has been demonstrated [3].

While hydrothermal synthesis does lead to the production of high quality mesoporous materials, it has several disadvantages. The size of the bomb leads to a limited amount of silicate produced each time, and often there is slight variation between different batches. This is presumably due to slightly different circumstances each time; caused by slight changes in temperature, or the level to which the bomb is filled.

In Section 1.3 the desired properties of the materials to be used in the present studies were specified to be: regular pore structure, large specific surface areas and good thermal stability. The literature review identified the acid route as being the most likely candidate. The purpose of this chapter is to optimize the conditions of the acid synthesis route with these desired properties in mind.

The formation of mesoporous structures under acid conditions is strongly influenced by acid concentration. This may be because of the known fact that liquid-crystal phases of surfactants are heavily dependent on acidity [3]. The fact that the kinetics of the

hydrolysis of TEOS followed by condensation/polymerization are also highly dependent on acidity [4] is a further reason why the acid concentration of the reaction system is a key factor in determining the structure and morphology of mesoporous materials produced.

3.2 Effect of acid concentration on mesoporous structures

The effect of acid concentration on the synthesis of mesoporous silica was investigated using CTAB as the surfactant and TEOS as the silica source. 1.27 g of CTAB was dissolved in the 70 mL of acidic solution with concentrations ranging from 0.5 to 7 mol/L HCl. 6.24 g TEOS was added under two stirring regimes: moderate magnetic stirring and rapid mechanical propeller (4.5 mm) stirring at 1000 rpm. The magnetically stirred solution remained as a fairly clear, two phase system and product was formed at the interface between the phases, whereas the system stirred at 1000 rpm immediately formed an opaque emulsion. After stirring for 8 hours at room temperature, the resultant white precipitate formed with both stirring regimes was filtered, washed and dried at room temperature for several hours and calcined at 550°C to remove the template. The final samples were characterized by low angle XRD, BET surface area determination and BJH pore size measurements.

It is well known that the silicate solution is stable in basic media but that polymerization and precipitation occur in acidic media. In the present synthetic method, a white solid product was formed sometime after the first droplet of the TEOS solution as Si source was added into the acidic surfactant solution. TG analysis showed that the precipitates contained a substantial amount of surfactant molecules. In contrast, rather than a white precipitate, a transparent gel was formed when the TEOS solution was added into the surfactant-free acidic solution. These results indicate that the precipitation is not due to the self-polymerization of silicate species but to the interaction between the silicate species and surfactant molecules.

3.2.1 XRD characterisation of MCM-41 phases from at different acid concentrations

The mesoporous structures of the materials produced at different acid concentrations was investigated using XRD. Data for the uncalcined materials produced at acid concentrations ranging from 0.5 to 7.0 mol/L and for a stirring speed of 1000 rpm are summarized in Figure 3.1. The data for magnetically stirred systems were essentially the same. Data for the same materials after calcining are given in Figure 3.2

The intensity of the XRD peak (d_{100}) for both the precursor and calcined materials increased with increased acid concentration in the range of 0.5-2 mol/L indicating an increase in order of the structures over that acid concentration range. The reverse effect was observed in the concentration range of 4-7 mol/L. The optimum acid concentration for synthesis of highly ordered MCM-41 phases appeared to be from 2 to 4 mol/L, but highly ordered mesophases can be synthesised at acid concentrations ranging for 1 to 6 mol/L. These results differ significantly from the 0.4 mol/L optimum acid concentration reported by Zhao [5]

The sharp XRD peaks in the range of $2\theta=2.1$ to 2.6° were indexed as 100 diffractions and the two additional weak peaks in the range of 3.5 to 6° were indexed as 110 and 200 diffractions, characteristic of a one-dimensional hexagonal mesophase.

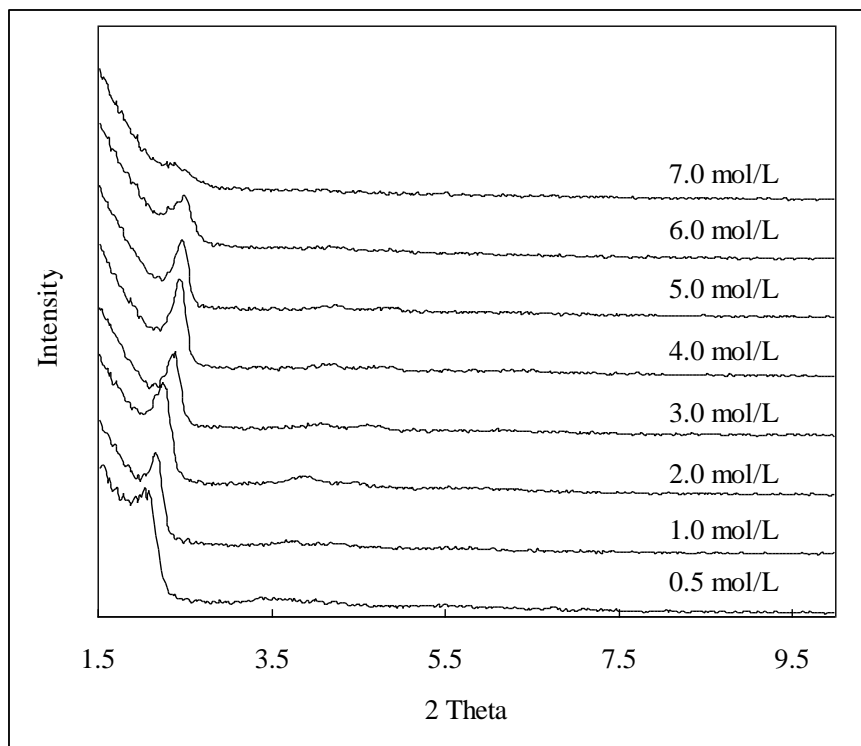


Figure 3. 1 XRD powder patterns for MCM-41 samples synthesised at different acid concentration.

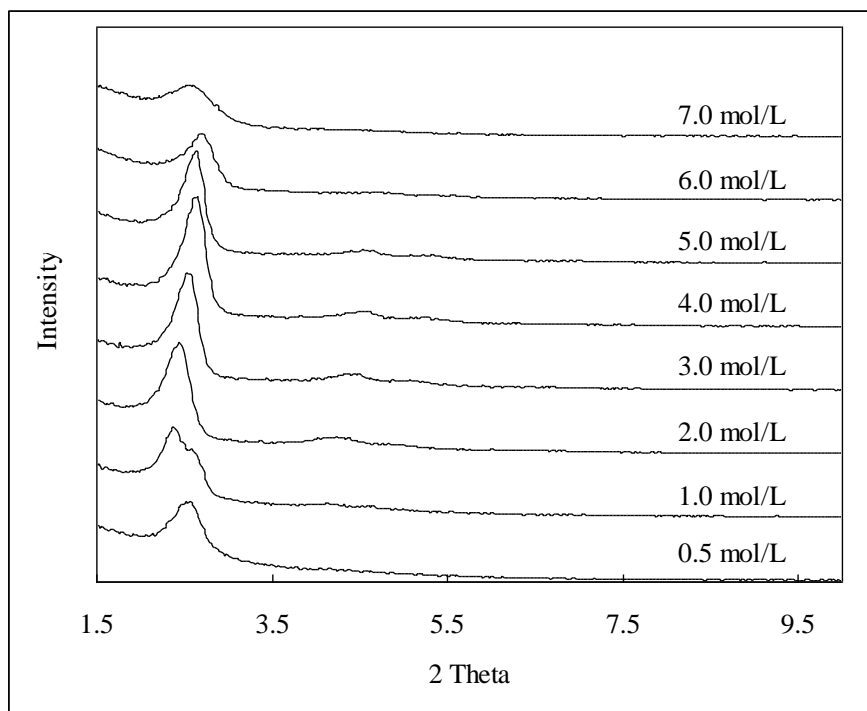


Figure 3.2 Powder of XRD patterns of the calcined MCM-41 samples synthesised at different acid concentrations.

The effect of acid concentration on the d_{100} spacing of both the as-synthesis and calcined samples are shown in Figure 3.3 and Table 3.1, where the d_{100} spacing values were calculated by means of $d = 2 \sin \theta / n \lambda$, where θ was the Bragg angle of the lowest angle peak and the value $n = 1$ was used.

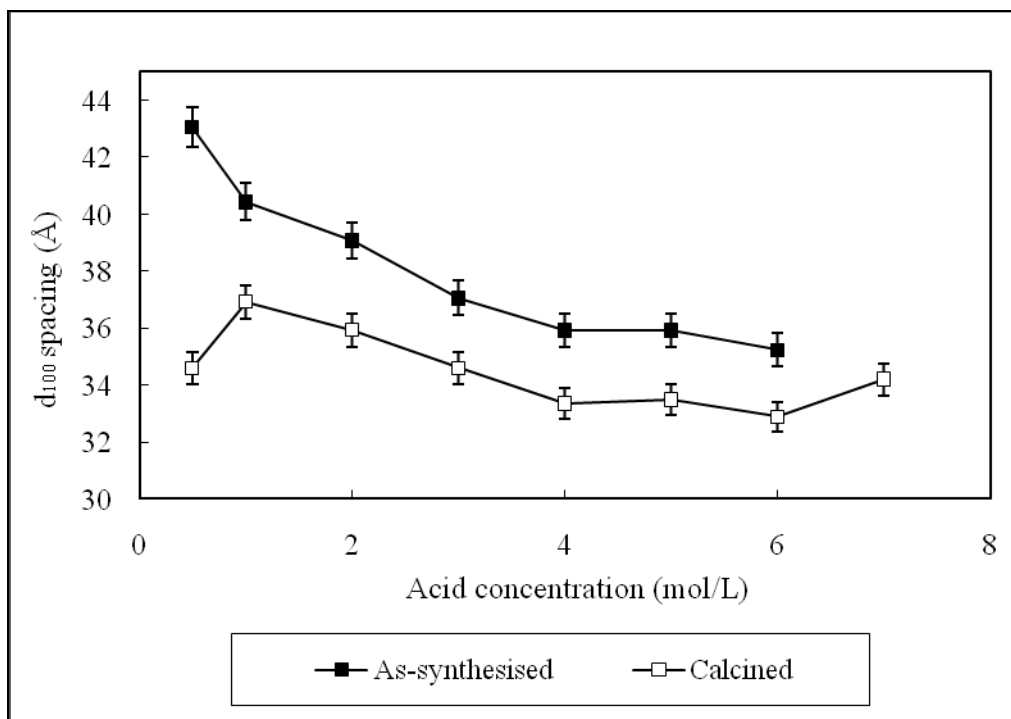


Figure 3.3 The change of d_{100} spacing for as-synthesised and calcined samples with the acid concentration from 0.5 to 7 mol/L. Error bars for the samples prepared at 0.5 mol/L acid are probably underestimates because peaks were poorly resolved and errors were expected to be much larger than for the other data plotted.

Table 3.1 d_{100} data for the as-synthesised and calcined samples for acid concentrations ranging from 0.5 to 7 mol/L

Acid conc.(mol/L)	0.5	1	2	3	4	5	6	7
d_{100} as syn.(± 0.3 , Å)	43.1	40.4	39.1	37.1	35.9	35.9	35.2	----
d_{100} calc.(± 0.3 , Å)	34.6	36.9	35.9	34.6	33.4	33.5	32.9	34.2
Contraction(± 0.5 , Å)	8.5	3.5	3.2	2.5	2.5	2.4	2.3	----

For as-synthesised samples, the d_{100} spacing decreased from 43.05 to 35.24 (Table 3.1) with increasing acid concentration, indicating that the unit cell decreased with increasing acid concentration.

The data also show that extremes of high and low acid concentration favoured the formation of disordered amorphous phases. At low HCl concentration (0.5 mol/L), the hydrolysis of TEOS was slow, taking about 90 min. to produce insoluble Si. Presumably the low $[H^+]$ concentration did not have ability to protonate or hydrolyze the silanol group. A glassy product was obtained giving only one broad XRD peak at about $2^\circ 2\theta$. When TEOS was added to the surfactant solution at acid concentrations above 1.0 mol/L, a rapid exothermic reaction occurred at the organic and inorganic interface. Flake-like precipitates appeared on the interface, after times that decreased from 30 min to 1 min with increasing acid concentrations over the range 1.0 mol/L to 7.0 mol/L.

The decrease in d_{100} spacing upon calcining from 8.5 to 2.4 (± 0.5) Å (20 to 7% reduction) with acid concentration indicated that shrinkage of the lattice was much greater for the poorly ordered phases formed at low acid concentrations. Shrinkage could occur because removal of the surfactant results in exposure of residual hydroxyl groups which undergoing condensation polymerization leading to a contraction of the pore center-to-center distance. The fact that this shrinkage decreased with increased acid concentration in the range 0.5 to 3 mol/L, might be explained by the observation that the higher acid concentration formed products with greater wall thicknesses. When acid concentration was above 3 mol/L, essentially constant contraction was observed.

A notable feature of the XRD data was the decrease in the intensity of the peaks at high and low acid concentrations. XRD intensity data for the as-synthesised and calcined samples are summarised in Figure 3.4 and Table 3.2 below.

Table 3.2 d_{100} intensities for the as-synthesised and calcined samples at acid concentrations from 0.5 to 7 mol/L.

Acid conc. (mol/L)	0.5	1	2	3	4	5	6	7
Intensity as syn. (± 140)	1170	1760	1940	1480	1700	1370	1140	
Intensity calc. (± 240)	5030	5750	7150	7430	8340	7220	4280	3310
FWHH	0.56	0.53	0.45	0.44	0.4	0.42	0.47	0.84

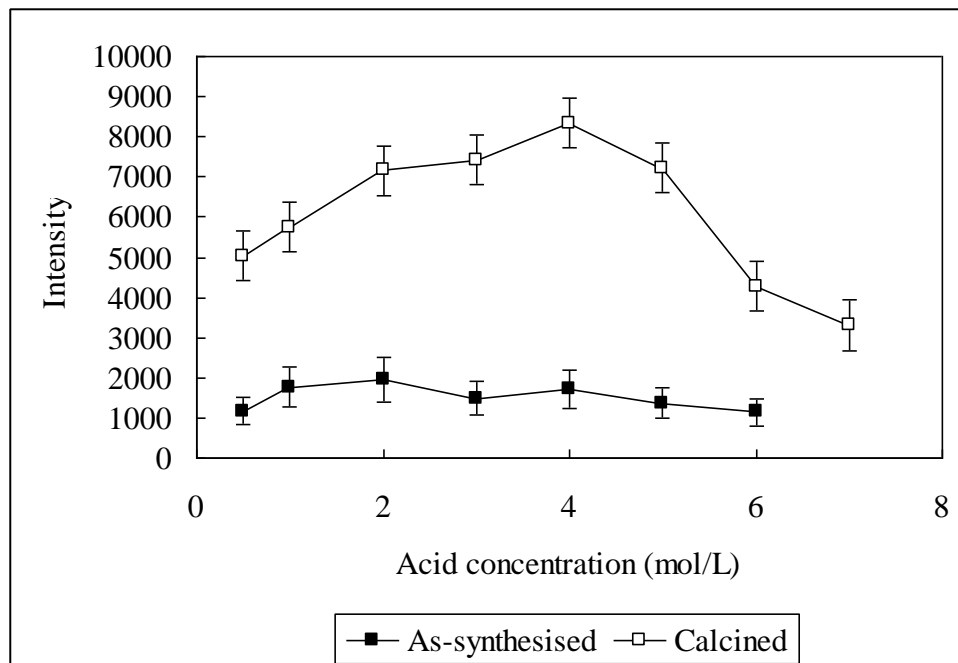


Figure 3.4 The change of intensity of d_{100} the as-synthesised and calcined samples with the acid concentration from 0.5 to 7 mol/L

The considerable increase in intensity and narrowing of the XRD peaks observed for the calcined samples indicates an improvement of the mesoporous order induced by the combined effects of the removal of the surfactant and the ensuing condensation polymerization reaction. The intensity of the d_{100} XRD peak increased with increased acid concentration in the range of 0.5-4 mol/L, and vice versa in the range of 4-7 mol/L. Another indicator of structural ordering is the full width at half height (FWHH) of XRD peaks. The FWHH of the d_{100} reflection decreased with increased acid concentration in the range of 0.5-4 mol/L, and vice versa in the range of 4-7 mol/L, giving further evidence for an optimum acid concentration for high ordering of approximately 4 mol/L.

A feature of the more highly ordered phases formed at intermediate acid concentrations was the appearance of more than a single XRD peak. Three peaks have been indexed as (100), (110) and (200). The d values for these peaks are summarized in Tables 3.3 and 3.4, along with the d_{100} : d_{110} and d_{110} : d_{200} ratios.

Table 3.3 d_{100} , d_{110} , and d_{200} data for the as synthesised samples at acid concentration from 2 to 5 mol/L.

HCl Conc. (mol/L)	d_{100} (Å)	Spacing	d_{110} (Å)	Spacing	d_{200} (Å)	Spacing	d_{100}/d_{110}	d_{110}/d_{200}
2		39.1		22.7		19.8	1.72	1.15
3		37.1		21.8		19.1	1.7	1.14
4		35.9		20.9		18.1	1.72	1.15
5		35.9		20.7		18.0	1.73	1.15

For the materials to be of a hexagonal arrangement, the ratio of d_{100}/d_{110} should be $\sqrt{3} = 1.732$ (as for the hexagonal system $d_{hkl} = 1/\sqrt{(4/3a^2)(h^2+k^2+hk)+(l^2/c^2)}$).[6] Similarly, the ratio of d_{110}/d_{200} should be $2/\sqrt{3}=1.155$. Both of the d_{100}/d_{110} and d_{110}/d_{200} ratios for the as-synthesised and calcined materials are close to the expected values, providing further evidence of the hexagonal arrangement.

Table 3.4 Data for XRD of the calcined samples acid concentration from acid concentration 2 to 5 mol/L

HCl Conc. (mol/L)	d_{100} (Å)	Spacing	d_{110} (Å)	Spacing	d_{200} (Å)	Spacing	d_{100}/d_{110}	d_{110}/d_{200}
2		35.9		20.7		18.2	1.74	1.14
3		34.6		20.0		17.3	1.73	1.15
4		33.4		19.4		16.8	1.73	1.15
5		33.5		19.3		16.9	1.73	1.15

3.2.2 N₂ adsorption–desorption isotherm of MCM-41

The specific surface area and pore structures of the MCM material formed at different acid concentrations were characterized by multi-point adsorption desorption studies using the NOVA instrument (See Section 2.5.2). Isotherms are presented in Figure 3.5 and surface areas and pore characteristics are summarised in Table 3.5

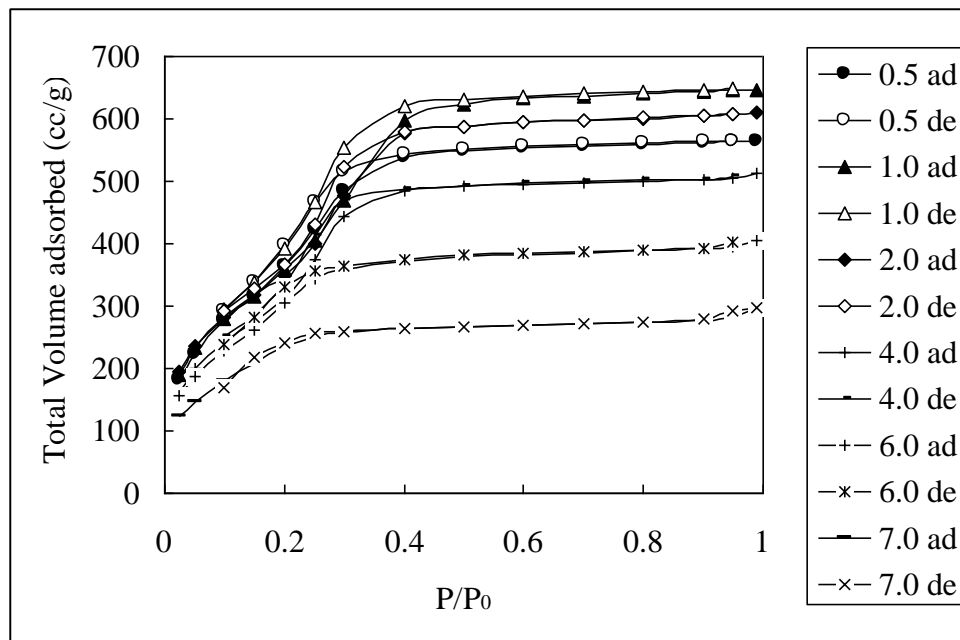


Figure 3.5 The effect of synthesis solution acid concentration on multi-point N₂ adsorption-desorption isotherms of calcined MCM-41 phases [ad.(adsorption), de.(desorption)]

Table 3.5 The effect of synthesis solution acid concentration on structural properties of calcined MCM-41 phases.

HCl conc. (mol/L)	Unit cell a_0 nm (± 0.03)	Pore size diameter nm (± 0.1)	Wall thickness nm (± 0.04)	Surface area m ² /g (± 70)	Total pore volume cc/g (± 8)
0.5	3.98	2.55	1.43	1540	872
1	4.25	2.98	1.27	1460	1000
2	4.13	2.80	1.33	1460	943
3	3.98	2.55	1.43	1570	914
4	3.84	2.40	1.44	1340	735
5	3.85	2.31	1.54	1340	725
6	3.78	2.10	1.68	1170	628
7	3.93	2.10	1.83	843	458

The effect of synthesis acid concentration on the surface areas of the calcined products was greatest at acid concentrations greater than 3 mol/L where a significant decrease in surface area was observed. Total pore volumes showed a similar decline with acid concentration above 3 mol/L.

The acid content of the synthesis solution also had a large effect on the pore size

distributions. This is illustrated in Figure 3.6.

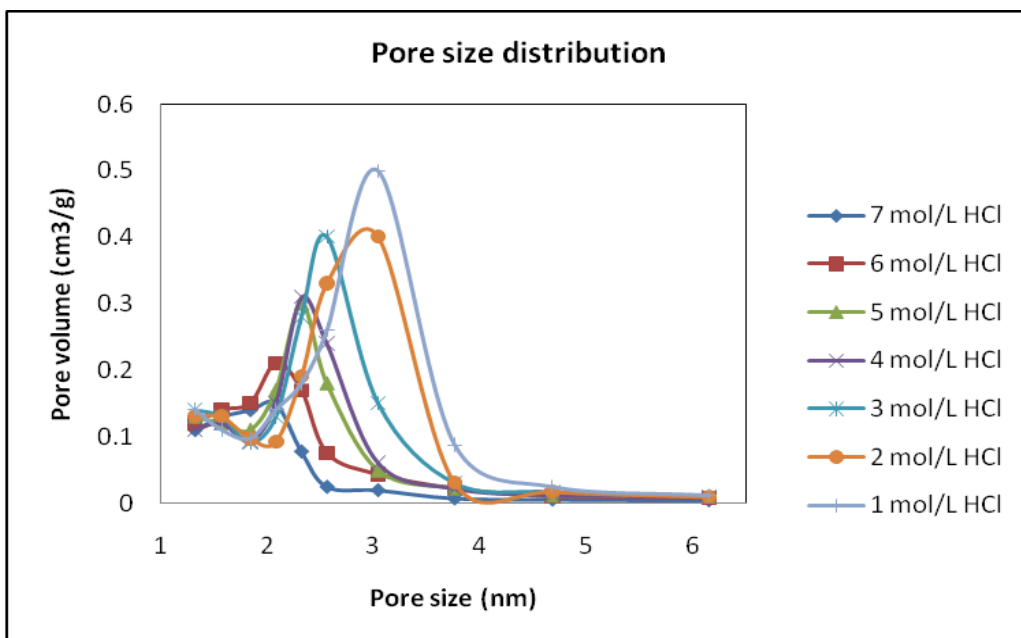


Figure 3.6 The effect of synthesis solution acid concentration on the pore size distribution of calcined MCM-41 samples.

The pore size distribution was analyzed using N₂ multi-point adsorption-desorption data following the BJH method. The pore size corresponding to the maximum in the pore size distribution curve (tabulated in Table 3.6) was then used with the unit cell parameters a_0 obtained from the XRD data (using the formula $a_0 = 2d_{100}/\sqrt{3}$, to estimate wall thickness according to the procedure outlined in Section 2.5.2 where (wall thickness = a_0 – pore size diameter). Data are summarized in Table 3.5.

In contrast to the surface area, pore size distribution for the MCM-41 samples varied much more widely with acid concentration, decreasing from 2.98 to 2.1 nm with increasing acid concentration. Increased acid concentration in the synthesis solution can be expected to compress the double layer thickness of the outer surface of the micelle, reducing the effective template diameter and hence the pore size. However, the unit cell parameter was much less affected by the acid concentration so thicker pore walls resulted. Thicker pore walls offer the potential advantage of enhanced thermal stability of the calcined materials.

3.2.3 Effect of acid concentration on Si yield

The Si % yield was determined from the ratio of the silica added to the synthesis mixture to the silica content of the final product. The as-synthesized product consisted of silica, surfactant and water. The water is evaporated and the surfactant is decomposed during the calcining, so that the final product after calcining consists of silica alone. Hence the final weight of the calcined product divided by the weight of silica expected from the weighed amount of TEOS added allows the % yield to be determined. Data for % yield as a function of acid concentration are summarized in Figure 3.7.

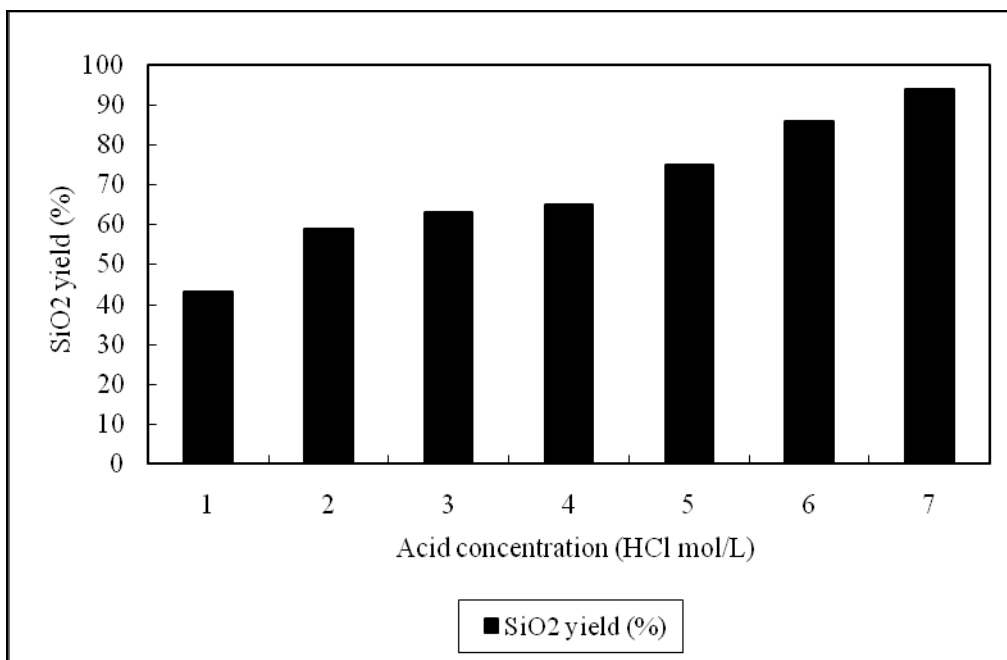


Figure 3.7 Silica yield as a function of synthesis solution acid concentration

The data show that the Si yield increases with acid concentration from 43% to 94%.

3.2.4 Effect of acid concentration on the Si/CTAB ratio in MCM-41 precursor

The weight loss of the dry precursor phase allowed an estimation of the amount of surfactant encapsulated in the precursor phase. Data are summarized in Figure 3.8

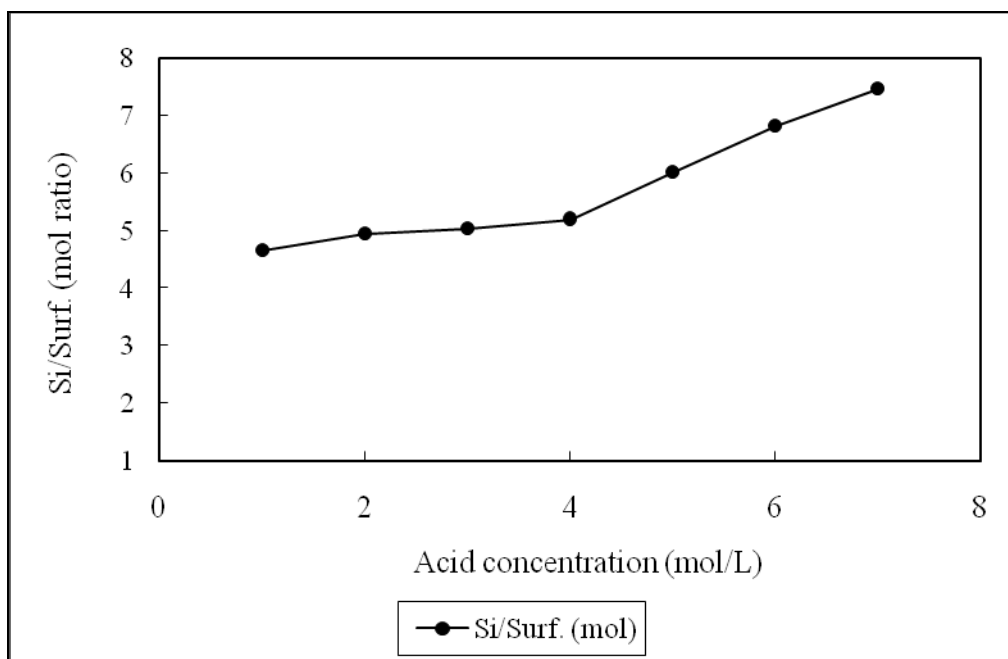


Figure 3.8 Effect of acid concentration on the Si/CTAB ratio in MCM-41 precursor

The Si/Surfactant ratio of precursor products increased fairly linearly with increasing acid concentration with a much steeper rate of increase above an acid concentration 4 mol/L. At the highest acid concentration used, more than two silica atoms were on average associated with each surfactant molecule.

3.3 The effect of reactant concentration

Mesoporous silica was synthesized using CTAB as the surfactant and TEOS as the silica source following the general procedure described in Section 2.4. Amounts of CTAB and TEOS (1.27 and 6.24 g respectively) were added to varying amounts of 2.5 mol/L acid to give surfactant concentrations ranging from 1.27 to 4.23 wt% (0.035 to 0.12 mol/L) for a constant Surfactant:Si ratio of 0.12. The surfactant was added to the acid and the TEOS was then added slowly with magnetic stirring. After stirring for 8 hours at room temperature, the resultant white precipitate was filtered, washed and dried at room temperature for several hours, followed by calcining at 550°C to remove the template. The final samples were characterized by low angle XRD, BET surface area determination and BJH pore size measurements.

3.3.1 Effect of reactant concentration on mesoporous structures

Representative XRD data for the precursor phases formed are given in Figure 3.11. Data for the calcined phases are given in Figure 3.12. The low intensities of the calcined phases can be attributed to deterioration of instrument beam intensity between preparation and calcining. This was indicated by much reduced intensity of the d_{100} line of a MCM-41 standard that was routinely run with experimental samples. Thus a direct comparison cannot be made between the intensities of the as synthesised and calcined materials. Trends in the position and intensity of the d_{100} peak however do reflect changes that occur upon calcining.

The XRD data indicate that MCM-41 phases were formed for all the surfactant concentrations used and that the structure remained intact after calcining.

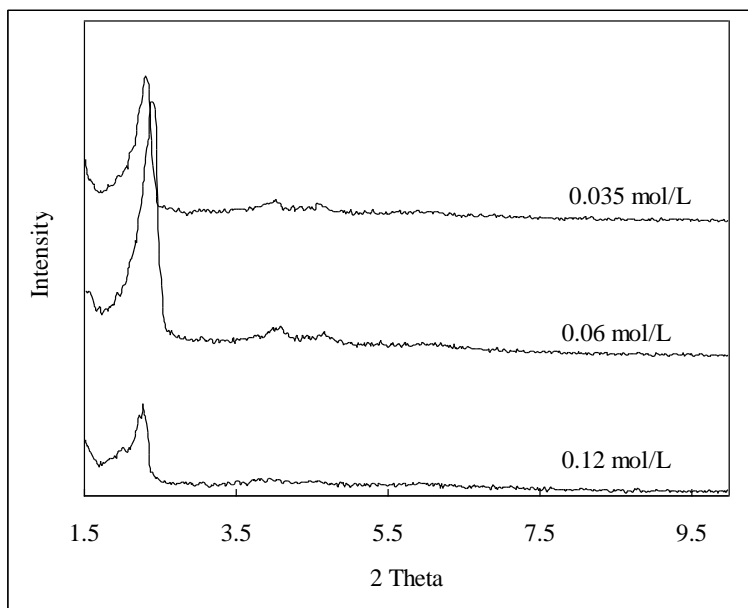


Figure 3.11 XRD patterns of the as synthesis samples synthesised with different surfactant concentrations.

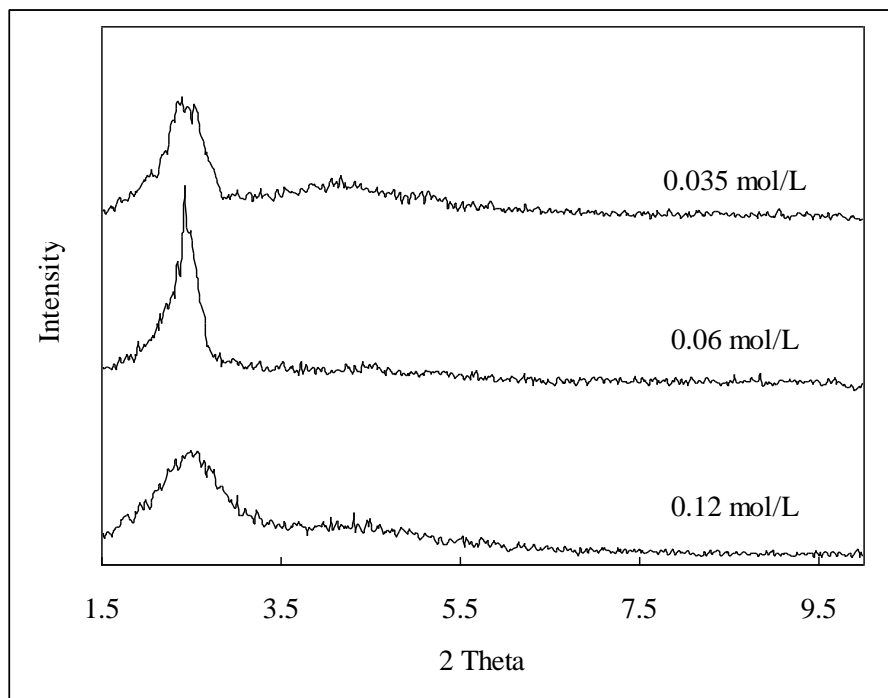


Figure 3.12 XRD patterns of the calcined samples synthesised with different surfactant concentrations.

The XRD data were used to determine d_{100} spacing (Figure 3.13) and relative intensities (Figure 3.14).

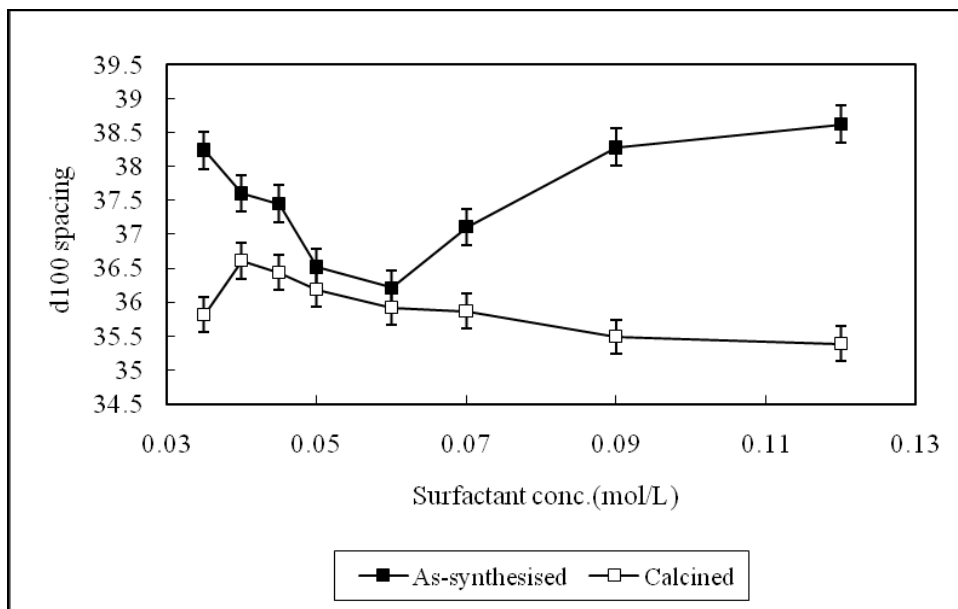


Figure 3.13 Variation of d_{100} spacing with surfactant concentration (0.035 to 0.12 mol/L) for as synthesised and calcined samples.

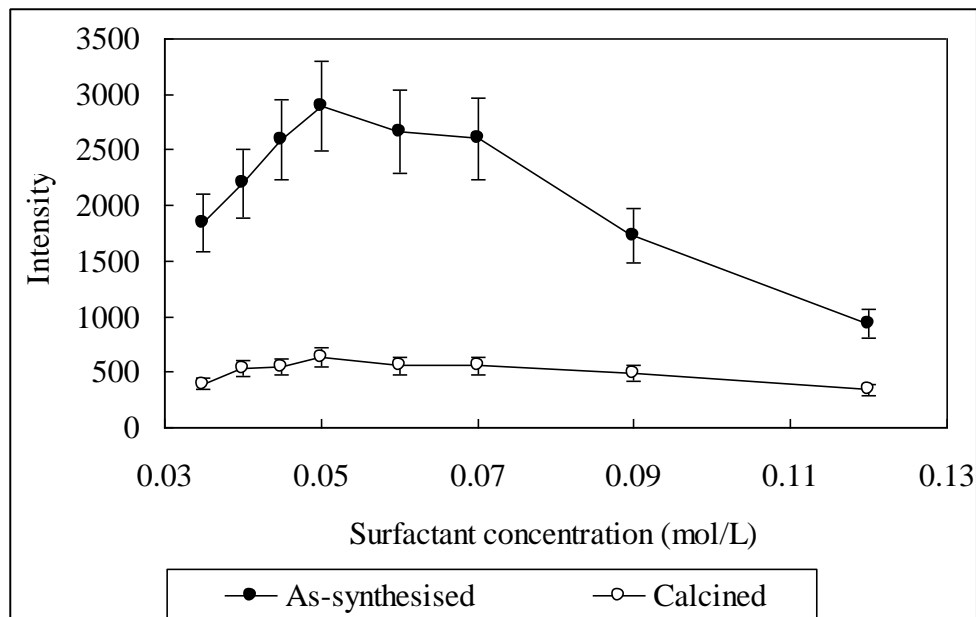


Figure 3.14 Variation of d_{100} spacing relative intensity with surfactant concentration (0.035 to 0.12 mol/L) for as synthesised and calcined samples.

Samples synthesised in the surfactant concentration range of 0.045 to 0.07 mol/L show well-resolved XRD patterns with one major peak (in the range of $2\theta = 2.1\text{-}2.6^\circ$ indexed to 100 diffractions) and two weak peaks (in the range of $3.5\text{-}6^\circ$ indexed to 110 and 200 diffractions in the range of 0.5-3). These are characteristic of a one-dimensional hexagonal structure, identical to that of MCM-41.

Figures 3.13 and 3.14 indicate that variations of the structure determined by XRD with surfactant concentration can be divided into two steps. Firstly, for the as-synthesised samples, the intensity of the d_{100} peak increased, and d_{110} , d_{200} peaks gradually appeared with increased surfactant concentration in the range from 0.035 to 0.05 mol/L. This indicated an ordering effect of the increased concentrations. The d_{100} spacing decreased from 38.2 to 36.5 Å over the same concentration range, indicating a slight contraction of the unit cell.

Over the concentration range from 0.06 to 0.12 mol/L, the relative intensity of the d_{100} peak decreased, and the d_{110} , d_{200} peaks gradually disappeared with decreasing the surfactant concentration. These trends indicated a lessening of the ordering within the

product. The d_{200} peak disappeared completely at surfactant concentration of 0.12 mol/L, suggesting a loss of the hexagonal symmetry. The d_{100} spacings increased from 36.2 to 38.6 with increasing surfactant concentration. The above results demonstrate that the optimum surfactant concentration for synthesis of highly ordered MCM-41 phases was from 0.05 to 0.06 mol/L, but ordered mesophases can be synthesised at surfactant concentrations ranging for 0.045 to 0.07 mol/L.

The optimum surfactant concentration determined for the as-synthesised materials was confirmed by XRD data for the calcined samples (see Figure 3.14). Tables 3.6 and 3.7 summarise d_{100} spacings and relative intensity data for the as-synthesised and calcined samples.

Table 3.6 d_{100} data the as-synthesised and calcined samples prepared at surfactant concentrations from 0.035 to 0.12 mol/L

Conc. (mol/L)	0.035	0.04	0.045	0.05	0.06	0.07	0.09	0.12
d_{100} as synth. ($\pm 0.25 \text{ \AA}$)	38.2	37.6	37.5	36.5	36.2	37.1	38.3	38.6
d_{100} calcined ($\pm 0.25 \text{ \AA}$)	35.8	36.6	36.4	36.2	35.9	35.9	35.5	35.4
Contraction ($\pm 0.5 \text{ \AA}$)	2.4	1.0	1.1	0.3	0.3	1.2	2.8	3.2

Table 3.7 The relative intensity of the d_{100} XRD peaks of the as synthesis and calcined samples prepared at surfactant concentrations from 0.035 to 0.12 mol/L

Surf. conc.(mol/L)	0.035	0.04	0.045	0.05	0.06	0.07	0.09	0.12
Intensity (± 130)	1800	2200	260	2900	2700	2600	1700	940
Intensity C (± 50)	390	530	550	630	560	560	490	340

The increase in the low angle reflection for the calcined silica samples corresponds to a decrease in the d_{100} spacing ranging from. 3.23 to 0.29 \AA . This decrease is consistent with condensation polymerization of residual hydroxyl groups and concomitant contraction of the pore center-to-center distance. The shrinkage was least at 0.06 mol/L surfactant concentration.

The trends indicated in the data given above may result from changes in concentrations of both the surfactant and the TEOS starting materials and the alcohol formed as a by-product of the reaction. Even at the highest surfactant concentration, rod shaped

micelles would not be formed in a simple aqueous solution. In the mixed surfactant-TEOS system the intensity and contraction data are consistent with micelle formation being most favoured at a surfactant concentration of approximately 0.06 mol/L (and a TEOS concentration of 0.5 mol/L). Conditions favouring micelle formation can be expected to give more ordered products that will be less affected by calcining.

A complicating feature of the experiment as performed was the increasing concentration of alcohol produced by the hydrolysis of the increasing concentrations of TEOS used (one molecule TEOS produces 4 molecules of ethanol during hydrolysis). The presence of alcohol can be expected to disturb micelle characteristics. The organic component of the alcohol is likely to favour absorption within the hydrophobic micelle core increasing the rod diameters and possibly destabilizing the micelle structure. The observed result is that beyond the optimum composition of reaction solution, the pore size increases and order decreases with the increasing concentration of by-product alcohol in the synthesis system.

3.3.2 Effect of reactant concentration on N₂ adsorption–desorption isotherms

Nitrogen adsorption isotherms for the calcined material are given in Figure 3.15 and structural properties derived from the isotherms and the XRD data are summarised in Table 3.8. The calcined materials synthesised from surfactant concentrations in the range of 0.035 to 0.12 mol/L surfactant exhibit typical type IV isotherm behavior (See Figure 3.15). The steep capillary condensation step for these samples is characteristic of a high uniform mesoporous structure.

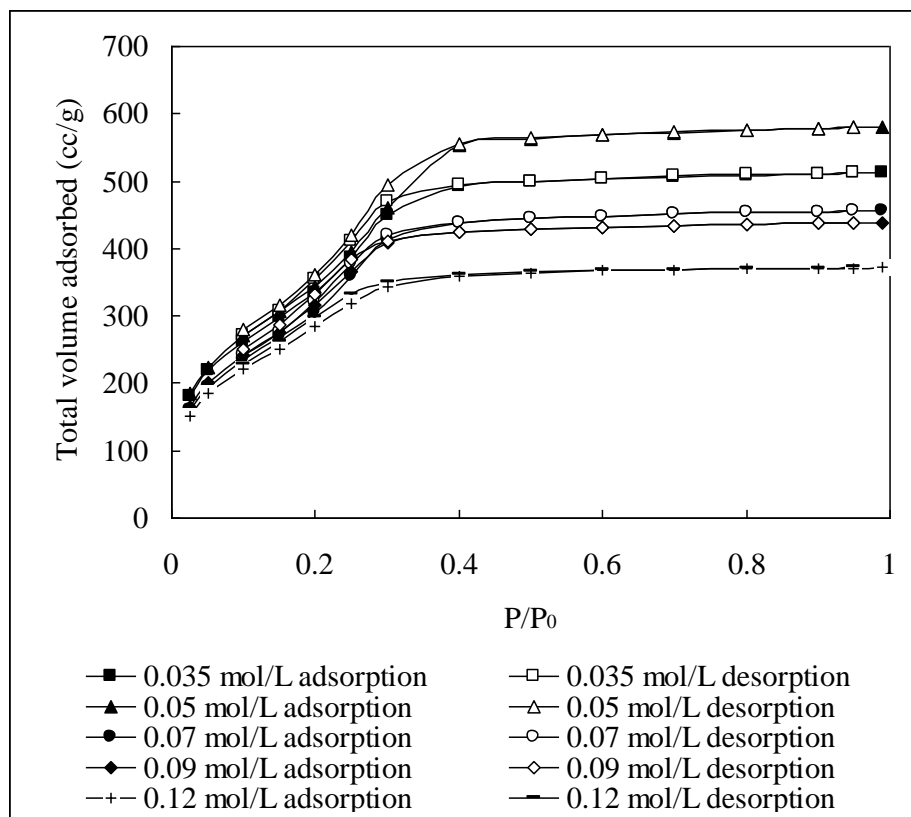


Figure 3.15 The effect of surfactant concentration on multi-point N₂ adsorption-desorption isotherms of calcined MCM-41 phases

Table 3.8 summarizes the structural features obtained from analysis of the XRD data and the isotherm data and includes the unit cell a_0 , mean pore diameter, wall thickness, total surface area and total pore volume calculated by the procedures described in Sections 2.5.

Table 3.8 The effect of surfactant concentration on structural properties determined from XRD diffraction and N₂ adsorption-desorption isotherms of calcined MCM-41

Surfactant concentration (mol/L)	Unit cell nm(± 0.025)	Pore size diameter nm(± 0.01)	Wall thickness nm(± 0.035)	Surface area m ² /g (± 70)	Total pore volume cc/g (± 8.6)
0.035	4.14	2.57	1.57	1230	480
0.04	4.21	2.55	1.66	1400	510
0.045	4.19	2.75	1.44	1430	530
0.05	4.18	2.98	1.20	1520	580
0.06	4.15	2.99	1.16	1420	580
0.07	4.13	2.57	1.56	1290	460
0.09	4.10	2.44	1.66	1290	440
0.12	4.09	2.19	1.90	1100	370

The BET specific surface areas range from 1098 to 1521 m²/g increasing with surfactant concentration from 0.035 to 0.05 mol/L, and then decreasing from 1521 to 1098 m²/g with concentrations increasing from 0.05 to 0.12 mol/L. The optimum surfactant concentration for achieving maximum surface area is approximately 0.05 mol/L.

Pore volume trends (Table 3.8) are similar to those of specific surface areas.

The trends in unit cell dimension, pore size diameter and wall thickness are shown in Figure 3.16.

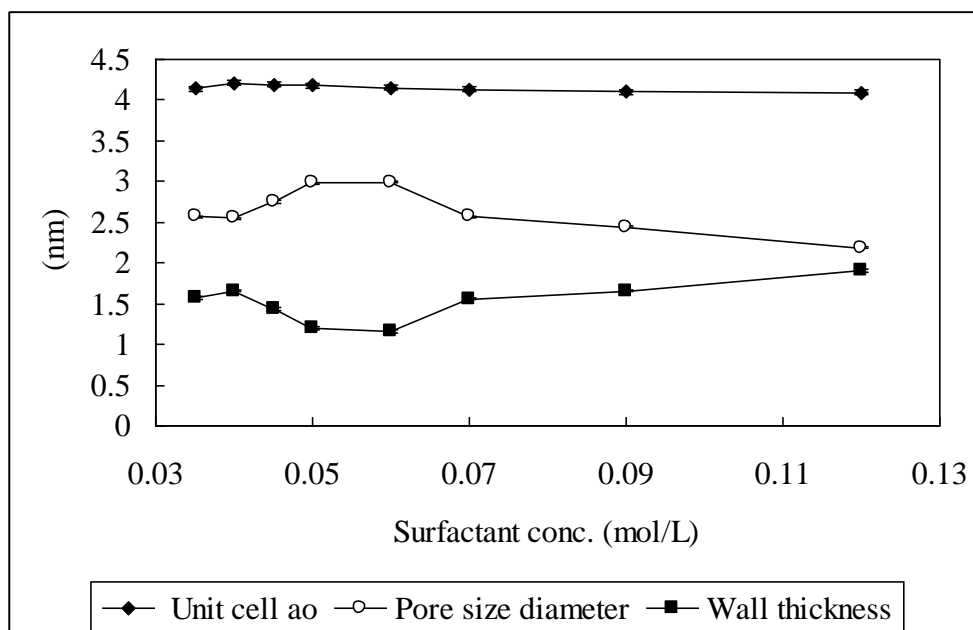


Figure 3.16 Trends in unit cell dimension, pore size diameter and wall thickness

Surfactant concentration appears to have little effect on the unit cell dimension of the calcined product but there are significant changes in pore diameter and wall thickness. The wall thicknesses are least and the pore diameters are largest at the optimum surfactant concentrations of 0.05 to 0.06 mol/L. The thicknesses increase and the pore diameters decrease on either side of this optimum.

It is reasonable to suppose that the unit cell parameter (a_0) of the as-prepared MCM-41,

which passes through a minimum at the optimum concentration between 0.05 to 0.06 mol/L., reflects micelle geometry in the synthesis solution. This will be affected by the presence of both the surfactant and silica components. The cell parameter of the calcined material will be determined solely by the packing of the silica. The larger size of the cell parameter of the as-synthesised material is consistent with a larger micelle in the synthesis solution which would favour the incorporation of more silica into the micelle. After calcining, this extra silica contributes to the greater wall thickness and smaller pore diameter of those materials prepared at other than the optimum concentrations.

The increased micelle size at the higher synthesis concentrations might be explained by the role of the alcohol released during the reaction. [7] The expanded micelle resulting from the absorption of the alcohol would have greater surface film volume and hence a greater volume for silica incorporation. It is less obvious why the micelles should be larger at composition less than the optimum. It may be that at lower surfactant concentrations, relatively More silica is incorporated into fewer micelles making the moiccles larger overall. Pore size distribution curves are shown in Figure 3.17

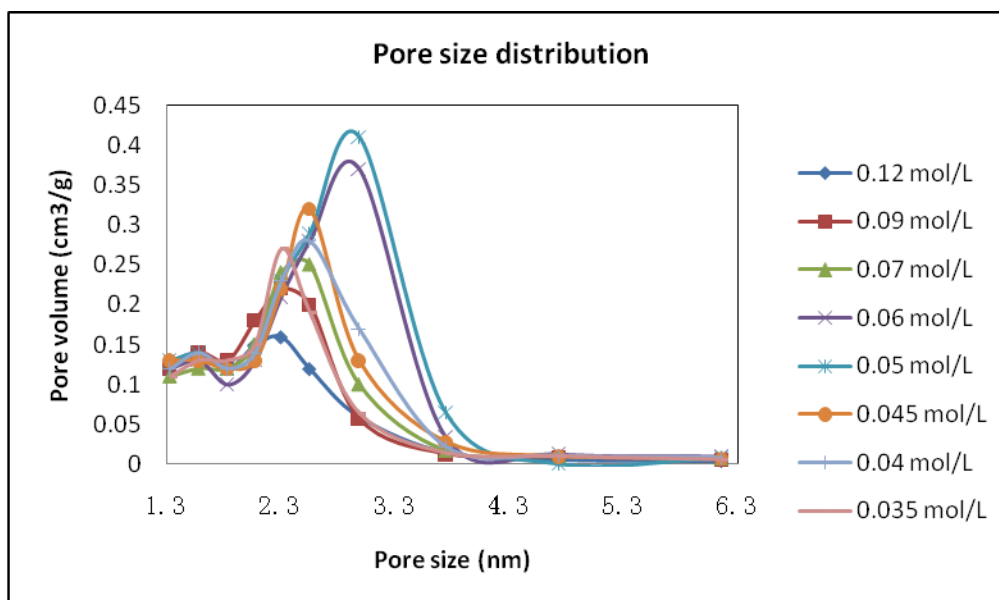


Figure 3.17 BJH-derived pore size distribution curves for MCM-41 prepared at various reagent concentrations

It is apparent that while the pore sizes and volumes are much larger at the optimum synthesis concentrations, the pore size distributions are similar.

3.3.3 Effect of reactant concentration on Si based yield

The MCM-41 yields calculated from the weight of calcined product compared with the Si content of the TEOS starting material, for the varying synthesis mixtures are given in Figure 3.18

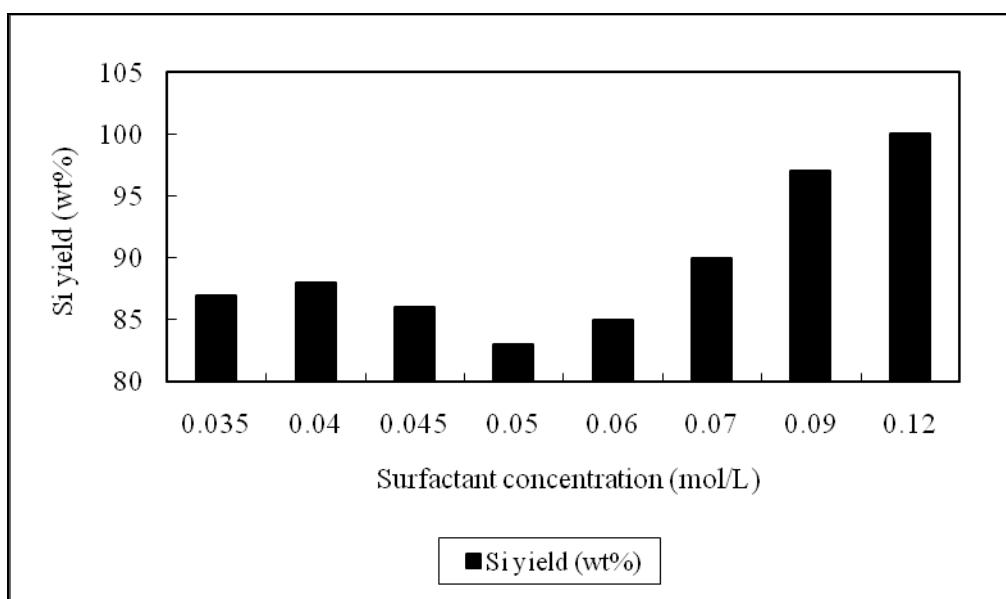


Figure 3.18 The Si yield for various synthesis compositions

Yields for the optimum product were approximately 85% and while yields increased to 100% when the reagent compositions were increased, the product formed was inferior.

3.4 The effect of reaction time

Mesoporous silica was synthesized using CTAB as the surfactant and TEOS as the silica source following the general procedure described in Section 2.3, for reaction times ranging up to 72 hours. After magnetic stirring (approximately 300 rpm) at room temperature, the resultant white precipitate was filtered, washed and dried at room temperature for several hours, followed by calcining at 550°C to remove the template.

Both the as synthesized and calcined MCM-41 mesophases were characterized, where appropriate, by low angle XRD, BET surface area, BJH pore size distribution and Si based yields of products.

3.4.1 Effect of reaction time on mesoporous structures

It was found that with stirring at 300 rpm, an induction time of 30 minutes from addition of TEOS was necessary before white precipitates were observed. At times between 30 minutes and three hours the semi opaque product obtained gave only one broad XRD peak at about $2^\circ 2\theta$, indicating a disordered amorphous phase. Evidence for composite mesophases was obtained only after 3 hours of reaction. Thus the first sample for detailed characterization was taken from the reaction mixture after 3 hours. A further 7 seven samples were taken over the subsequent 69 hours.

XRD data for the synthesised and calcined samples are given in Figures 3.19 and 3.20.

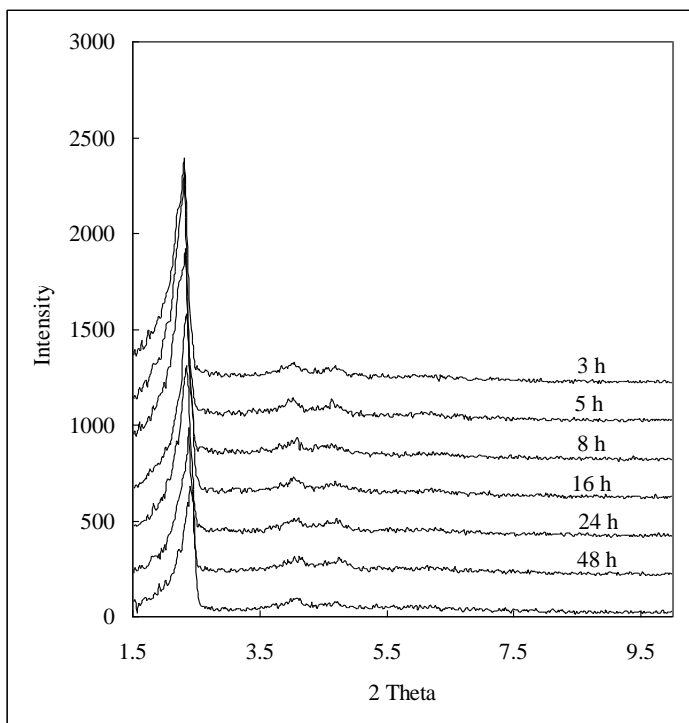


Figure 3.19 XRD patterns of the as synthesised samples after reaction times ranging from 3 to 72 hours.

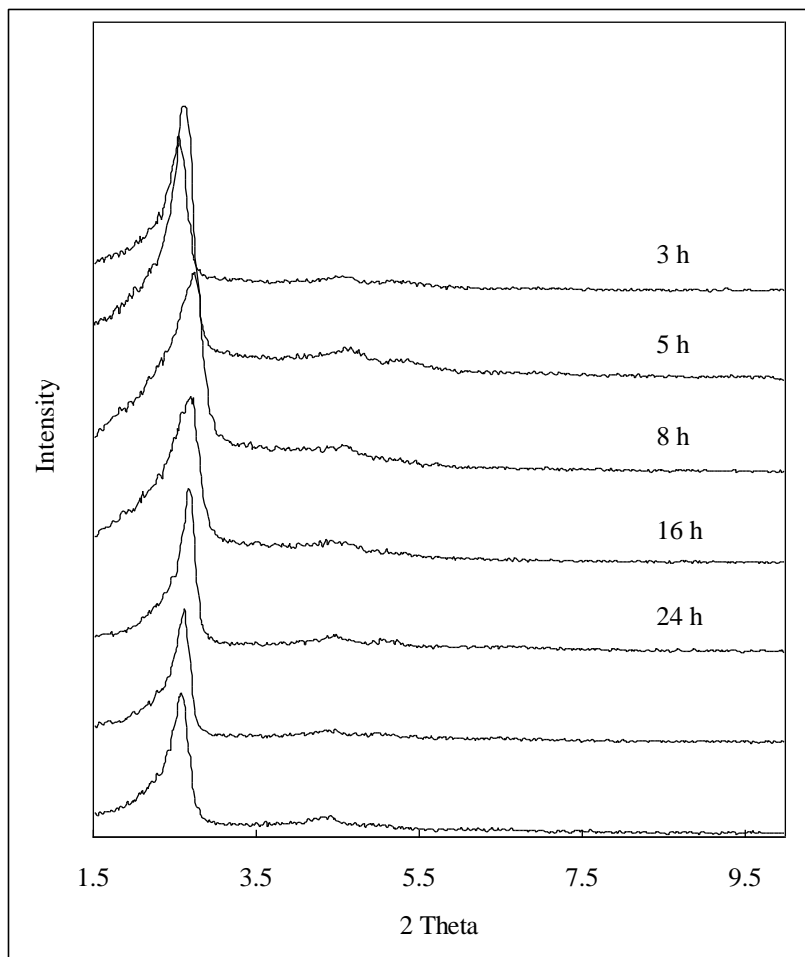


Figure 3.20 XRD patterns of the calcined samples after reaction times ranging from 3 to 72 hours.

The XRD data confirmed that MCM-41 was the only product formed for reaction times varying from 3 to 72 hours and the structure remained intact after calcining. There was no evidence for the growth of impurity phases. The assignment of the three main peaks was as discussed in Section 3.

Some variation in d_{100} spacing and line intensity for both as synthesized and calcined samples was observed. The variation with reaction time of d_{100} spacing is shown Figure 3.21 and Table 3.9 and variation in line intensity is shown in Figure 3.22 and Table 3.10.

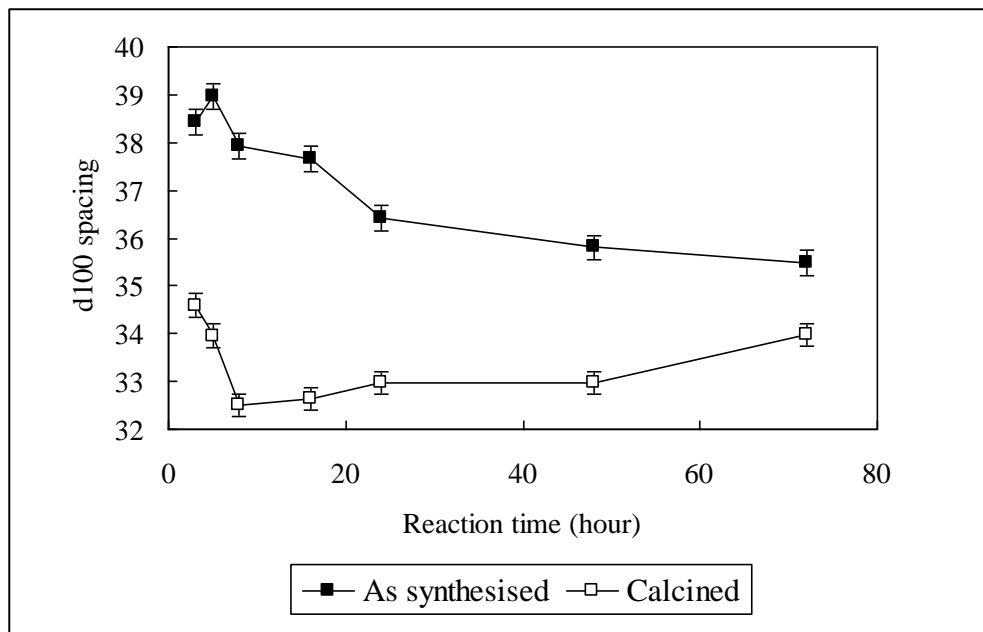


Figure 3.21 Variation of d_{100} spacing with reaction time (3 to 72 h) for as synthesised and calcined samples.

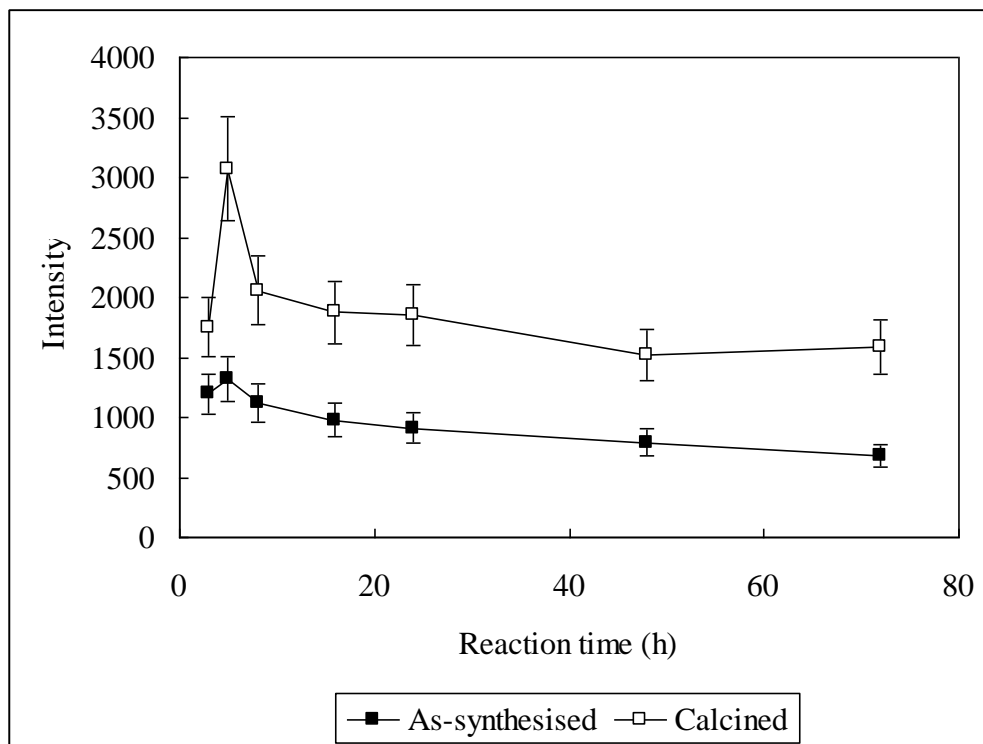


Figure 3.22 Variation of d_{100} intensity with reaction time (3 to 72 h) for as synthesised and calcined samples.

Table 3.9 XRD d_{100} data for the as-synthesised and calcined samples reacted for times varying from 3 to 72 h.

Reaction time (hours)	3	5	8	16	24	48	72
d_{100} as syn.(± 0.3 , Å)	38.4	39.0	37.9	37.7	36.4	35.8	35.5
d_{100} C.(± 0.3 , Å)	34.6	34.0	32.5	32.7	33.0	33.0	34.0
Contraction(± 0.4 , Å)	3.8	5.0	5.4	5.0	3.4	2.8	1.5

Table 3.10 Relative intensity data for the d_{100} XRD peaks of the as synthesis and calcined samples reacted for times varying from 3 to 72 h.

Reaction time (hours)	3	5	8	16	24	48	72
Intensity as syn.(± 140)	1200	1320	1120	980	910	790	680
Intensity C. (± 240)	1720	3860	1780	1340	1200	1090	1160
Δ Intensity (± 280)	520	2540	660	460	390	300	480

The variation of structural characteristics of the as synthesized and calcined materials showed significant differences as reaction time increased. The as synthesised material gave d_{100} peak intensities that increased with reaction time over the first 5 hours of reaction and then decreased indicating that the product achieved maximum order after 5 hours reaction time. The maximum in peak intensity correlated with a maximum in d_{100} spacing. Beyond five hours reaction time peak intensities and d_{100} spacings both decreased. In the case of the calcined materials, the same trend in peak intensities occurred, a maximum being observed after 5 hours reaction time. However the d_{100} spacings initially decreased with reaction time rather than increasing and were minimum at a reaction time of 8 h.

Tables 3.9 and 3.10 summarise the effects of calcinations on the structural properties. The lattice contraction, as indicated by the decrease in the d_{100} spacing, went through a maximum for the synthesis time of 8 h. Whereas peak intensities went through a sharp maximum at 5 hours synthesis time. The facts that the as synthesised and calcined materials both had maximum d_{100} peak intensities and the increase in peak intensity increase upon calcinations was greatest at a reaction time of 5 hours, is evidence that the optimum reaction time for the synthesis of ordered MCM-41 phases was 5 h. However,

ordered mesophases can be synthesised at reaction times ranging from 3 to 72 h.

The considerable increase in intensity and narrowing of the d_{100} XRD peaks observed for all calcined sample indicates an improvement of the mesoporous order induced by the combined effects of the removal of the surfactant and the condensation polymerization reaction. At longer reaction times, the contraction was smaller which might be explained by a higher degree of polymerization of the silicate and a thickening of the pore walls. Longer reaction times might thus offer the advantage of enhanced thermal stability of the calcined materials.

3.4.2 N₂ adsorption–desorption isotherms

Multi-point adsorption desorption studies were carried out using the NOVA instrument (See Section 2.5.2). Isotherms of the calcined samples are presented in Figure 3.23. In all cases, the calcined materials exhibited typical type IV isotherm behavior. The steep capillary condensation step for these samples is characteristic of well ordered and uniform mesoporous structure.

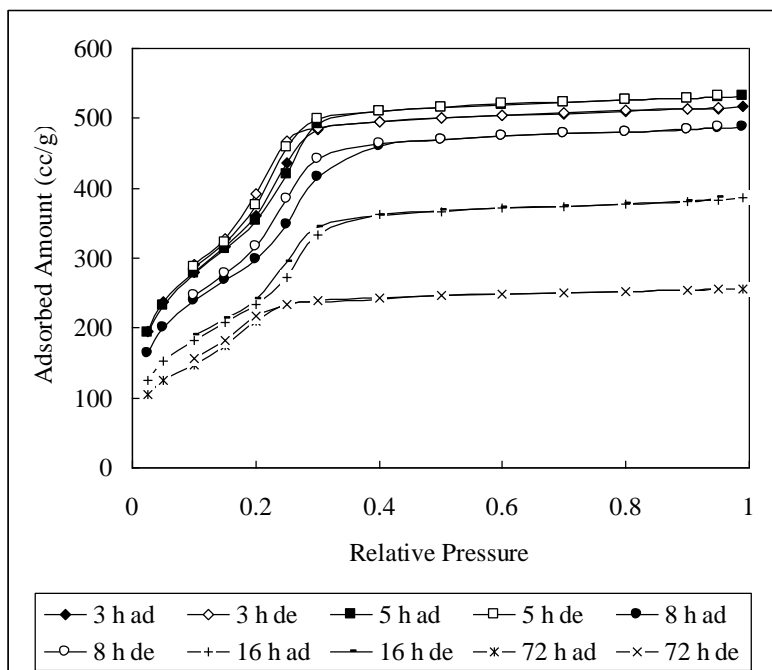


Figure 3.23. Effect of synthesis time on nitrogen adsorption isotherms for calcined MCM-41

Table 3.11 summarises the structural features obtained from analysis of the XRD data and the isotherm data, and includes the unit cell a_0 , mean pore diameter, wall thickness, total surface area and total pore volume calculated by the procedures described in Section 2.5.

Table 3.11. Effect of synthesis time on unit cell and pore characteristics.

Reaction Time Hours	Unit cell a_0 nm (± 0.03)	Pore size diameter nm (± 0.01)	Wall thickness nm (± 0.04)	Surface area m^2/g (± 70)	Total pore volume cc/g (± 8)
3	3.98	2.30	1.68	1520	517
5	3.90	2.44	1.46	1510	531
8	3.74	2.57	1.17	1270	488
16	3.75	2.57	1.18	1010	387
24	3.80	2.32	1.48	960	341
48	3.80	2.18	1.62	870	278
72	4.02	2.07	1.95	730	256

The BET specific surface area decreased from 1510 to 730 m^2/g with the increasing reaction time from 3 to 72 h. The total pore volumes increased slightly from 517 to 531 cc/g with the increasing reaction time from 3 to 5 h and then decreased from 531 to 256 cc/g with reaction times from 5 to 72 h. The pore size increased slightly from 2.30 to 2.57 nm with increasing reaction time from 3 to 8 h, and then decreasing from 2.57 to 2.07 nm with reaction times from 16 to 72 h. In contrast, the pore size decreased from 1.68 to 1.17 nm with increasing reaction time from 3 to 8 h, and then increased from 1.18 to 1.95 nm with increasing reaction time from 16 to 72 h. However, the unit cell parameter was much less affected by the reaction time so thicker pore walls resulted.

The pore size distribution was analyzed using N_2 multi-point adsorption-desorption data following the BJH method. Results are summarised Figure 3.24. It is apparent that the pore diameter of the maximum in the distribution curve for the MCM-41 samples increased with reaction time reaching a maximum after 8 hours and then decreased.

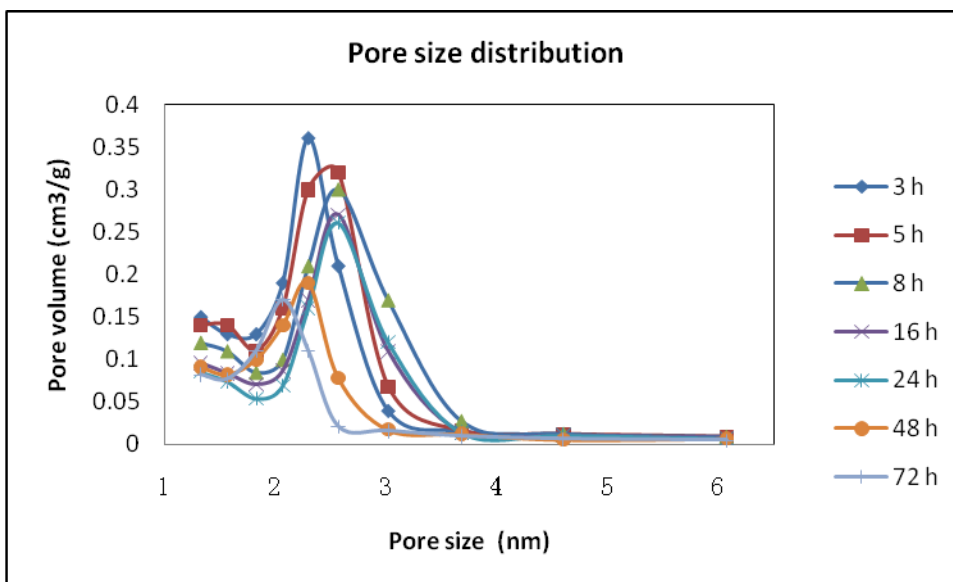


Figure 3.24 The effect of reaction time on the pore size distribution of calcined MCM-41 samples.

3.4.3 Effect of reaction time on Si yield

The MCM-41 yields calculated from the weight of calcined product compared with the Si content of the TEOS starting material, for the varying synthesis times are given in Figure 3.25

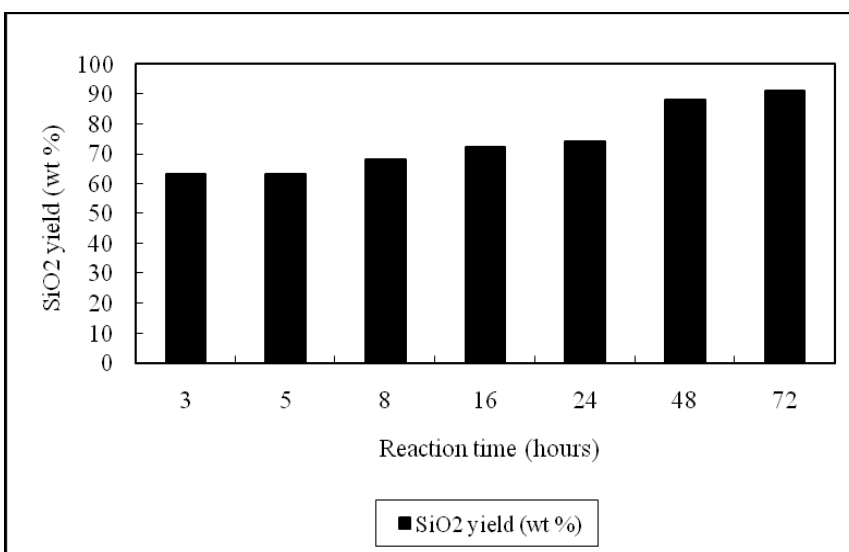


Figure 3.25 The effect of reaction time on the silica yield.

The yield of silica base, i.e. mesoporous silica materials, increased with the increasing

reaction time. This can be explained by the increased silicate polymerization, transportation into the channels from the mother liquor and continued wall building. The siliceous species may use the free space at the silicate/surfactant interface for further polymerization, so that the contraction of the unit cell upon calcination decreased, the wall thickness increased, and the yield of silica increased with increasing reaction time.

3.5 The effect of stirring rate

3.5.1 Introduction

It has been reported [8] that stirring rate can be used to tune the morphology of MCM-41, particularly to increase surface area and wall thickness. The different shear rates associated with different stirring conditions influence the shape and aggregation of micelles, as well as the interfacial growth of the silica-surfactant mesophase, resulting in distinct morphologies. This knowledge not only promotes an understanding mesoporous materials formation, but also enables the flexible design and construction of new functional the mesoporous materials As part of the program to optimize synthesis conditions, a range of stirring rates were used in conjunction with the previously optimized reaction time of 8 hours and other synthesis conditions described in Section 2.3.

3.5.2 Experimental

Mesoporous silica was synthesized using CTAB and PD respectively as the surfactant and TEOS as the silica source following the general procedure described in Section 2.3. An IKA[®] stirrer fitted with a 4.5 cm diameter propeller was used to achieve controlled stirring conditions with stirring speed ranging from 50 to 1000 rpm

3.5.3 Effect of stirring rate on induction times

The induction time for the formation of white precipitates decreased from 2 to 15 minutes

when the stirring rate was increased from 50 to 1000 rpm. In addition, three different product morphologies were observed, depending upon stirring rate. In the first, the inorganic phase (lower) and organic phase (upper) were completely separated when the stirring rate was less than 50 rpm. Flake-like white precipitates which fell into the inorganic phase, were observed to form at the inorganic-organic (TEOS) interface. The induction time was short, (about 2 min). The second morphology was observed when the stirring rate was increased from 50 to 200 rpm. Ribbon-like precipitation occurred at the inorganic-organic (TEOS) interface and diffused into the inorganic phase. At stirring rates between 200 and 1000 rpm, the TEOS immediately dissolved to generate a homogeneous and transparent solution with an induction time of about 15 min before the solution turned cloudy with the formation of colloidal white precipitates.

3.5.4 Effect of stirring rate on structural features

XRD data for the as synthesized and calcined MCM-41 materials prepared at different stirring speeds are given in Figures 3.26 to 3.29. All materials gave typical MCM-41 diffraction patterns consistent with one sharp peak in the range of $2\theta=2.1-2.6^\circ$ indexed to d_{100} diffractions and two additional weak peaks in the range of $3.5-6^\circ$, indexed to d_{110} and d_{200} diffractions, which are characteristic of the one-dimensional hexagonal mesophase. In all cases the ratio of $d_{100}:d_{110}$ is 1.732 and $d_{110}:d_{200}$ is 1.155 indicating highly ordered hexagonal mesoporous structures. Stirring rate did not significantly affect the internal structure of the mesoporous product.

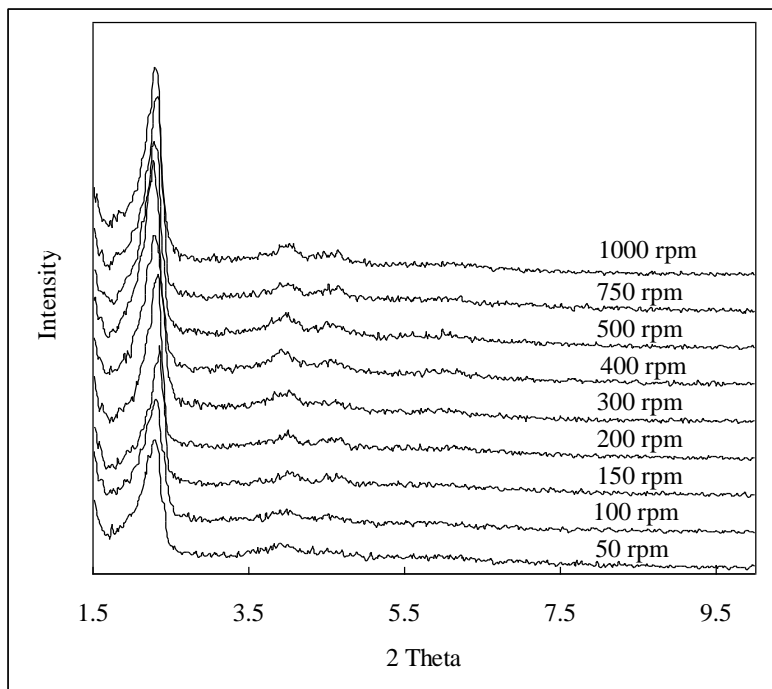


Figure 3.26 Effect of stirring rate on powder XRD patterns of the as-synthesised samples (CTAB template).

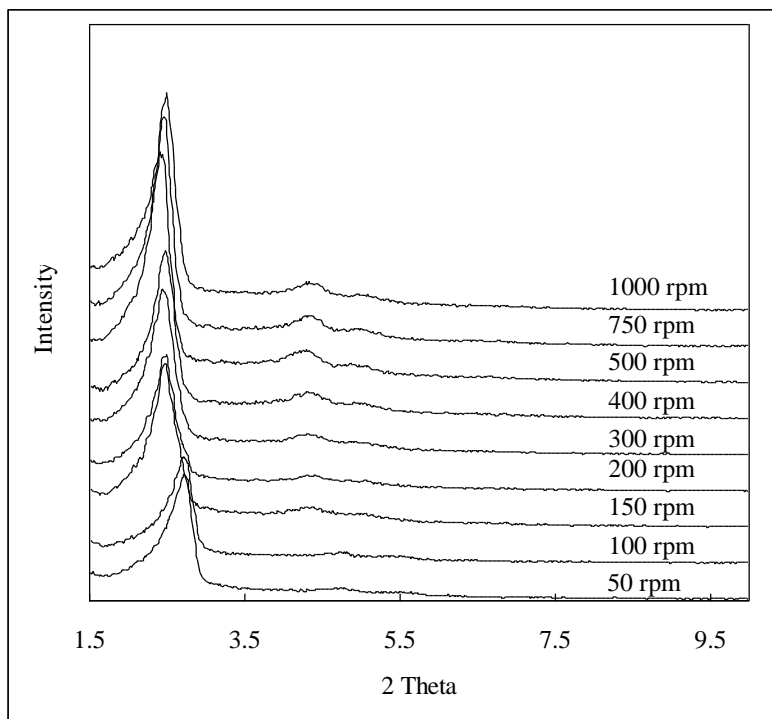


Figure 3.27 Effect of stirring rate on powder XRD patterns of the calcined samples (CTAB template).

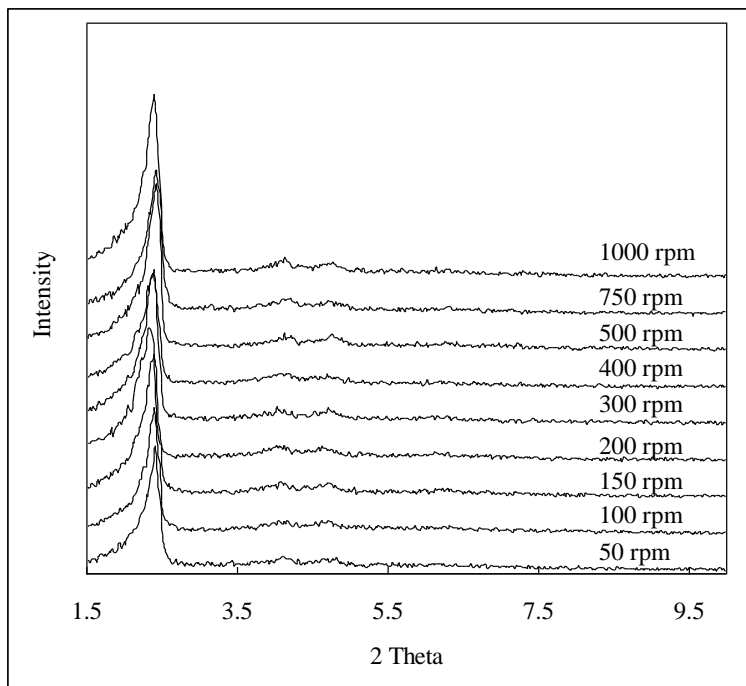


Figure 3.8 Effect of stirring rate on powder XRD patterns of the as-synthesised samples (PD template)

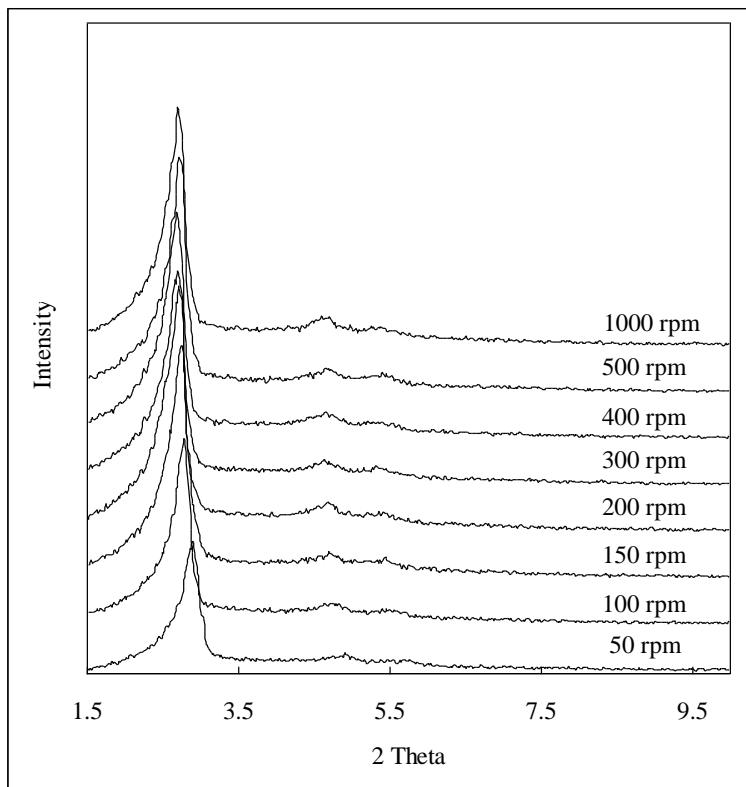


Figure 3.29 Effect of stirring rate on powder XRD patterns of the calcined samples (PD template)

The effect of stirring rate on the d_{100} spacing and XRD intensities for the as synthesised and calcined samples are summarized in Figures 3.30 and 3.31.

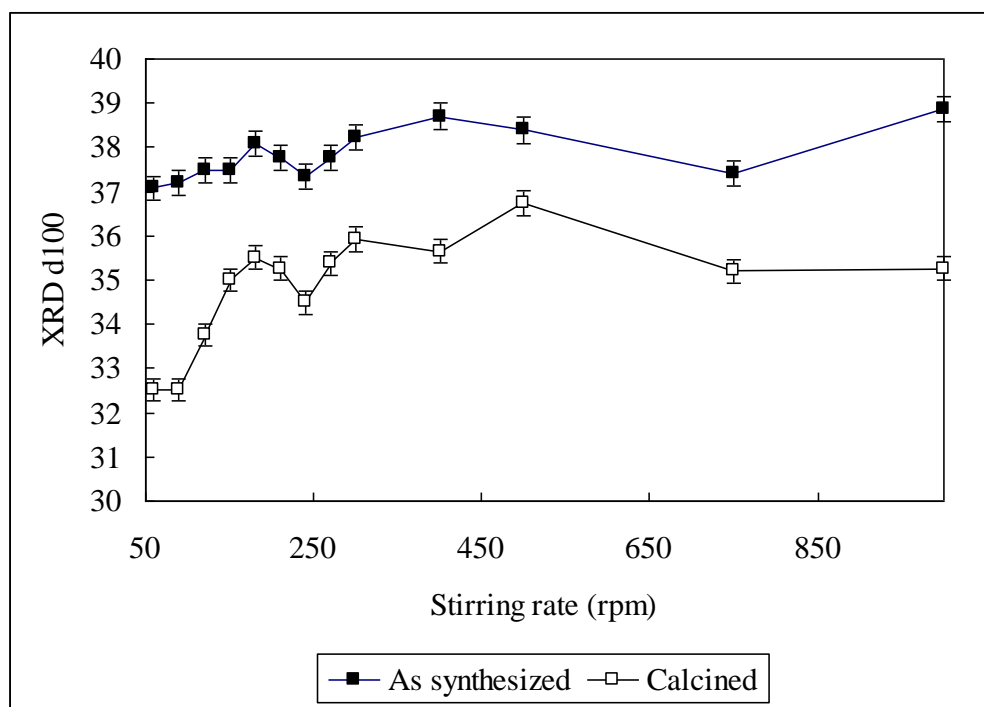


Figure 3.30 Effect of stirring rate on d_{100} spacing of the as-synthesis samples (CTAB template)

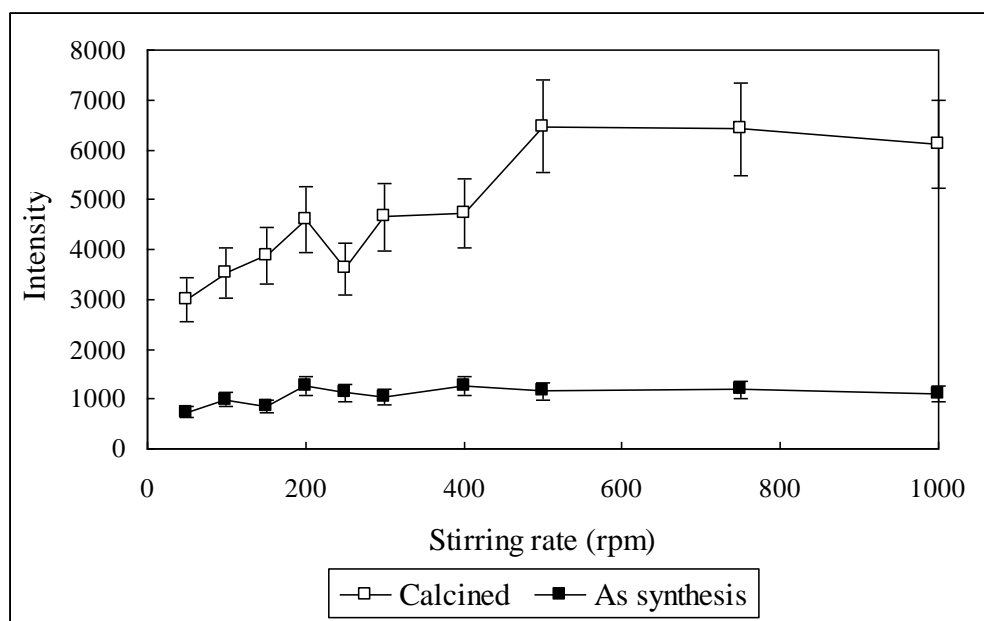


Figure 3.31 Effect of stirring rate on d_{100} intensity of the as-synthesis samples (CTAB template)

Table 3.12 Effect of stirring rate on d_{100} spacing of the as-synthesis samples (CTAB template)

Stirring rate(rpm)	50	100	150	200	250	300	400	500	750	1000
d_{100} as syn.($\pm 0.3, \text{\AA}$)	37.1	37.2	37.5	37.8	37.4	38.2	38.7	38.4	37.4	38.9
d_{100} C.($\pm 0.3, \text{\AA}$)	32.5	33.8	35	35.3	34.5	35.9	35.7	36.7	35.2	35.3
Contraction	4.6	3.4	2.5	2.5	2.9	2.3	3	1.7	2.2	3.6

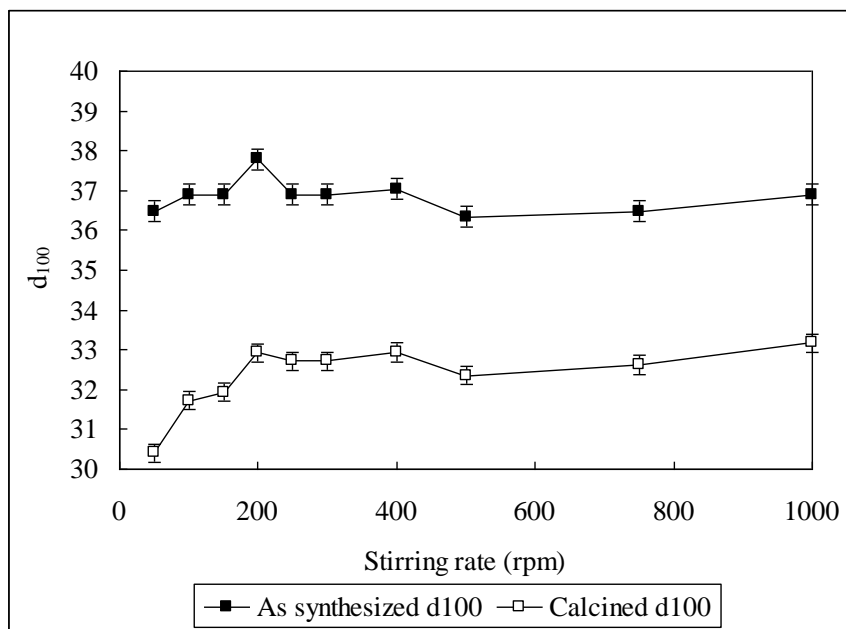
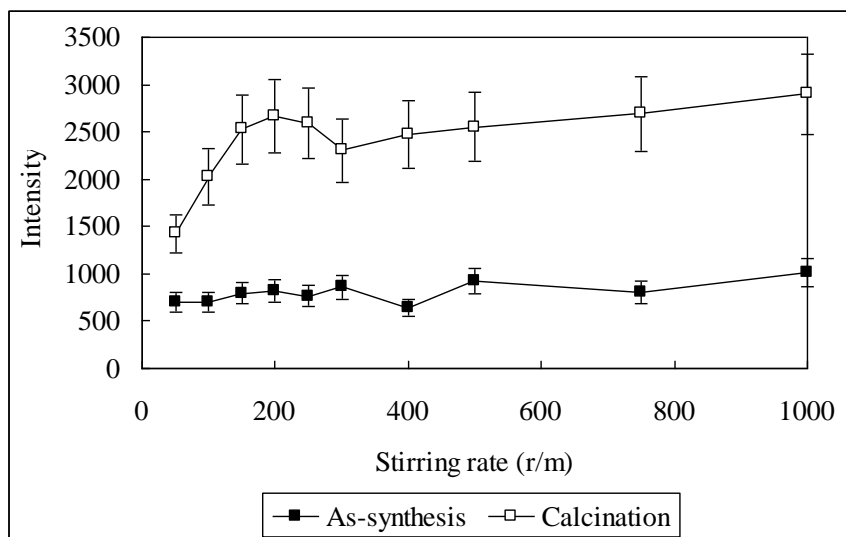
Figure 3.32 Effect of stirring rate on d_{100} spacing of the as-synthesis samples (PD template)Figure 3.33 Effect of stirring rate on d_{100} intensity of the calcined samples (PD template)

Table 3.13 Effect of stirring rate on d_{100} spacing of the as-synthesis samples (PD template)

Stirring rate r/m	50	100	150	200	250	300	400	500	750	1000
d_{100} as syn. ($\pm 0.3, \text{\AA}$)	36.5	36.9	36.9	37.8	36.9	36.9	37	36.3	36.5	37
d_{100} C. ($\pm 0.3, \text{\AA}$)	30.4	31.7	31.9	32.9	32.7	32.7	32.9	32.4	32.6	33.2
Contraction	6.1	5.2	5	4.9	4.2	4.2	4.1	3.9	3.9	3.8

Figures 3.30, 3.31, 3.32 and 3.33 show that stirring rate has little effect on the structure of the as-prepared MCM-41 derived from both CTAB and PD templates. XRD intensities and d_{100} spacings show slight increases over the stirring speed range.

After calcining, there is a decrease in the value of d_{100} spacing for all calcined samples, but the contraction varied with the stirring rate used in the preparative step. Over the stirring rate range from 50 to 200 rpm, the d_{100} spacing contraction decreased from 4.6 to 3.5 Å for the CTAB template and from 6.1 to 4.9 for the PD template (Tables 3.12 and 3.13). The intensity of the d_{100} XRD peaks of the calcined materials increased with the stirring rate used in the preparative step. It appears that higher stirring rates, while not significantly affecting the structure of the as-prepared materials, do favour the formation of more robust phases able to better maintain their structures when the template is removed.

3.5.5 Effect of stirring speed on particle morphology

Particle morphology of the as-synthesised material was studied by SEM to determine whether stirring speed had any effects on particle size and shape. Data for the MCM-41 phases formed using both CTAB and PD templates and prepared at stirring speeds ranging from 50 to 1000 rpm are summarized in Figures 3.34 to 3.41

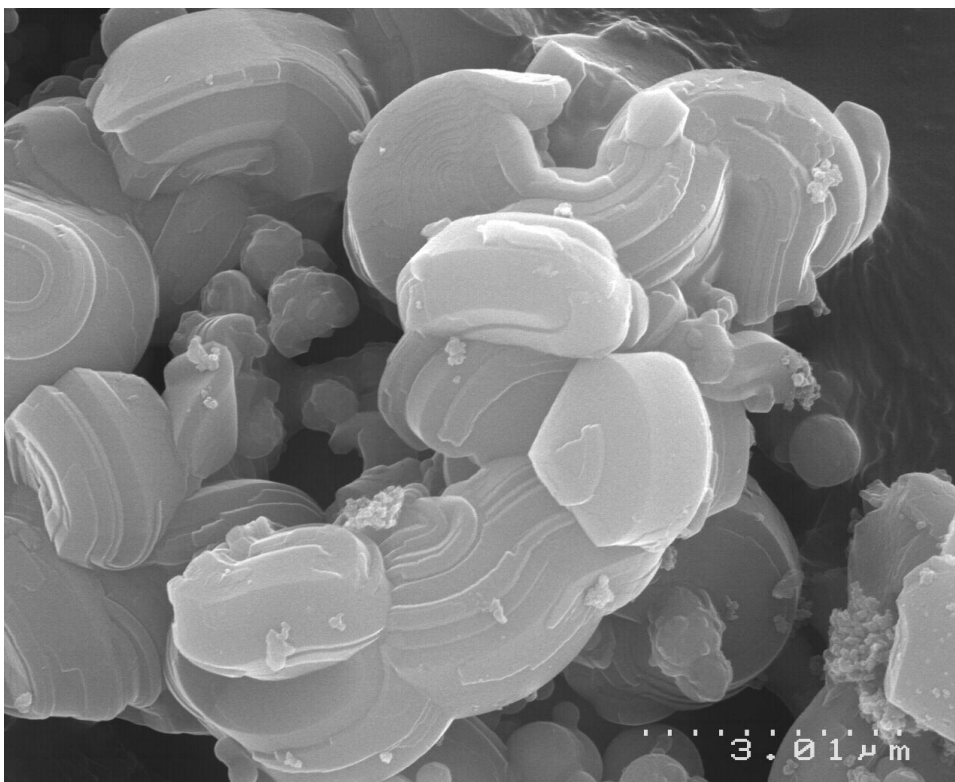


Figure 3.34 SEM Image CTAB as template stirring rate 50 rpm

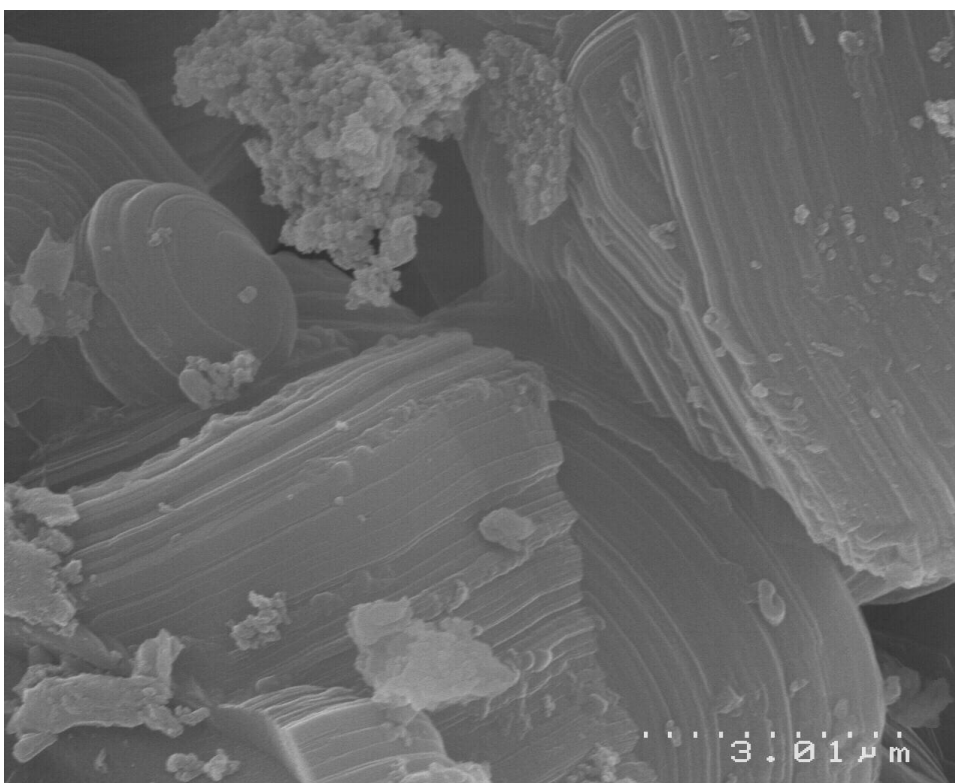


Figure 3.35 SEM Image CTAB as template stirring rate 200 rpm

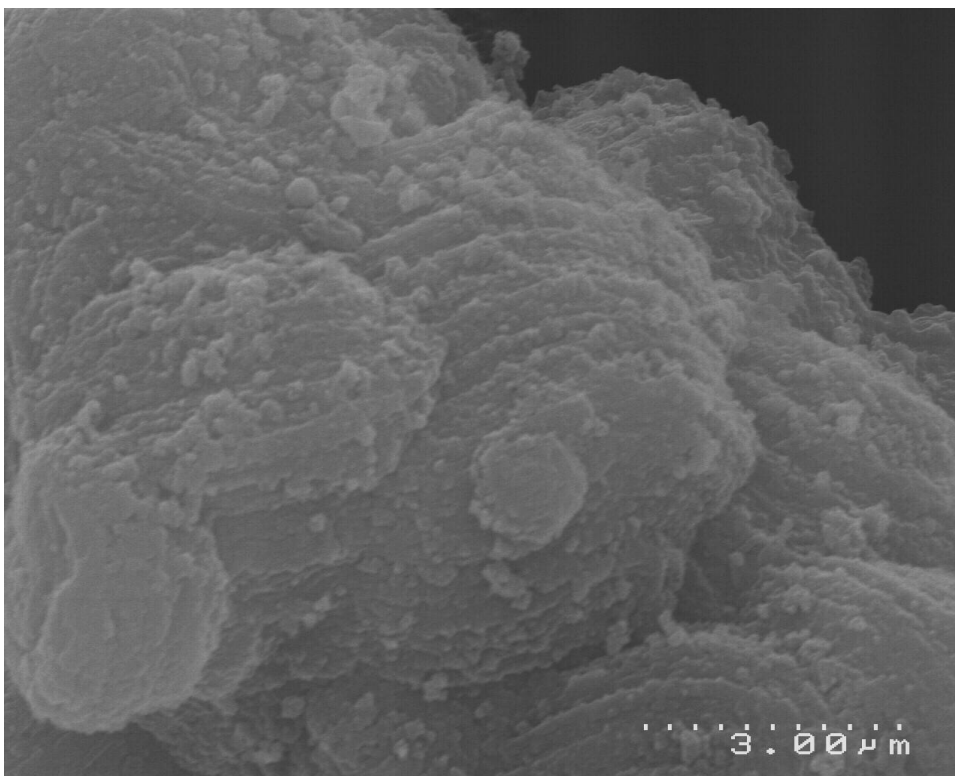


Figure 3.36 SEM Image CTAB as template stirring rate 400 rpm

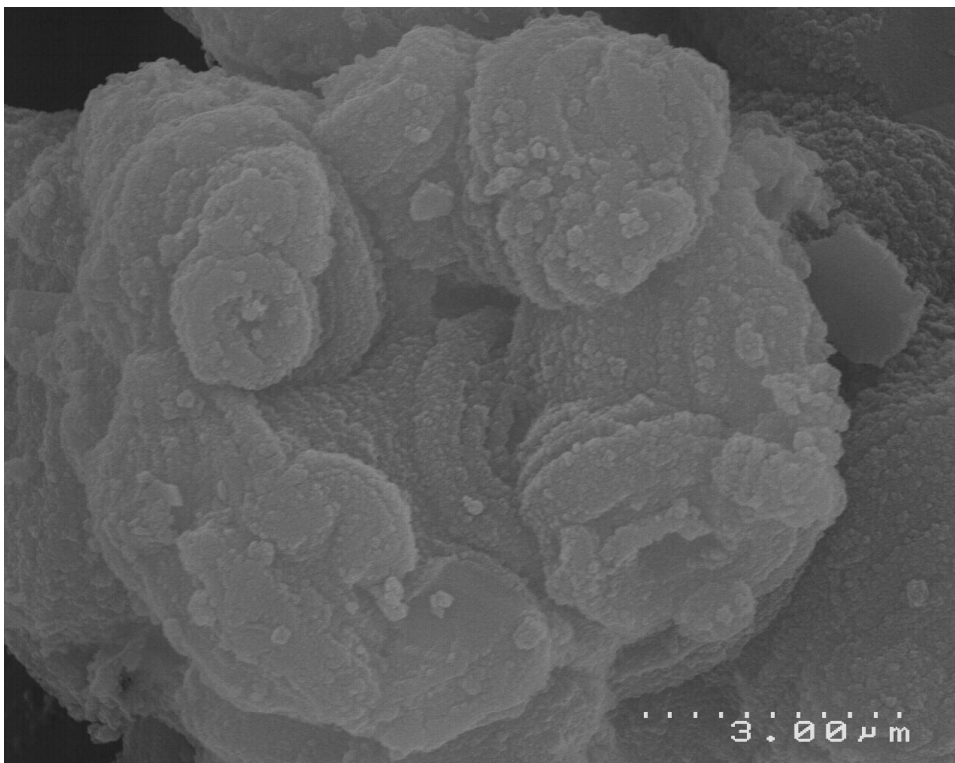


Figure 3.37 SEM Image CTAB as template stirring rate 1000 rpm

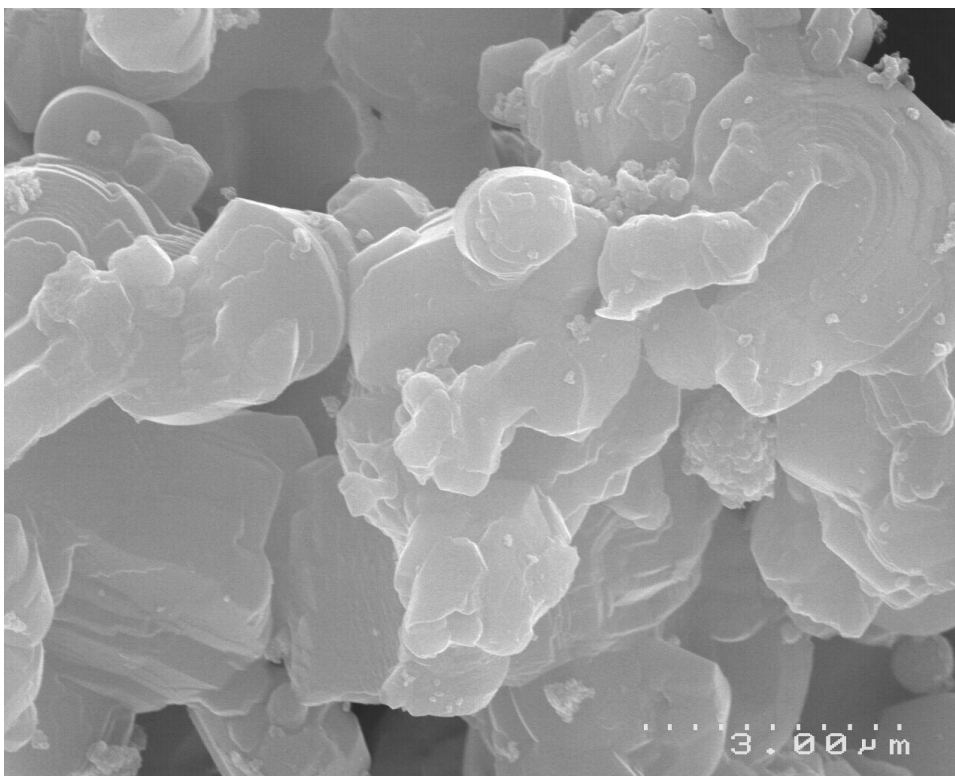


Figure 3.38 SEM Image PD as template stirring rate 50 rpm

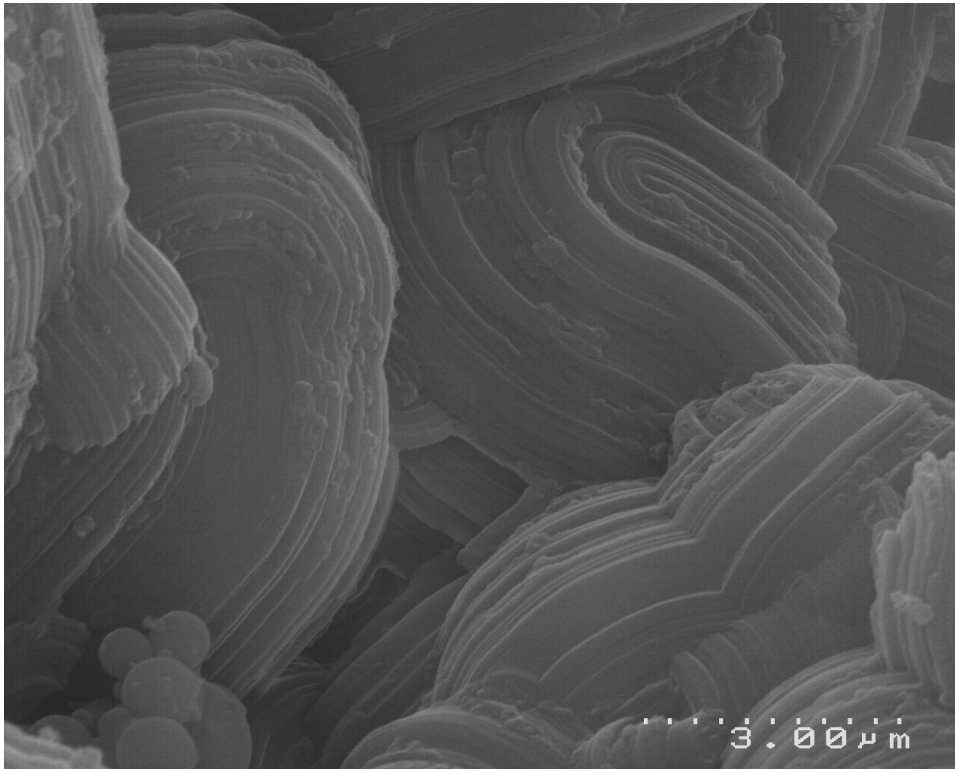


Figure 3.39 SEM Image PD as template stirring rate 200 rpm

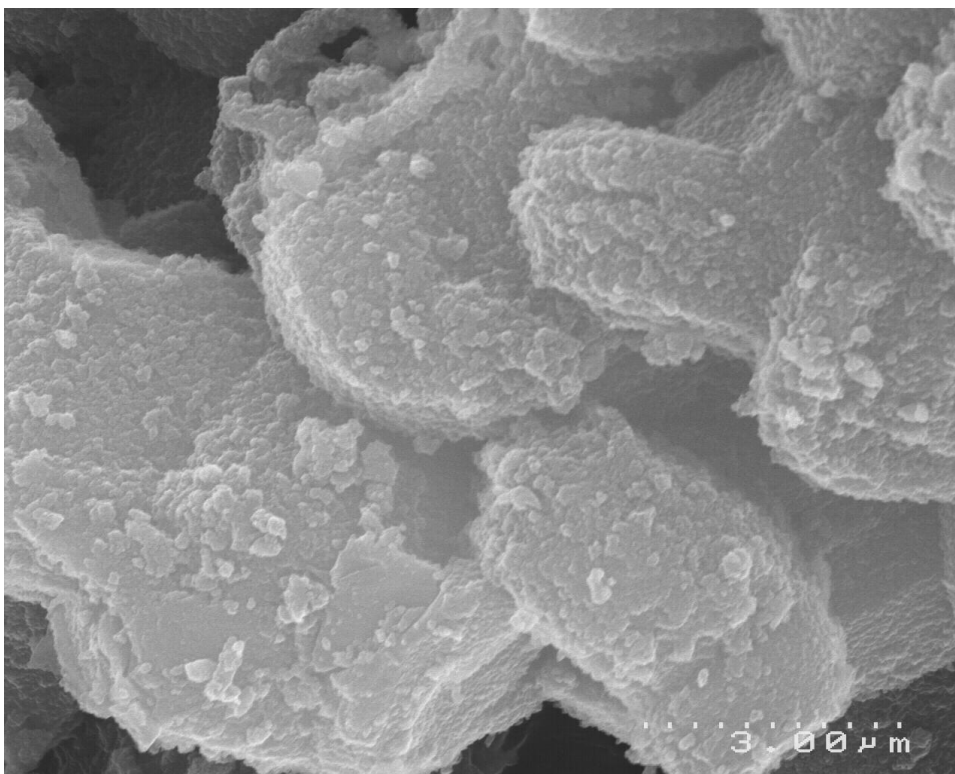


Figure 3.40 SEM Image PD as template stirring rate 400 rpm

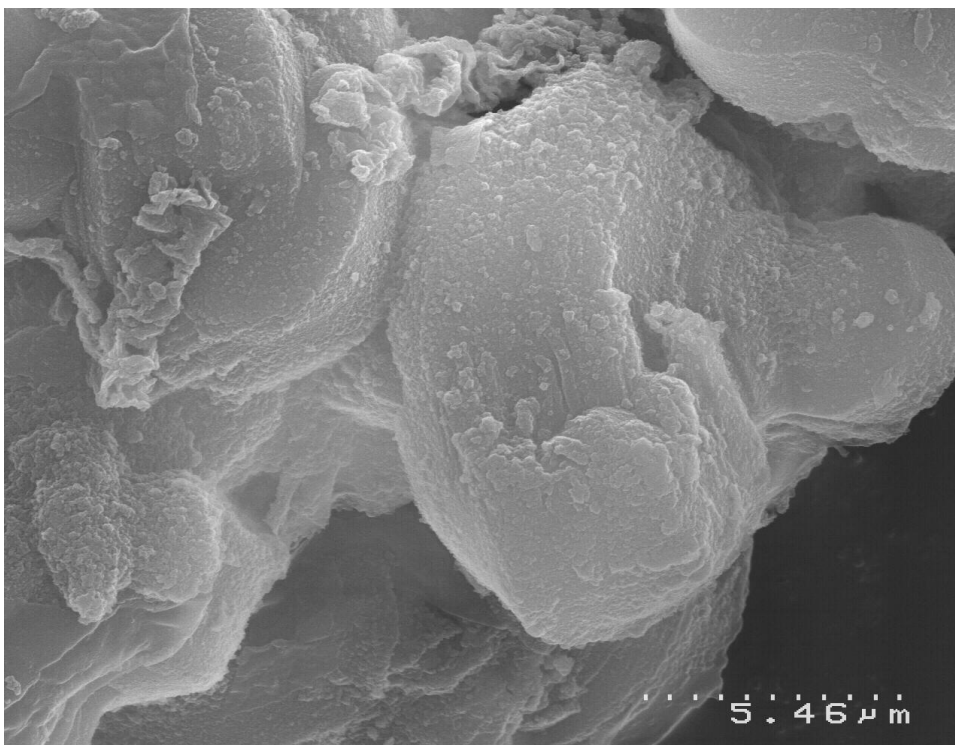


Figure 3.41 SEM Image PD as template stirring rate 1000 rpm

SEM images of the exterior surfaces of the samples prepared at the lowest stirring speed showed relatively smooth small particles with distinct growth step edges of about 300 nm height. At the higher stirring speeds, the particles tended to have rougher outlines and in most cases appeared to consist of inter grown particles made up of flake-like layers approximately 300 nm thick. Surfaces were generally rough and covered by small particles possibly indicating nucleation and growth on the surfaces.

3.5.6 Effect of stirring speed on N₂ adsorption-desorption characteristics

The nitrogen isotherms and their BJH PSD curves for the samples prepared at different stirring speeds are presented in Figure 3.4-17. All isotherms were type IV isotherms and showed a sharp increase in N₂ adsorption at P/P_0 of ca. 0.2~0.3, consistent with capillary condensation of N₂ in uniform, sized mesopores.

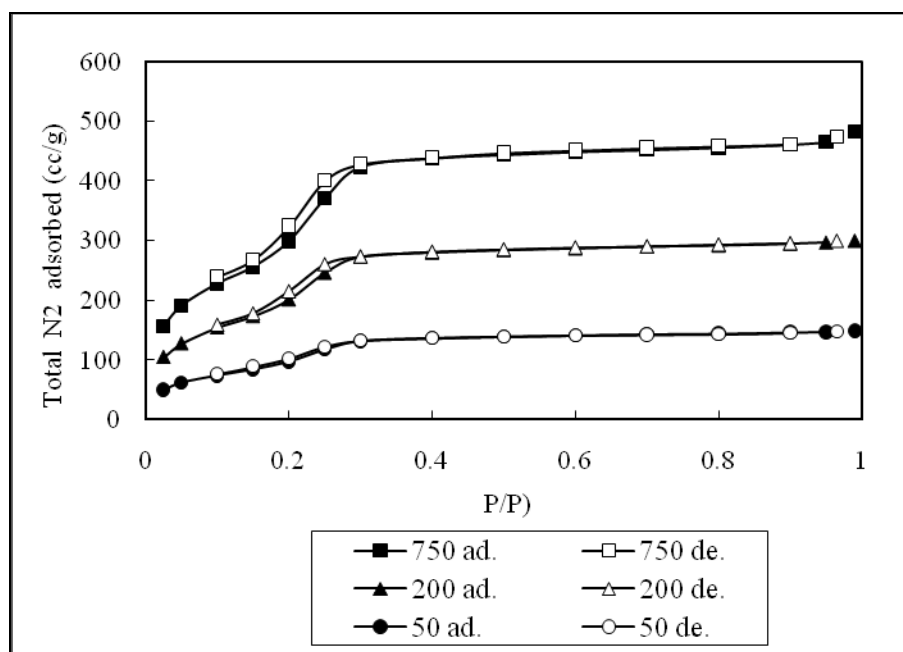


Figure 3.42 The effect of stirring on N₂ adsorption-desorption isotherms (CTAB as template)

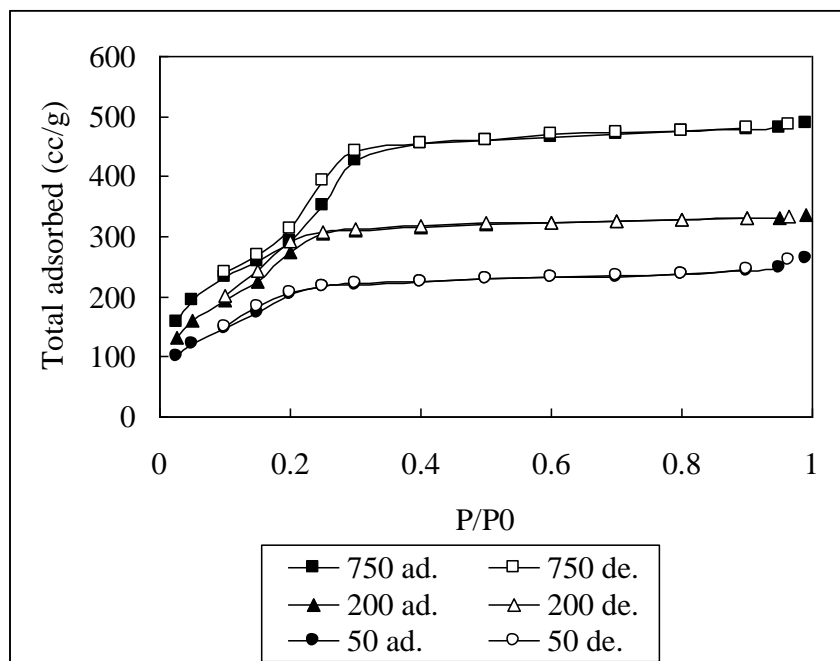


Figure 3.43 The effect of stirring on N₂ adsorption-desorption isotherms (PD as template)

The specific surface area values (S_{BET}) and the pore volume of samples based on the BET method are summarized in Tables 3.15 and 3.16 and plotted in Fig 3.44 and 3.45. Very high S_{BET} values of more than 1000 m²/g were obtained for all samples except the sample prepared at a stirring rate 50 rpm. The surface area increased steadily from 845 to 1572 m²/g as the stirring speed was increased from 50 to 200 rpm. From 200 rpm to 300 rpm there was no further positive effect (a small negative effect is indicated by the data). Above 300 rpm, increasing the stirring rate produced a further increase in surface area of the calcined products. The increases in surface area of calcined products formed at increasing stirring rates are mirrored by increases in XRD d_{100} intensities (See figures 3.32 and 3.33).

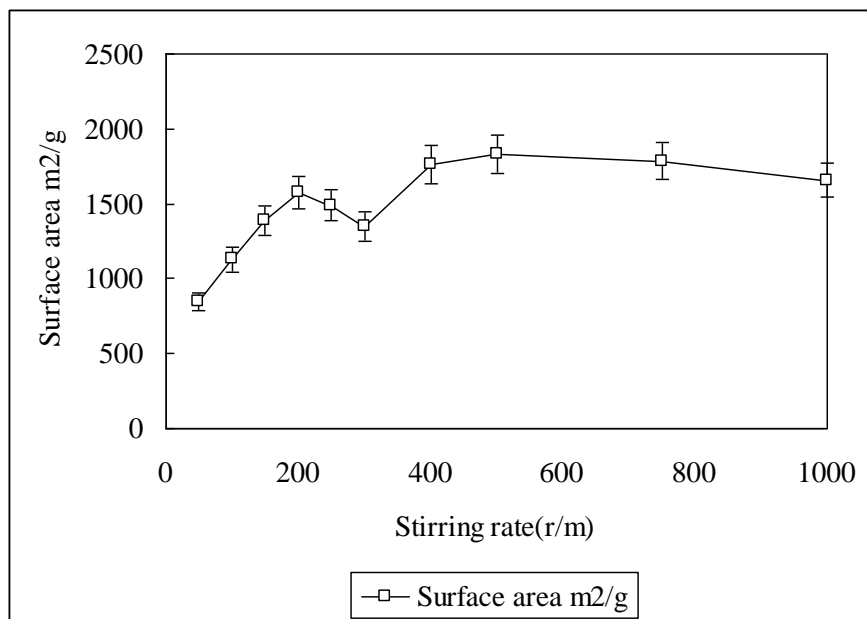


Figure 3.44 The surface area CTAB as template at different stirring rate

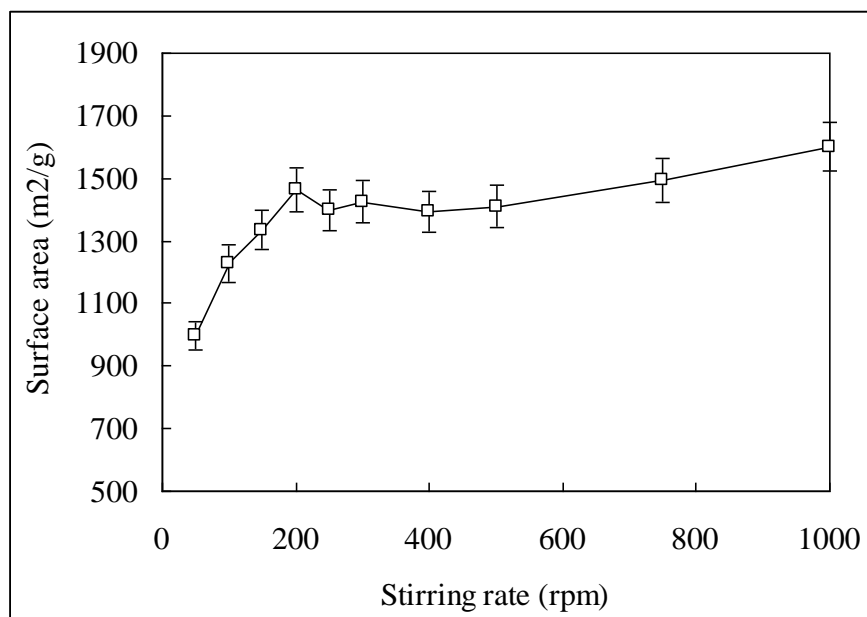


Figure 3.45 The surface area PD as template at different stirring rate

The effect of stirring on pore size distribution is plotted in Figure 3.46 and 3.47. The isotherms and the corresponding pore size distributions show a narrow pore size distribution for the all samples. Samples synthesised at high stirring rates had larger meso pore areas. Although not resolved, micro pore area is indicated by pore area below

1.5 nm. Micro pore area increased with stirring rate for the CTAB surfactant but much less so with the PD surfactant.

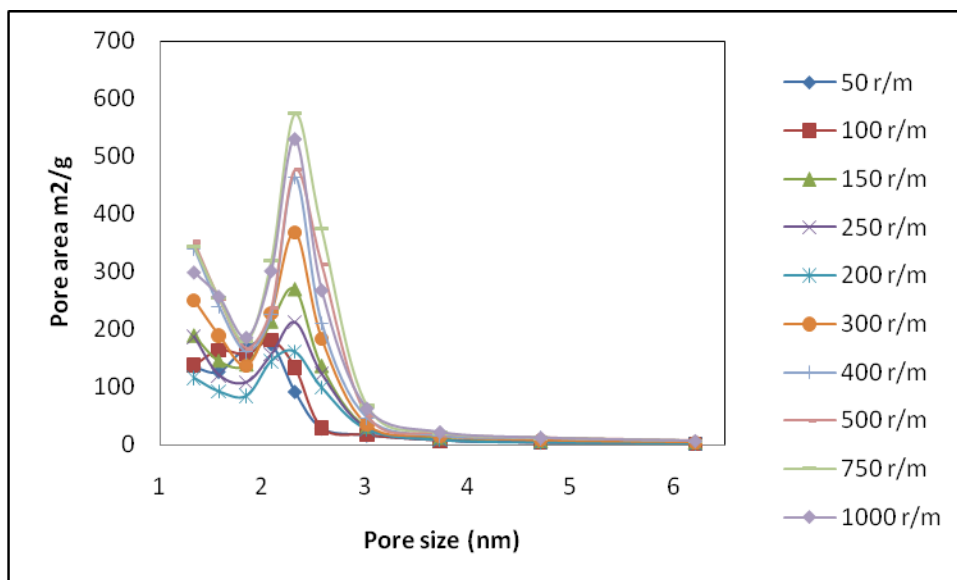


Figure 3.46 The effect of stirring rate on the pore size distribution (CTAB as template)

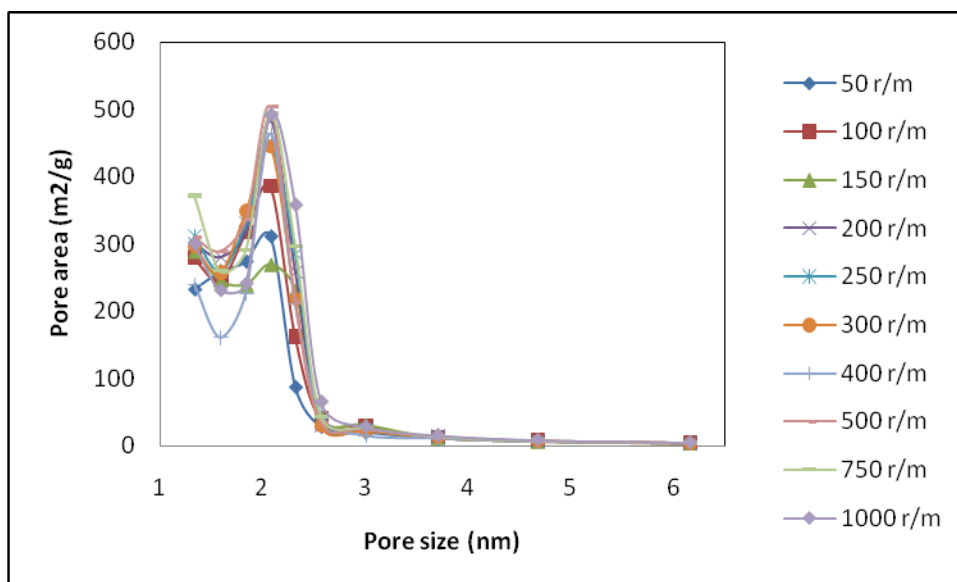


Figure 3.47 The effect of stirring rate on the pore size distribution (PD as template)

A summary of structural parameters, including calculation of wall thickness is presented in Table 3.15 and 3.16

Table 3.15 The effect of the stirring rate on structural properties of calcined MCM-41 phases (PD as template)

Stirring rate (rpm)	Unit cell a_o nm (± 0.03)	Pore size diameter nm (± 0.01)	Wall thickness nm (± 0.04)	Surface area m^2/g (± 70)	Total pore volume cc/g (± 8)
50	3.04	2.08	0.96	1000	312
100	3.17	2.08	1.09	1230	385
150	3.19	2.07	1.12	1340	437
200	3.29	2.07	1.22	1460	483
250	3.27	2.07	1.20	1400	446
300	3.27	2.07	1.20	1430	444
400	3.29	2.06	1.23	1390	475
500	3.24	2.06	1.18	1410	503
750	3.26	2.06	1.20	1490	523
1000	3.32	2.07	1.25	1600	492

Table 3.16 The effect of stirring rate on the structural properties of calcined MCM-41 phases (CTAB as template)

Stirring rate (rpm)	Unit cell a_o nm (± 0.03)	Pore size diameter nm (± 0.01)	Wall thickness nm (± 0.04)	Surface area m^2/g (± 70)	Total pore volume cc/g (± 8)
50	3.25	2.32	0.93	850	174
100	3.38	2.31	1.07	1130	181
150	3.50	2.32	1.18	1390	269
200	3.53	2.30	1.20	1570	349
250	3.45	2.31	1.14	1490	395
300	3.59	2.34	1.25	1350	369
400	3.57	2.34	1.23	1760	464
500	3.67	2.32	1.35	1830	477
750	3.58	2.30	1.28	1790	575
1000	3.53	2.30	1.23	1660	530

Although the unit cell dimension increased with increasing stirring rate in the range from 50 to 200 rpm, the mean pore size diameter remained the same. The increased unit cell dimension is reflected in increased wall thickness. When the stirring rate was higher than 200 rpm, all samples have a similar unit cell, pore size and wall thickness, indicating that the stirring rate had little effect on the final calcined structures. These trends are summarized in Figures 3.48 and 3.49

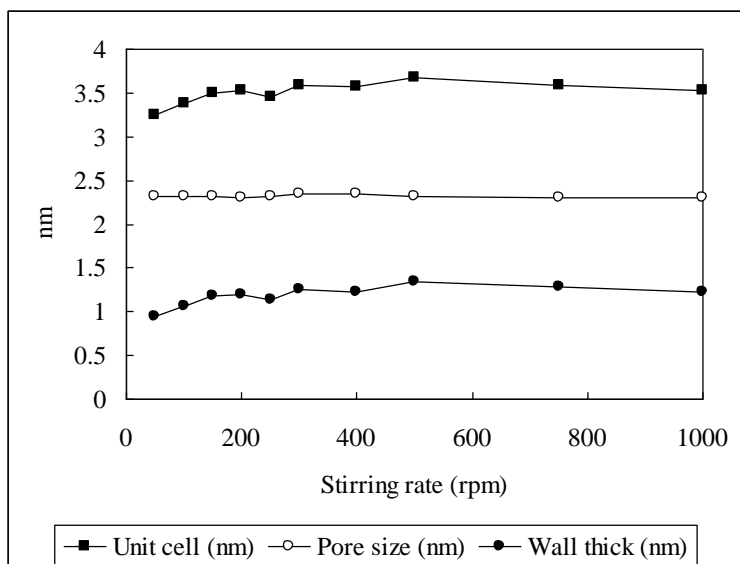


Figure 3.48 Effect of stirring speed on structural properties (CTAB as template)

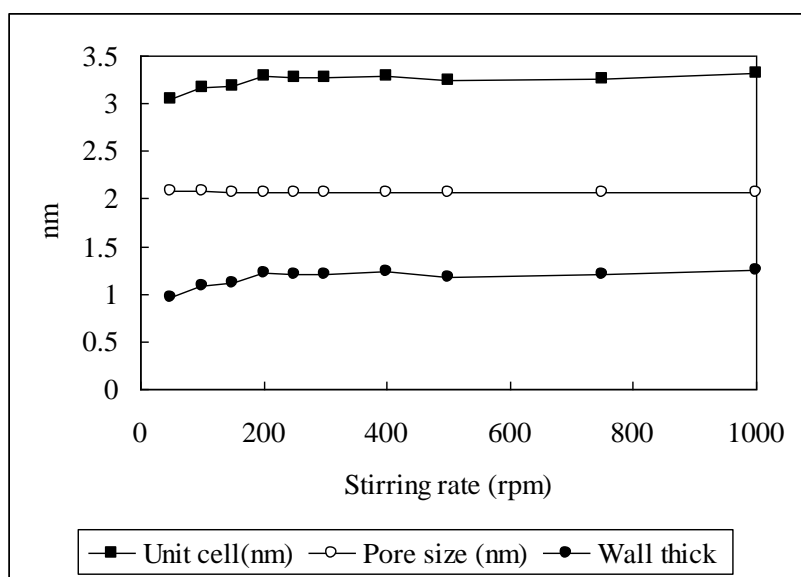


Figure 3.49 Effect of stirring rate on structural properties (PD as template)

3.5.7 Effect of stirring rate on Si yield

The percentage of silica recovered as MCM-41 product (i.e. yield) as a function of stirring rate are shown in Figures 3.50 and 3.51. They show that there is a significant decrease in the yield of the product with an increase in stirring rate. While the yield is lower, the XRD and nitrogen adsorption data point to the products formed at higher stirring rates as being more ordered and having greater specific surface area.

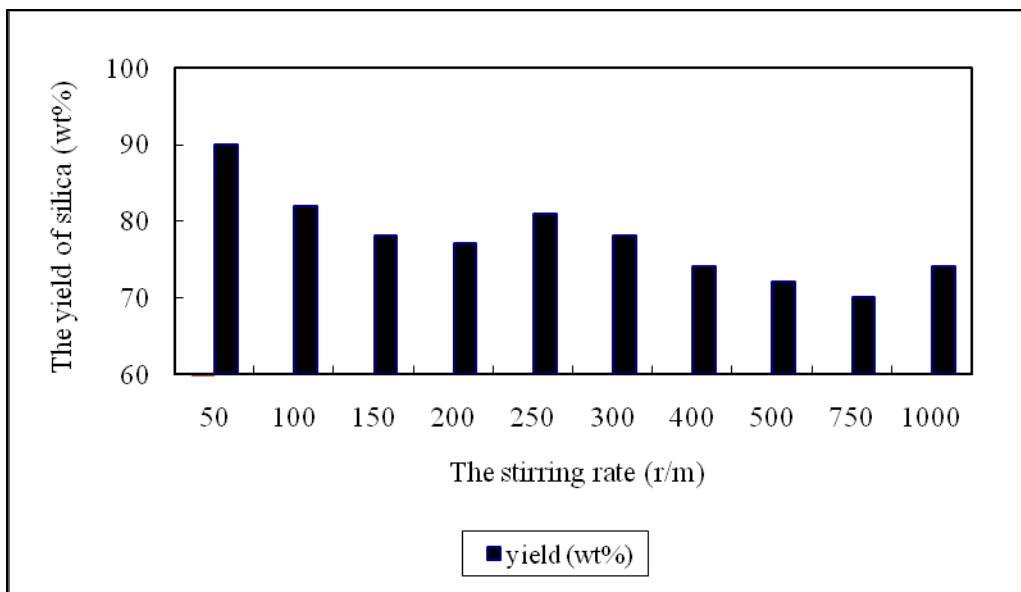


Figure 3.50 The effect of stirring rate on yield (CTAB as template)

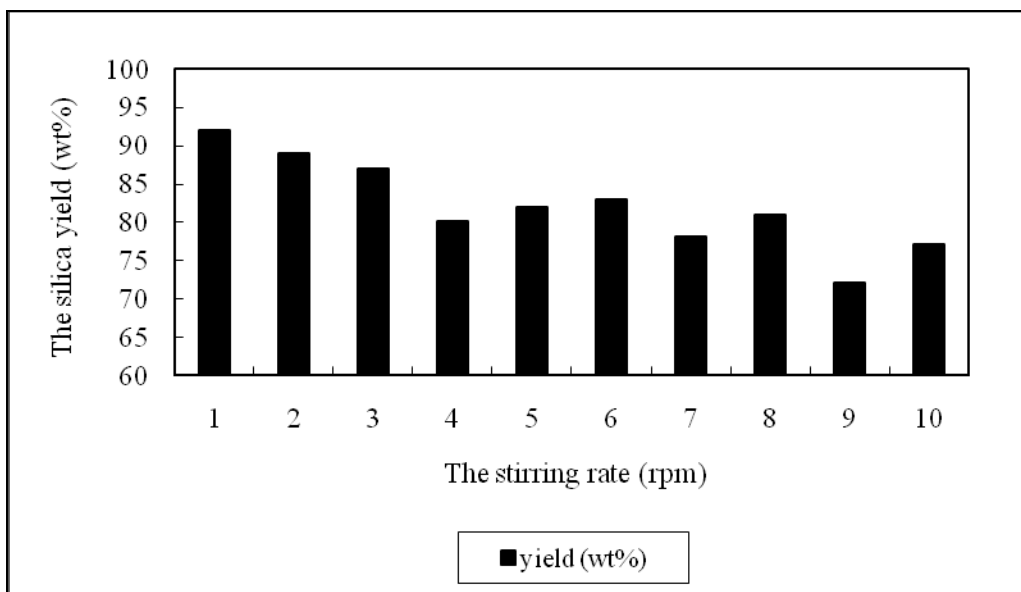


Figure 3.51 The effect of stirring rate on yield (PD as template)

3.5.8 Conclusion

It has been demonstrated that stirring can be used as a convenient tool for controlling aspects of the structure of MCM-41 synthesised from TEOS under acid conditions. To achieve well ordered phases with maximum specific surface areas, narrow pore size

distributions and thick walls, stirring speeds greater than 500 rpm should be used.

3.6 Studies of product stability

Applications envisaged for the mesoporous silicas studied in the work include their use as absorbents and catalysts. These applications may involve a variety of thermal and hydrothermal conditions. It is thus of interest to determine how stable the phases prepared by the acid hydrolysis method were under such conditions.

Mesoporous silica was synthesized following the general procedure described in Section 2.3. The as-synthesized and calcined samples were then subjected to a variety of stability tests including: aging, thermal stability, resistance to acids and bases and hydrothermal stability. XRD and nitrogen adsorption experiments were used to assess the changes brought about by these treatments.

3.6.1 Effect of aging

As synthesized and calcined samples were stored in air tight vials and sampled periodically for XRD and adsorption analysis. XRD data for the as synthesised and calcined MCM-41 materials after varying periods of aging are summarised in Figures 3.52 and 3.53 and in Tables 3.17 and 3.18 respectively.

Table 3.17 The effect of aging on d_{100} spacing of as-synthesised MCM-41

Aging period (Month)	3	6	12	24	36
2 Theta	2.44	2.47	2.45	2.44	2.45
d_{100} spacing (± 0.3 , Å)	36.2	35.9	36.1	36.2	36.1
Intensity (± 140)	1274	489	1260	1089	894

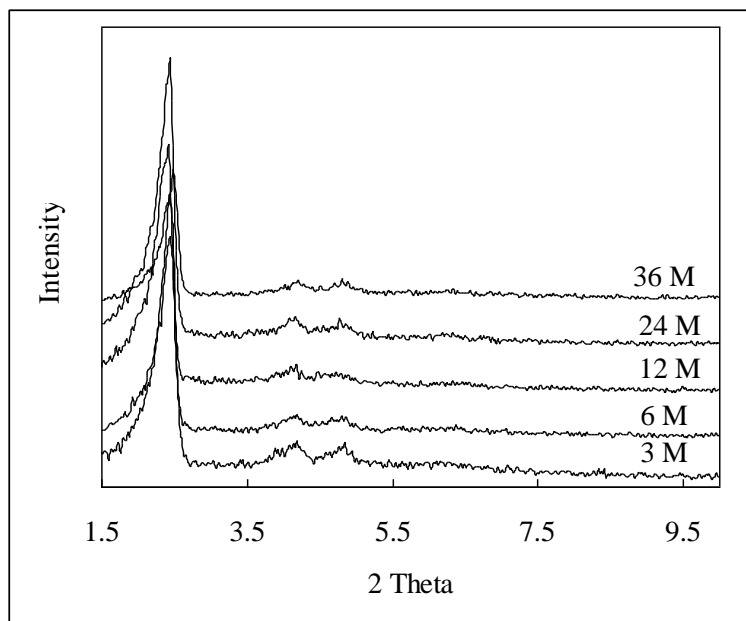


Figure 3.52 The effect of aging on XRD powder patterns for as-synthesised MCM-41.

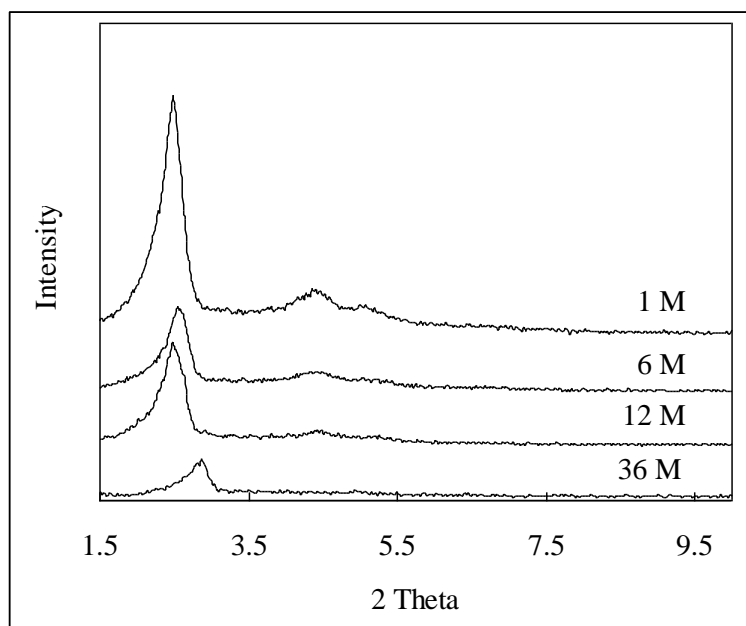


Figure 3.53 The effect of aging on XRD powder patterns for calcined MCM-41

Table 3.18 The effect of aging on d_{100} spacing and intensity of calcined samples

Aging period (Months)	1	6	12	36
2 Theta	2.49	2.55	2.49	2.83
d_{100} spacing (± 0.3 , Å)	35.3	34.6	35.3	31.2
Intensity (± 140)	2329	827	992	358

While the variation of d_{100} line intensities for the as synthesized samples was greater than experimental error, the d_{100} spacing remained constant. The variation in the intensities was probably due to variation in beam intensity and beam alignment rather than deterioration of the mesophase ordering. The peak sharpness does not change and the d_{110} and d_{200} peaks remain well resolved. Furthermore, a calcined material prepared from the three year old as-synthesized material produced XRD patterns very similar to the calcined product prepared from freshly synthesized material. It can be expected that the template will preserve the structure of the as-synthesized material indefinitely.

In contrast, the calcined samples showed significant changes upon aging. From the XRD patterns presented in Figure 3.53, it is clear that, even allowing for changes in beam intensity, the d_{100} peak intensity decreased with sample age, the d_{100} spacing changed, the peaks broadened and the d_{110} and d_{200} peaks became less obvious. These changes all indicate a deterioration of structural ordering with time. After three years, only a single weak broad peak was observed, the d_{110} and d_{200} peaks having completely disappeared. The decrease in the unit cell from 35.3 to 31.2 Å and the decrease in specific surface area both indicate a gradual collapse with age of the mesoporous structure.

Further evidence of the collapse of the pore structure of the calcined samples with age is provided by the pore size distribution (Figure 3.54). The isotherms and the corresponding pore size distributions show a narrow pore size distribution for the freshly calcined sample whereas the sample aged for 3 years under ambient conditions gave no peak in the pore distribution.

The surface area decreased from 1423 to 474 m²/g over the 3 year aging period. The remaining surface area was associated with the pores in the micropore region below about 2 nm, presumably in the remnants of the mesopore walls. The mesoporous structure had almost completely degraded.

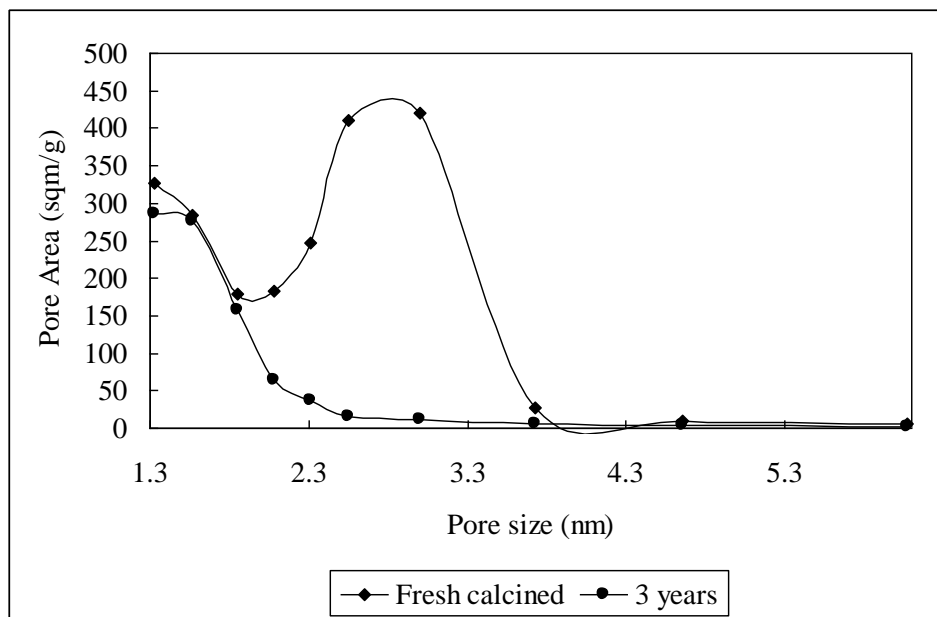


Figure 3.54 The effect of sample age on pore size distribution for calcined samples

It is clear from these results that the mesoporous structure deteriorates with time. However, after 12 months the calcined material still exhibited the characteristic XRD diffraction pattern of MCM-41. Thus while applications based upon the mesoporosity of calcined material can not rely indefinitely on the structural integrity, useful lifetimes of up to 12 months can be anticipated.

While the mesoporous structure deteriorates with time, the materials still retain their relatively large surface area because of the microporous structure associated with the pore walls. This appears to remain intact even after the pores themselves have collapsed. Far fewer Si-O-Si bond rearrangements would be required for the collapse of the mesopore structure than for the collapse of the micro pore structure.

3.6.2 The thermal stability of calcined product

Calcined samples were heated at temperatures ranging from 100 to 700°C for 24 hours and then characterized by low angle XRD, BET surface area determination and BJH pore size measurements.

XRD data for the calcined MCM-41 materials heated at different temperatures are summarized in Table 3.19. Below 500°C, the d_{100} spacing decreased from 33.5 to 32.5 Å (contraction of approximately 3%), but the peak intensity was not significantly changed. At 550 °C, the d_{100} spacing decreased significantly (from 33.5 to 30.7 Å or about 9%) and the intensity increased to a value approximately twice that of the original calcined material. At temperatures of 600°C and above, large decreases in d_{100} spacing occurred (from 33.5 to 27.8 Å, or about 20%) and the d_{100} intensity decreased indicating collapse of the mesoporous structure.

Table 3.19 The effect of thermal treatment on d_{100} spacing of calcined samples

Temperature (°C)	Original	100	500	550	600	700
2 Theta	2.63	2.67	2.72	2.88	3.00	3.18
d_{100} spacing (± 0.3 , Å)	33.5	33.1	32.5	30.7	29.4	27.8
Intensity (± 140)	960	819	1205	1812	968	575

A summary of structural parameters derived from adsorption measurements, including wall thickness is presented in Table 3.20. The unit cell parameter decreased with the increasing temperature, the mean pore size diameter remained the same, indicating that the wall thickness decreased with increasing temperature. This implies that the density of wall increased with increasing heat temperature. At 550°C and below, the surface area was not obviously changed with increasing temperature. Above 550°C, the surface area decreased from 1350 to 474 m²/g as the temperature was increased from 550 to 700°C.

Table 3.20 The effect of the thermal treatment on structural properties of calcined MCM-41 phases

	Unit cell a_0 nm (± 0.03)	Pore size diameter nm (± 0.01)	Wall thickness nm (± 0.04)	Surface area m ² /g (± 70)	Total pore volume cc/g (± 8.6)
Original	3.58	2.08	1.5	1430	518
100	3.54	2.08	1.46	1396	498
500	3.48	2.06	1.42	1363	475
550	3.28	2.06	1.22	1350	438
600	3.15	2.08	1.07	746	341
700	2.97	----	----	474	209

3.6.3 The effect of acid and base on product stability

In order to evaluate the stability of MCM-41 material in the presence of acid or base, the calcined samples was immersed in 10% HCl and 5% potassium hydroxide and heated at 75°C for 3 h. The treated samples were filtered and dried at room temperature and characterized by low angle XRD, BET surface area determination and BJH pore size measurements.

No data was obtained for the base treatments. The MCM-41 completely dissolved at 10% KOH and even in 5% KOH, an amorphous powder was produced giving only a broad XRD diffraction peak.

XRD data for the MCM-41 materials treated by HCl are summarized in Tables 3.21 and 3.22 and Figures 3.55, 3.56. The material treated by HCl exhibited sharper XRD peaks with higher intensities indicating that there was an improvement of structural ordering after HCl treatment. The fact there was no significant loss of silica indicated that the change was not due to the removal of disordered material.

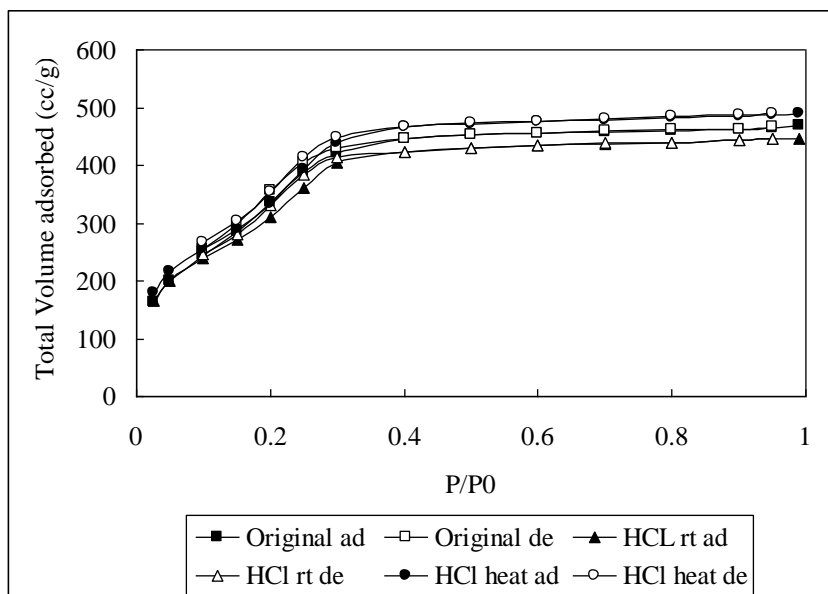


Figure 3.55 The effect of HCl treatment on N₂ adsorption-desorption isotherms

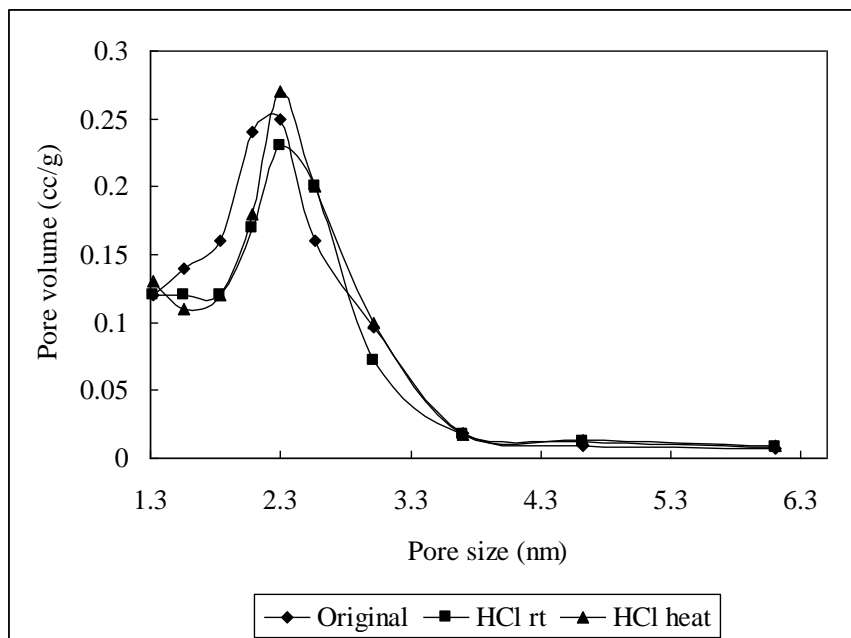


Figure 3.56 The effect of HCl treatment on the pore size distribution

Table 3.21 Effect of HCl treatment on d_{100} spacings and intensity of the calcined samples

	Original	HCl (20°C)	HCl (75°C)
d_{100} spacing (± 0.3 , Å)	34.9	33.7	33.4
Intensity (± 140)	1230	1500	1570

The nitrogen adsorption measurements confirmed a slight increase in uniformity of pore structure by the sharpness of the step of capillary condensation at $P/P_0=0.2$ (Figure 3.55 and 3.56), a slight narrowing of the pore size distribution and a slight increase in the mean pore diameter. These changes are consistent with the removal of small amounts of free silica from the pore walls but no significant structural change.

Table 3.22 The effect of HCl treated on structural properties of calcined MCM-41 phases

	Unit cell ao nm (± 0.03)	Pore size diameter nm (± 0.01)	Wall thickness nm (± 0.04)	Surface area m ² /g (± 70)	Total pore volume cc/g (± 8.6)
Original	4.01	2.19	1.82	1362	468
HCl rt	3.87	2.30	1.57	1270	447
HCl heat	3.84	2.30	1.54	1383	490

The XRD and the nitrogen adsorption data presented above indicate that while the

specific surface area remained essentially constant, the mesoporous pore size increased and unit cell decreased., These effects are consistent with shrinkage of the microporous silica wall material leading to larger pores, thinner walls and decreased unit cell.

3.6.4 The effect of the stirring rate on the age stability

It has been previously observed that increased stirring speed during synthesis produced MCM-41 phases of greater wall thicknesses. It is of interest to determine whether the increased wall thickness imparts greater resistance to aging. Samples prepared at 1000 and 200 rpm were calcined and sealed in vials at room temperature for 2 years. The initial and aged samples were characterized by low angle XRD. Data are presented in Figures 3.57 and 3.58 and summarized in Table 3.23.

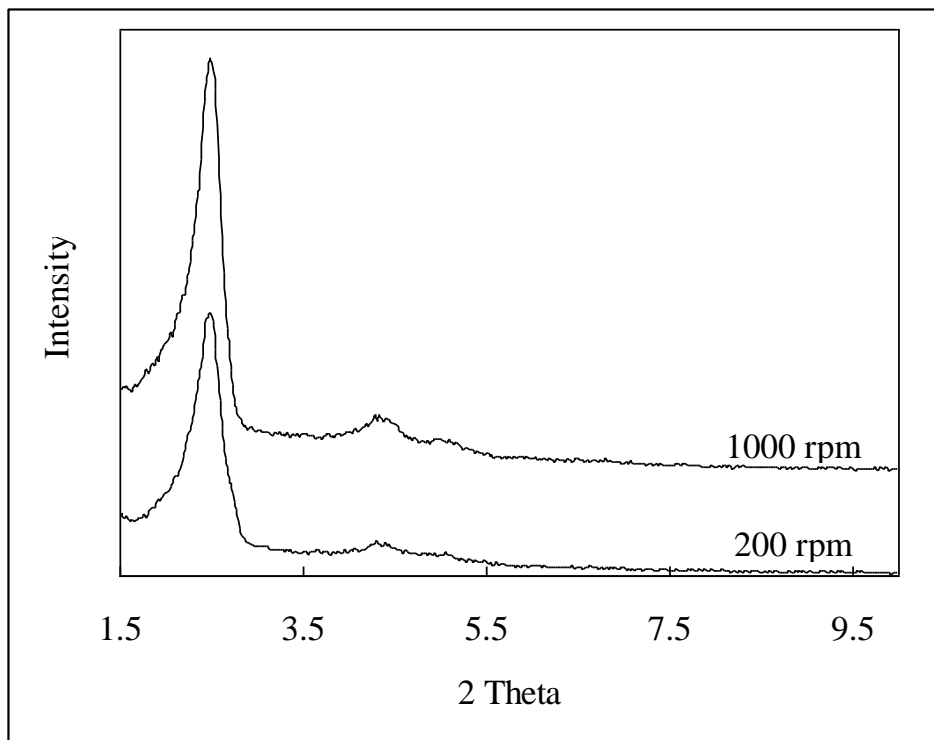


Figure 3.57 XRD patterns of the freshly calcined samples prepared at 200 and 1000 rpm

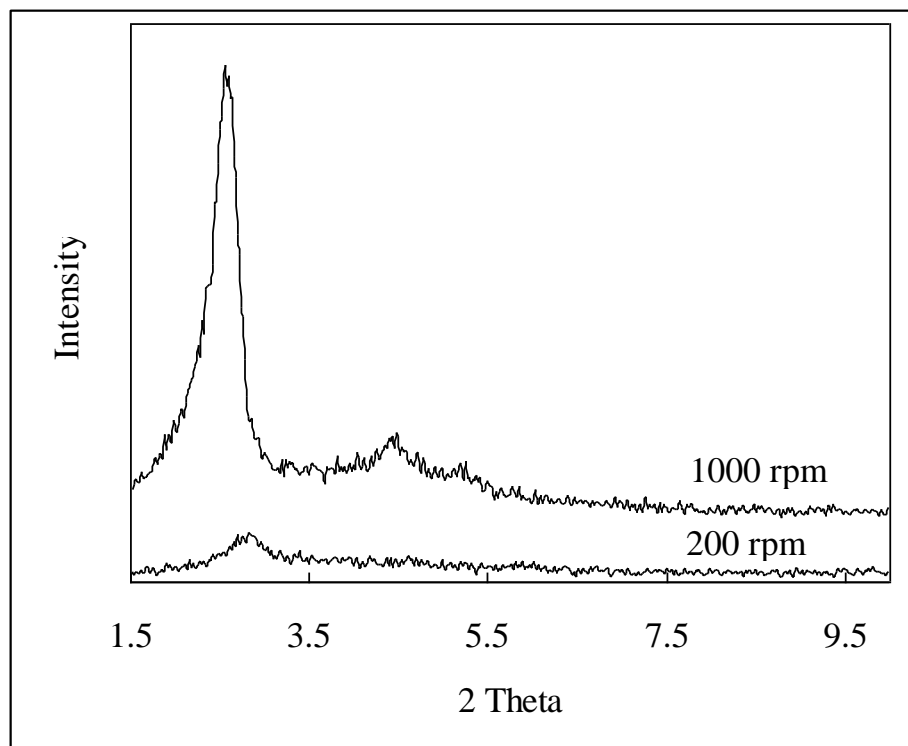


Figure 3.58 XRD patterns of the calcined samples prepared at 200 and 10000 rpm and aged for 2 years

Table 3.23 d_{100} spacing and intensity of freshly prepared and aged calcined samples prepared at 200 and 1000 rpm

Stirring rate (rpm)	1000 fresh	1000 aged 2 y	200 fresh	200 aged 2 y
Intensity ± 140	2083	827	1316	89
d_{100} spacings (± 0.3 , Å)	35.3	34.6	35.3	31.4
Contraction (± 0.6 , Å)	0.7		3.9	

It is clear that preparation at the higher stirring speed has produced a product, which upon calcining, displays superior resistance to aging. This is likely to result from the fact that the higher stirring speed leads to the formation of a product with thicker pore walls. The higher peak intensity of d_{100} peak of the original 1000 rpm sample was most likely to have been caused by variation of instrument beam intensity rather than structural change of the sample. Although the noise on the trace for the aged material is greater, the full width at half height (FWHH) of the d_{100} reflection, and the presence of d_{110} and d_{200} peaks and absence of significant contraction, point to a product of superior stability.

3.6.5 Hydrothermal stability

An indication of the hydrothermal stability of MCM-41 prepared according to Section 2.3 and calcined at 500°C was obtained by immersing the product in boiling water for times varying from 3 to 24 hours.. The treated samples were filtered, dried at room temperature and characterized by low angle XRD, BET surface area determination and BJH pore size measurements. Data are given in Figures 3.59 and Table 3.24

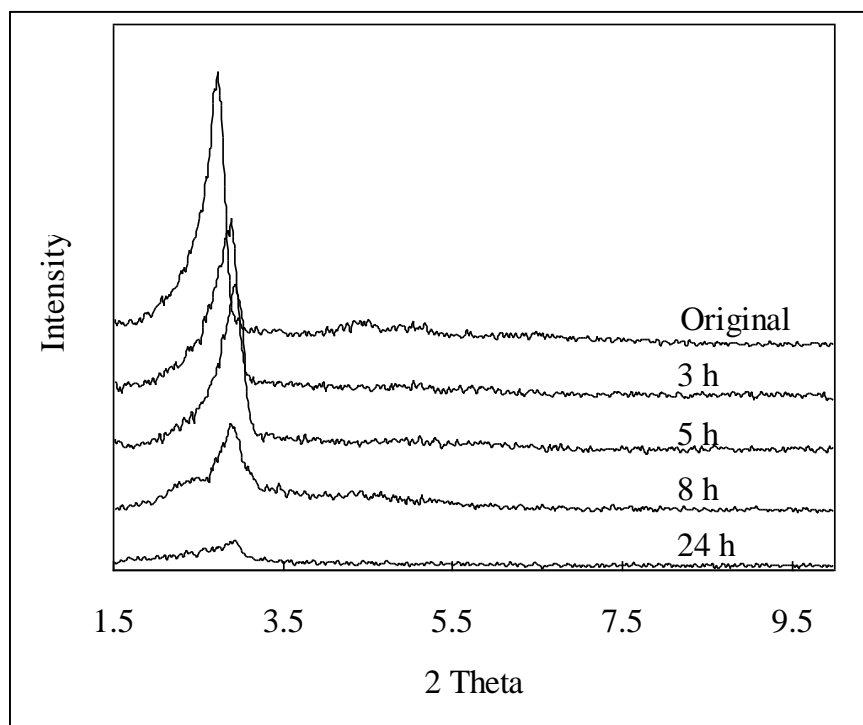


Figure 3.59 The effect of treatment by boiling water on Powder XRD patterns for the calcined MCM-41.

The XRD data (Figure 3.59) show a progressive deterioration of mesoporous structure with prolonged boiling water treatment. The d_{100} peak intensity is decreased, and other peaks due to d_{110} and d_{200} gradually disappear. After 24 hours, only a single broad peak remained indicating the almost complete destruction of the mesoporous structure. It is likely that the siloxane bridges of the walls had been broken under these conditions.

Table 3.24 The effect of varying boiling times on the powder XRD patterns of the calcined MCM-41

	Original	3 h	5 h	8 h	24 h
2 Theta	2.73	2.89	2.93	2.89	2.93
d_{100} spacing (± 0.3 , Å)	32.3	30.5	30.1	30.5	30.1
Intensity (± 140)	1027	688	647	327	111

The nitrogen isotherms and their BJH PSD curves for the calcined samples heated in boiling water for different periods of time are summarized in Figure 3.60 and 3.61. It can be seen that the capillary condensation step became broader with increasing boiling time and completely disappeared after 24 h.

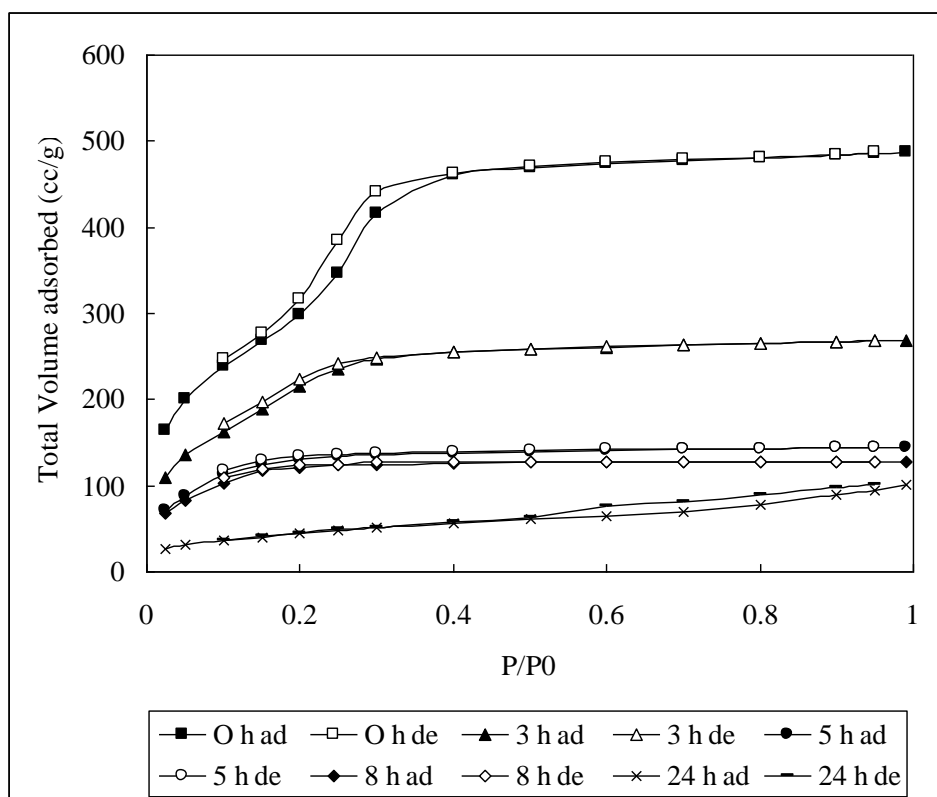


Figure 3.60 N_2 adsorption-desorption isotherms of the calcined samples after exposure to boiling water for different periods of time.

There was an associated gradual broadening of pore size distributions, a movement towards smaller pore size and eventually disappearance of peaks on the PSDs consistent with structure collapse.

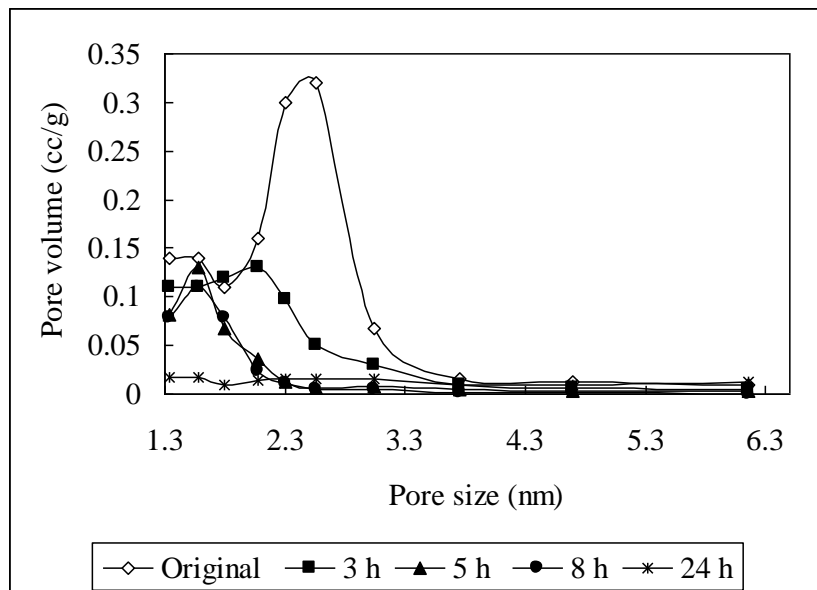


Figure 3.61 The effect of heated water on the pore size distribution

A summary of structural parameters, including calculation of wall thickness is presented in Table 3.25

Table 3.25 The effect of boiling water treatment on structural properties of calcined MCM-41

Refluxing Time Hours	Unit cell a_0 nm (± 0.03)	Pore size diameter nm (± 0.01)	Wall thickness nm (± 0.04)	Surface area m^2/g (± 70)	Total pore volume cc/g (± 8.6)
0	3.43	2.56	0.87	1236	475
3	3.26	2.08	1.18	801	268
5	3.22	1.58	1.64	439	144
8	3.26	1.58	1.68	402	128
24	3.22	-----	-----	162	101

There is a large and progressive decrease in the surface area with boiling water treatment. However some surface area still remains even after 24 hours treatment. This surface area appears to be associated with a broad distribution of pore sizes.

3.7 Mechanism of MCM-41 precursor formation

Mesa [9] has recently proposed a revised mechanism for the formation of MCM-41 silica. This is based upon the belief that at the surfactant concentrations employed, the micelles

in the synthesis system would be spherical rather than rod shaped as used in earlier explanations. When the surfactant CTAB is used for the synthesis of MCM-41 mesoporous silica, a concentration of 2.0% is typically used. Rod shaped micelles typically are formed in the concentration range of 11-20.5 wt%. [9] The initial size of these spherical micelles can be expected to vary with temperature and acid concentration. Mesa [9] suggests that TEOS molecules are absorbed into the micelles and the siliceous species formed by hydrolysis, migrate into and are adsorbed on the outside surface of a palisade layer of the hydrocarbon tails of the surfactant molecules forming the spherical micelle. The acid induced poly-condensation of these TEOS molecules contributes to an increase in micelle size with reaction time. The negative charges of the anions in double layer adjacent to the spherical micelle surface become screened by the silica polymers thus reducing repulsions between the micelles. When enough silica condensation has occurred, and as the inter-micellar repulsive interactions diminish, the elongated polycondensed silicate species act as a bridge to link the spherical micelles which restructure to form the rod-like micellar mesophase. Further coating with the polycondensed silica reinforces the cohesion, and increases the stiffness of the rod-like micelles which then aggregate to form the mesoporous precursor phase.

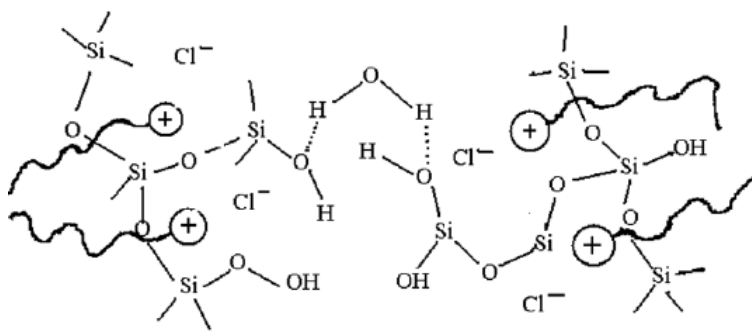


Figure 3.62 Schematic representation of the interaction between the siliceous species and the micelle of surfactant (Mesa) [9]

The diameter of a spherical micelle of CTAB can be expected to be determined by the length of the hydrocarbon chain and the ionic environment that determines electrostatic repulsion of the positively charged head groups. Other factors that contribute to micellar size include the hydrophobic, hydrophilic and electrostatic interactions between the hydrocarbon tail groups, charged head groups and the ions in the suspending solution.

In the acid synthesis route, the acid concentration is the main factor which controls the geometrical packing of the surfactant micelle. At 25°C, the value of the CMC (critical micelle concentration) of the surfactant CTAB is around 10^{-3} mol/L or 0.032 wt.%, the mean aggregation number N is around 80 (function of the concentration). While Mesa argues that increased acid concentration causes greater electrostatic repulsion between polar head groups resulting in decreased mean aggregation number [10], we believe that the increased ionic strength of the higher acid concentration would cause a compression of the double layer and a reduction in micelle size. We extend this reasoning by noting that the penetration into the micelle of the silica polymers and the condensation of the spherical micelles to form rod shaped micelles would result in rod shaped micelles with a silica skin. This silica skin would exert a compressive force due to surface tension and would result in folding of the hydrocarbon chain in the central core and reduction of micelle diameter. This explanation is consistent with the pore diameter being much less than the unmodified micelle diameter and the observations that pore size decreases with acid concentration and wall thickness increases with acid concentration. If silica condensed on the outside of a preformed rod shaped micelle, the pore diameter would be expected to have a diameter close to that of an unmodified micelle (6.4 nm). The Mesa model also accounts for microporosity. Because the silica condenses around the hydrocarbon tails of the monomer units of the surfactant palisade, when these monomers are removed by calcining the molecular imprints left remaining will provide pores of sub-nanometer dimensions.

3.8 Reference for Chapter 3

1. Schacht, S.; Huo, Q.; Voigt-Martin, I.G.; Stucky, G.D.; Schüth, F. *Science* 273, **1996**, 768.
2. Lin, H.P.; Liu, S.B.; Mou, C.Y.; *Chem. Commun.* **1999**, 583.
3. Che, S.; Sakamoto, Y.; Terasaki, O.; Tatsumi, T. *Chem. Lett.* 2, **2002**, 214.
5. Huo, H.; Margolese, D.I.; Ciesla, U.; Demuth, D.G.; Feng, P.; Gier, T.E.; Sieger, P.; Firouzi, A.; Chemelka, B.F.; Schüth, F.; Stucky, G.D. *Chem. Mater.* 6, **1994**, 1176
6. Klug, H.P.; Alexander, L.E; *X-ray Diffraction Procedures*, 2nd Edition ed., Wiley Interscience, New York, **1974**.
7. Srinivasu, P.; Lim, S. H.; Kubota, Y.; Tatsumi, T. *Catalysis Today* 111, **2006**, 379–384
8. Yu, C.Z; Fan, J; Tian, B.Z; Zhao, D.Y; *Chem. Mater.* 16, **2004**, 889-898
9. Mesa, M; Sierra, L; Guth, J.L. *Microporous and Mesoporous Materials*. 102, **2007**, 70–79
10. Ulmins, J; Lindman, B; Lindblomand, G; Drakemberg, T; *J. Colloid Interface Sci.* 65, **1978**, 88

Chapter 4 Preparation of metal loaded MCM-41***by immersion treatment of preformed phases*****4.1 Introduction**

In Chapter 3, the optimum reaction conditions to produce pure silica MCM-41 with high surface area and well ordered pore structures were investigated. In the present chapter conventional loading by immersion was used to load organometallic complexes into the calcined silica phases prepared as described in Section 2.3. Typically previous workers have used toluene and THF as the solvent in immersion loading studies involving organic or organometallic compounds and have used limited rinsing to remove excess. In the present study we were concerned about the possibility of solvent effects. We also wished to load the organometallic compound into the pores in such a way so to minimize the size of the metal particles that would be formed upon calcining. Thorough rinsing was used to remove free complex that would otherwise precipitate when the solvent was evaporated. Precipitated complex was considered likely to sinter during calcining to form the larger particles that have been observed in previous studies of this sort. It was considered that by removing all except the complex adsorbed onto the walls of the mesopores, aggregation and sintering effects would be minimized and the formation of metal particles smaller than pore dimensions would be favoured.

4.2 The effect of solvent immersion on the preformed MCM-41 structure

In many cases reported in the literature, the loading of MCM-41 by imbibing has resulted in modification of the MCM-41 structure (see Section 1.2.12). It was of interest to determine whether it was the metal loading or the solvent that caused this modification and if the solvent was responsible, to find a solvent for which the effect was minimal.

Dry calcined MCM-41 (0.5 g) was suspended in 10 mL of a range of dry solvents (THF, toluene, ethyl acetate, and dioxane) stirred in an ice bath for 24 h under partial vacuum. The solid was recovered by filtration, washed with dichloromethane, dried under high vacuum for 3 hours and then calcined at 550°C for 5 h in air. The solvent treated samples were characterized by low angle XRD, BET surface area determination and BJH pore size measurements after the air drying and calcining steps. Preliminary experiments (data not reported) had shown that rinsing with dichloromethane had no effect on pore structure.

4.2.1 Effect of solvent on mesoporous structure

XRD data for the original calcined materials, solvent treated samples after vacuum drying and solvent treated samples after calcining are presented in Figures 4.1 to 4.4 and Tables 4.1 and 4.2. All materials gave typical MCM-41 diffraction patterns, indicating ordered hexagonal mesoporous structures but some were significantly modified by solvent treatment.

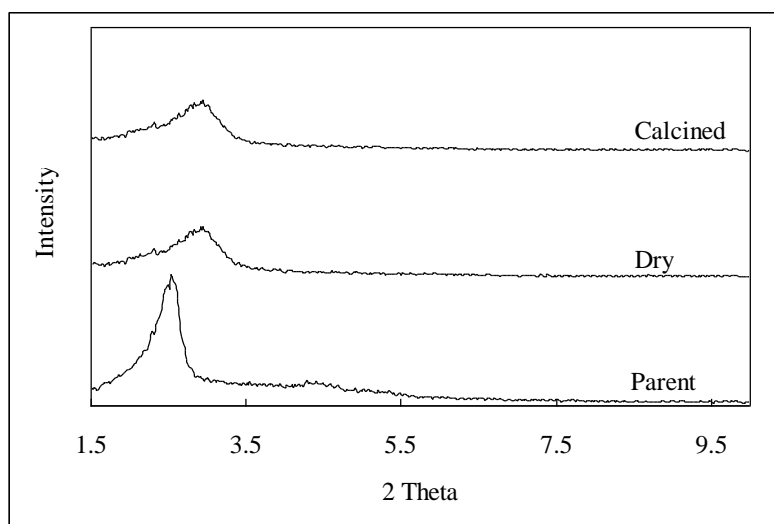


Figure 4.1 The effect of THF on XRD pattern of MCM-41.

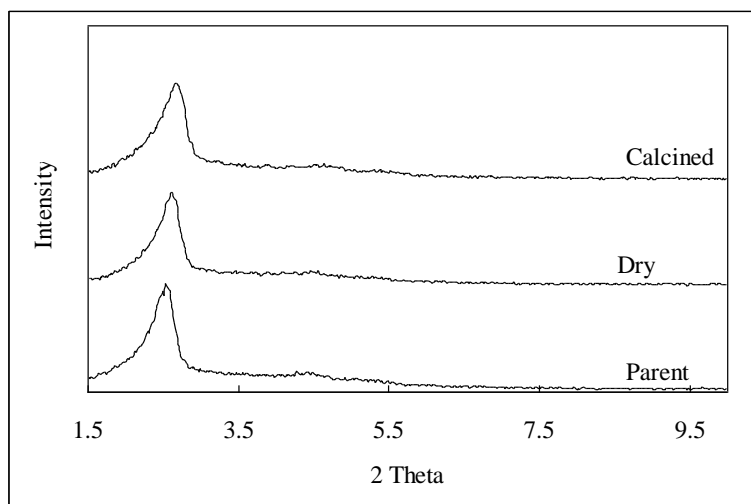


Figure 4.2 The effect of toluene on XRD pattern of MCM-41.

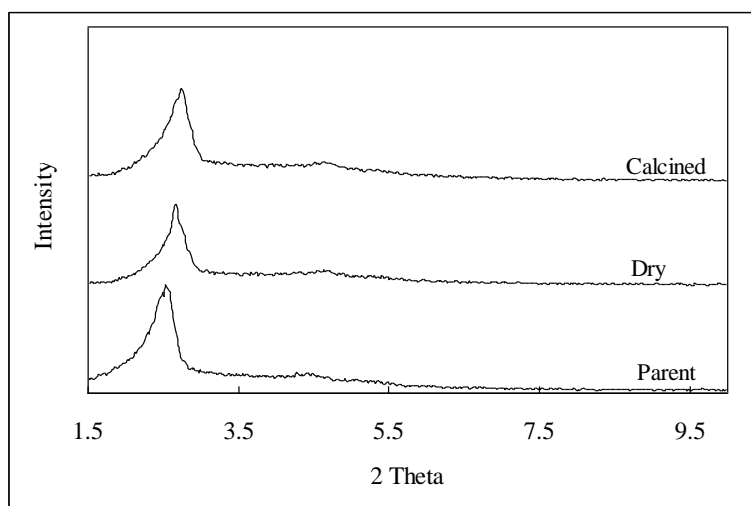


Figure 4.3 The effect of dioxane on XRD pattern of MCM-41.

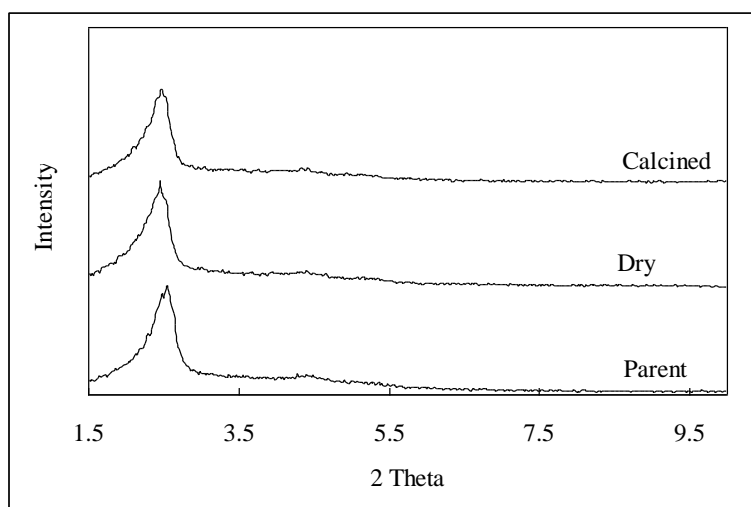


Figure 4.4 The effect of ethyl acetate on XRD pattern of MCM-41.

Table 4.1 The effect of solvent treatment on XRD d_{100} spacings (C = calcined).

	Original	THF	Dioxane	Toluene	Ester
d_{100} spacing Dry (± 0.3 Å)	34.9	33.0	33.0	33.7	36.5
Change		-1.9	-1.9	-1.2	+1.6
d_{100} spacings C (± 0.3 Å)	34.9	30	32.1	33.2	35.8
Change		-4.9	-2.8	-1.7	+0.9

Table 4.2 The effect of solvent treatment on XRD d_{100} intensity.

	Original	THF	Dioxane	Toluene	Ester
Intensity Dry (± 0.3 Å)	2080	1540	1610	1820	2080
Intensity C (± 0.3 Å)	2080	850	1840	1910	1820

All solvent treated samples were slightly affected. Effects on XRD intensity were greatest for THF, both after air drying and after subsequent calcining. The effect of the other solvents on intensities were minor. THF also had greatest effect on d_{100} spacing, causing a massive 4.9 Å contraction upon calcining. Both toluene and dioxane produced more modest contractions both at the air dried and calcined stages. In contrast ethyl acetate treatment lead to slight expansion of the d_{100} spacing.

4.2.2 Effect of solvent on nitrogen adsorption

The effect of the various solvent treatments on the nitrogen adsorption/desorption isotherms and BJH pore sizes is more revealing. Data are summarized in Figures 4.5 to 4.8

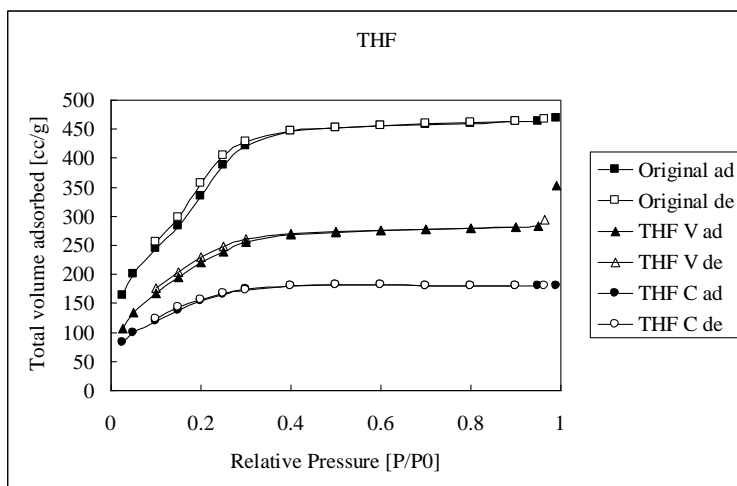


Figure 4.5 The effect of THF on N_2 adsorption-desorption isotherms (V = vacuum dried).

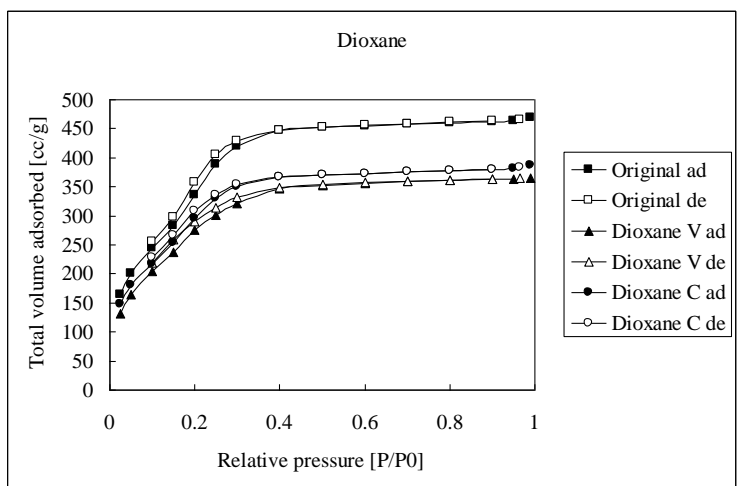


Figure 4.6 The effect of dioxane on N_2 adsorption-desorption isotherms.

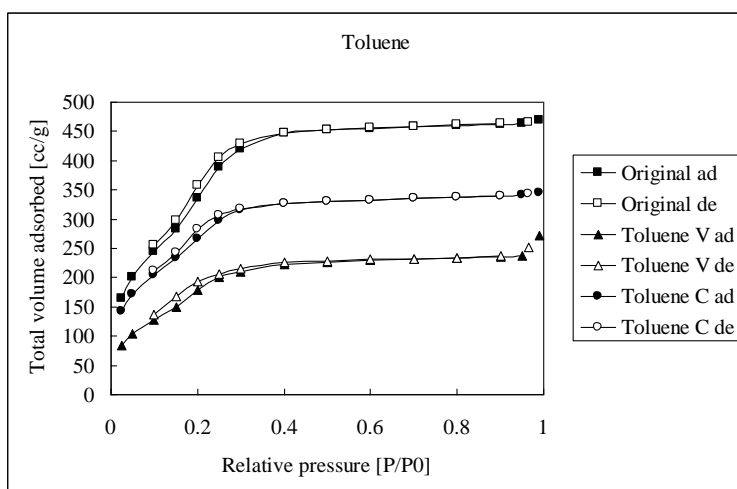


Figure 4.7 The effect of toluene on N_2 adsorption-desorption isotherms.

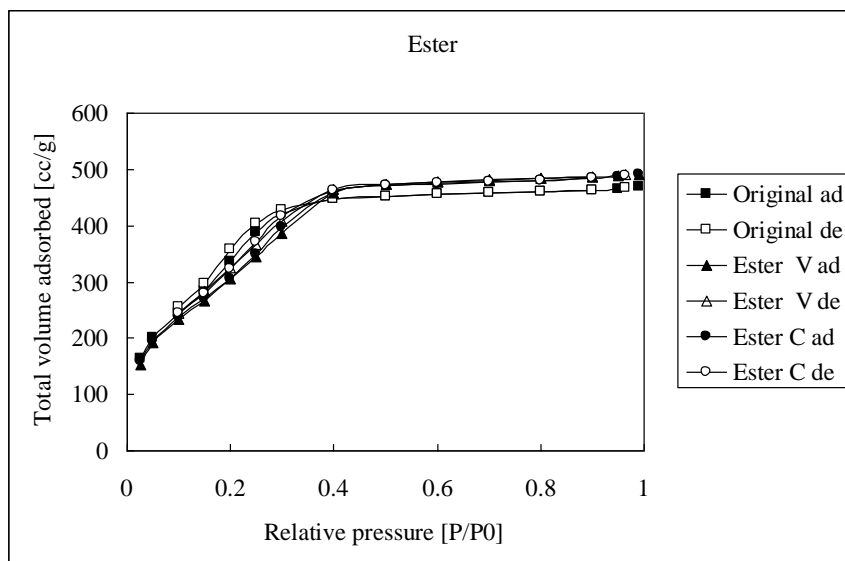


Figure 4.8 The effect of ethyl acetate on N₂ adsorption-desorption isotherms.

All the materials exhibit type IV isotherms, typical for mesoporous materials. After the THF, dioxane and toluene treatments, the plateaus of the N₂ sorption curves were displaced to lower adsorption values relative to the original MCM-41, indicating decreases in pore volumes. However, after calcining of the dioxane and toluene treated materials, plateau adsorption values were increased, indicating partial recovery of the pore volumes. For the THF treated materials however, the plateau values of the N₂ sorption curves decreased further upon calcining, indicating further loss of the pore volume. Only for ethyl acetate treated systems was there little effect on nitrogen adsorption.

Pore size distribution curves (see Figures 4.9 to 4.12) provide further evidence for solvent effects on MCM-41 structure. Only for the ethyl acetate treated system did the pore structures remain relatively unaffected.

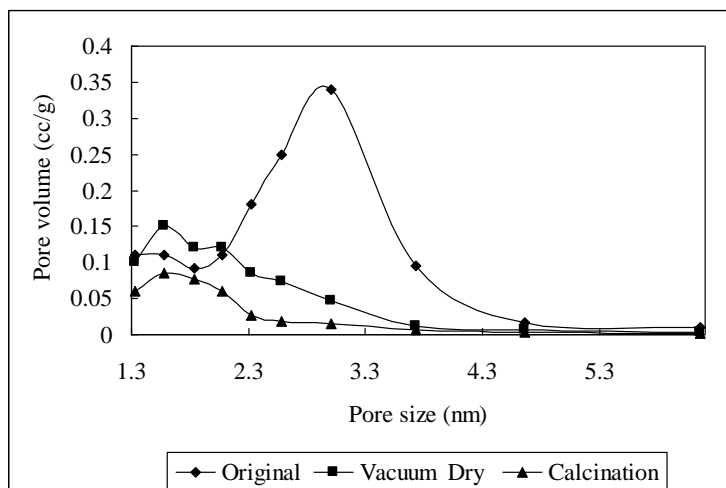


Figure 4.9 Pore size distribution for the solvent THF

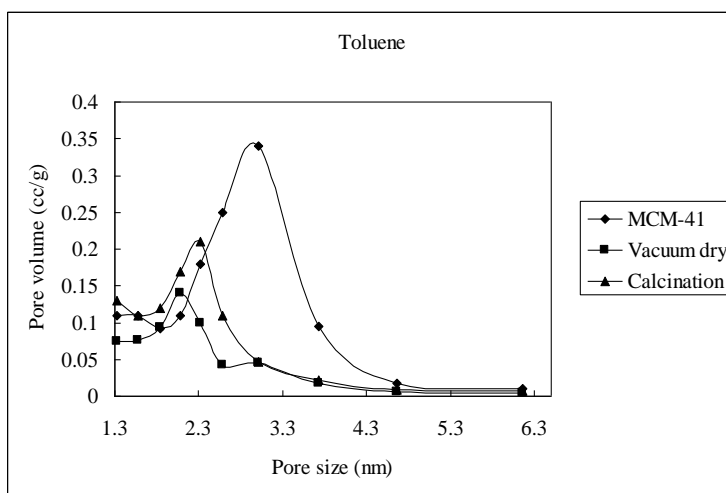


Figure 4.10 Pore size distribution for the solvent toluene.

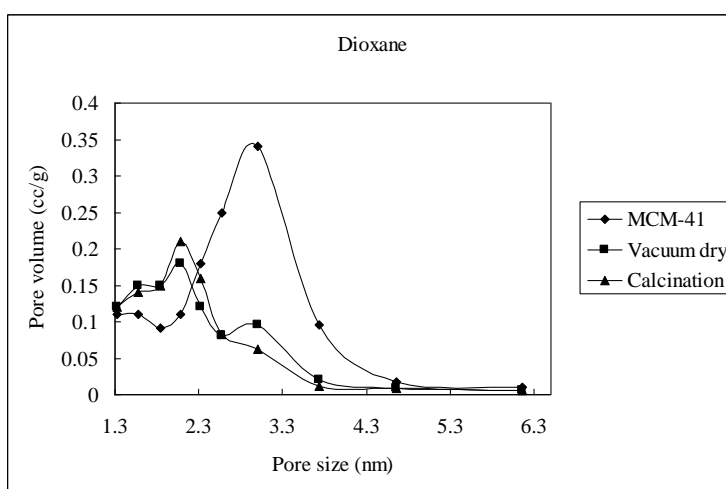


Figure 4.11 Pore size distribution for the solvent dioxane.

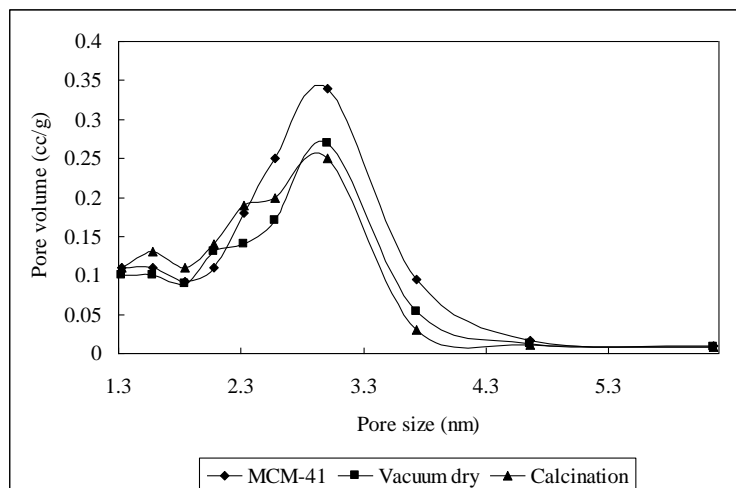


Figure 4.12 Pore size distribution for the solvent ethyl acetate

Tables 4.3 and 4.4 summarize details of the pore structures of the solvent treated materials and allow comparison with the parent material.

Table 4.3 The effect of the solvent treatment on structural properties of calcined MCM-41 phases after drying.

	Unit cell a_0 nm (± 0.03)	Pore size diameter nm (± 0.01)	Wall thickness nm (± 0.04)	Surface area m^2/g (± 70)	Total pore volume cc/g (± 8)
Parent	3.94	2.76	1.18	1362	468
THF Dry	3.80	1.58	2.22	820	354
Dioxane Dry	3.80	2.07	1.73	1050	365
Toluene Dry	3.88	2.31	1.57	1010	344
Ester Dry	4.20	2.98	1.22	1220	491

Table 4.4 The effect of the solvent treatment on structural properties of calcined MCM-41 phases after drying and subsequent calcining.

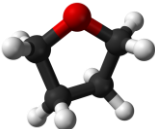
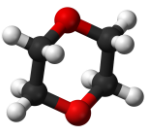
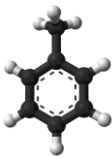
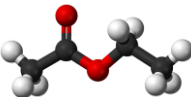
	Unit cell a_0 nm (± 0.03)	Pore size diameter nm (± 0.01)	Wall thickness nm (± 0.04)	Surface area m^2/g (± 70)	Total pore volume cc/g (± 8)
THF C	3.45	1.59	1.86	420	148
Dioxane C	3.69	2.07	1.62	1130	387
Toluene C	3.82	2.18	1.64	1158	401
Ester C	4.12	3.01	1.11	1220	492

Consistent with earlier results, the vacuum dried, THF treated, system showed the largest pore size contraction (from 2.76 nm to 1.58 nm, i.e. about 43% contraction). The pore wall thickness showed a significant increase (from 1.18 nm to 2.22 nm). The surface area was significantly decreased from 1362 to 820 m²/g after THF treatment and decreased still further to 420 m²/g after calcining.

4.2.3 Discussion of solvent effects on the MCM-41 structure

The studies reported in the previous section indicate that solvents can have major effects on the MCM-41 mesoporous structure. Of the solvents studied, the magnitude of the effects were generally in the order THF>Dioxane>Toluene> Ethyl acetate. Some clues as to what may be involved in causing these effects can be gained by a consideration of the molecular properties of the solvents summarized in Table 4.5

Table 4.5 Summary of some important solvent properties [3]

Name	THF	Dioxane	Toluene	Ethyl acetate
Molecular structure				
Molecular Weight	72.10572 [g/mol]	88.10512 [g/mol]	92.13842 [g/mol]	88.10512 [g/mol]
Molecular Formula	C ₄ H ₈ O	C ₄ H ₈ O ₂	C ₇ H ₈	C ₄ H ₈ O ₂
Density	0.8892 g/cm ³	1.033 g/cm ³	0.8669 g/mL	0.897 g/cm ³
Melting point	-108.4 °C	11.8 °C	-93 °C	-83.6 °C
Boiling point	66 °C	101.1 °C	110.6 °C	77.1 °C
Solubility in water	Miscible	Miscible	0.47 g/l	83 g/l
Viscosity	0.48 cP at 25 °C	1.54 cP at 20 °C	0.590 cP at 20 °C	0.426 cP at 25 °C
Topological Polar Surface Area [2]	9.2	18.5	0	26.3
Complexity [3]	22.8	26.5	42	49.5

It is proposed that for the solvent to have an effect on the mesoporous structure, it is necessary for the solvent to penetrate the silica matrix beyond the mesopores i.e. to penetrate the micropores of the silica cell walls. Having penetrated the cell wall, it would be further necessary for the solvent to interact strongly with the lattice in such a way that disruption of the Si-O-Si framework is induced. One possibility is that the polar portions of oxygen containing solvents interact with surface hydroxyl groups of MCM-41. However, other factors must be involved because ethyl acetate, which has two oxygen atoms has very little effect whereas toluene which has no oxygen, has an appreciable effect while the largest effect is observed for THF which has only one oxygen atom. Further, the effects for ethyl acetate and dioxane are different even though they have same molecular formula and contain two oxygen atoms.

Reference to Table 4.5 suggests that the best correlations between solvent molecular property and their effect on mesoporous structure is obtained for the parameters called complexity and polar surface area.

The topological Polar Surface Area (PSA), defined as the sum of surface contributions of polar atoms (usually oxygens, nitrogens and attached hydrogens) in a molecule [2], has been shown to correlate well with drug transport properties, such as intestinal absorption, or blood-brain barrier penetration. Of the three oxygen containing solvents, THF has the lowest PSA and thus will penetrate most readily what is likely to be the mainly hydrophobic environment of the micropores. Having penetrated the pores, strong hydrogen bonds can be formed with the surface hydroxyl groups of the silica matrix causing structural disruption. Most of the effect is thus likely to occur during the initial contact with the solvent rather than any possible surface tension effects as the sample is subsequently dried. There is no correlation between the magnitude of the solvent effects and surface tension. At the other extreme, according to this explanation, ethyl acetate, while containing two oxygen atoms and having the same molecular formula as dioxane has a much lesser effect on mesostructure because its

larger effective size prevents access into the micropores. Toluene, which has no oxygen atoms so as PSA value is zero, will readily penetrate the pores, but because it will not strongly interact with the wall, its structure modifying effect is limited.

A parameter that correlates well with the structure modifying effect of the solvents is their molecular complexity. Molecular complexity takes into account the connectivity and closely related structural features of a molecule such as branching, cyclicity and symmetry [3]. The small, compact cyclic and symmetric THF and dioxane molecules have low values of complexity which may facilitate their ready penetration into the micropores.

In addition to the effect of initial exposure to the solvents, further changes in structure occur upon calcining. Again the order is THF>dioxane>toluene>ethyl acetate. The fact that post drying effects occur is evidence for strongly bound solvent causing disruption during their release during calcining. The THF and dioxane are likely to be hydrogen bonded to the surface hydroxyl groups whereas the toluene is likely to be strongly bound to the hydrophobic environment of the silicon micropore walls. The sample exposed to ethyl acetate showed little effect even upon calcining after drying, presumably because the solvent hadn't penetrated the micropores.

4.2.4 Summary

The results of this investigation have demonstrated that solvents used in the imbibing of organometallic compounds into MCM-41 can have a significant effect on the mesoporous structure. Solvents that interact strongly with silanol groups, for example THF, can result in large decreases in porosity, surface area and structural stability. Suitable solvents for immersion studies are ethyl acetate and toluene.

4.3 The loading of Fc and substituted Fc (S-Fc) complexes into MCM-41 by the I method

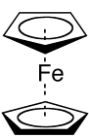

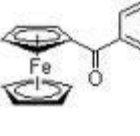
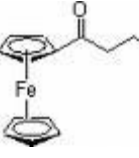
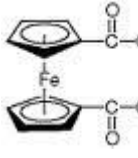
According to the I method, the calcined material is exposed to a solution of the metal containing species, the solution is imbibed into the pores under vacuum and the solvent is then evaporated leaving behind a deposit of the metal species.

For this work the solvent toluene was chosen because it has a relatively high boiling point and is a good solvent for all the complexes of interest. While having some effect on mesoporous structure (see section 4.2) its effect is much less than THF, the other high boiling point solvent typically used for work of this type. Ethyl acetate, while having less effect on mesoporous structure was judged to be unsuitable because its low boiling point would preclude the vacuum step needed to fill the mesopores (see Section 2.4) and its poor solvent properties for the complexes of interest.

Six organometallic compounds were used to explore aspects of loading by the I Method. They were Ferrocene (Fc), Acetyl ferrocene (Fac), Butyrylferrocene (Ft), Benzoylferrocene (Fb), di-Acetylferrocene (Fd), Iron acetylacetonate (Fa), Cyclopentadienyl iron dicarbonyl dimer (Fy). Structural formulae are summarized in Table 4.6.

The Fc, Fac and Fy are ferrocene type compounds. Fac is of interest because it should indicate the effect on loading of substitution on the pentamethyl ring. Fy is of interest because it contains two metal atoms and should produce higher Fe loadings for a given complex mol/L concentration. It is also of interest because if rather than having the two metal atoms of the same element, different metals were incorporated, this may provide a means of loading mixed metal particles of defined chemical composition into the pores. Fy is also a bulky molecule with high polarity resulting from the 4 oxygen atoms and so that structural effects on the silica matrix may result.

Table 4.6. Molecular properties of ferrocene and substituted ferrocene complexes.

Molecular name	Ferrocene (Fc)	Acetyl ferrocene (Fac)	Benzoyl ferrocene (Fb)	Butyryl ferrocene (Ft)	Diacetyl ferrocene (Fd)
Molecular Formula	$C_{10}H_{10}Fe$	$C_{12}H_{12}OFe$	$C_{17}H_{14}OFe$	$C_{14}H_{16}FeO$	$C_{14}H_{14}O_2Fe$
Molecular structure					
Molar mass	187.97 g/mol	228.07 g/mol	290.14 g/mol	256.12 g/mol	270.1 g/mol
Metal content	29.23 %	24.09 %	18.94 %	21.45 %	20.34 %
Molecular volume	198 \AA^3	252 \AA^3	342 \AA^3	288 \AA^3	306 \AA^3
Topological Polar Surface Area	0 \AA^2	23.1 \AA^2	17.1 \AA^2	17.1 \AA^2	46.1 \AA^2
Complexity	11.6	170	242	176	159

Experiments were performed to determine the effect of concentration upon loading.

4.3.1 The effect of Fc and S-Fc complexes concentration on the metal loading

Varying amounts of substituted ferrocene (S-Fc) were dissolved into 10 mL toluene to give S-Fc concentrations ranging from 1 to 100 g/L. Dry calcined MCM-41 (0.5 g) was suspended in this solution under vacuum for 24 hours as described in Section 2.4. The material was thoroughly rinsed until rinsing were colourless and then dried under vacuum. The dried, as immersed, material was analyzed for iron according to Section 2.3. Data for Fe loadings (wt% of as-immersed product) achieved are summarised in Figure 4.13 and Table 4.7.

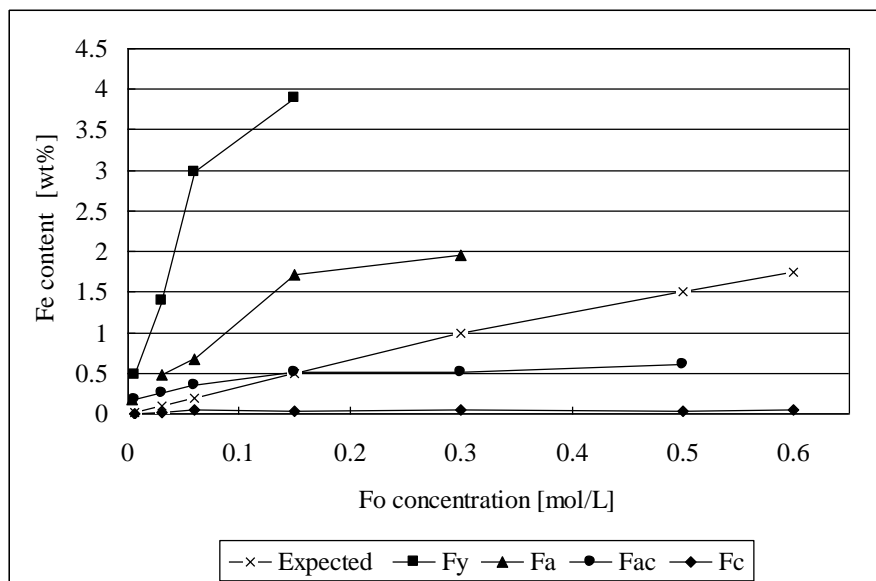


Figure 4.13 The effect of complex concentration on Fe loading by the I-Method (24 hour exposure)

Table 4.7 Relative loadings of MCM-41 by the I method for different organometallic complexes at a single concentration (S-Fc concentration = 0.15 mol/L).

	Fc	Fac	Ft	Fb	Fd	Fa	Fy
Fe content (wt%)	0.06	0.67	1.10	0.99	2.22	1.96	3.89

Also shown in the figure is the uptake that would be expected if all the pore volume was filled with complex solution and all the complex was retained during the exhaustive rinsing. It is clear that processes occur during the experiment that profoundly modified this expected result. Much less Fc than expected is taken up and at concentrations above 0.06 mol/L and increased concentration has no effect on final loading. In contrast, much more Fy and Fa is taken up than can be accounted for by the volume of solution expected to be imbibed into the pores. The Langmuirian shape of the plot of amount loaded versus concentration is typical of an adsorption process with uptake increasing with concentration up to a saturation limit. Fac uptake also shows adsorption characteristics, with saturation adsorption being achieved at 0.15 mol/L.

The low uptake of Fc is puzzling. It may be that this complex is only weakly adsorbed onto the pore walls so that most of the imbibed complex was lost during the rinsing. The results clearly indicate that the silica matrix of the pores has different affinities for the various complexes used. The order of loading obtained by the I method was $Fy > Fa, Fd > Ft, Fb, Fac > Fc$. This order is consistent with the number of S-Fc containing C=O groups (4 C=O groups for Fy, 3 for Fa, 2 for Fd, 1 for Fac, Ft and Fb, and 0 for Fc). The increasing affinity of the silica matrix for molecules containing polar C=O groups follows the trend of greater matrix interaction previously observed for solvents containing C=O groups (see Section 4.2).

4.3.2 Effect of loading S-Fc complexes on mesoporous structures

XRD powder patterns were determined for the dried as-immersed samples prepared by imbibing 0.15 mol/L S-Fc solutions. Results are given in Figure 4.14.

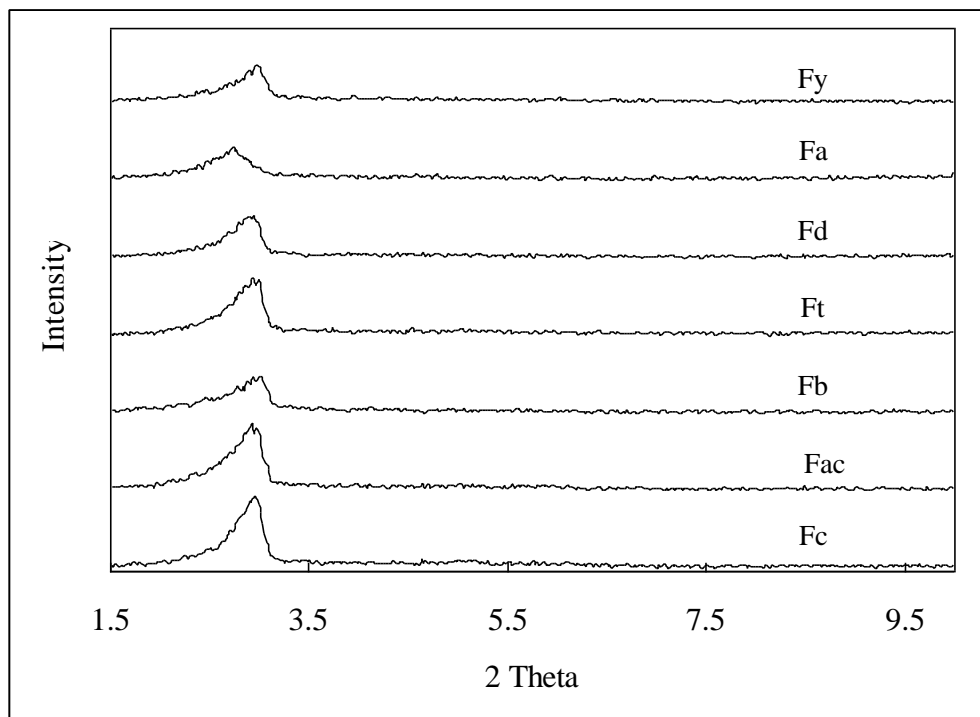


Figure 4.14 The effect of loading different S-Fc complexes on XRD patterns of MCM-41.

All materials gave only one main peak in the range of $2\theta = 2.90$ to 2.97° , which was

indexed as a 100 diffraction. The peaks expected in the range of 3.5 to 6 ° due 110 and 200 diffractions were not present. The diffracted intensities decreased significantly after the imbibing of S-Fc (see table 4.8), indicating that while the ordered hexagonal mesoporous structures were maintained, they were significantly modified by S-Fc treatment.

Table 4.8 The effect of loading different S-Fc complexes on d_{100} intensity of MCM-41.

	Fc	Fac	Ft	Fb	Fd	Fa	Fy
d_{100} Intensity	480	470	390	260	290	240	260

4.3.3 Effect of loading S-Fc complexes on N₂ adsorption-desorption characteristics

Nitrogen adsorption data, including nitrogen adsorption/desorption isotherms and BJH pore sizes, for samples described in section 4.3.2, are presented in Figures 4.15 and 4.16. In all cases, the loaded samples were vacuum dried before nitrogen adsorption experiments. All but the Fy loaded complex exhibited typical type IV isotherms and all except the Fc loaded product showed decreased plateau values relative to the parent material after saturation with pure toluene and vacuum drying (see Figure 4.17). The plateau values and capillary condensation decrease with increased loading of the S-Fc. Capillary condensation is almost entirely absent for the highly loaded Fy system, which when taken with the XRD data, indicate blocking of mesopores and disruption of mesoporous structure by the imbibed complex. However, micropore condensation at low nitrogen pressures is little affected by the loading.

The corresponding BJH desorption pore diameter distribution patterns (see Figure 4.19) reflect the above trends. The pore diameter decreased with increasing the amount of loading organometallic complex, indicating that the loading of S-Fc into the structure has filled the pore structure, reducing the pore volumes and pore diameters.

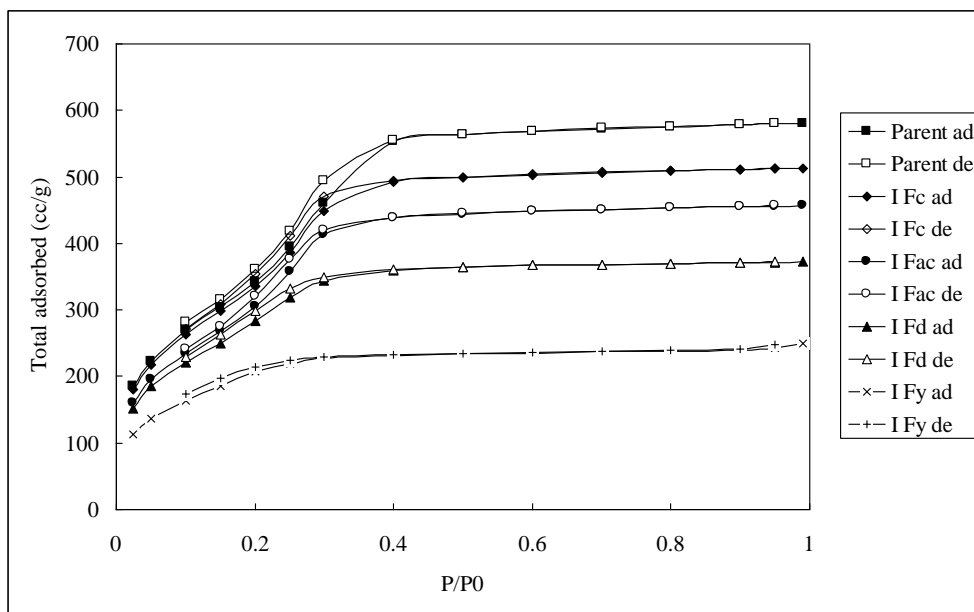


Figure 4.15 The effect of different organometallic complexes loading on N_2 adsorption-desorption isotherms.

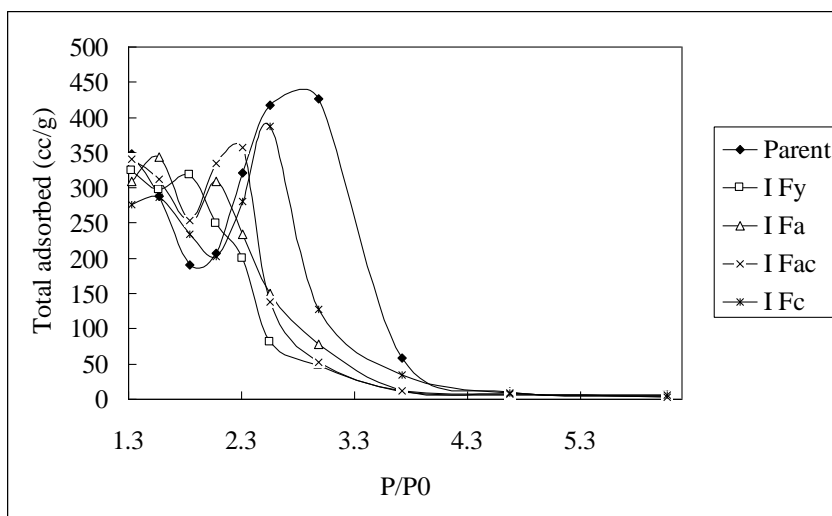


Figure 4.16 The effect of different organometallic complexes loading on the pore size distribution

4.3.4 Kinetic effects during loading

The possibility of increased loading resulting from a sorption process was tested by a kinetic experiment. MCM-41 was exposed to the most strongly adsorbed complex (Fy)

for various adsorption times. Results are shown in Fig 4.17.

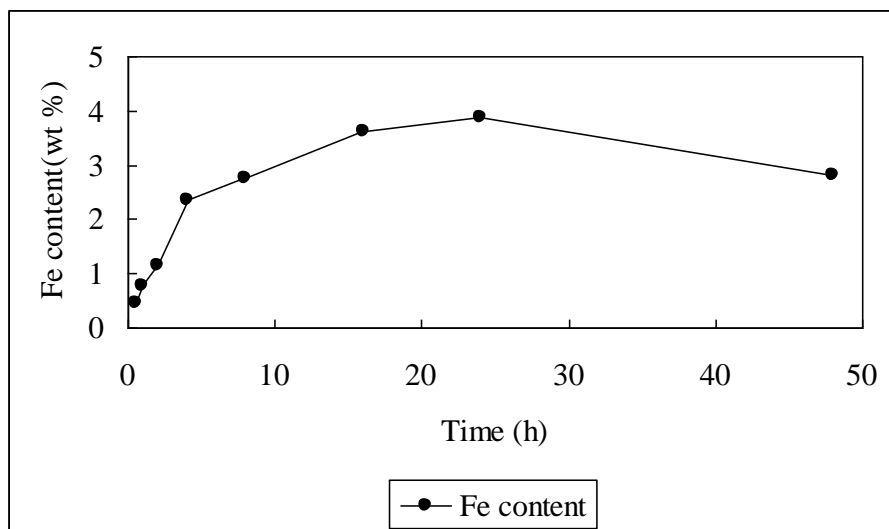


Figure 4.17 Kinetics of F_y uptake by the I-method

Figure 4.17 shows that the iron content in final sample increased to a maximum with increasing immersion time over the range 0 to 24 hours. The fraction of maximum uptake (F_y) was used to construct F_y vs \sqrt{t} and $\ln(1 - F_y)$ vs t plots (see figures 4.18 and 4.19). The linearity of both plots meant it was not possible to discriminate between a simple first order adsorption process or a diffusion controlled mechanism as being responsible for the adsorption kinetics.

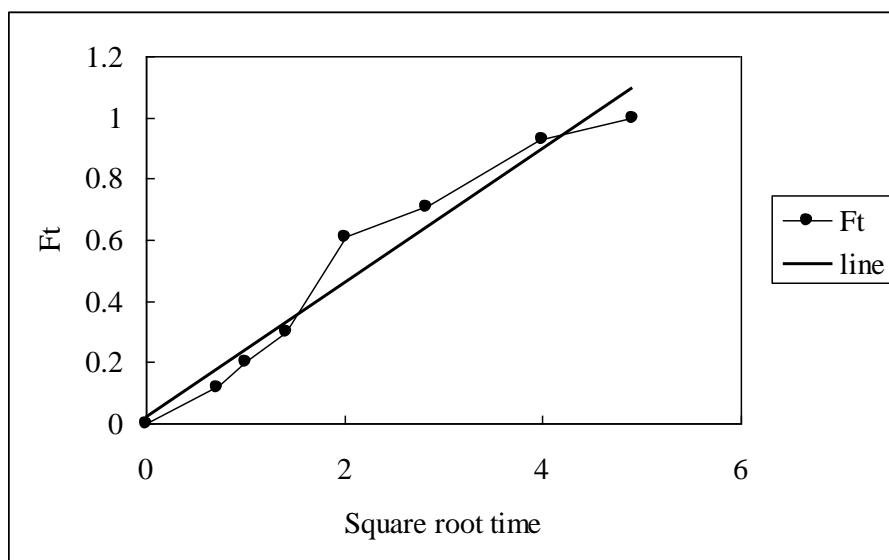


Figure 4.18 Plot of adsorption fraction (F_t) versus square root of time

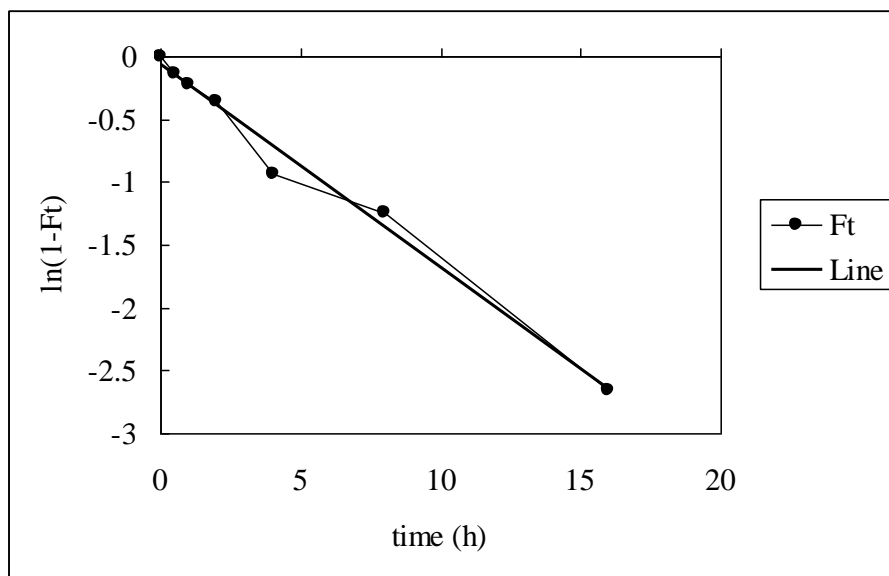


Figure 4.19 Plot of log of adsorption sites remaining [$\ln(1-F_t)$] versus time

Diminished loading beyond the first 24 hours was probably caused by degradation of the mesoporous structure, which had previously been observed in studies of solvent effects (see Section 4.2) and was further indicated by decreased plateau gas adsorption and reduced XRD intensities. The fact that uptake over the first 24 hours is kinetically controlled is evidence that uptake is an adsorption process.

4.3.5 Effect of immersion time loading on mesoporous structure

Effect of immersion loading time on XRD

XRD powder patterns were measured for the dried as-immersed samples. Results for Fy treated MCM-41 are given in Figure 4.20. Loading with Fy caused a systematic decrease over time of the diffracted intensities. The d_{100} spacing also decreased with time. While the contraction of the d_{100} spacing could have been a solvent effect (see Section 4.2), the effect on intensity could only have been caused by the loading.

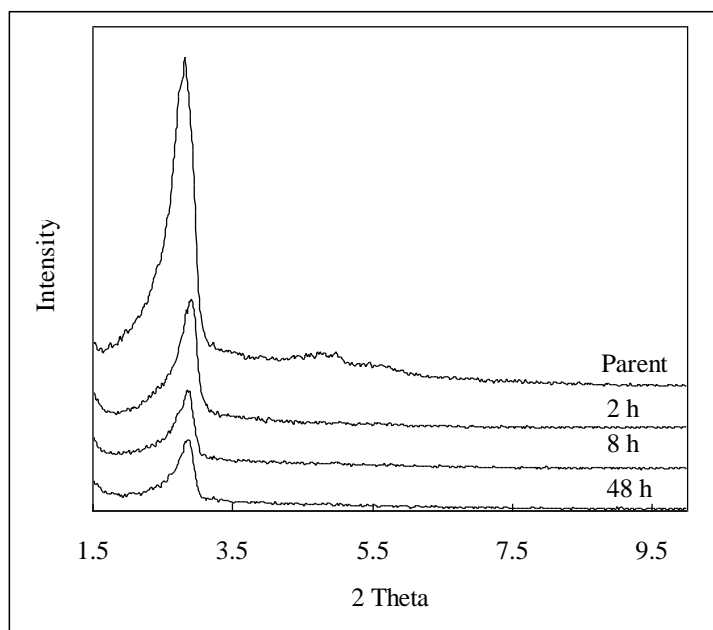


Figure 4.20 The effect of Fy immersion time on XRD pattern of MCM-41.

Effect of immersion loading time on nitrogen adsorption.

Data for the effect of the Fy immersion time on the nitrogen adsorption/desorption isotherms and BJH pore sizes are summarized in Figures 4.21 and 4.22. The interpretation of this data is complicated by the previous observation that changes in the adsorption /desorption isotherms and BJH pore sizes were also brought about by contact with the solvent alone (see Figures 4.7 and 4.10). The trends were all in the same direction i.e. towards lower adsorption and smaller pore sizes but were much greater after the same exposure time for the loading experiment.

After short immersion times the materials exhibited typical type IV isotherms. The plateau values decreased with loading time and the capillary condensation stage decreased and disappeared after 48 hours indicating the disappearance of the mesopores.

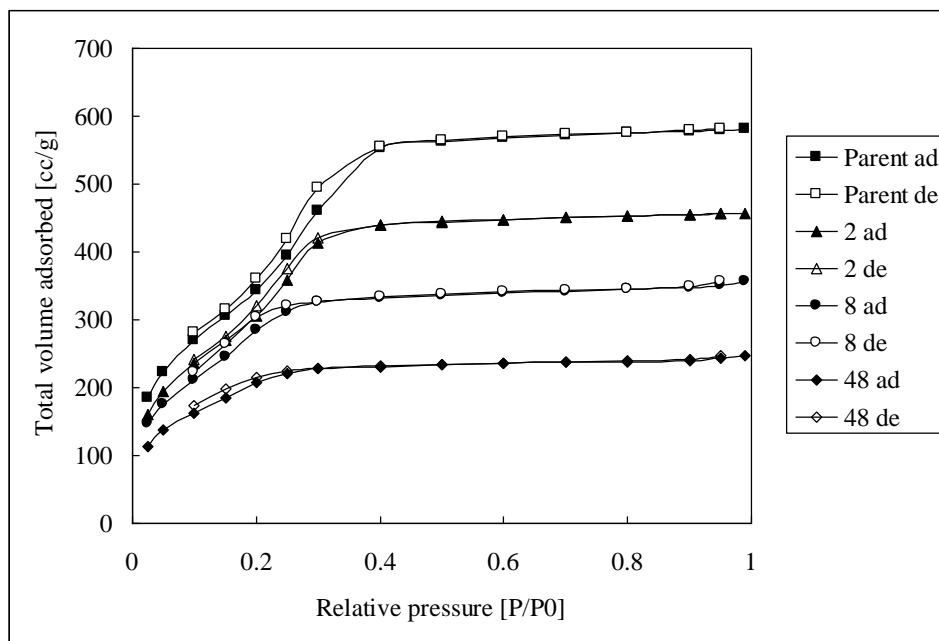


Figure 4.21 The effect of Fy solution immersion time on N₂ adsorption-desorption isotherms.

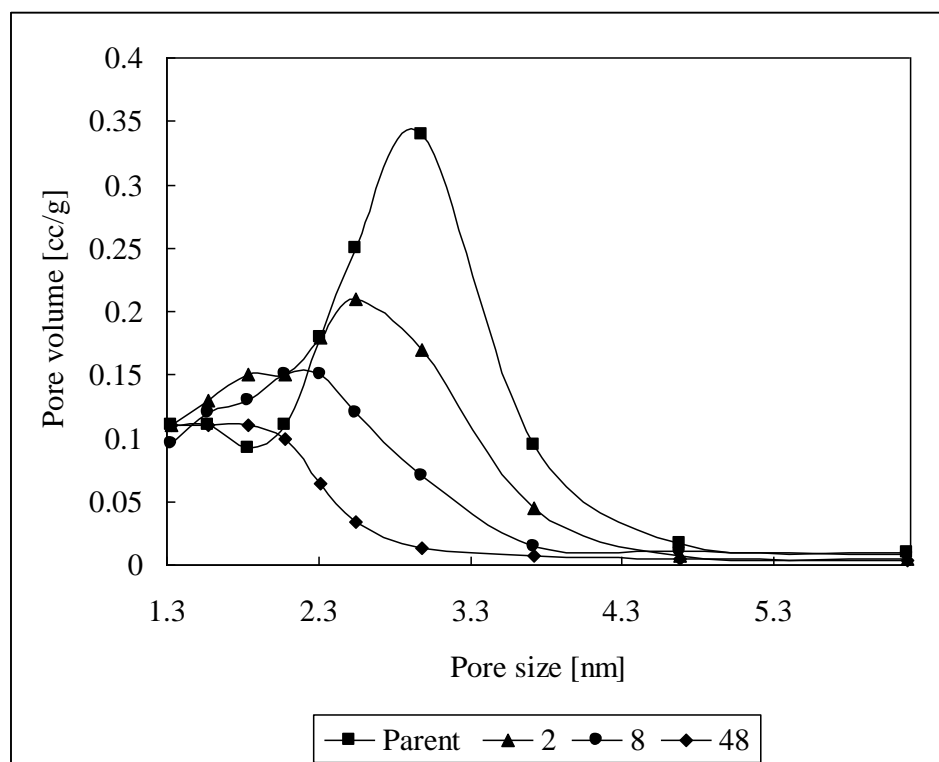


Figure 4.22 The effect of immersion time of Fy solution on the pore size distribution

The corresponding BJH desorption pore diameter distribution patterns (see Figure 4.22) reflect these trends showing. The loading of Fy into the structure has

significantly destroyed the pore structure reducing the pore volumes and pore diameters consistent with structural shrinkage and pore filling.

These changes follow decreases in specific surface area as shown in Figures 4.23.

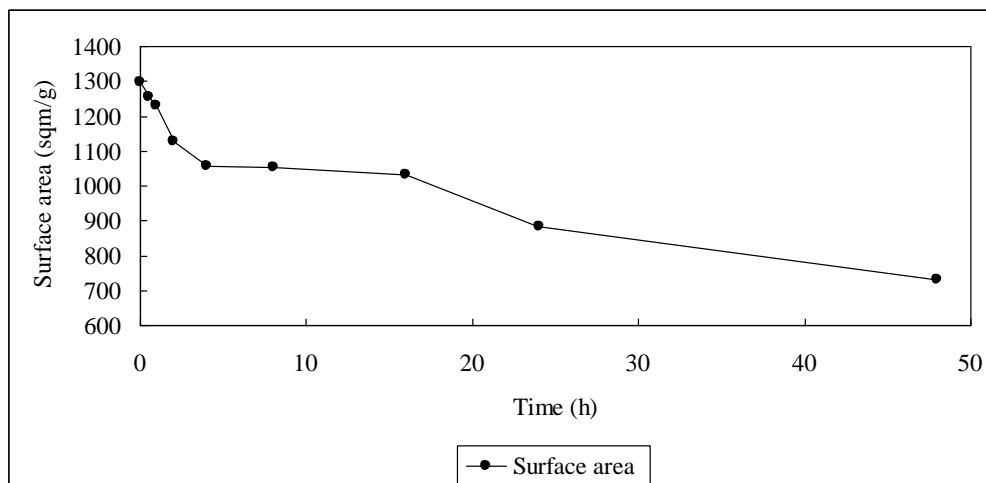


Figure 4.23. The effect of Fy loading on specific surface area

Loading of the iron complexes has had a significant effect on the specific surface areas and pore volume of the loaded materials. For Fy, increased loading achieved by increased immersion times led to reduced specific surface areas and pore volumes and increased structural changes indicated by reduced XRD intensities and shorter d_{100} spacings.

It is likely that at least some of these changes, for example decreased specific surface area and pore volume, are due to the physical filling of the pores with the complex molecules leaving less area and volume for nitrogen uptake. Calcining the material to decompose the complex might be expected to at least partially regenerate the specific surface area and pore volumes of the highly loaded materials. This is discussed further in Section 4.4.

4.3.6 Summary

Loading MCM-41 phases with organometallic compounds by the I Method produces at least two effects depending on the solvent used and the complex loaded. It is clear from the results for the four complexes used to investigate the I Method that uptake results from interactions within the pore walls and is not merely passive trapping of the solution within the pores. The order of uptake was $Fy > Fa$, $Fd > Fac$, Ft , $Fb > Fc$. This order follows the order of the polar surface areas and molecular complexities of these molecules. Only for Fc can the amount taken up be explained by physical imbibing of the solution with no concentrating effect. The imbibed complex was weakly bound and much was lost during rinsing

4.4 The calcining of S-Fc loaded MCM-41 (I method)

In order to investigate the thermal properties of Fy loaded MCM-41, the material of maximum loading (24 hours at 0.15 mol/L) was calcined at 500°C for times ranging from 2 to 8 hours. The calcined samples were characterized by low angle XRD, BET surface area determination and BJH pore size measurements.

4.4.1 The effect of calcining time on S-Fc MCM-41 (I method)

XRD data for the effect of calcining time on Fy MCM-41 materials is given in Figure 4.24.

The data show an initial increase in XRD intensities over the first 4 hours of calcining, indicating that an increase in the order of mesoporous structure is associated with the decomposition of organometallic compound. After prolonged calcining from 4 to 8 hours, decreased intensities indicate partial collapse of the ordered structure without significant change in d_{100} spacing.

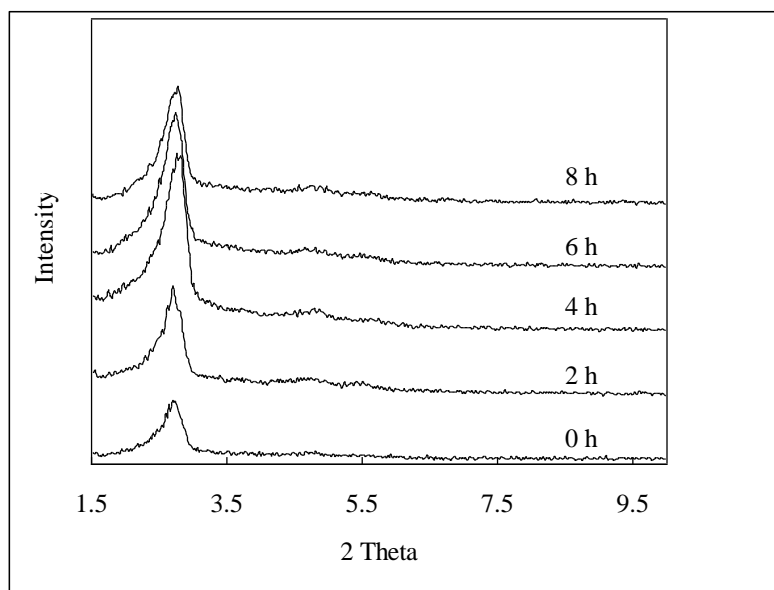


Figure 4.24 Effect of calcining time on XRD patterns of Fy loaded MCM-41

4.4.2 Effect of calcining time on nitrogen adsorption of S-Fc loaded MCM-41

Data for the effect of the calcining time on the nitrogen adsorption/desorption isotherms and BJH pore sizes are presented in Figures 4.25 and 4.26.

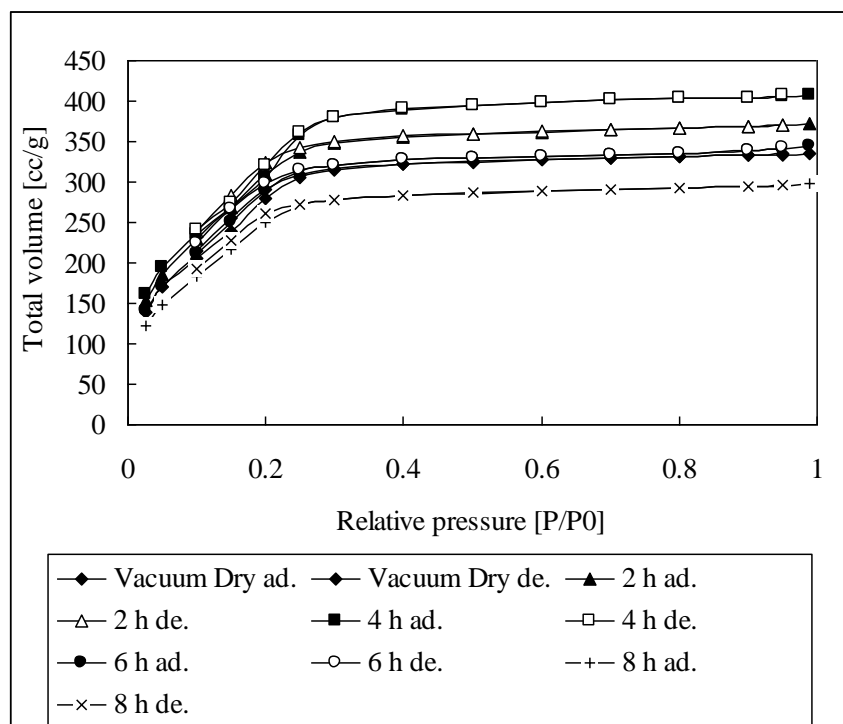


Figure 4.25 The effect of calcining time on N₂ adsorption-desorption isotherms of Fy loaded

MCM-41.

After the calcining, some recovery of specific surface area and mesoporous pore volume was indicated by increases in plateau adsorption and the reappearance of the capillary condensation stages in the N₂ sorption curves. It is likely that the recoveries were due to the decomposition of the Fy in the mesopores, releasing the spaces previously occupied by the large molecules of the iron complexes.

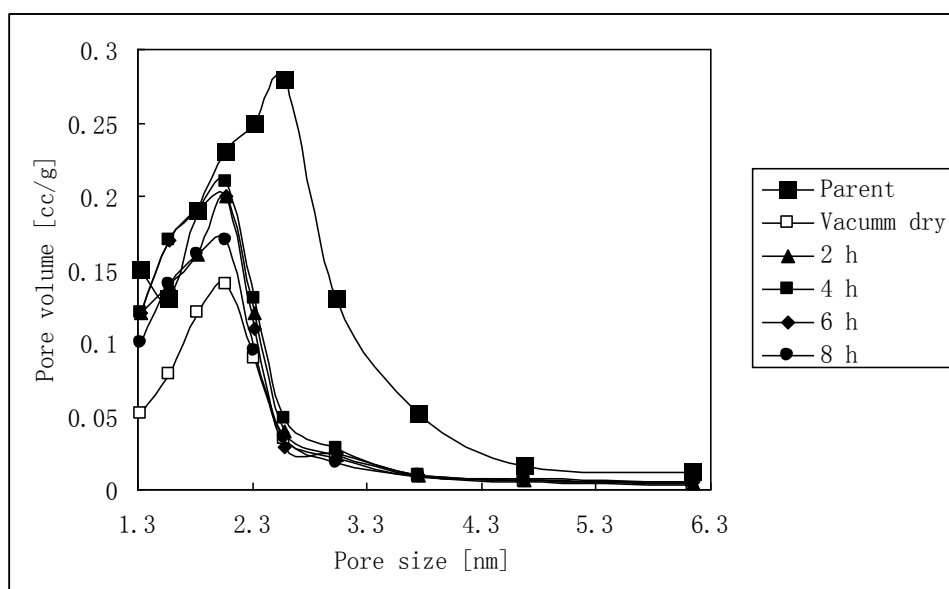


Figure 4.26. The effect of calcining time on the pore size distribution of Fy loaded MCM-41.

Data for the effect of the calcining time on the structure properties are presented in Table 4.9.

Compared with the parent (2.98 nm), pore sizes of the calcined Fy-MCM-41 were significantly smaller (2.07 nm), indicating that the effect of the ferric oxide deposited within the pores was to occupy pore space thus reducing effective pore size.

Table 4.9 The effect of calcination time on structural properties

Calcining Time Hours	Unit cell a_o nm (± 0.03)	Pore size diameter nm (± 0.01)	Wall thickness nm (± 0.04)	Surface area m^2/g (± 70)	Total pore volume cc/g (± 8.6)
V Dry	3.76	2.98	0.78	564	340
2	3.76	2.07	1.69	1030	520
4	3.68	2.07	1.61	1140	575
6	3.71	2.07	1.64	910	460
8	3.65	2.08	1.57	1050	532

4.4.3 Thermal studies of S-Fc MCM-41

DTA and TGA data for air dried Fy MCM-41 are presented in Figure 4.25. Results for air dried solvent treated MCM-41 are included in Figure 4.24 for comparison

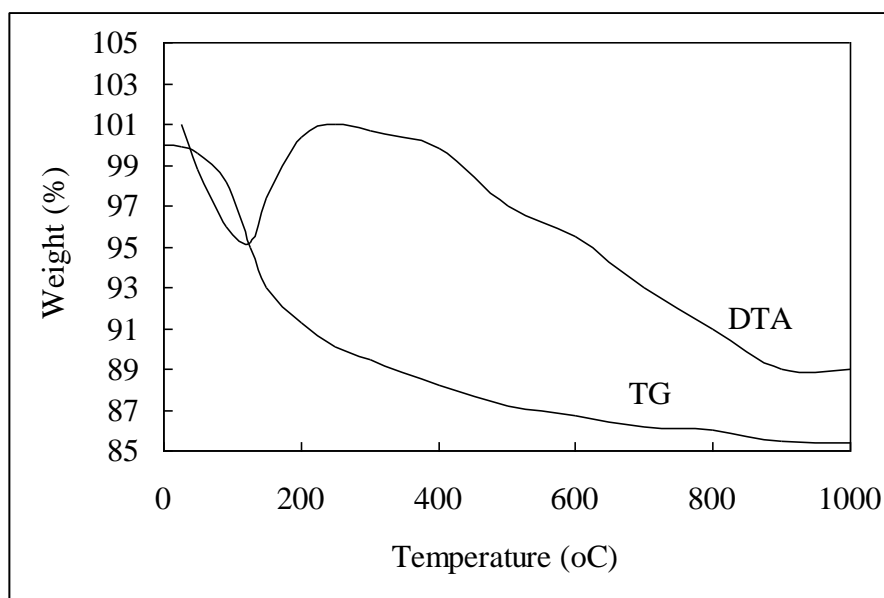


Figure 4.24. Thermal analysis curves for toluene saturated MCM-41

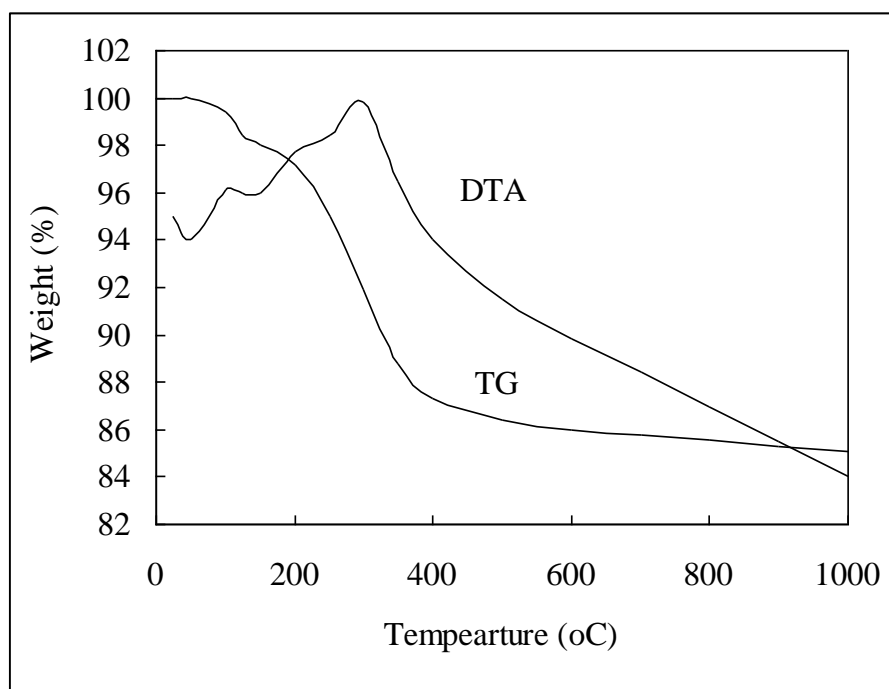


Figure 4.25. Thermal analysis curves for Fy MCM-41

The weight loss curve for Fy MCM-41 indicates a weight loss in two steps. The first step from 50 to 120°C can be assigned to release of small amounts of toluene solvent, while the second step from 200 to 400°C corresponds to the strongly exothermic decomposition of Fy. The thermal analysis curves for the toluene saturated system showed only one endothermic weight loss step.

4.4.4 XRD evidence for the formation of iron oxide in the calcined S-Fc MCM-41

All of the calcined ferrocene loaded MCM-41 materials were reddish brown in colour with intensities that roughly corresponded to the Fe loading. This indicates that calcinations led to the decomposition of the organometallic complexes and the formation of iron oxide. An experiment was performed to investigate the crystallinity of this oxide. First a sample of ferrocene was heated at 500°C for 4 hours to produce a reddish brown iron oxide. This was mixed with pure silica to give a 2 % mixture of iron oxide dispersed in mesoporous silica. XRD powder patterns of the pure iron oxide, the physical mixture of iron oxide and pure silica and the calcined Fy MCM-41

containing initially 3.89% iron which upon decomposition and oxidation would produce 5.6% iron oxide. Data are presented in Figure 4.26.

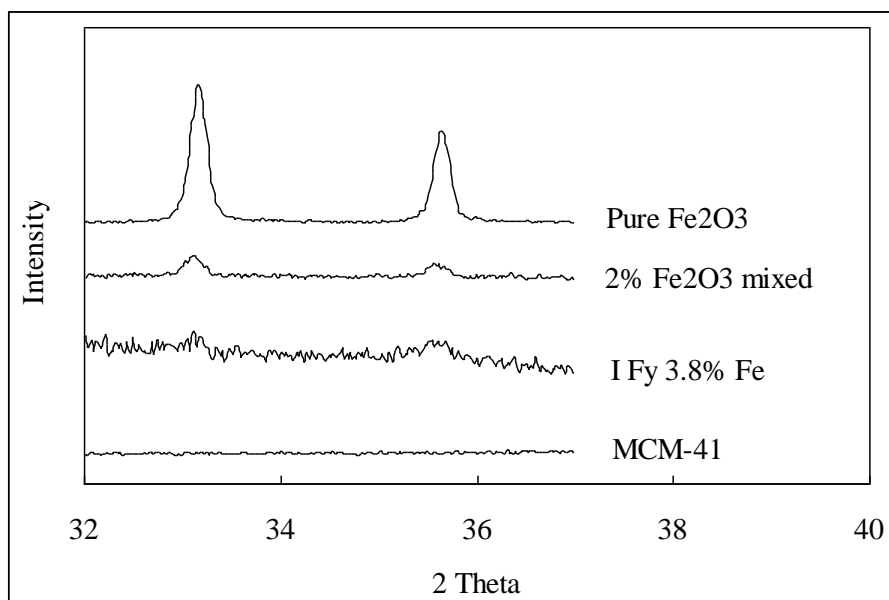


Figure 4.26 XRD powder patterns of the iron oxide formed by the decomposition of ferrocene, a physical mixture of this oxide with pure silica and calcined Fy loaded MCM-41.

Data for the three samples over the 2θ range from 32 to 37 degrees are shown in Figure 4.26. Though the iron concentration is much higher in the calcined Fy loaded MCM-41, the intensity of the diffraction lines at 31.2° and 35.5° 2θ are lower and much broader than the lines for the lower iron content physical mixture. Both of these effects are consistent with the particles of oxide formed in the mesopores being of much smaller particle size.

4.4.5 Summary

The principal results gained from the experiments described in this section are that upon calcining, some recovery of surface and pore volume lost by loading is achieved but prolonged heat treatment then leads to a reversal of this trend and results in final surface areas and pore volumes even lower than those resulting after loading. The Thermal analysis results indicated that for the heavily loaded Fy MCM-41, the Fy

species displaced most of the solvent from the pores. XRD of the highly loaded calcined Fy loaded MCM-41 indicated that the iron oxide formed by decomposition of the Fy species was more amorphous (smaller particle size) than the oxide formed by decomposing pure ferrocene.

4.5 The loading of other organometallic complexes into MCM-41 by I Method

Studies up to this time have focused on iron complexes. It was of interest to confirm that other metals can be loaded into the MCM-41 by the I method already used for iron complexes. The organometallic compounds of Mn, Mo and Co used were methylcyclopentadienyl manganese tricarbonyl (O-Mn), cyclopentadienyl-molybdenum tricarbonyl dimer (O-Mo) and 3-methylidyne-tricobalt nonacarbonyl (O-Co). Loading was performed by the I method. A summary of molecular properties is given below:

Table 4.10 Summary of some important properties of the organometallic compounds [4]

Abbreviation	Fy	O-Mn	O-Mo	O-Co
Molecular formula	$\text{Fe}_2(\text{C}_5\text{H}_5)_2(\text{CO})_4$	$\text{Mn}(\text{C}_5\text{H}_5)\text{CH}_3(\text{CO})_3$	$\text{Mo}_2(\text{C}_5\text{H}_5)_2(\text{CO})_6$	$\text{CH}_3\text{CCO}_3(\text{CO})_9$
Molar mass	353.925 g/mol	218.09 g/mol	489.96 g/mol	455.07 g/mol
Metal content	31.05%	25.6%	39.16%	38.68%
Molecular size	360 \AA^3	288 \AA^3	432 \AA^3	
Appearance	Dark purple crystals	pale yellow liquid herbaceous odour	dark red crystalline solid	
Density	1.77 g/cm^3 , solid		1.38 g/cm^3	
Melting point	$194 \text{ }^\circ\text{C}$	$-1 \text{ }^\circ\text{C}$ (272 K)	$222 \text{ }^\circ\text{C}$	
Boiling point	decomposition	$232\text{-}233 \text{ }^\circ\text{C}$	decomposition	
Solubility in water	insoluble	low	insoluble	
Solubility in other solvents	benzene, THF, chlorocarbons	alkane (petrol)		
Topological Polar Surface Area	4 \AA^2	3 \AA^2	6 \AA^2	9 \AA^2
Complexity	21.6	43.3	21.6	218

The O-Mo, O-Mn, and Co are of interest because they provide examples of organometallic complexes containing other catalytically interesting metals. O-Mo is

of particular interest because it has a structure similar to that of Fy but contains more polar carbonyl groups.

In the all cases, concentrations close to the saturation limit of the organometallic compounds were used. For Fy, O-Mn and O-Mo the concentrations used were 0.15, 0.5 and 0.1 mol/L, respectively. Dry calcined MCM-41 (0.5 g) was suspended in these solutions under vacuum for 24 hours as described in Section 2.3. The material was rinsed until risings were colourless and dried under vacuum. The dried as immersed material was analyzed for metal according to Section 2.3

4.5.1 Results for the loading with other organometallic complexes into MCM-41

Data for metal loadings (wt% of as-immersed product) achieved are summarised in Table 4.11 The table also includes data for Fy loading reported in Section 4.3 for comparison

Table 4.11 Metal contents for metal loadings (I-Method)

	Fy	O-Mn	O-Mo	O-Co
Concentration(mol/L)	0.15	0.5	0.1	0.1
Metal content (% wt)	3.89 (Fe)	2.65 (Mn)	5.05 (Mo)	0.59 (Co)

4.5.2 The effect of loading other organometallic complexes into MCM-41 on XRD

XRD powder patterns were measured for the dried as-immersed samples. Results for Fy, O-Mn, O-Mo and O-Co treated MCM-41 are given in Figure 4.27. There was a significant decrease in the diffracted intensities for all metal loaded samples, indicating that loading process disrupted the MCM-41 structure. The d_{100} spacing also decreased after loading. These effects are much greater than the effects observed with the solvent alone (see Section 4.2) and indicate disruption of the lattice by the

adsorbed metal complexes.

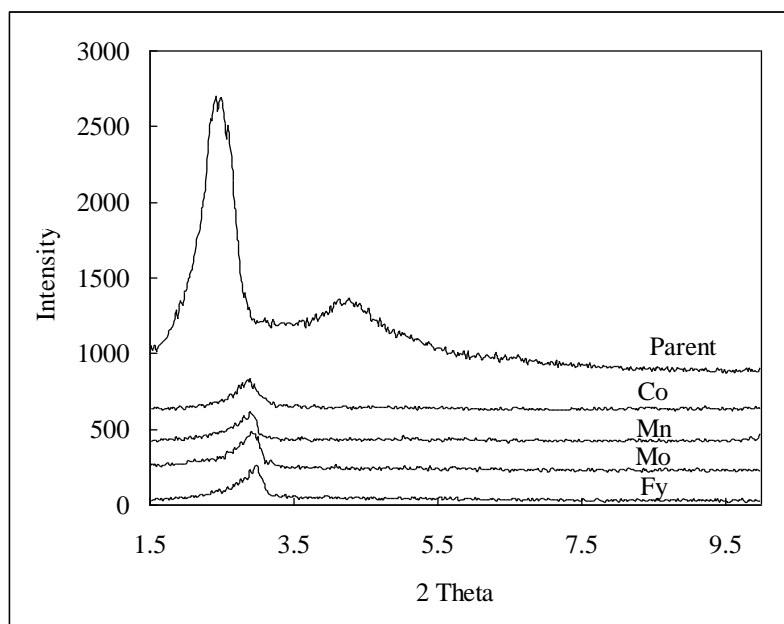


Figure 4.27 The effect of loading with Mo, Mn, Co and Fe on XRD patterns of MCM-41.

4.5.3 The effect of loading other organometallic complexes into MCM-41 on nitrogen adsorption

Data for the effect of loading with the O-Mn, O-Mo, and Fy on the nitrogen adsorption/desorption isotherms and BJH pore sizes are shown in Figures 4.28, 4.29 and 4.30.

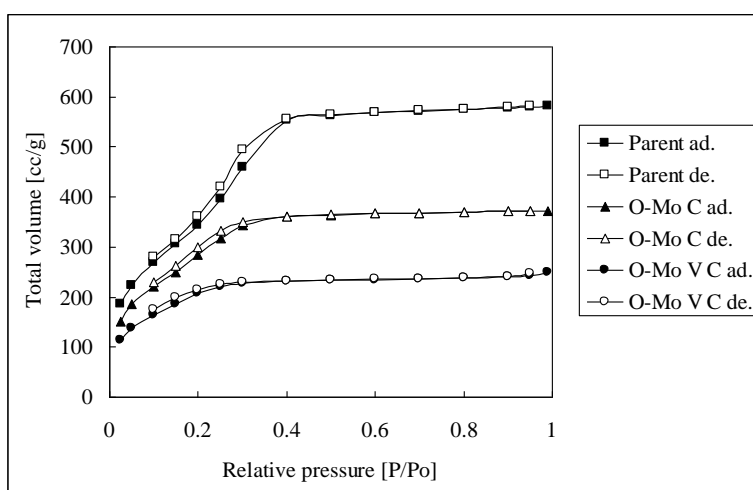


Figure 4.29 The effect of loading with O-Mo on N_2 adsorption-desorption isotherms.

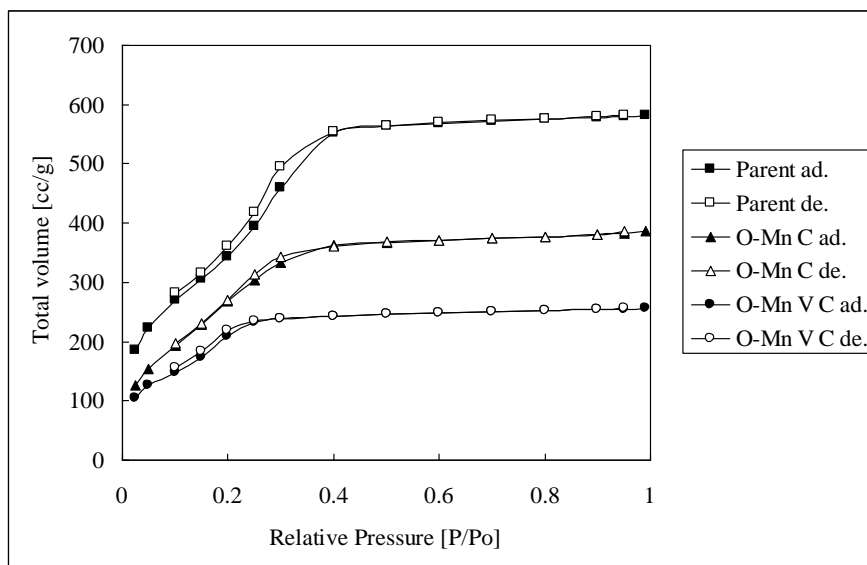


Figure 4.30 The effect of loading with O-Mn on N_2 adsorption-desorption isotherms.

After immersion, all the materials exhibited very similar nitrogen adsorption isotherms with considerably lower plateaus adsorptions than the original calcined material. After the loaded materials were calcined to decompose the metal complex there were large increases in the amount of capillary condensation. It likely that the recoveries were due to the free volume produced in the pores by the decomposition of the bulky organic components of the organometallic compounds.

Pore size distributions calculate from the adsorption data are summarised in Figures 4.31, 4.32, 4.33.

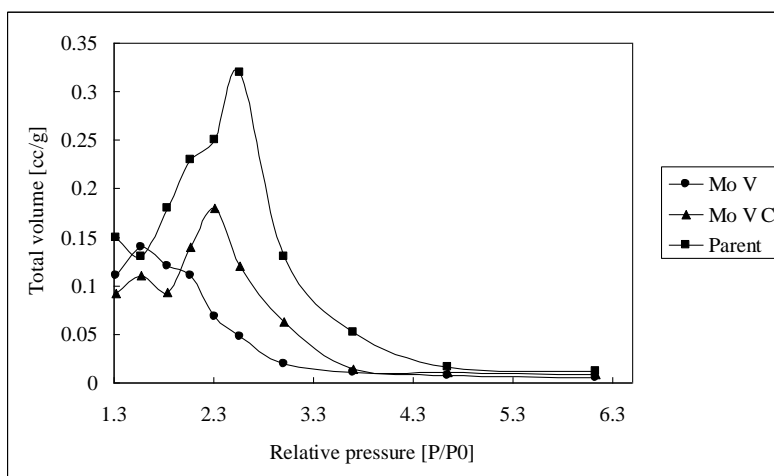


Figure 4.32. The effect of loading O-Mo on the pore size distribution.

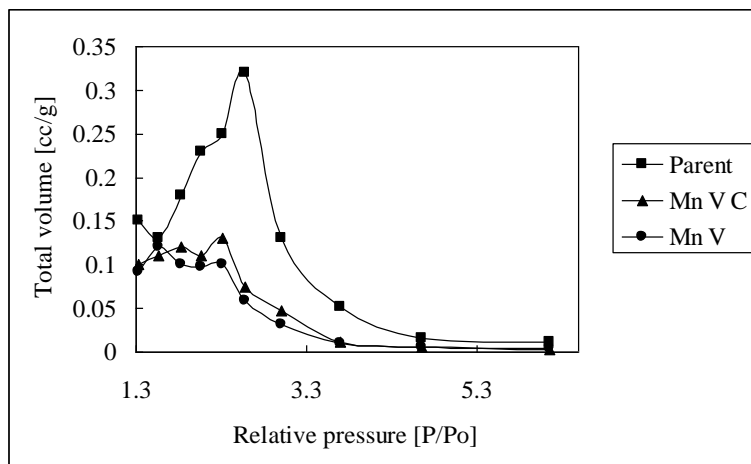


Figure 4.33. The effect of O-Mn on the pore size distribution

The XRD data and the BJH desorption pore diameter distribution patterns show that the loading of metal into the structure significantly reduced the pore volumes and pore diameters consistent with pore filling and also caused lattice disruption and structural shrinkage.

Data for the effect of the O-Mn, O-Mo and Fy on specific surface areas and pore volume are summarized in Table 4.9. They show that surface areas and pore volumes are decreased by loading the pore with metals.

Table 4.9 The effect of loading and calcining on specific surface area and pore volume.

	Parent	Fy	O-Mn	O-Mo
Surface area (m ² /g) Vacuum dry	1342	564	597	609
Surface area (m ² /g) Calcined		1140	985	1080
Total volume (cc/g) Vacuum dry	735	340	305	329
Total volume (cc/g) Calcined		575	504	595

4.5.4 The infrared spectrum

Infra red absorption data for the pure silica, the pure metal complexes and the metal

complex loaded silicas are shown in Figures 5.34, 5.35 and 5.36. The infrared spectra of both Mo-MCM-41 and Mn-MCM-41 exhibit the characteristic strong terminal metal carbonyl bands in the range from 2000 to at 1900 cm^{-1} (1955 and 1940 cm^{-1} for Mo MCM-41 and 2023 and 1939 cm^{-1} for Mn MCM-41 characteristic of the pure material.

The IR spectrum for Sample Fy-MCM-41 provided very little evidence of encapsulated Fy. Fy is soluble in organic solvents giving deep-red solutions and these oxidize gradually in air and precipitate brown iron (III) oxide. The absence of IR absorbance and the brownish colour of the product indicated that decomposition to the oxide had occurred.

The IR spectra for all calcined samples were identical to the spectrum for pure silica MCM-41 indicating complex decomposition to metal or metal oxide. While there was no IR evidence for the formation of oxides, concentrations were probably too low for them to be seen.

4.6 References for Chapter 2

1. Besson, S; Gacoin, T; Ricolleau, C; Boilot, J.P. *Chem. Commun.* 360, **2003**.
2. Ertl, P.; Rohde, B.; Selzer, P. *J. Med. Chem.* 43 (20), **2000**, 3714–3717
3. Hendrickson, J.B.; Huang, P.; Toczko, A.G. *J. Chem. Inf. Comput. Sci.* 27, **1987**, 63-67
4. Milan, R.; Dejan, P. C. *Chemica Acta CCACAA* 75 (1) 107, **2002**, 116

***Chapter 5 The loading of MCM-41 by organometallic compounds
during synthesis by the M and T Methods***

5.1 Introduction: Loading of metals in MCM-41 during synthesis

Chapter 3 has described how MCM-41 phases can be loaded post synthesis by the I-Method where an organometallic complex is introduced into the structure by imbibing the complex dissolved in an appropriate solvent. A major objective of the present study was to explore other methods of introducing the metal into the structures. Two novel possibilities were loading the structures during synthesis by the incorporation of the organometallic complex into the core of the micelle and dissolution of the complex into the TEOS. These methods have been called the M-Method and T-Method. The procedures have been described in Chapter 2 and results using these synthetic procedures will be described in this chapter.

5.2 The effect of reaction conditions on the Fc-MCM-41

In Chapter 3, the optimum reaction conditions to produce pure silica MCM-41 with high surface area and well ordered pore structures were found be 2.5 mol/L HIt was of interest to determine whether these conditions were also optimum for the loading of ferrocene into the structures by the T and M methods. The two variables having most effect in the pure silica syntheses were reaction time and acid concentration. These variables were investigated in conjunction with a constant loading concentration of ferrocene.

5.2.1 The effect of reaction time on loading and structural properties of Fc-MCM-41

Fc-MCM-41 mesoporous silica was synthesized using CTAB as the surfactant and

TEOS as the silica source following the general procedures for the M Method and the T Method as described in Section 2.3. The amount of Fc in the synthesis mixture was fixed at 2.5% by wt of surfactant, and 2.5 mol/L HCl solution was used for all reactions. Reaction times with magnetic stirring (approximately 300 rpm) ranged from 3 to 72 hours at room temperature. The resultant precipitate was filtered, washed and dried at room temperature for several hours. The final samples Fc-MCM-41(T) and Fc-MCM-41 (M) were characterized by low angle XRD, BET and Fe content as determined by AA (see Section 2.5)

Data for Fe loadings (wt% of as-synthesised product) prepared according to the T method and the M method for different reaction times are summarized in Figure 5.1

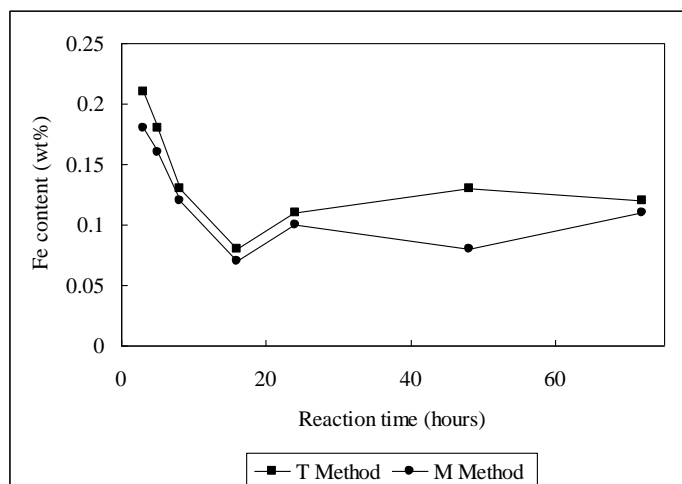


Figure 5.1 Fe content for the as-synthesised samples prepared by T and M methods for reaction times varying from 3 to 72 h.

The Fe content of the as synthesized materials decreased steadily with increasing reaction time over the period from 3 to 16 hours and then remained fairly constant. Similar loading was achieved by both methods although in most cases loading by the T method was slightly higher than the M method.

XRD data for the as-synthesized MCM-41 materials loaded with Fc for varying reaction times are given in Figures 5.2 and 5.3. All materials gave typical MCM-41 diffraction patterns, consistent with a regular hexagonal pore structure.

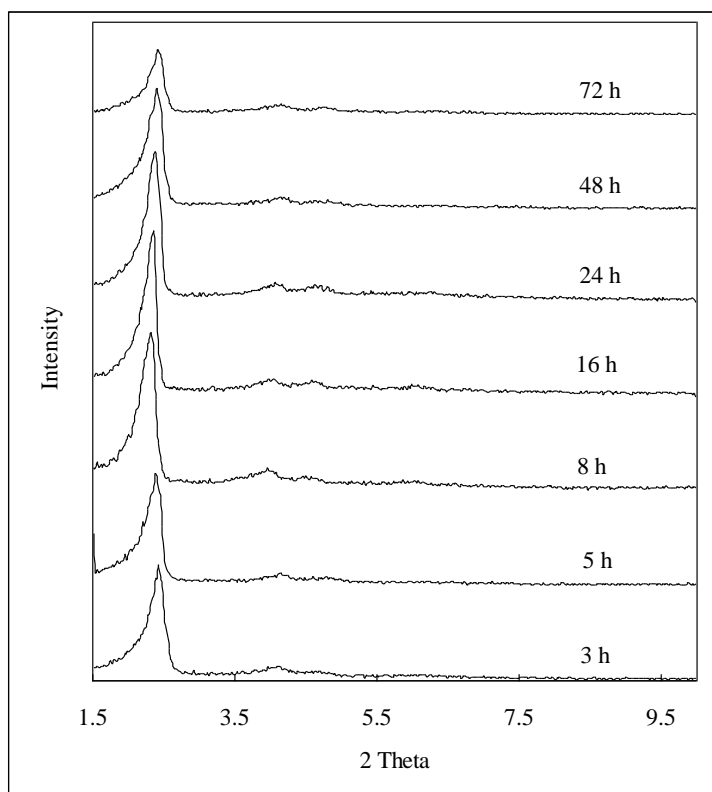


Figure 5.2 The effect of reaction time on the XRD patterns of as synthesized Fc loaded MCM-41 (T Method)

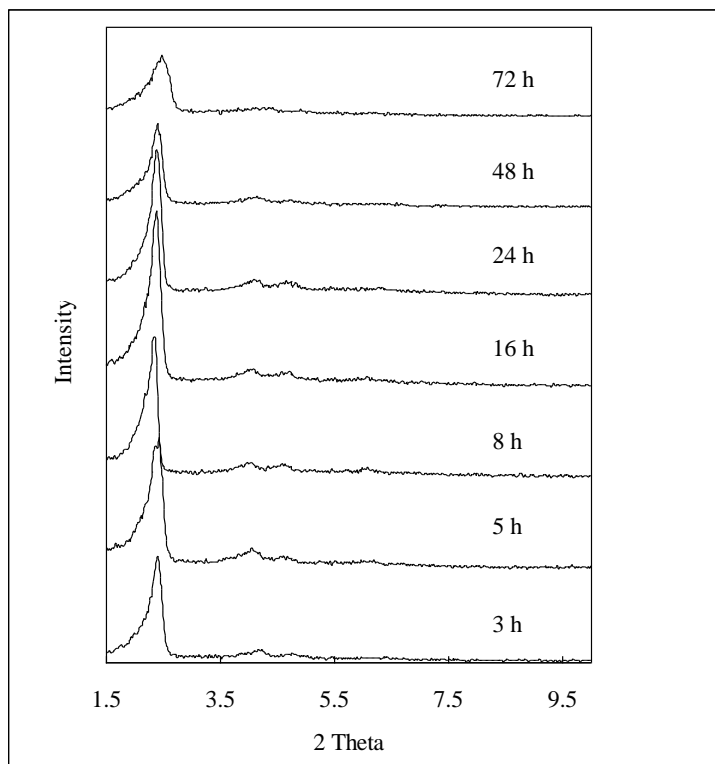


Figure 5.3 The effect of reaction time on the XRD patterns of as synthesized Fc loaded MCM-41 (M Method)

Systematic trends in the d_{100} spacing and line intensity were observed. These are shown in Figure 5.4 and 5.5

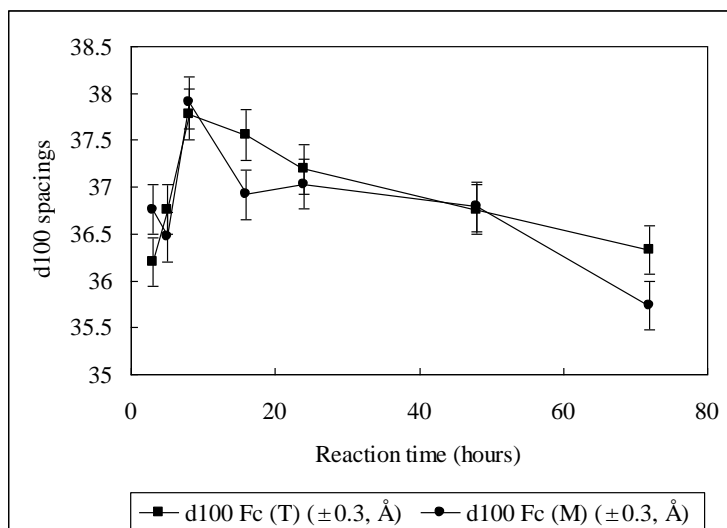


Figure 5.4 The effect of reaction time on the XRD d_{100} spacings of as synthesized Fc loaded MCM-41 (T and M Methods)

The effect of reaction time on the structural characteristics of the loading Fc materials was very similar to that of the pure silica material (see Section 3.1) except that the d_{100} spacing maxima occurred after somewhat longer reaction times (8 hours rather than 5 hours).

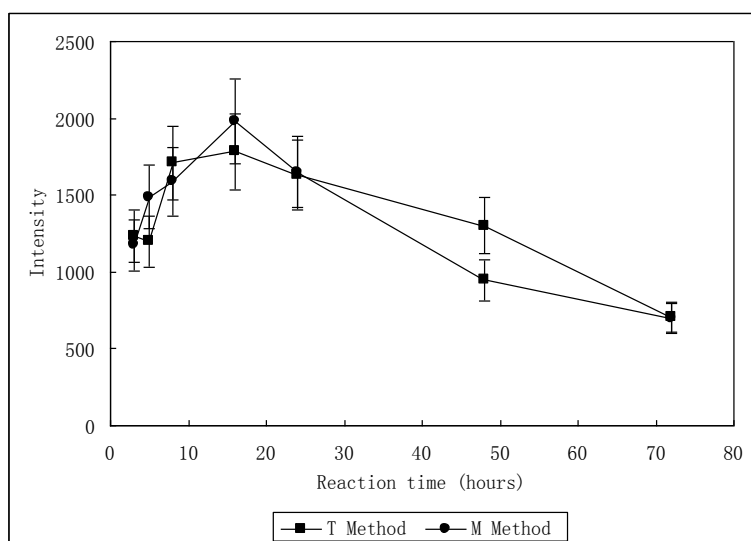


Figure 5.5 The effect of reaction time on the XRD d_{100} intensities of as synthesized Fc loaded MCM-41 (T and M Methods)

Line intensities also peaked at longer reaction times for the Fc loaded materials (16 hours for the Fc loaded materials compared with 5 hours for the pure silicas).

Data for the specific surface areas of the Fc loaded materials after calcining are shown in Figure 5.5

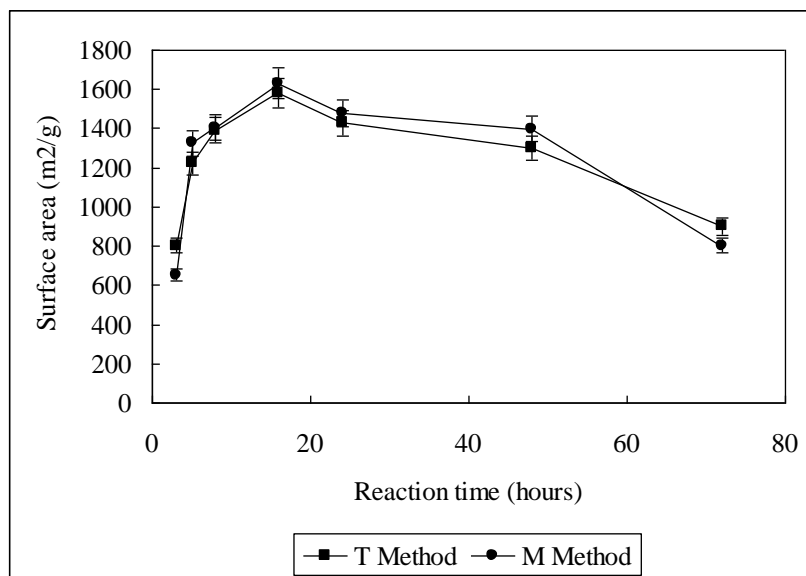


Figure 5.5 The effect of reaction time on the specific surface area of calcined Fc loaded MCM-41 (T and M Methods)

The BET specific surface areas of Fc-MCM-41 (T) increased from 800 to 1580 m²/g with the increasing reaction time from 3 to 16 hours, and then decreased from 1580 to 900 m²/g with reaction times from 16 to 72 h. A very similar trend was observed for Fc-MCM-41 (M). This trend in surface area correlated roughly with the trend in XRD intensities. These trends are similar to those observed with the pure silicas except the maxima occurred earlier times.

It appears that the effect of the Fc in the reaction mixture is to initially inhibit the formation of well ordered high surface area phases. As the structures subsequently become more ordered, Fc is excluded. Finally, the tendency towards less ordered, lower surface area systems after prolonged reaction times, observed in the pure silica

systems, dominates to produce materials that have both lower Fc loadings and reduced order and surface area.

5.2.2 The effect of acid concentration on Fc loading and MCM-41 mesoporous structures

The effect of acid concentration on Fc loading of MCM-41 by the M and T methods was investigated following the procedures described in Section 2.3. The amount of Fc in the synthesis solution was fixed at 2.5% by wt of surfactant (CTAB), and HCl concentrations ranging from 1 to 4 mol/L were used. After magnetic stirring (approximately 300 rpm) at room temperature for 8 hours, the resultant white precipitate was filtered, washed and dried at room temperature for several hours. The samples Fc-MCM-41(T) and Fc-MCM-41(M) were characterized by low angle XRD, and the Fe content was determined by AA.

Data for Fe loadings (wt% of as-synthesised product) prepared according to the T method and the S method for different acid concentration are presented in Figure 5.6

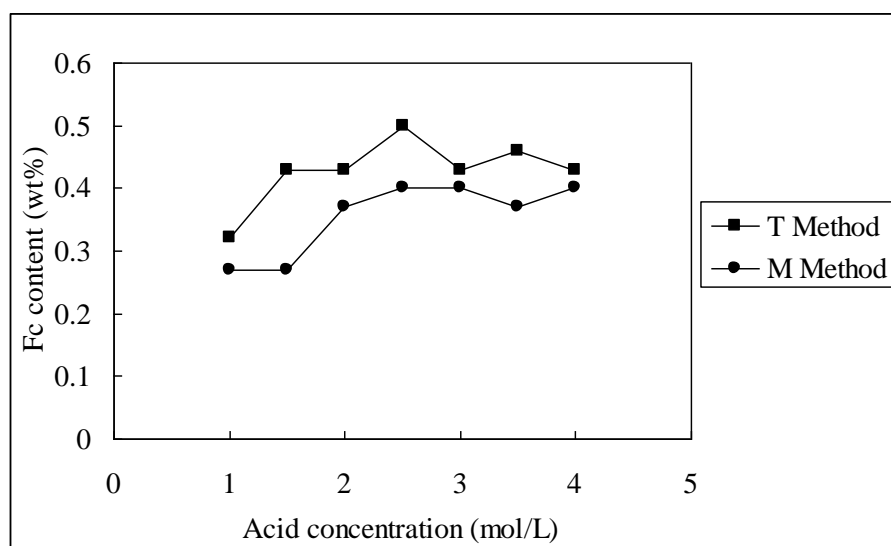


Figure 5.6 The effect of acid concentration on Fe content for the as-synthesised samples (T and M methods).

The Fe content in product increased with increasing acid concentration from 1 to 2.5

mol/L, and then remained essentially constant with further increases in acid concentration. As was the case for increased reaction times, Fe loadings obtained by the T method were higher than those obtained by the M method.

5.3 The effect of Fc concentration on the loading of MCM-41 by the M and T Methods

The effect of Fc concentration on loading was determined at Fc concentrations ranging from 0.5 to 3% by wt of surfactant (where the surfactant content was kept constant). After magnetic stirring (approximately 300 rpm) at room temperature, the resultant precipitate was filtered, washed and dried at room temperature for several hours, followed by calcining at 550°C to remove the template. Both the as-synthesized and calcined MCM-41 materials were characterized by low angle XRD, BET surface area, BJH pore size distribution.

The maximum Fc loading of the surfactant micelles using the M method was 3.0 wt % (where the weight of Fc is expressed as a percentage of the weight of surfactant). Beyond this limit, excess red solid Fc precipitated when the surfactant/Fc/dichloromethane solution was added to acid synthesis solution. By the T Method, the limit of Fc loading was 25 wt % of the surfactant used in the synthesis. Beyond this limit no further Fc could be dissolved in the TEOS. In order to compare the efficiency of loading by the two methods, Fc loadings from 0.5 to 3 wt% of the surfactant were used in both preparative methods.

Two precautions were necessary for preparations according to the M method. Firstly, because of the tendency for the Fc to be extracted into the organic TEOS phase, it was necessary to add the TEOS to the Fc loaded surfactant slowly and with rapid stirring to ensure that product was formed before significant transfer of the Fc to the TEOS phase occurred. Secondly, because the Fc was rapidly oxidized from the yellow (zero valent Fe) to a blue (divalent Fe) form, it was necessary to prepare the acid Fc loaded

micelle solutions immediately before the reaction.

5.3.1 Determination of ferrocene content

The color of the Fe-containing samples provided a simple indication of Fc loading in the final product. Colours from a pale yellow to deep yellow indicated increased loadings of Fc.

A more accurate estimation of metal loading was obtained by AA (See section 2.3). Data for Fe loadings (wt% of as-synthesised product) achieved according to the T method and the S method for different Fc wt% relative to the surfactant are given in Figure 5.7. The results show that approximately 60% and 83% respectively of the Fc was encapsulated using the M method and T methods.

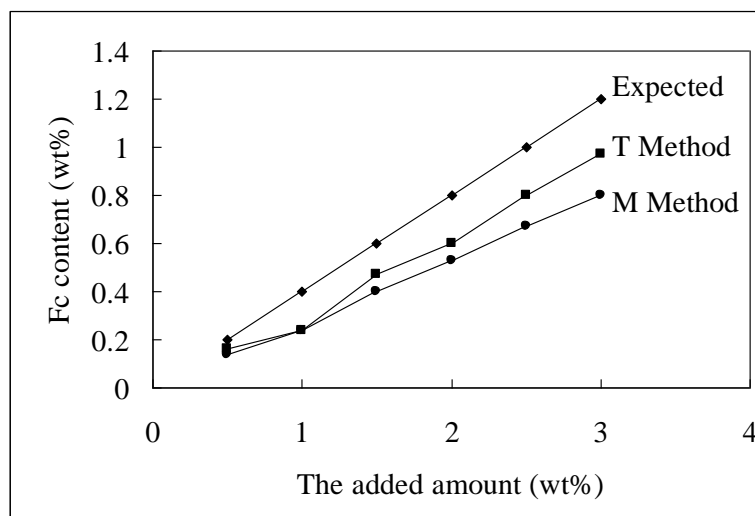


Figure 5.7 The Fc content of MCM-41 loaded by the M and T Methods. The expected line represents the loading that would be obtained if all the Fc added to the synthesis was retained.

5.3.2 Effect of Fc loading on structural features

The X-ray diffraction patterns of the MCM-41 loaded by the T method (Fc-MCM-41(T)) and the MCM-41 loaded by the M method (Fc-MCM-41(M)) are

given in Figures 5.8-5.12. XRD patterns of all samples correspond to the regular hexagonal pore structure of Fc-MCM-41 and were not affected by Fc loading. The MCM-41 structure was maintained after calcining although some peaks were slightly weaker and broader.

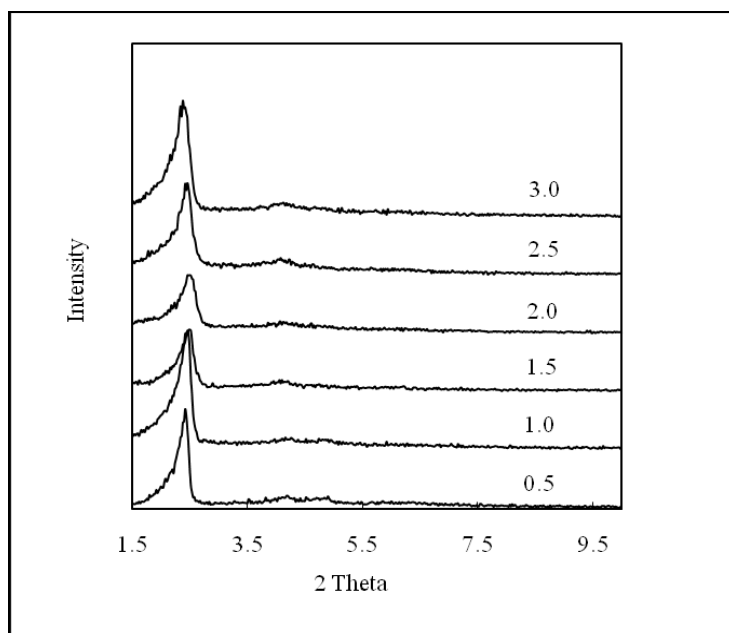


Figure 5.8 The effect of Fc loading on XRD powder patterns for as-synthesised MCM-41 (M Method). The Fc/surfactant weight ratio is given for each set of data.

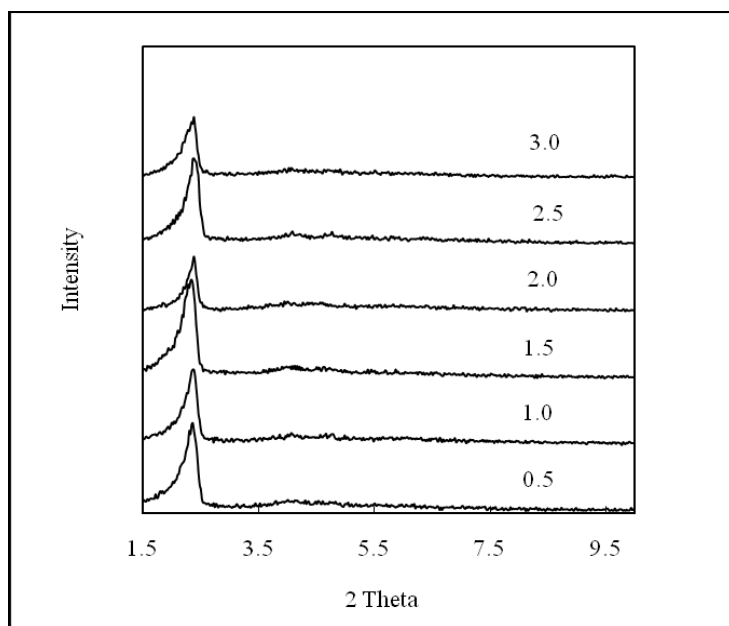


Figure 5.9 The effect of Fc loading on XRD powder patterns for as-synthesised MCM-41 (T Method). The Fc/surfactant weight ratio is given for each set of data.

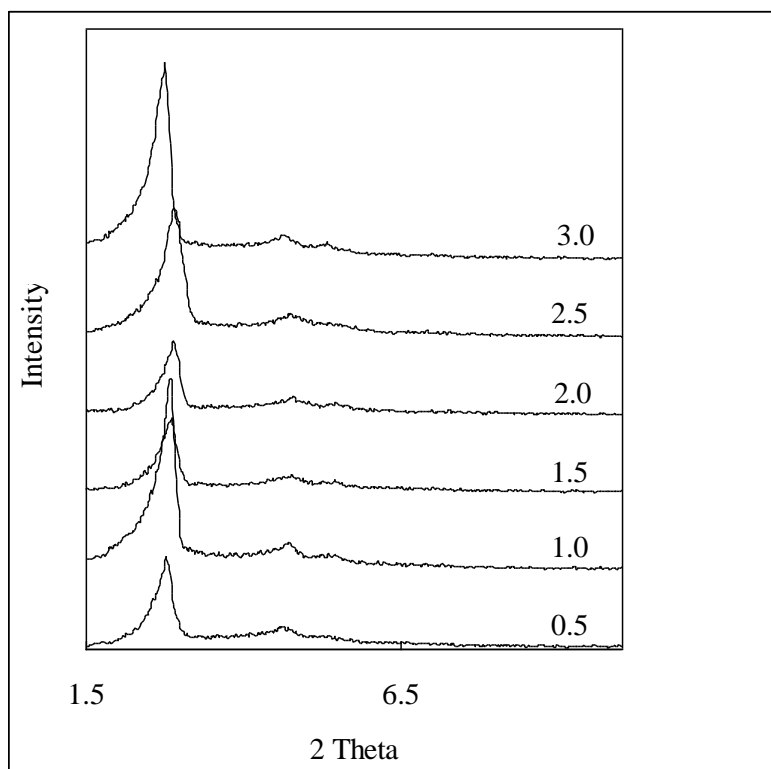


Figure 5.10 The effect of Fc loading on XRD powder patterns for calcined MCM-41 (M Method) where Fc content expressed as a % of surfactant content was 0.5, 1.0, 1.5, 2.5 and 3.0 %

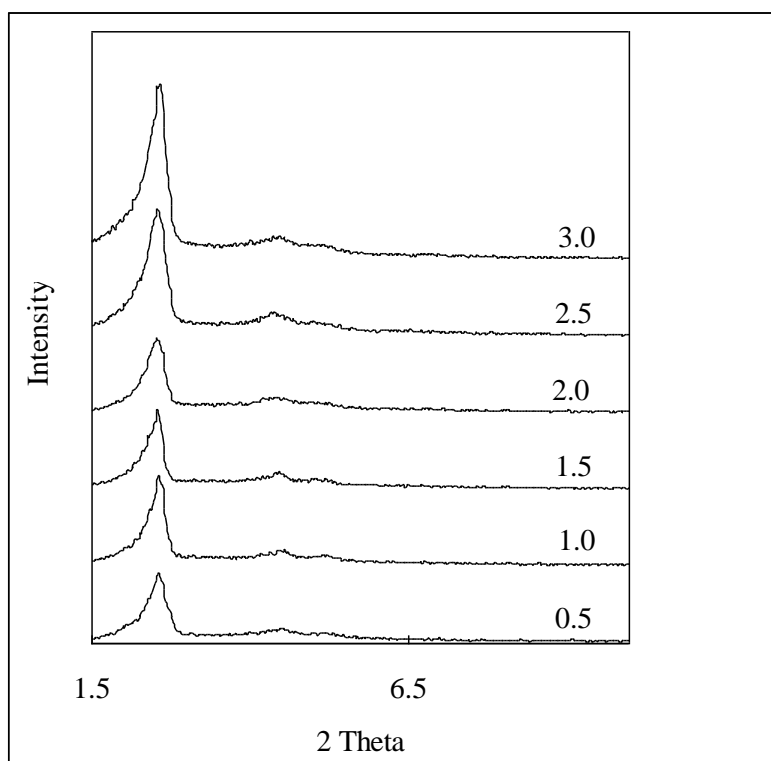


Figure 5.11 The effect of Fc loading on XRD powder patterns for calcined MCM-41 (T Method) where Fc content expressed as a % of surfactant content was 0.5, 1.0, 1.5, 2.5 and 3.0 %.

Data for d_{100} spacings for the as-synthesised and calcined materials are given in Figures 4.12 and 4.13 and summarized Tables 4.1 and 4.2.

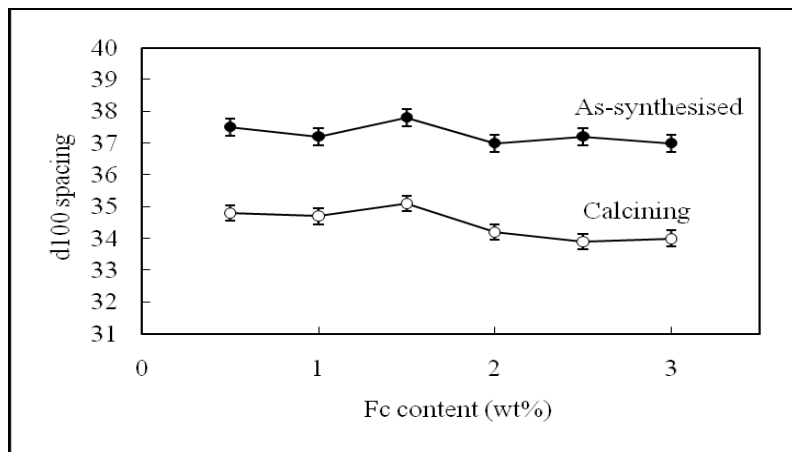


Figure 5.12 The effect of Fc reaction mixture concentration on d_{100} spacing of as-synthesized and calcined samples (T Method)

Table 5.1 The effect of Fc reaction mixture concentration on d_{100} spacing of as-synthesized and calcined samples (T Method)

Fc (wt% surfactant)	0.5	1.0	1.5	2.0	2.5	3.0
d_{100} as syn.(± 0.3 , Å)	37.5	37.2	37.8	37.0	37.2	37.0
d_{100} calc.(± 0.3 , Å)	34.8	34.7	35.1	34.2	33.9	34.0
Contraction Å	2.7	2.5	2.7	2.8	3.3	3.0

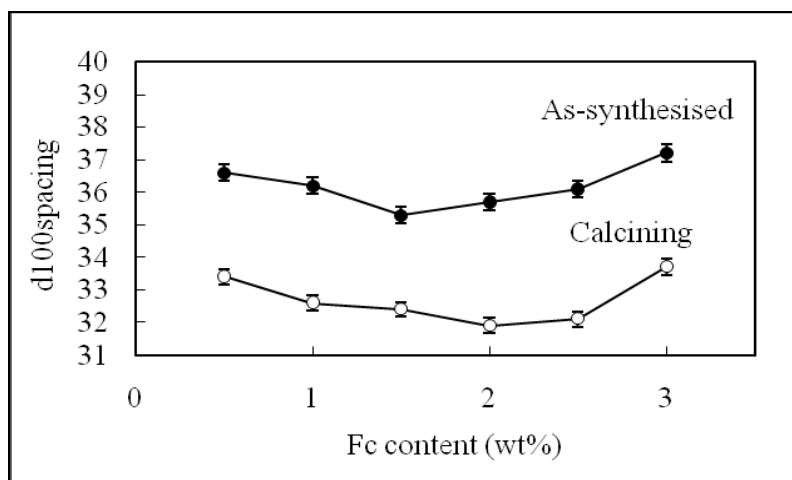


Figure 5.13 The effect of Fc reaction mixture concentration on d_{100} spacing of as-synthesized and calcined samples (M Method)

Table 5.2 The effect of Fc reaction mixture concentration on d_{100} spacing of as-synthesized and calcined samples (M Method)

Fc (wt% surfactant)	0.5	1.0	1.5	2.0	2.5	3.0
d_{100} as syn. (± 0.3 , Å)	36.6	36.2	35.3	35.7	36.1	37.2
d_{100} calc. (± 0.3 , Å)	33.4	32.6	32.4	31.9	32.1	33.7
Contraction	3.2	3.6	2.9	3.8	4.0	3.5

In the case of MCM41 loaded by the T method, lattice parameters were essentially unaffected by metal loading. For the systems loaded by the M method, there is some evidence that the d_{100} spacing went through a minimum at approximately 1.5 wt% Fc for both the as synthesized and calcined samples. However, the effect is small and not much greater than the error in the measurements. The contraction of d_{100} spacing upon calcining for the M method was larger than that for T method.

For Fc-MCM-41-T there is no obvious change in the unit cell parameter (a_0) with the increased ratio of ferrocene to surfactant. This is consistent with the Fc in the synthesis mixture not being held the micelles micelles whose size was thus largely unaffected by the Fc associated with the TEOS i.e. the Fc did not enter the cores of the preformed micelles. This implies that the hexagonal pore structure would not be affected and the lattice parameters d_{100} of Fc-MCM-41-T would be independent of Fc loading. According to this interpretation, it is expected that Fc will be incorporated into mesoporous structure during the hydrolysis of the TEOS. Rather than the pore walls being built up by polymerization of TEOS they are formed by aggregation of the TEOS/Fc “complex”. Because the micelle core structure is not affected, the lattice parameters d_{100} of Fc-MCM-41(T) will not be affected by Fc loading, and this was observed.

For Fc-MCM-41-M the unit cell parameter (a_0) first decreased from 36.6 to 35.3 Å with increasing Fc/surfactant wt% ratio and then increased to 37.2 at weight ratio of 3%. During the M method, the Fc is loaded into the micelle before the addition of TEOS and so it can be assumed to be contained within the micelle core where the

hydrophobic environment of the surfactant tails provide a compatible environment for the hydrophobic Fc molecules. When lightly loaded with ferrocene, the strong interactions between Fc and the hydrocarbon tails are likely to lead to a contraction of the micelle size. As more Fc is loaded into the micelles, the core will need to expand to accommodate them. Thus the lattice parameters d_{100} of Fc-MCM-41 can be expected to decrease with initial Fc loading, go through a minimum and then increase.

5.3.3 Effect of Fc loading on N₂ adsorption-desorption characteristics

Multi-point adsorption desorption studies were carried out using the NOVA instrument (See Section 2.3). A representative isotherm of the calcined samples is presented in Figure 5.14. In all cases, the calcined materials exhibited typical type IV isotherm behaviour. The steep capillary condensation step, characteristic of a highly uniform mesoporous structures, indicated that the mesoporous structures of Fc-MCM-41 (T) and Fc-MCM-41 (M) were well preserved.

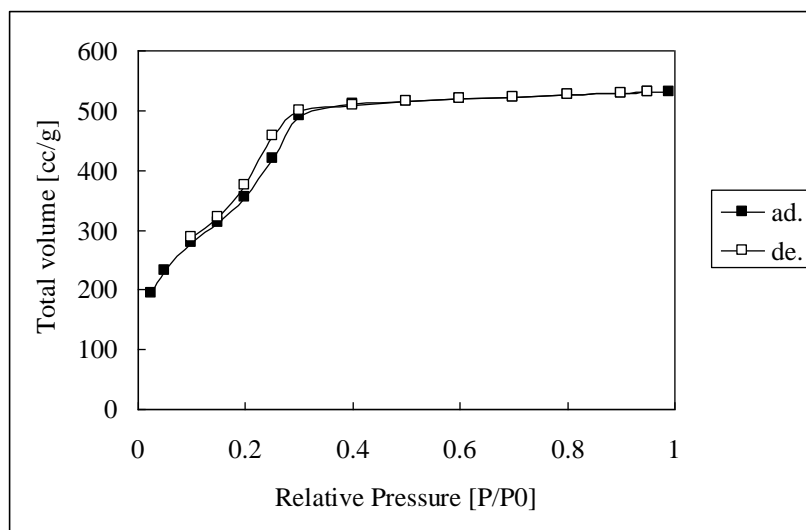


Figure 5.14 Representative N₂ adsorption /desorption curve

The pore size distribution was analyzed using N₂ multi-point adsorption-desorption data following the BJH method. Results are presented in Figures 5.15 and 5.16. It is

apparent that the all samples have a similar shape of pore size distribution pattern.

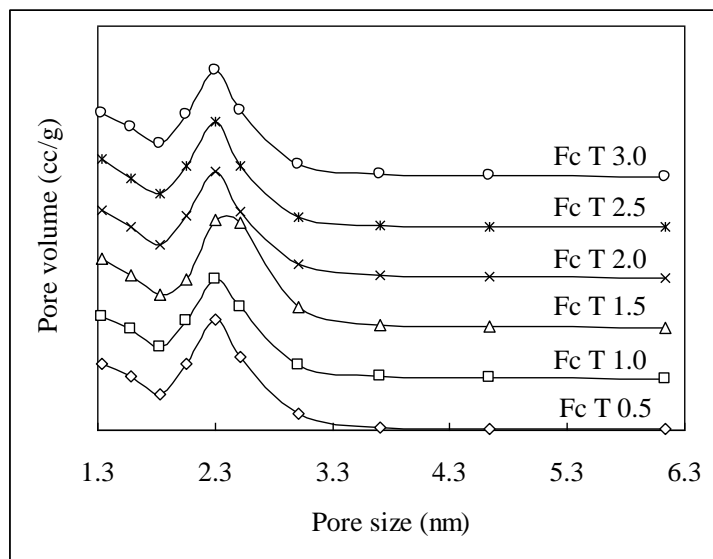


Figure 5.15 The effect of Fc loading on pore size distribution (T method).

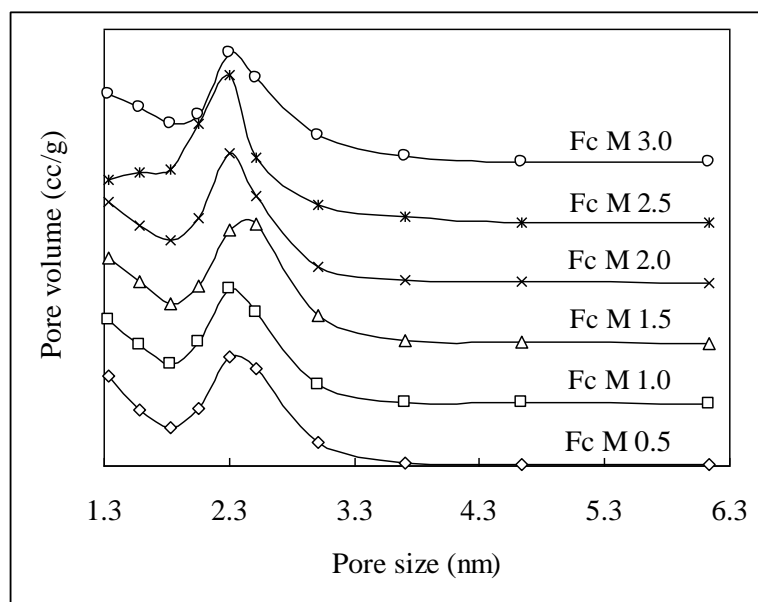


Figure 5.16 The effect of Fc loading on pore size distribution (M method)

A summary of structural parameters of the MCM-41(T) and MCM-41(M) derived from the XRD data and the isotherm data, including the unit cell a_0 , mean pore diameter, wall thickness, total surface area and total pore volume is presented in Tables 5.3 and 5.4

Table 5.3 The effect of Fc loading on structural properties of calcined MCM-41(T)

T method	Unit cell a_0 nm (± 0.03)	Pore size diameter nm (± 0.01)	Wall thickness nm (± 0.04)	Surface area m^2/g (± 70)	Total pore volume cc/g (± 8)
0.5	4.00	2.30	1.7	1398	645
1.0	3.99	2.30	1.69	1480	691
1.5	4.04	2.38	1.66	1550	713
2.0	3.93	2.30	1.63	1548	729
2.5	3.90	2.30	1.60	1550	712
3.0	3.91	2.30	1.61	1439	698

Table 5.4 The effect of Fc loading on structural properties of calcined MCM-41(M)

M method	Unit cell a_0 nm (± 0.03)	Pore size diameter nm (± 0.01)	Wall thickness nm (± 0.04)	Surface area m^2/g (± 70)	Total pore volume cc/g (± 8)
0.5	3.84	2.40	1.64	1590	732
1.0	3.75	2.35	1.40	1560	698
1.5	3.73	2.42	1.31	1560	715
2.0	3.67	2.30	1.37	1470	682
2.5	3.69	2.30	1.39	1600	756
3.0	3.88	2.30	1.53	1630	763

For the T Method, the pore size and the wall thickness were largely unaffected by Fc loading. However for the M Method, the wall thickness initially decreased from 1.64 to 1.31 nm with increasing Fc content over the range from 0.5 to 1.5 wt% (relative to surfactant), and then increased from 1.31 to 1.53 nm with increasing Fc content from 1.5 to 3 wt%.

It is clear from the gas adsorption studies, as was observed with the XRD studies, that the Fc-MCM-41(T) and Fc-MCM-41(M) products, while they were very similar, never-the less exhibited significant structural differences that pointed to the likelihood that the Fc was encapsulated in the pores of the Fc-MCM-41(M) material, and into the walls of the Fc-MCM-41(T) material. These differences could be reflected in the nature and distribution of metal nanoparticles formed when the loaded materials are calcined. The potential advantage of incorporating the metal during synthesis rather

than by post synthesis imbibing is that the metal could be expected to be more homogeneously distributed.

5.4 Preparation and properties of metal loaded MCM-41 by the M and T methods using substituted ferrocenes (S-Fc)

In section 5.2, the loading of MCM-41 by the organometallic compound ferrocene (Fc) was described and it was found that the ferrocene loaded by the M method caused small changes in the d spacing of the product formed. It was of interest to determine whether ferrocene molecules containing bulky substituted group would produce larger structural effects and whether loading would be affected by molecular bulk. In order to test this idea, a series of substituted ferrocenes were used in the T and M synthetic methods.

The ferrocene and the substituted ferrocenes (S-Fc) used were: ferrocene (Fc), acetyl ferrocene (Fac), diacetyl ferrocene (Fd), butyryl ferrocene (Ft), benzoyl ferrocene (Fb), and were synthesised as described in Section 2.2

The reaction conditions for loading substituted ferrocenes (S-Fc) into MCM-41 by the M Method and the T Method have been described in Section 2.3. CTAB was the surfactant and TEOS was the silica source. The amount of S-Fc added was varied to give S-Fc concentrations ranging from 0.5 to 20 by wt% of surfactant. 2.5 mol/L HCl acid solution was used for all reactions. After magnetic stirring (approximately 300 rpm) for 8 hours at room temperature, the resultant precipitate was filtered, washed and dried at room temperature for several hours, and calcining at 550°C to remove the template. The as synthesized and calcined MCM-41 mesophases were characterized by low angle XRD, and the calcined material were characterised by low angle XRD, BET surface area and BJH pore size distribution.

Again it was necessary during M method preparations to add the TEOS to the S-Fc

loaded surfactant slowly and with rapid stirring to avoid the tendency for the S-Fc to be extracted into the organic TEOS phase. No problems with ferrocene oxidation were observed for the substituted ferrocenes.

5.4.1 Determination of organometallic content

As with preparation of the Fc derivatives, the colour of the Fe-containing samples synthesized gave a qualitative indication of S-Fc loading. The samples exhibited colours from white to pale yellow to brown with the increasing incorporation of the S-Fc compounds. After calcining, the samples ranged in colour from white to brown with the increasing of iron content.

A more accurate estimation of metal loading was obtained by extraction and analysis using AA (See section 2.5). Data for Fe loadings (wt% of as-synthesised product) achieved according to the T method and the S method for different S-Fc to surfactant ratios are summarised in Figure 5.17 to 5.21. Also shown are the theoretical loadings that would be expected if all the S-Fc was retained by the product formed.

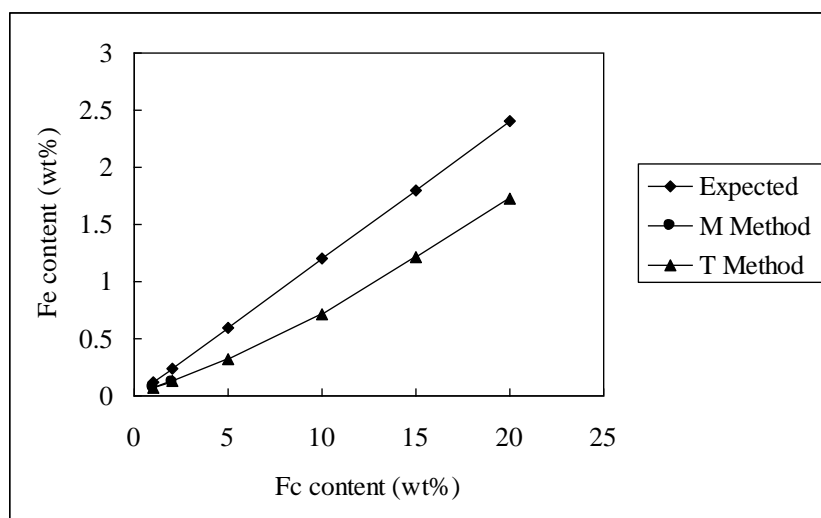


Figure 5.17 The Fc content of MCM-41 loaded by the M and T Methods. Data for the M method were limited to 3% Fc content by the solubility of Fc in water. The results obtained were the same as those for the T Method.

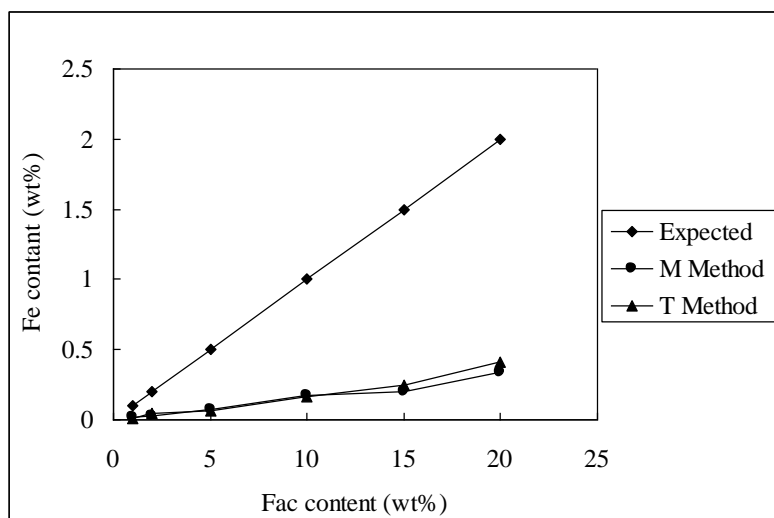


Figure 5.18 The Fac content of MCM-41 loaded by the M and T Methods.

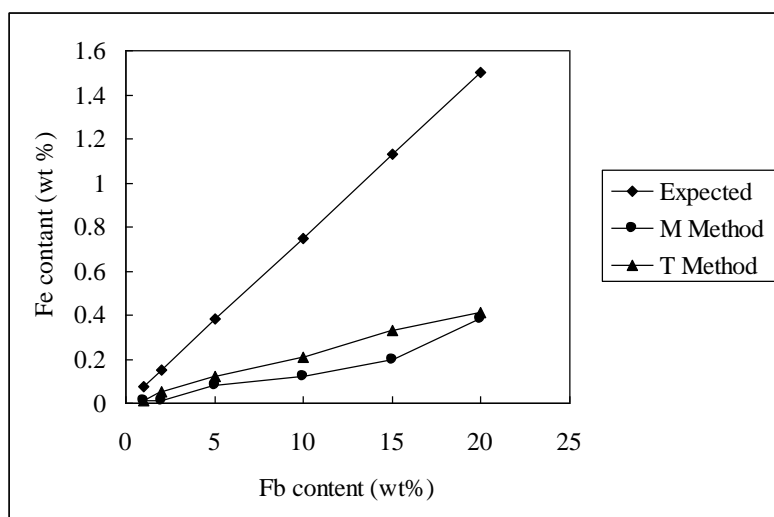


Figure 5.19 The Fb content of MCM-41 loaded by the M and T Methods.

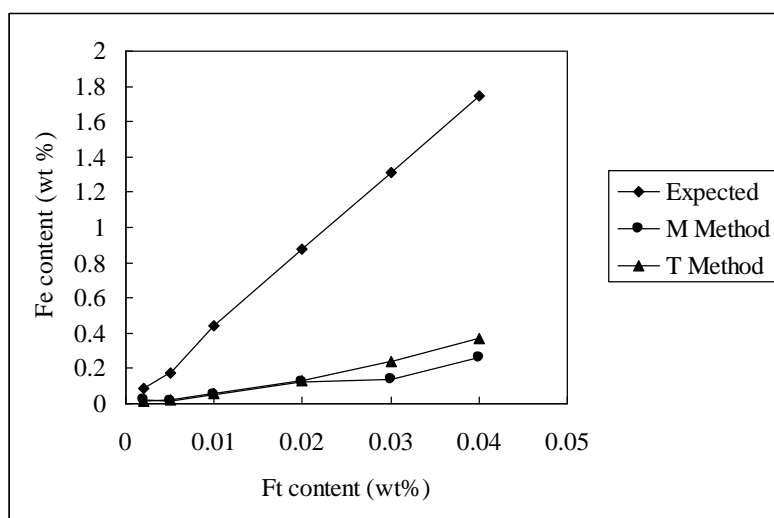


Figure 5.20 The Ft content of MCM-41 loaded by the M and T Methods

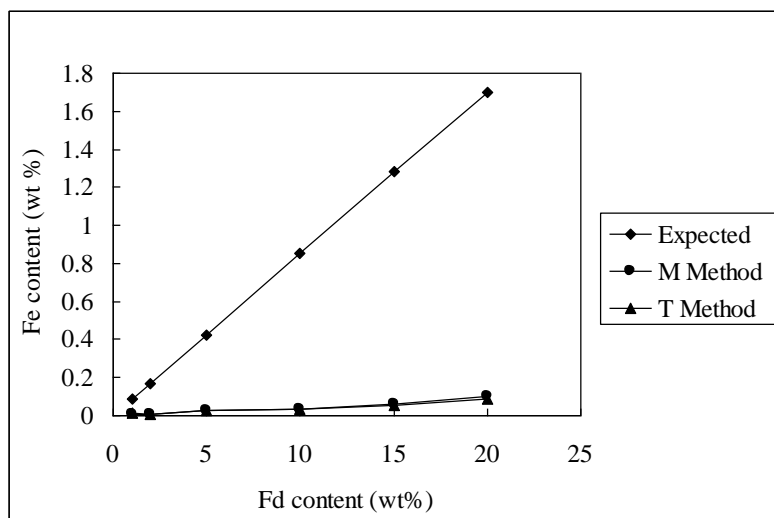


Figure 5.21 The Fd content of MCM-41 loaded by the M and T Method

In all cases, the iron content in final sample increased with the increasing concentration of S-Fc in the reaction mixture. The amount of iron loaded at a given concentration appeared to be affected by two molecular properties of the S-Fc species: its molecular volume and shape and its polar surface area. Molecular volume and shape will affect the ability of the molecule to pack into the micelle core. More hydrophobic compounds (i.e. with lower polar surface areas). will tend to be preferentially partitioned into the organic phases of the synthesis mixture. These phases are the core of the micelle and the TEOS reactant phase. The highest complex uptake by the M Method for a ferrocene to surfactant ratio of 0.02 was the 0.12% by weight obtained for the unsubstituted Fc, the smallest species. The lowest complex uptake under the same conditions was the 0.01% by weight uptake obtained for Fd, the ferrocene which has the highest polar surface area and hence the lowest hydrophobicity. Loadings achieved by the T Method were in the order $Fc > Fac = Fb = Ft \gg Fd$. Again the loading was greatest for the smallest molecule and least for the least hydrophobic molecule. For the Fac, Fb and Ft the trend towards lower loading for higher molecular weight appeared to compensate for the trend towards higher loading at higher hydrophobicity in such a way that the loading of the three species is about the same.

5.4.2 Effect of S-Fc loading on structural features

XRD data for the as synthesized and calcined MCM-41 materials loaded with the various S-Fc compounds are given in Figures 5.22 to 5.29. All materials gave typical MCM-41 diffraction patterns with one sharp peak in the range of $2\theta = 2.1\text{-}2.6^\circ$ indexed to 100 diffraction and two additional weak peaks in the range of $3.5\text{-}6^\circ$ indexed to 110 and 200 diffractions, consistent with a regular hexagonal pore structure.

For the purposes of comparing the effect molecular properties of the S-Fc species on the structural properties of the MCM-41 phases prepared, structural data for the Fc, Fac and Fd experiments (where the ferrocenes contained 0, 1 and 2 methyl ester groups) were compared to illustrate the effect of increasing carbonyl group substitution and data for the Fac, Fb and Ft experiments were compared to illustrate the effect of increasing the size of the a single ester group (methyl, propyl and benzoyl esters)

The M Method

Data for d_{100} spacings for first group (showing the effect of increasing C=O content) of the as-synthesised and calcined materials are given in Figures 5.22 and 5.23.

Comparison of the unit cell parameter (a_o) indicates that increasing C=O content of S-Fc from 0 to 2 causes a significant increase of the unit cell. The effect is consistent with the decreasing hydrophobicity of the S-Fc as the C=O content increases. The less hydrophobic S-Fc molecules will be more disruptive of the structure of the micelle core, cancelling out any tendency to contract (as was the case for Fc0 at low loadings) and causing it to expand at higher loadings. The decrease in unit cell above a S-Fc loading of approximately 5% is not easily explained.

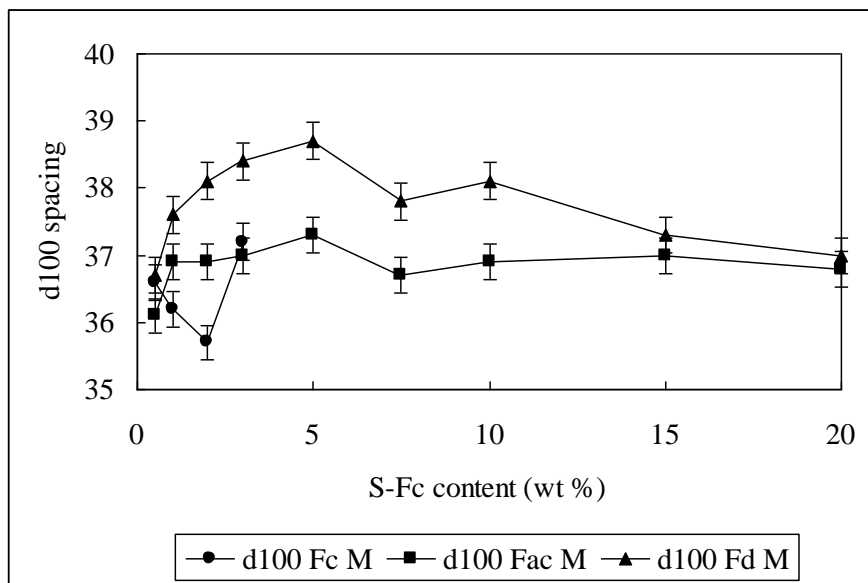


Figure 5.22 The effect of C=O substitution of S-Fc (Fc, Fac and Fd) on d_{100} spacing of as-synthesized samples (M Method). S-Fc content is the S-Fc/surfactant weight ratio expressed as a % in the synthesis mixture.

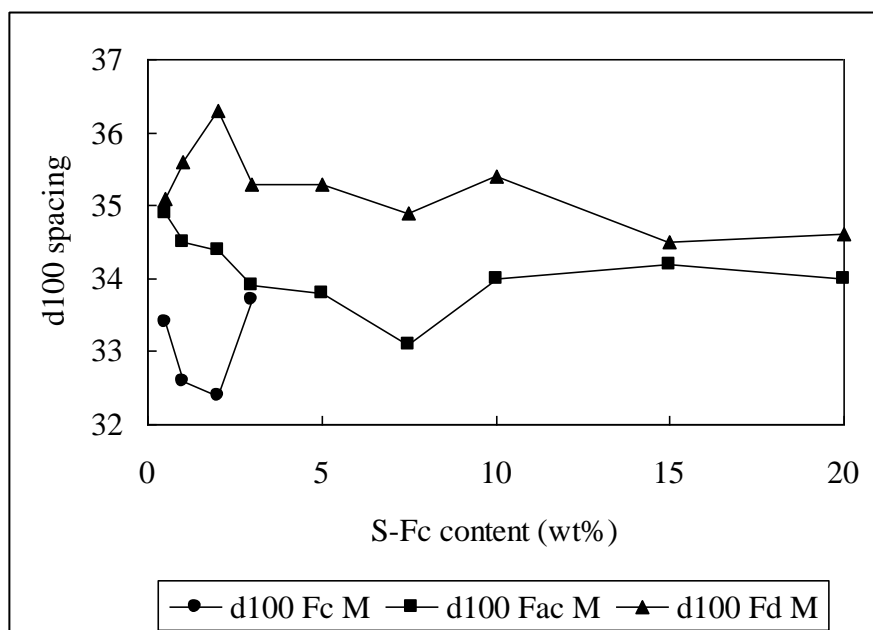


Figure 5.23 The effect of C=O content of S-Fc (Fc, Fac and Fd) on d_{100} spacing of calcined samples (M Method)

Data for d_{100} spacings for the second group of MCM-41 phases with encapsulated S-Fc species (all with one C=O group but of increasing size) are given in Figures 5.24 and 5.25.

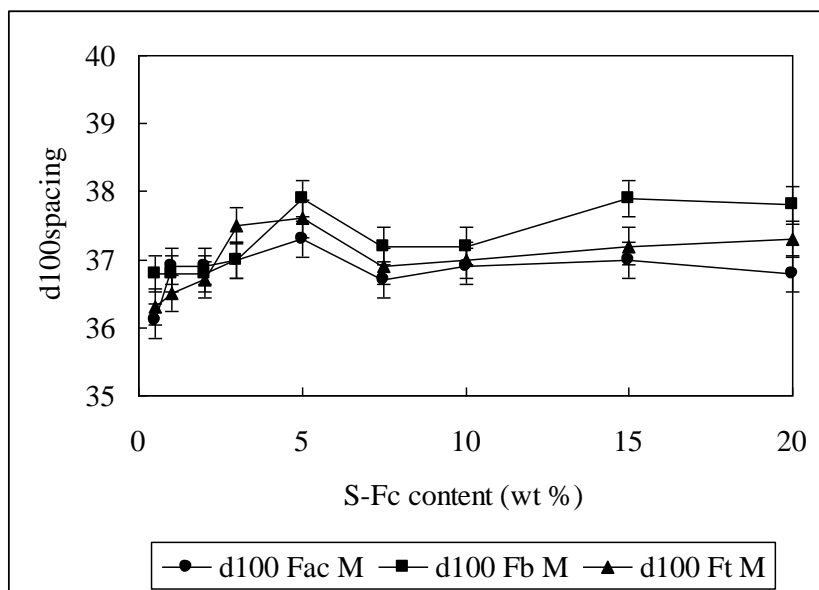


Figure 5.24 The effect of molecular weight of S-Fc species each containing one C=O group (Fac, Fb and Ft) on d_{100} spacing of as-synthesized samples (M Method).

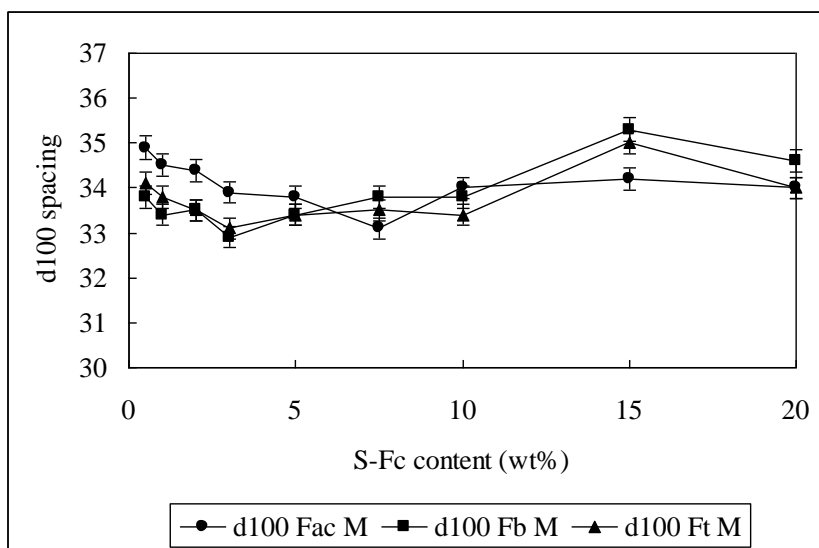


Figure 5.25 The effect of molecular weight of S-Fc species each containing one C=O group (Fac, Fb and Ft) on d_{100} spacing of calcined samples (M Method)

While the unit cell parameter (a_0) appeared to increase with increasing S-Fc concentration from 0.5 to 5 wt%, there was no significant difference in the a_0 values for the Fac, Ft and Fb loaded materials. The bulkiness of the substituted group does not appear to have much effect on the mesoporous structure.

The T Method

The effect of C=O content of S-Fc (Fc, Fac and Fd) on d_{100} spacing of as synthesised and calcined samples (T Method) is illustrated by data summarized in Figures 5.26 and 5.27.

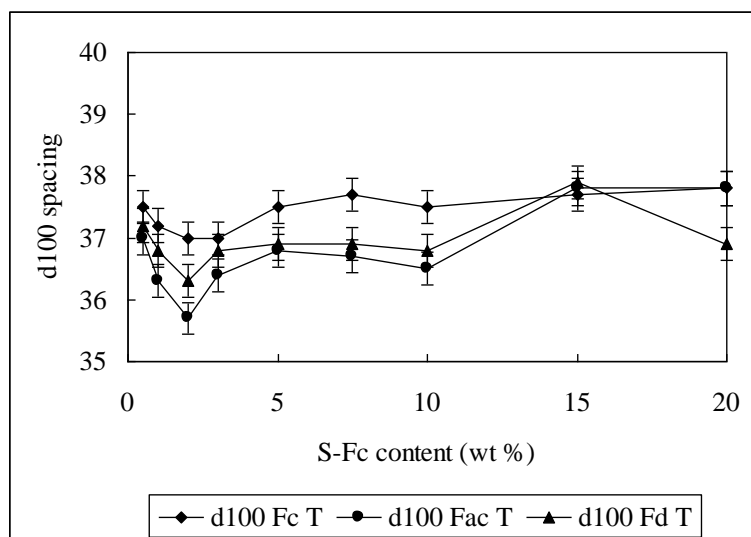


Figure 5.26 The effect of C=O content of S-Fc (Fc, Fac and Fd) on d_{100} spacing of as synthesised samples (T Method)

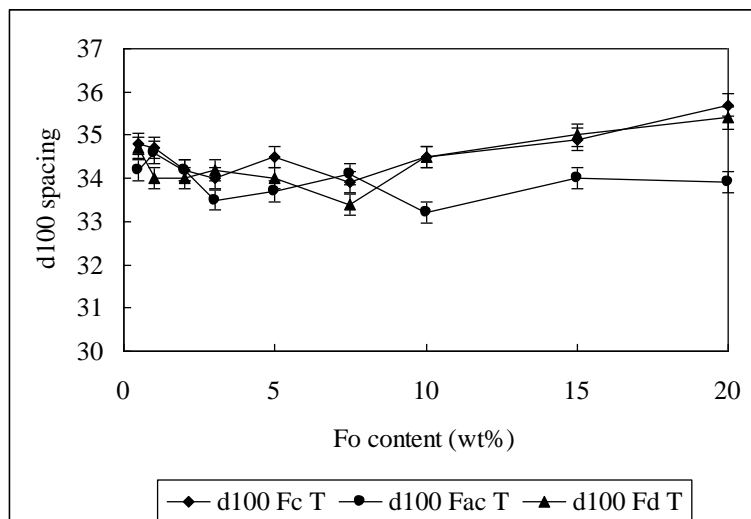


Figure 5.27 The effect of C=O content of S-Fc (Fc, Fac and Fd) on d_{100} spacing of calcined samples (T Method)

While the expected contraction of the lattice occurred upon calcining, the data of Figures 5.26 and 5.27 indicate that the C=O content of the S-Fc had little effect on the

d_{100} parameter. The d_{100} values for the Fc are slightly larger in the as prepared material possibly reflecting the higher loading of Fc in the material. However this difference disappears upon calcining.

The effect of molecular weight of S-Fc species each containing one C=O group (Fac, Fb and Ft) on d_{100} spacing of the as synthesised and calcined samples (T Method) are given in Figures 5.28 and 5.29.

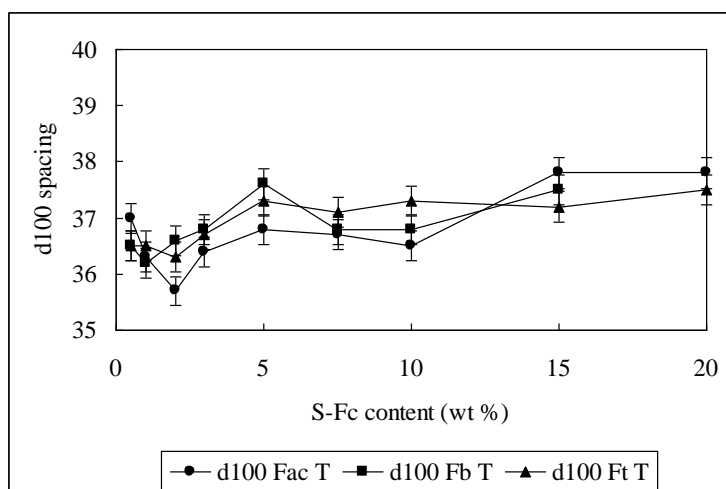


Figure 5.28 The effect of molecular weight of S-Fc species each containing one C=O group (Fac, Fb and Ft) on d_{100} spacing of as synthesised samples (T Method)

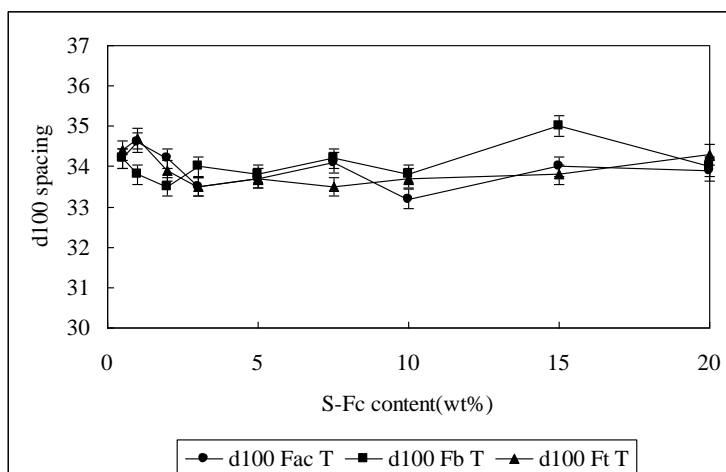


Figure 5.29 The effect of molecular weight of S-Fc species each containing one C=O group (Fac, Fb and Ft) on d_{100} spacing of calcined samples (T Method)

Molecular weight appears to have no discernable effect on the d_{100} parameter. Comparison of the results for the M and T methods reveals that the materials prepared

by the M method have significantly larger d_{100} parameters for both the as prepared and calcined materials when Fd, the S-Fc molecule containing two C=O groups, is used in the synthesis procedure. For all the other systems investigated, molecular weight and C=O content had little effect on the MCM-41 structures

5.4.3 Effect of S-Fc loading on N₂ adsorption-desorption characteristics

The BET surface area for the calcined materials are presented Figures 5.30 to 5.33. Loading with the various S-Fc species had significant effects (mainly increases) on the BET surfaces areas. Normally, the purely silicious MCM-41 synthesized according to the procedure of Section 2.4 had a specific surface area of about 1300 m²/g.

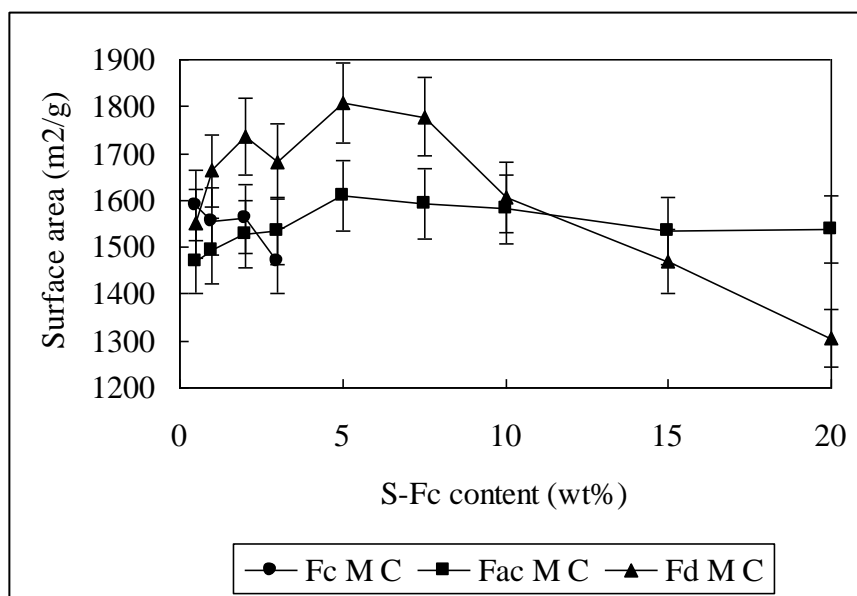


Figure 5.30 The effect of C=O content of S-Fc (Fc, Fac and Fd) on specific surface area of calcined samples (M Method)

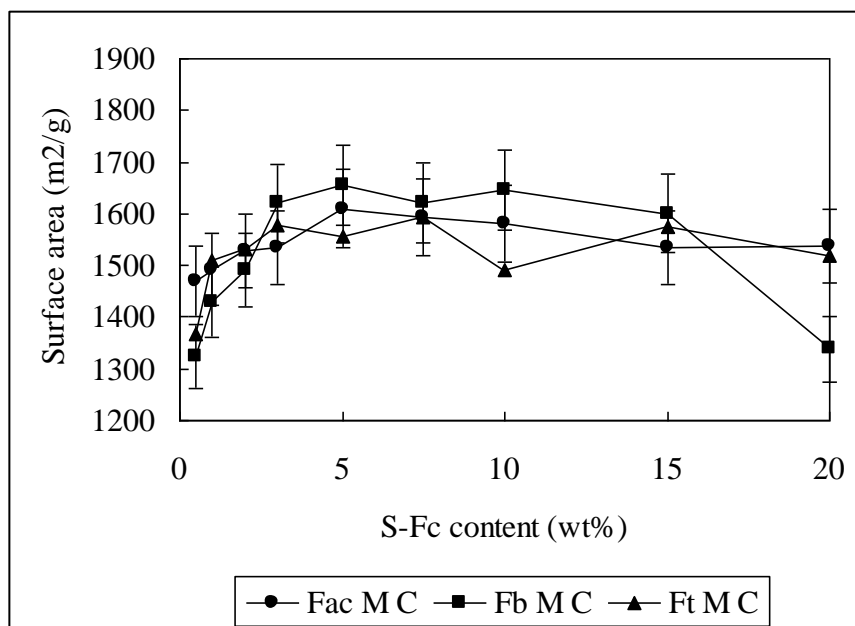


Figure 5.31 The effect of molecular weight of S-Fc species each containing one C=O group (Fac, Fb and Ft) on specific surface area of calcined samples (M Method)

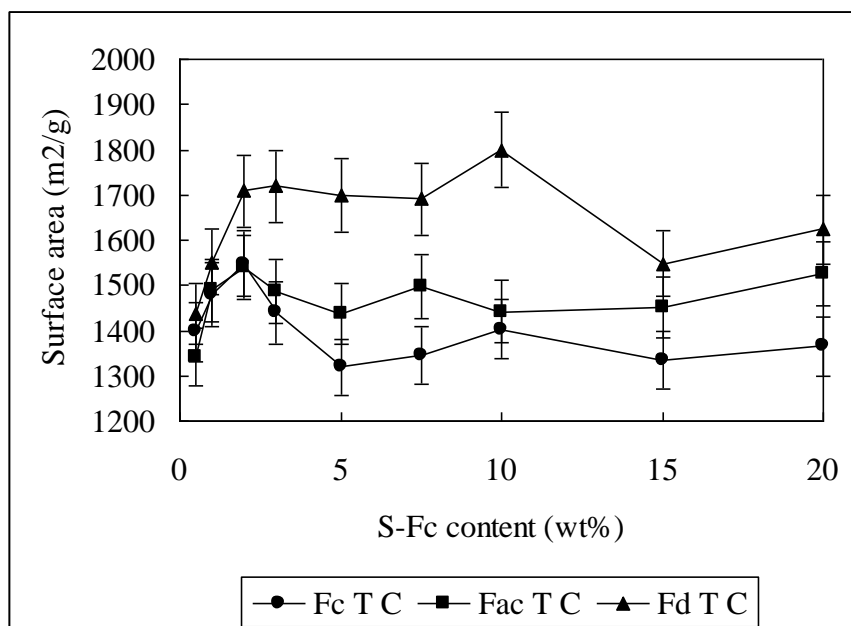


Figure 5.32 The effect of C=O content of S-Fc (Fc, Fac and Fd) on specific surface area of calcined samples (T Method)

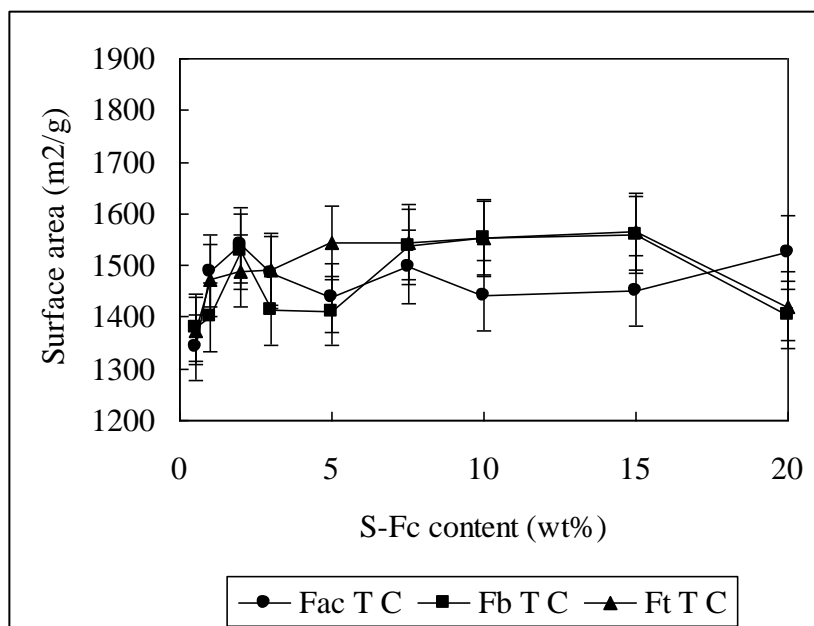


Figure 5.33 The effect of molecular weight of S-Fc species each containing one C=O group (Fac, Fb and Ft) on specific surface area of calcined samples (T Method)

For all samples there appeared to be an increase in specific surface area with increased loading of S-Fc (i.e. higher S-Fc concentrations used in the synthesis mixture). This was correlated with greater XRD intensities indicating that the increase in specific surface area was associated with more highly ordered MCM-41 phases stabilized by S-Fc loading. At higher loading, a reverse trend was observed where XRD intensities and specific surface area decreased with increased loading. Apparently there is an optimum loading for maximum order and specific surface area.

Superimposed upon this trend were molecular effects associated with the specific S-Fc species used to load the MCM-41 and the method of loading used. Molecular effects were most pronounced when Fd was used and were common to both the M and T synthetic routes. For loadings of Fd in the range of 2.5 to 10%, surface area of up to 1800 m²/g were observed.

The high surface areas obtained for the S-Fc materials are of interest for two reasons: they appear to be higher than the 1500 m²/g surface area upper limit for MCM type material normally recorded in the literature, and in contrast to the normal significant

decrease in area with loading, show a pronounced increase in area with loading.

5.5 The loading of other organometallic compounds into MCM-41 by T and M Method

In section 5.3, the loading of MCM-41 by the different molecular size and shape substituted ferrocene compound was described and it was found that the different molecular size and shape loaded by the M method and T method caused some structural changes in the product formed. In this section, while the primary interest was to investigate the loading of different metals into MCM-41 phases, it was still of interest to determine whether other metal complexes would produce structural effects. The organometallic compounds of Mn, Mo and Co used were methylcyclopentadienyl manganese tricarbonyl (O-Mn), cyclopentadienyl molybdenum tricarbonyl dimer (O-Mo) and 3-methylidyne-tricobalt nonacarbonyl (O-Co). Loading was performed by the M method and T method.

The O-Mo, O-Mn and O-Co are of special interest because they provide examples of organometallic complexes containing other catalytically interesting metals. O-Mo is of particular interest because it has a structure similar to that of Fy but contains more polar carbonyl groups.

Metal-MCM-41 mesoporous silica was synthesized using CTAB as the surfactant and TEOS as the silica source following the general procedure the M Method and the T Method as described in Section 2.3. In the all cases, concentrations close to the saturation limit of the organometallic compounds were used. For Fy, O-Mo, O-Co and O-Mn, the concentrations used were 10, 10, 10 and 20 % relative to the weight of surfactant, respectively. 2.5 mol/L HCl solution was used for all reactions. Reaction time was 5 hours under stirring (1000 rpm) at room temperature. The resultant white precipitate was filtered, washed and dried at room temperature for several hours. The final samples Metal-MCM-41(T), Metal-MCM-41 (M) were characterized by low

angle XRD, BET and metal content as determined by AA (see Section 2.5)

5.5.1 Determination of metal content

The color of the metal-containing samples provided a visual clue as to the level of organometallic complexes loading in the final product. All the as synthesised samples were coloured suggesting the organometallic complexes had been incorporated. After calcined, in most case the colour changed to white for Mo-MCM-41 materials, light grey for Co-MCM-41 and light red for Fe-MCM-41.

Quantitative data for metal loading was obtained by AA (See section 2.6). Data for metal loadings (wt% of as-synthesised product) achieved according to the T method and the M method for different organometallic complexes wt% relative to the surfactant are summarized in table 5.7 and 5.8.

Table 5.7 Metal contents for single metal loadings (M-Method)

M Method	Mn	Mo	Fy	Co
Colour as syn.	brown	pink	yellow	blue
Colour calc.	brown	white	Light red	Light-grey
Metal content C. (wt%)	1.32	1.15	0.34	0.09

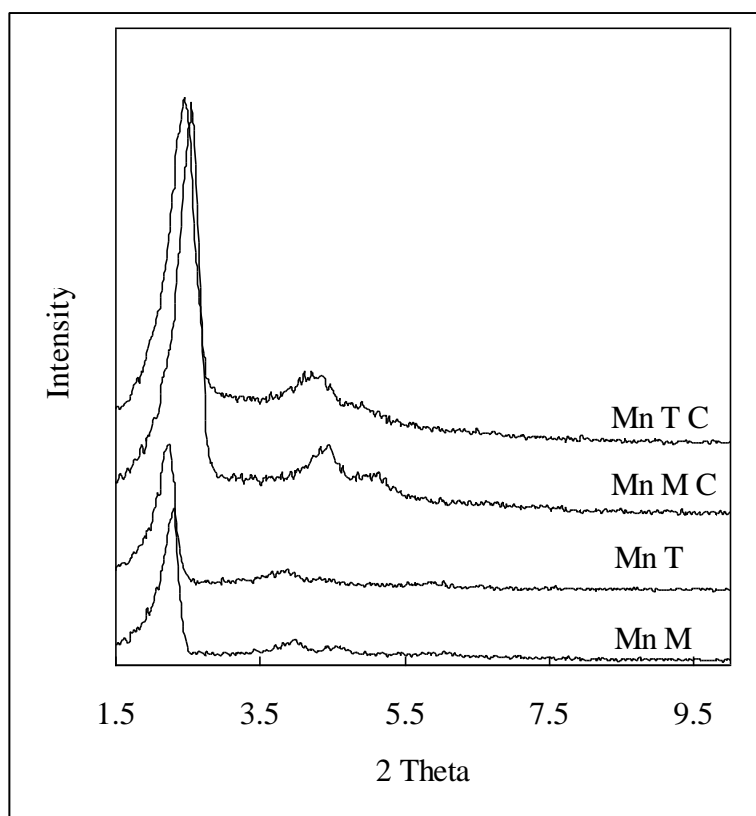
Table 5.8 Metal contents for single metal loadings (T-Method)

T Method	Mn	Mo	Fy	Co
Colour as synthesised	brown	pink	yellow	light blue
Colour C	dark brown	white	light brown	light grey
Metal content C. (wt%).	2.48	1.26	0.1	0.21

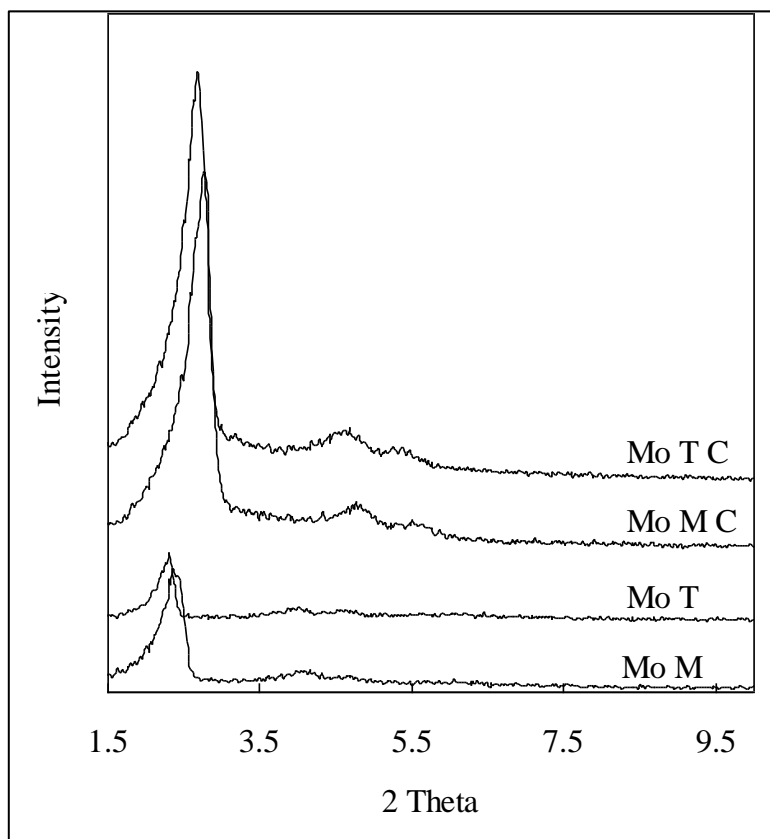
5.5.2 Effect of organometallic complex loading on structural features

The X-ray diffraction patterns of the Metal-MCM-41 loaded by the T method and the M method are summarized in Figures 5.34 to 5.37. XRD patterns of all samples corresponded to the regular hexagonal pore structure of Metal-MCM-41 and was not affected by organometallic complex loading. The Metal-MCM-41 structure was

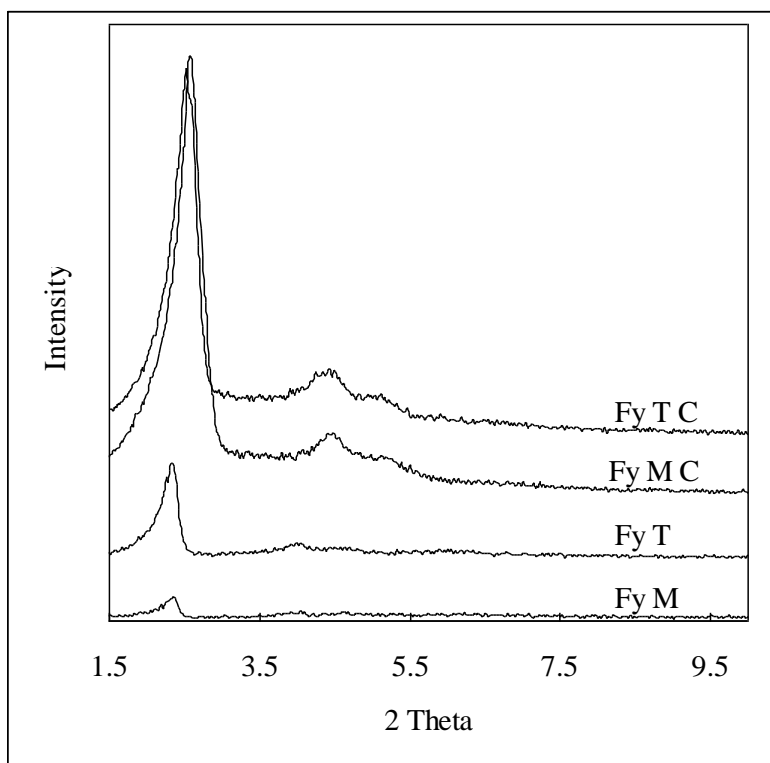
maintained after calcining with peak positions indicating lattice contraction and peak intensities revealing dramatic increases in structure ordering. The ordering effect upon calcining suggests that accommodation of the bulky organometallic complexes is structure disrupting and that upon their decomposition during calcining, the silica structure is able to revert to a more ordered form irrespective of whether the material was synthesised by the T or M method.



Figures 5.34 The effect of O-Mn loading on XRD powder patterns for as synthesized and calcined MCM-41.

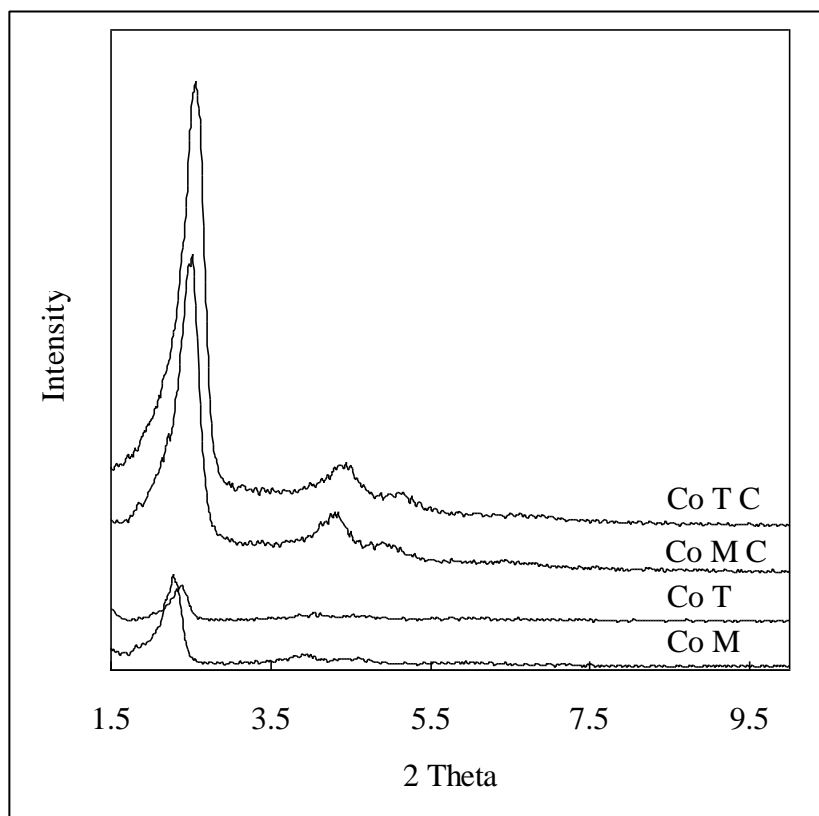


Figures 5.35 The effect of O-Mo loading on XRD powder patterns for as synthesized and calcined MCM-41.



Figures 5.36 The effect of Fy loading on XRD powder patterns for as synthesized and calcined

MCM-41.



Figures 5.37 The effect of O-Co loading on XRD powder patterns for as synthesized and calcined MCM-41.

Values of d_{100} for the as synthesised material and calcined material and the contraction upon calcining are given in Tables 4.7 and 4.8.

Table 5.7 d_{100} data for the as-synthesised and calcined samples for M Method

M Method	Fe	Mn	Mo	Co
d_{100} as syn. (± 0.3 , Å)	37.2	38.5	37.2	36.9
d_{100} calc. (± 0.3 , Å)	34.1	34.6	31.9	34.3
Contraction	3.1	3.9	5.3	2.6

Table 5.8 d_{100} data for the as-synthesised and calcined samples for T Method

T Method	Fy	Mn	Mo	Co
d_{100} as syn. (± 0.3 , Å)	37.6	39.6	38.5	38.5
d_{100} calc. (± 0.3 , Å)	34.9	36	33.1	34.9
Contraction	2.7	3.6	5.4	3.6

There was a significant difference in d_{100} spacing contraction upon calcining for the different organometallic complexes loaded. The d_{100} spacing contraction can result from two causes. A general contraction will occur due to the loss of the surfactant, exposing lattice hydroxyl which undergo condensation polymerisation causing a general shrinking of the product. Another contraction mechanism could result from decomposition of the loaded organometallic complexes releasing space and resulting in a contraction of the pore center-to-center distance. The fact that all samples contained the same surfactant, lends weight to the explanation that it was the decomposition of the different organometallic complexes that resulted in different d_{100} spacing contractions. The larger the molecule size and the higher the loaded amount, the larger the expected contraction. O-Mo has the largest molecular size and the second highest loading so it is not surprising that the contraction was greatest for this system for both the M and T synthetic methods. Although O-Mn has smallest molecule size of all organometallic complexes used, it had the highest loading and consequently gave the second highest contraction. The sample O-Fe has a larger molecule size than O-Mn, but a much lower loading and this resulted in a lower contraction.

5.5.3 The effect of loading with organometallic complexes on nitrogen adsorption

Data for the effect of loading with the O-Mn, O-Mo, Fy and O-Co on the nitrogen adsorption/desorption isotherms and BJH pore sizes are summarized in Figures 5.38 to 5.39 and 5.40.

All calcined materials exhibited typical type IV isotherm behaviour. The steep capillary condensation step, characteristic of a highly uniform mesoporous structures, indicated that the mesoporous structures of Metal-MCM-41 (T) and Metal-MCM-41 (M) were well preserved upon calcining.

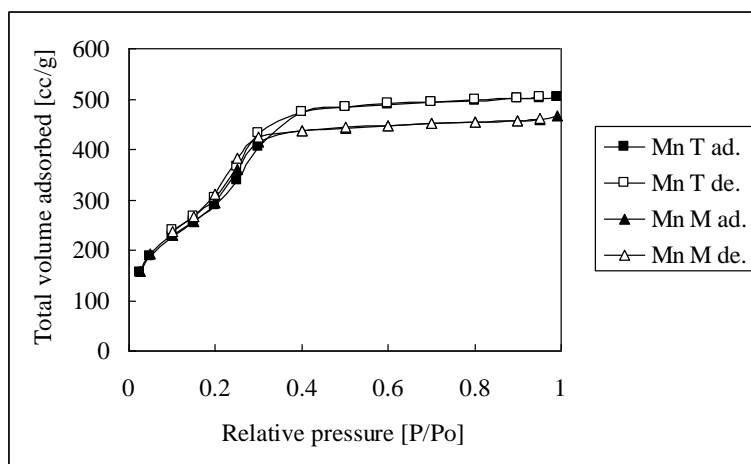


Figure 5.38 The effect of loading organometallic complex O-Mn on nitrogen adsorption desorption isotherms.

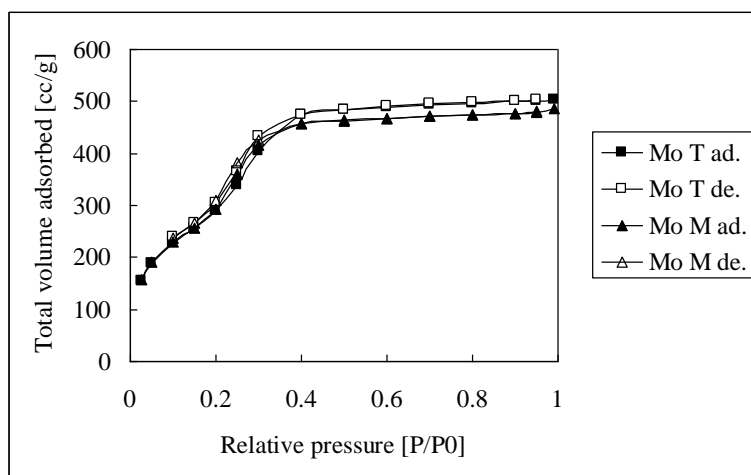


Figure 5.39 The effect of loading organometallic complex O-Mo on nitrogen adsorption desorption isotherms.

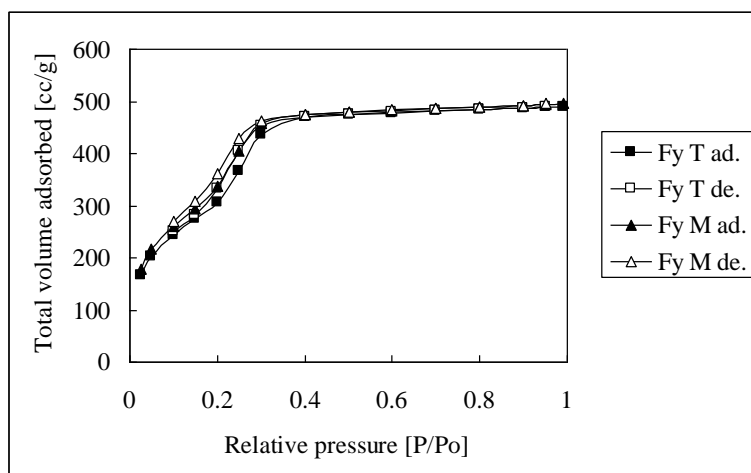


Figure 5.40 The effect of loading organometallic complex Fy on nitrogen adsorption desorption isotherms

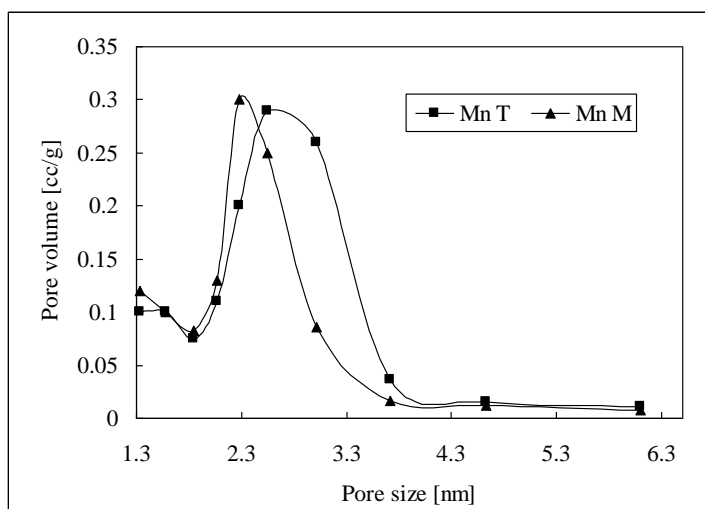


Figure 5.41 The effect of O-Mn loading on the pore size distribution

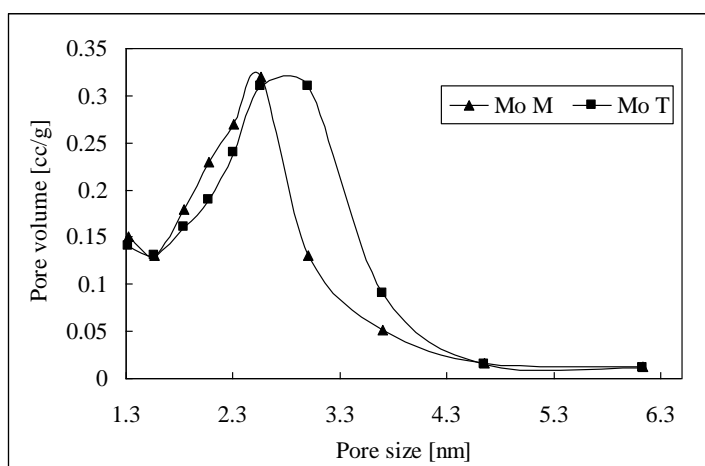


Figure 5.42 The effect of O-Mo loading on the pore size distribution

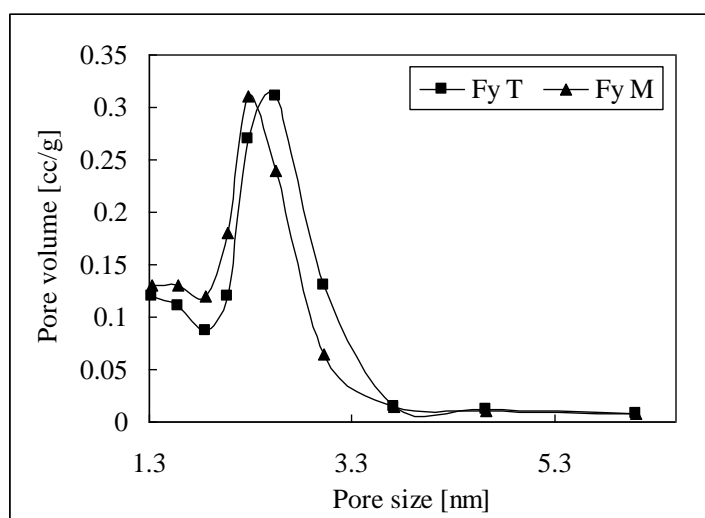


Figure 5.43 The effect of Fy loading on the pore size distribution

The differing effects of loading of metal into the mesoporous structures by T and M method are revealed by the different BJH desorption pore diameter distribution patterns. For the highest loaded O-Mn system the much broader pore diameter distribution for T Method product relative to the M Method product indicates that more variable wall thicknesses result when the complex encapsulated within the wall decomposes (T method) relative the effect on wall thickness resulting from decomposition of complex in the pores (M method).

A summary of structural parameters of the Metal-MCM-41(T) and Metal-MCM-41(M) derived from the XRD data and the isotherm data, including the unit cell a_0 , mean pore diameter, wall thickness, total surface area and total pore volume is presented in Tables 5.9

Tables 5.9 The effect of organometallic complex loading on structural properties of calcined

Organometallic Compounds	Unit cell a_0 nm (± 0.03)	Pore size diameter nm(± 0.01)	Wall thickness nm(± 0.04)	Surface area m^2/g (± 70)	Total pore volume cc/g (± 8)
O-Fy T	4.03	2.55	1.48	1340	0.76
O-Fy M	3.94	2.35	1.59	1440	0.77
O-Mn T	4.14	2.70	1.44	1240	0.78
O-Mn M	3.98	2.27	1.71	1290	0.72
O-Mo T	3.95	2.79	1.16	1390	0.76
O-Mo M	3.76	2.56	1.20	1330	0.76

The effects of loading the metal into the mesoporous structures by organometallic complexes of different sizes are reflected by the different structural properties of the final products. For the system prepared from the largest complex (O-Mo), the largest pore size and smallest wall thickness was obtained indicating that the larger molecules release more space during calcining.

5.6 Summary

Loading by the T and M methods provides some significant differences compared with loading by the I method. Generally less complex is taken up by the T and M methods and the effect of loading on the silica structure and specific surface area is much less even before calcining to decompose complex. After calcining surface area are always increased relative the area expected for pure silica. The increase in area could be the result of the formation of small metal particles that contribute surface area.

Chapter 6 The loading of mixed metal and bimetallic complexes into mesoporous solids by the M, T and I Methods

6.1 Introduction

In Chapters 4 and 5, the loading of MCM-41 phases with single metal complexes during synthesis and immersion was described. It was of interest to use the M, T and I methods to prepare mixed metal systems from mixtures of metal complexes and bimetallic complexes. Moreover, it can be expected that different synthetic methods will lead to different locations and coordination environments of metal species which could lead to different properties. In order to demonstrate this possibility, the mixture of metal complexes O-Mo and Fy (Mo+Fe), the mixture of metal complexes O-Mo and O-Co (Mo+Co), and the bimetallic complexes $\text{Cp}(\text{CO})_3\text{MoFe}(\text{CO})_2\text{Cp}$ (Mo-Fe) and $\text{Cp}(\text{CO})_2\text{Mo}[\text{Co}(\text{CO})_3]_2\text{CMe}$ (Mo-Co) were used in the T, M and I synthetic methods.

Metal-MCM-41 mesoporous silica was synthesized using CTAB as the surfactant and TEOS as the silica source following the general procedure the M Method and the T Method as described in Section 2.3. In the all cases, concentrations close to the saturation limit of the organometallic compounds were used. For Mo-Fe and Mo-Co, the concentrations used were 10 % relative to the weight of surfactant. For Mo+Fe and Mo+Co, the concentrations used were 5%+5% relative to the weight of surfactant. A 2.5 mol/L HCl solution was used for all reactions. Reaction time was 5 hours under stirring (1000 rpm) at room temperature. The resultant colour precipitate was filtered, washed and dried at room temperature for several hours.

For the I method, concentrations close to the saturation limit of the organometallic compounds were used. In the case of the metal complex mixtures, the concentrations in the for Mo+Fe mixture were 0.05 mol/L O-Mo and 0.075 mol/L Fy; for the Mo+Co

mixture the concentrations were 0.05 mol/L O-Mo and 0.05 mol/L O-Co and for the bimetallic complexes, Mo-Fe and Mo-Co, the concentrations used were both 0.1 mol/L. Dry calcined MCM-41 (0.5 g) was suspended in this solution under vacuum for 24 hours as described in Section 2.3. The material was rinsed until risings were colourless and dried under vacuum. The dried as immersed material was analyzed for metal according to Section 2.3. All the final samples Metal-MCM-41(T), Metal-MCM-41 (M) and Metal-MCM-41 (I) were characterized by low angle XRD and metal content as determined by AA (see Section 2.5), and the sample Mo+Fe was further characterized by gas adsorption.

6.2 Determination of metal content

The color of the metal-containing samples provided a simple indication of organometallic complexes loading in the final product. All the as synthesised samples were coloured suggesting the organometallic complexes had been incorporated. After calcining, the colour of the samples changed to black in the most case.

Quantitative data for metal loading was obtained by AA (See section 2.6). Data for metal loadings (wt% of calcined product) achieved according to the T method, the M method and the I method for different organometallic complexes wt% relative to the surfactant are summarized in Table 6.1 to 6.3.

For the samples Mo-Fe and Mo-Co, the final product exhibited a very similar mol ratio to the original bimetallic complex. For the samples Mo+Fe and Mo+Co, the final product exhibited significantly different mole ratios relative the 1:1 mole ratios in the preparative mixtures. This may have resulted from preferential interactions with the silica matrix in the case of the I method and preferential interactions within the core of the micelle or the TEOS solution respectively for the M and T methods.

Table 6.1 Metal contents for the mixed metal and bimetallic complexes loadings (I-Method)

I Method	Mo+Fe	Mo-Fe	Mo+Co	Mo-Co
Colour as synthesised	pink	pink	blue	blue
Colour calcined	red	brown-red	dark grey	dark grey
Metal content (wt%)	1.98/1.72	1.65/0.98	1.29/0.41	0.45/0.53

Table 6.2 Metal contents for the mixed metal and bimetallic complexes loadings (M Method)

M Method	Mo+Fe	Mo-Fe	Mo+Co	Mo-Co
Colour as synthesised	pink	pink	blue-grey	blue
Colour calcined	Very light red	light-red	dark grey	dark grey
Expected wt% metal ratio	0.51/0.42	0.79/0.47	0.51/0.34	0.97/1.2
Actual wt% metal ratio	0.43/0.06	0.53/0.28	0.46/0.13	0.62/0.73

Table 6.3 Metal contents for the mixed metal and bimetallic complexes loadings (T Method)

T Method	Mo+Fe	Mo-Fe	Mo+Co	Mo-Co
Colour as synthesised	light pink	yellow	Blue	blue
Colour calcined	very light red	light-red	dark grey	dark grey
Expected metal content (wt%)	0.51/0.42	0.79/0.47	0.51/0.34	0.97/1.2
Metal content (wt%)	0.42/0.03	0.46/0.21	0.48/0.09	0.57/0.62

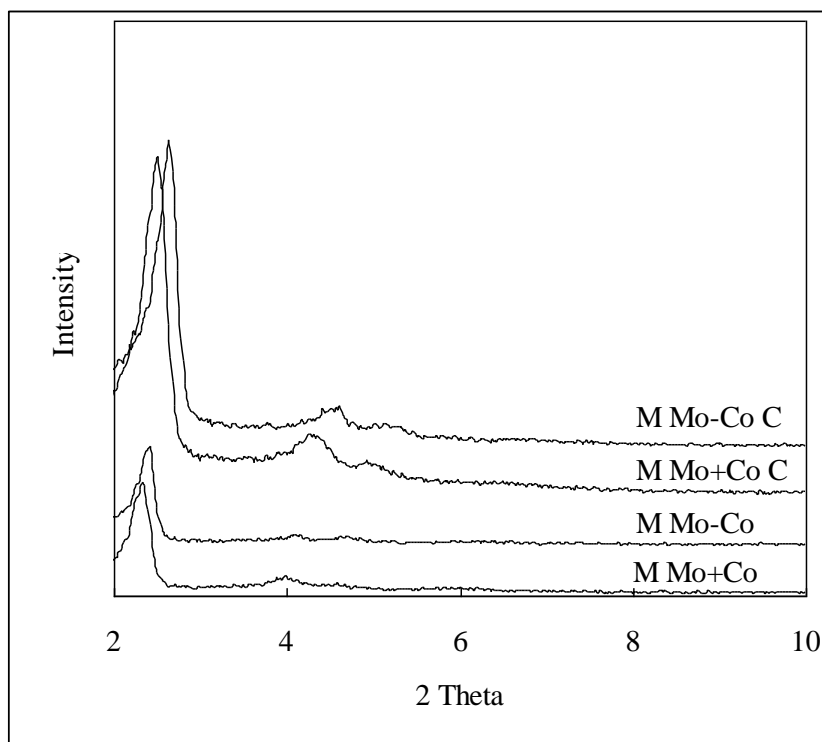
The total loading of metals for samples prepared by the T and M methods was higher when the bimetallic complexes were used. In contrast, the metal loading for samples prepared by the I method was higher when mixtures of monometallic complexes were employed.

6.3 Effect of mixed metal and bimetallic complexes loading on structural features

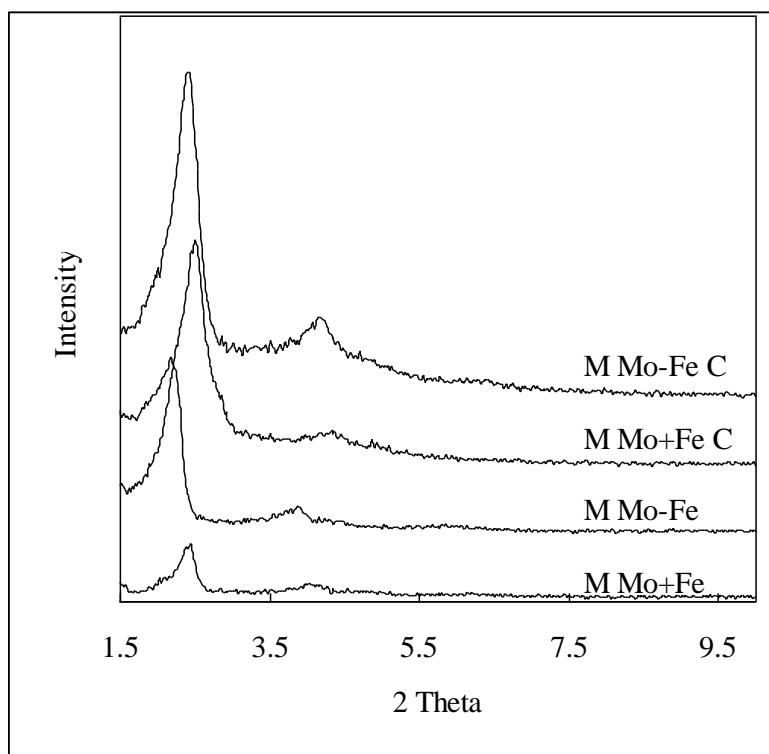
The X-ray diffraction patterns of the Metal-MCM-41 loaded by the T method and the M method are given in Figures 6.1 to 6.6. XRD patterns of the T and M method samples corresponded to the regular hexagonal pore structure of Metal-MCM-41 and were not affected by mixed metal and bimetallic complex loading. The Metal-MCM-41 structure was maintained after calcining with peak positions indicating lattice contraction and peak intensities revealing dramatic increases in

structure ordering.

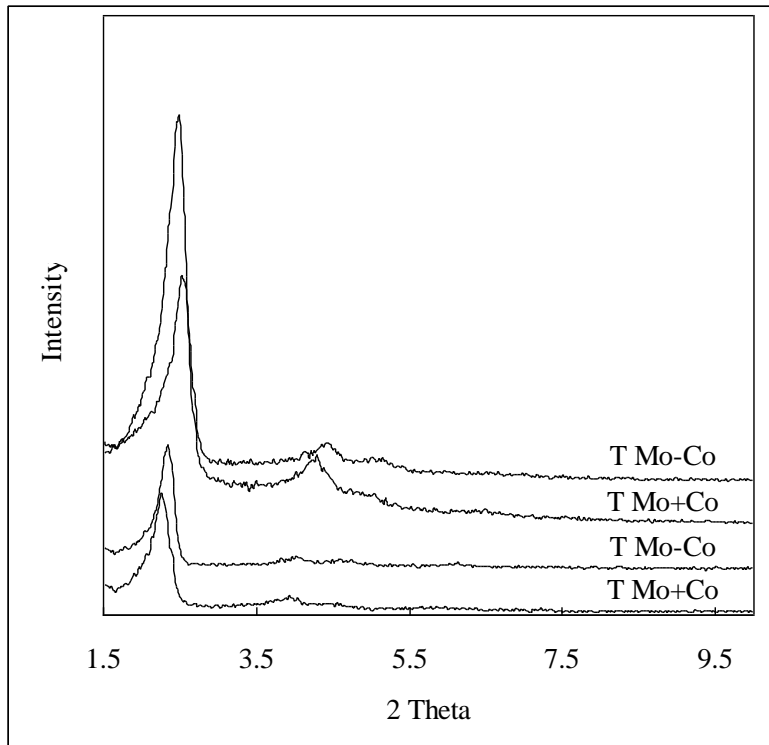
There was a significant decrease in the diffracted intensities for the I method samples, indicating that the quality of Metal-MCM-41 decreased. The d_{100} spacing also decreased after loading. In most cases, two peaks appeared in d_{100} position, indicating the possibility of pore modification into a regular array of pores with differing wall thicknesses resulting from deposition of the metal complex and/or calcined metal species.



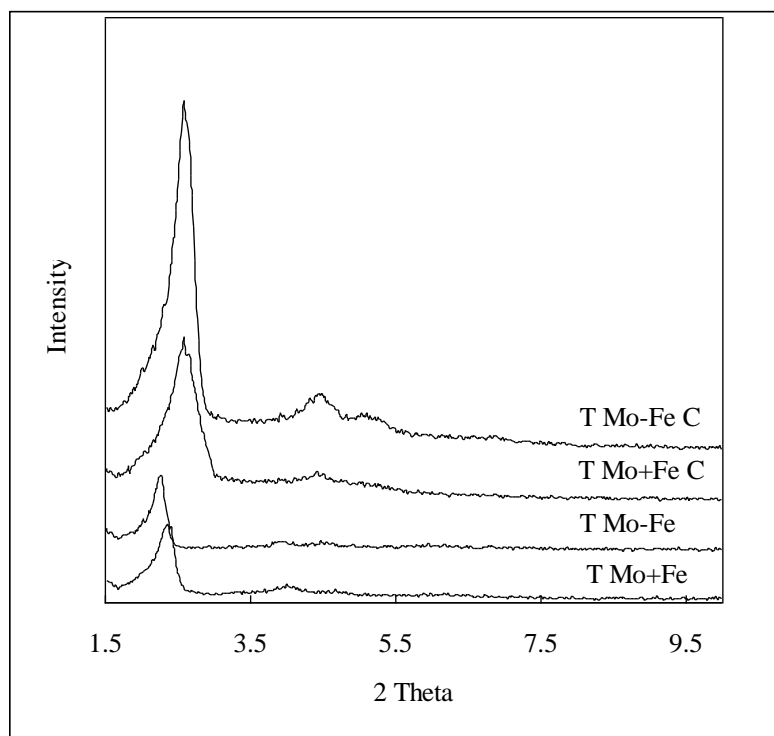
Figures 6.1 The effect of the Mo+Co and Mo-Co on XRD powder patterns for as synthesized and calcined MCM-41 for the M method.



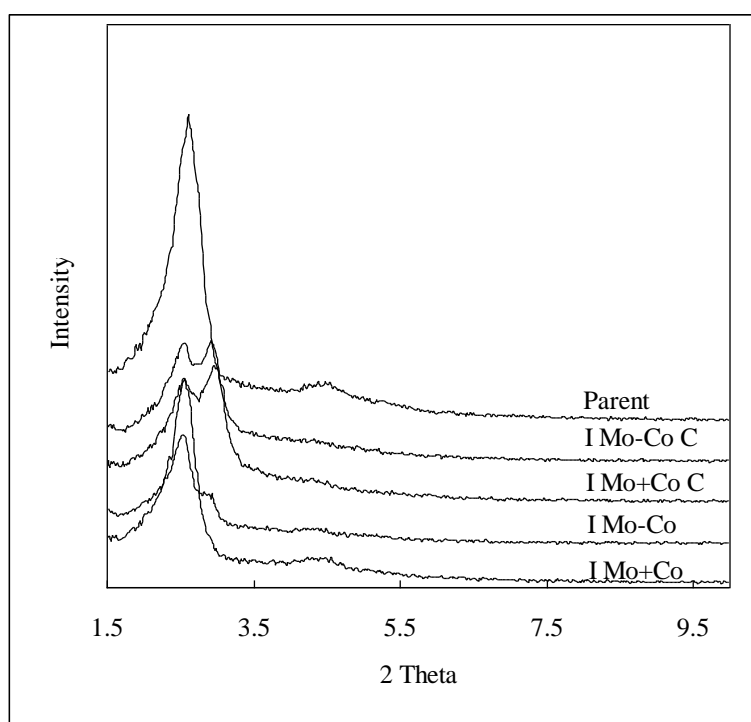
Figures 6.2 The effect of the Mo+Fe and Mo-Fe on XRD powder patterns for as synthesized and calcined MCM-41 for the M method.



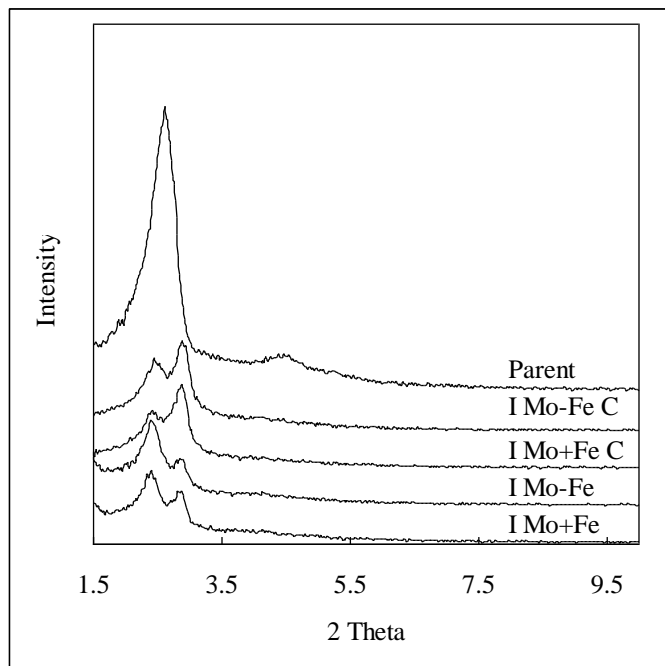
Figures 6.3 The effect of the Mo+Co and Mo-Co on XRD powder patterns for as synthesized and calcined MCM-41 for the T method.



Figures 6.4 The effect of the Mo+Fe and Mo-Fe on XRD powder patterns for as synthesized and calcined MCM-41 for the T method



Figures 6.5 The effect of the Mo+Co and Mo-Co on XRD powder patterns for as synthesized and calcined MCM-41 for the I method.



Figures 6.6 The effect of the Mo+Fe and Mo-Fe on XRD powder patterns for as synthesized and calcined MCM-41 for the I method.

6.4 The effect of loading mixed metal complexes on nitrogen adsorption

Data for the effect of loading with Mo+Fe by the I method on the nitrogen adsorption/desorption isotherms and BJH pore sizes are given in Figures 6.7 and 6.8

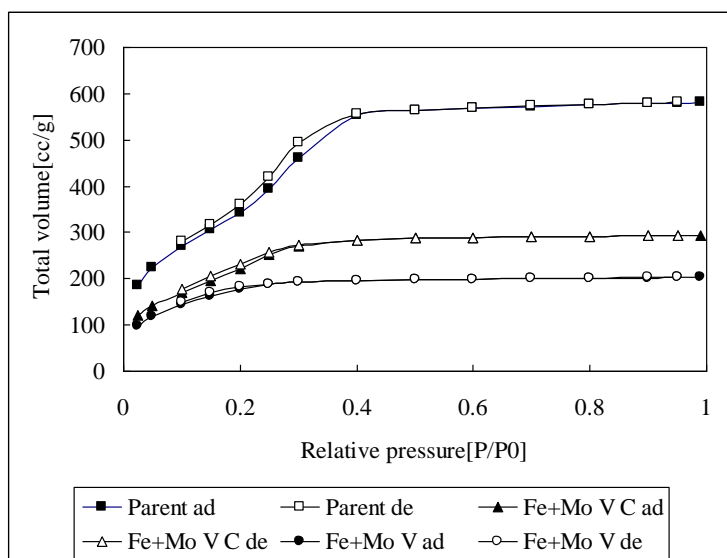


Figure 6.7 The effect of Fe+Mo mixed metal loading on nitrogen adsorption desorption isotherms (V = vacuumed dried, C = calcined).

After imbibing the materials exhibited very similar nitrogen adsorption isotherms with considerably lower plateaus adsorptions than the original calcined material. After the loaded materials were calcined to decompose the metal complex there were increases in the amount of sorption due to capillary condensation. It is likely that the recoveries were due to the free volume produced in the pores by the decomposition of the bulky organic components of the organometallic compounds.

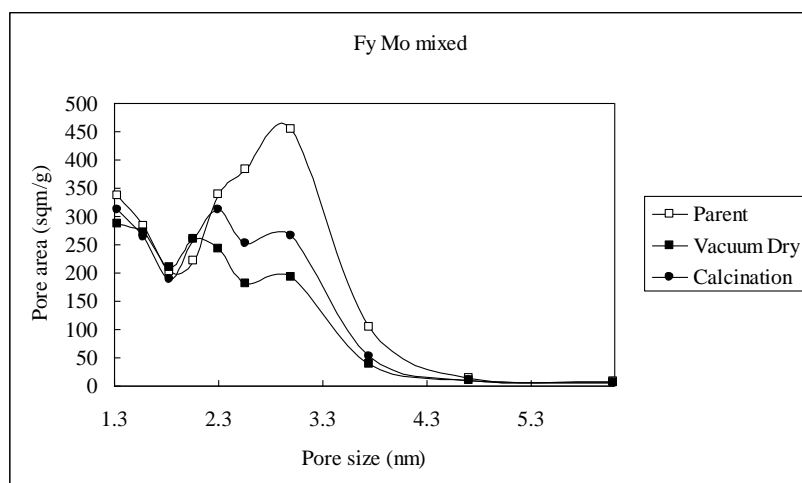


Figure 6.8. The effect of Fe+Mo mixed metal loading on the pore size distribution (V = vacuumed dried, C = calcined).

The BJH desorption pore diameter distribution patterns show that the loading of metal into the structure significantly destroyed the pore structure reducing the pore volumes and pore diameters consistent with structural shrinkage and pore filling.

6.5 The infrared spectrum

Infra red data for the samples Mo+Fe(T), Mo+Fe(M), Mo-Fe(T), Mo-Fe(M), Mo+Co(T), Mo+Co(M), Mo-Co(T) and Mo-Co(M) are given in 6.9 to 6.16 . The infrared spectra of the Mo+Fe(M), Mo-Fe(M), Mo+Co(M) and Mo-Co(M) exhibited the characteristic strong terminal metal carbonyl bands in the range from 2000 to at 1900 cm^{-1} indicating that the metal complexes had remained unaltered by

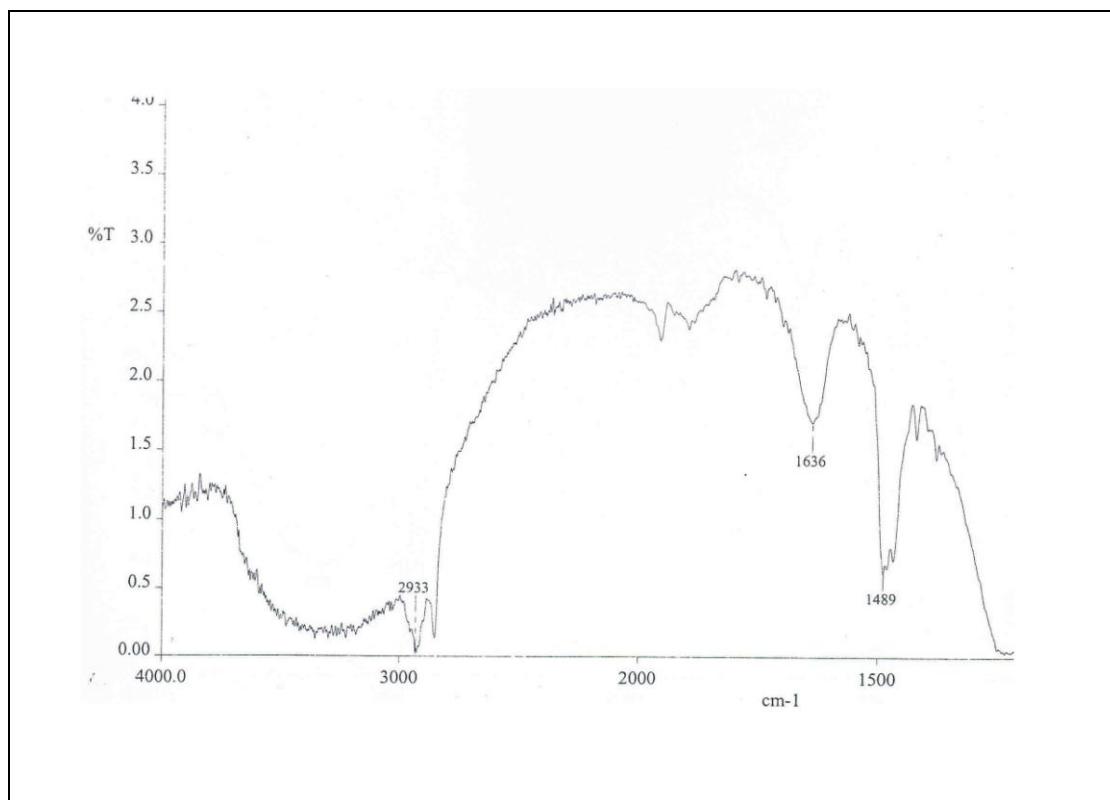


Figure 6.9 IR spectrum of M Mo+Fe

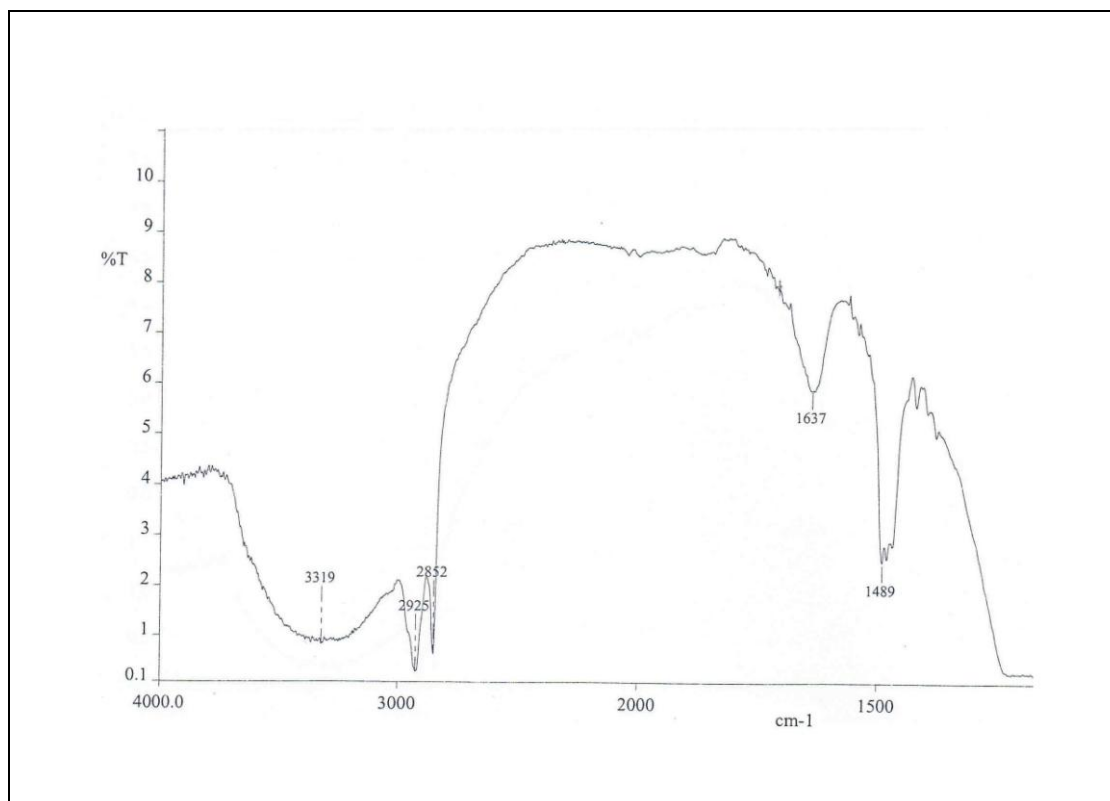


Figure 6.10 IR spectrum of T Mo+Fe

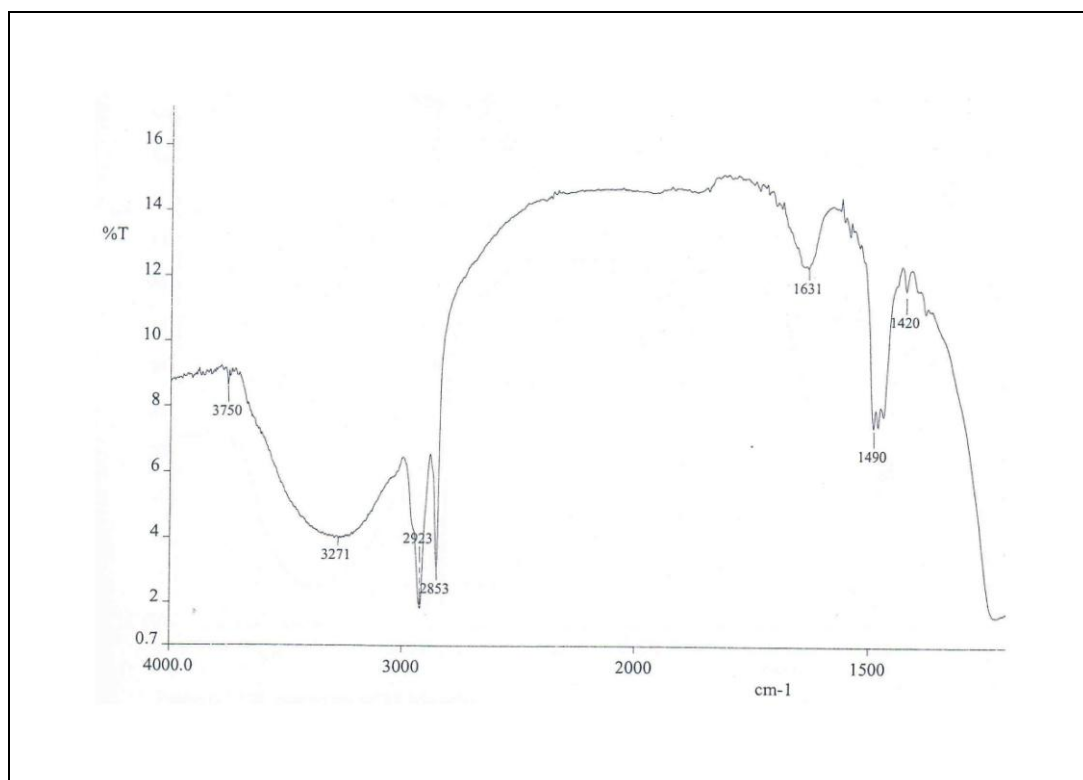


Figure 6.11 IR spectrum of M Mo-Fe

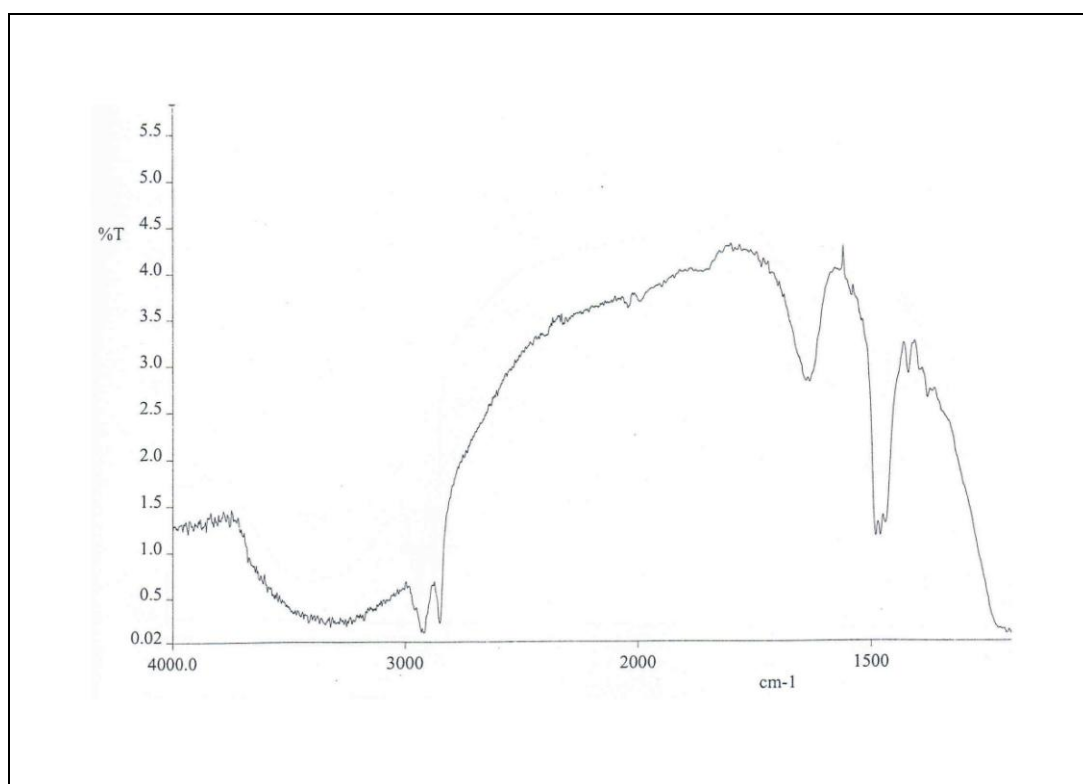


Figure 6.12 IR spectrum of T Mo-Fe

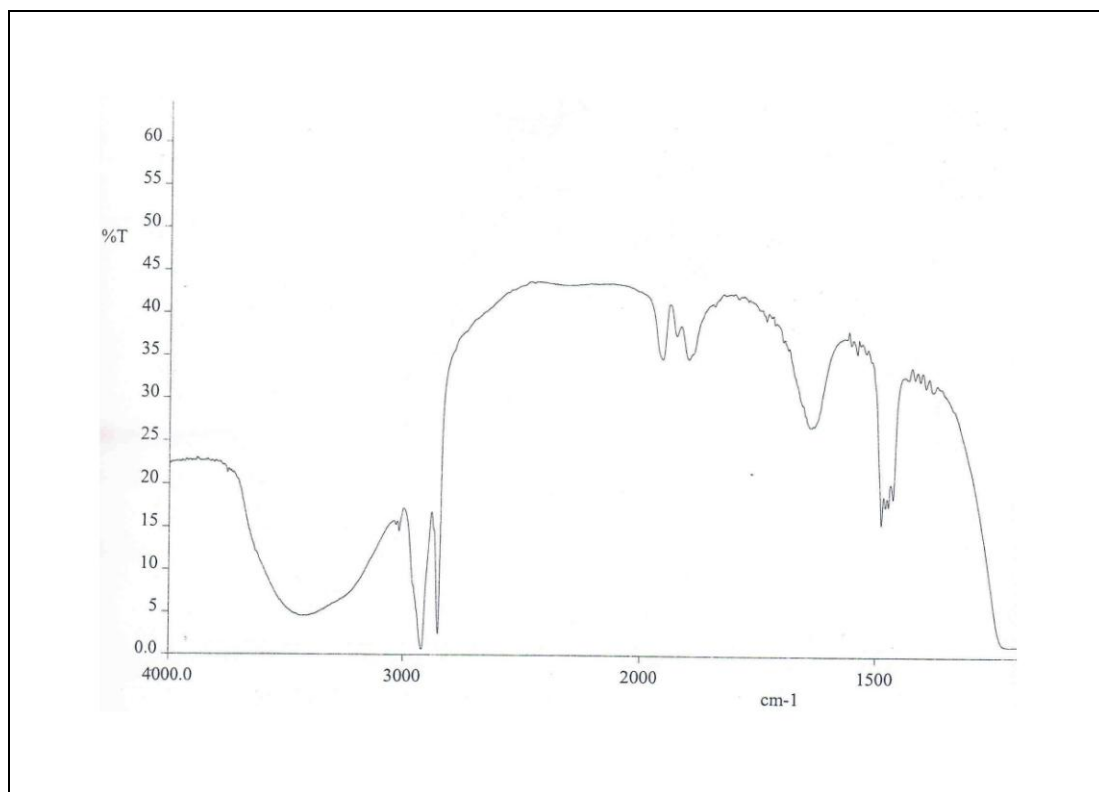


Figure 6.13 IR spectrum of M Mo+Co

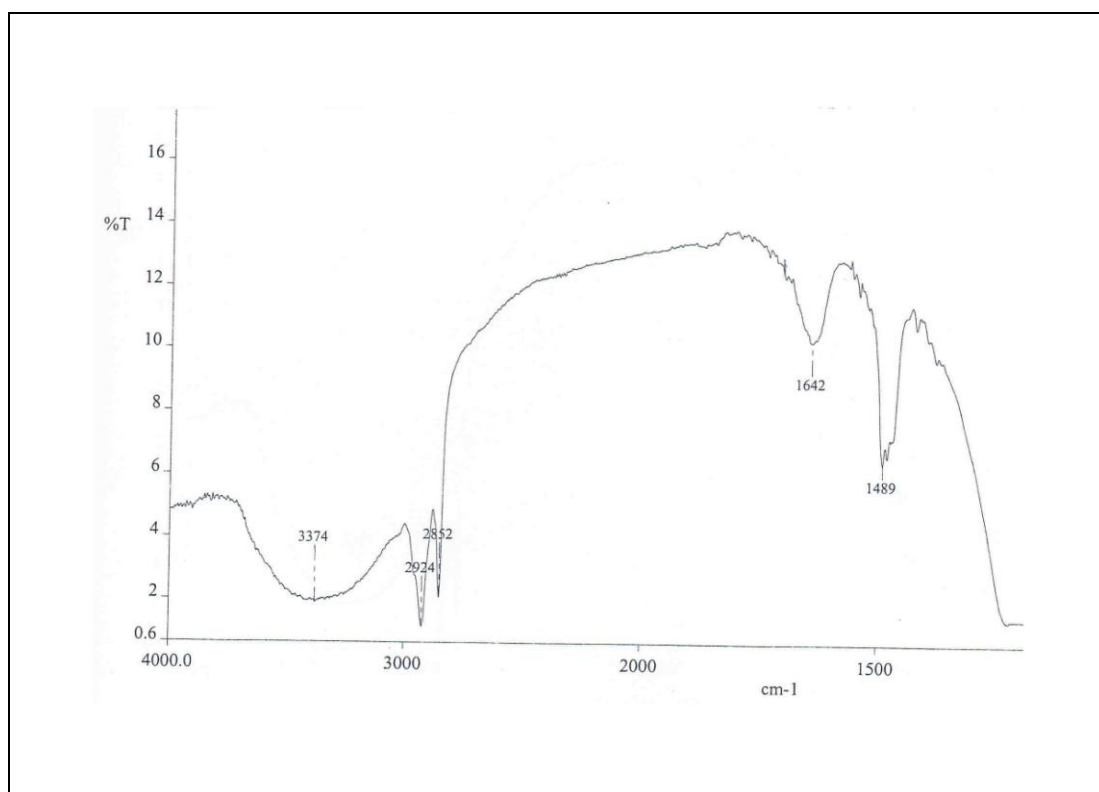


Figure 6.14 IR spectrum of T Mo+Co

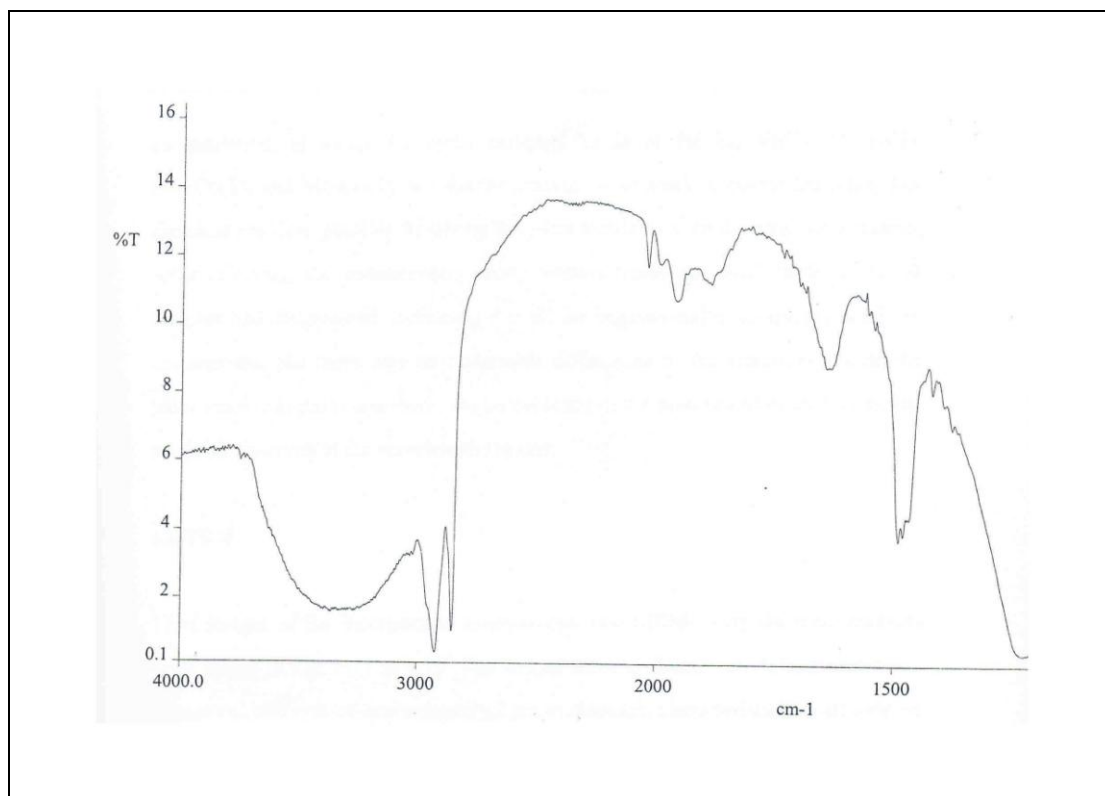


Figure 6.15 IR spectrum of M Mo-Co

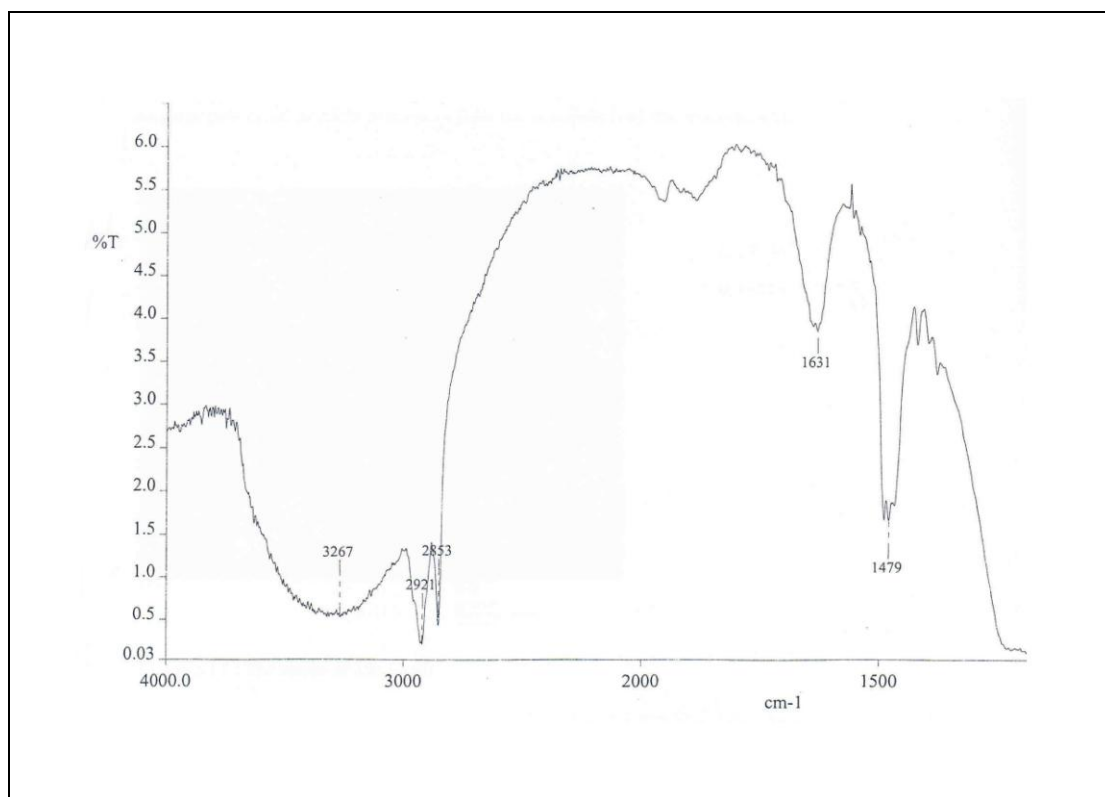


Figure 6.16 IR spectrum of T Mo-Co

encapsulation. However the metal carbonyl bands of the Mo+Fe(T), Mo-Fe(T), Mo+Co(T), and Mo-Co(T), for similar loadings were weak or absent indicating that chemical reaction, possibly involving the silica matrix, occurred during the synthesis. After calcining, the characteristic strong terminal metal carbonyl bands of the all samples had disappeared, indicating that all the organometallic complexes had been decomposed, but there was no observable differences in the vibrations due to the silica matrix. In particular there was no evidence of the presence of oxide phases that might be observed in the wavelength regions:

6.6 TEM

TEM images of the incorporated nanoparticles into MCM-41 by the three methods are shown in Fig. 6.17 to 6.19. The images show uniform, well-defined structures. Hexagonal channels of approximately 2 nm in diameter, characteristic of well-ordered MCM-41 are clearly visible. There were no obvious metal particles, either on the surfaces of the MCM-41 particles or within the pores indicating that the metal species were present had particle sizes less than the resolution of the micrographs.

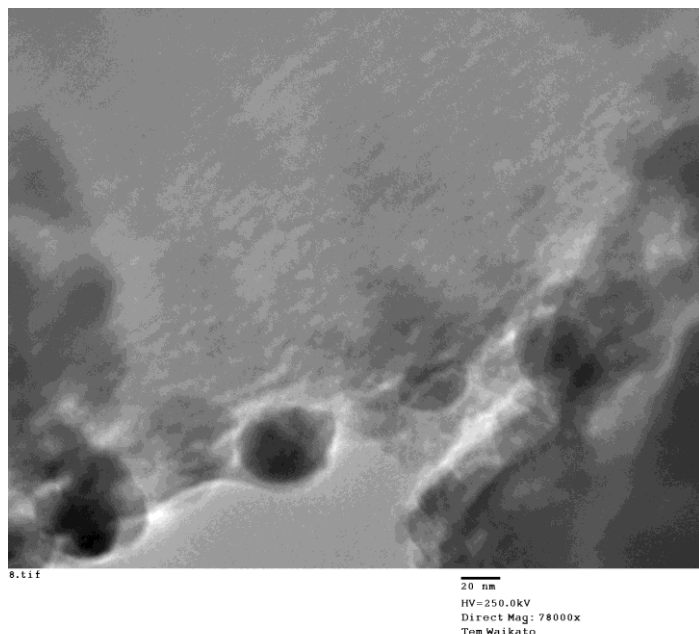


Figure 6.17 TEM image of Mo-Fe (I). The pore structure is just discernable but there is no evidence of particles large enough to be resolved.

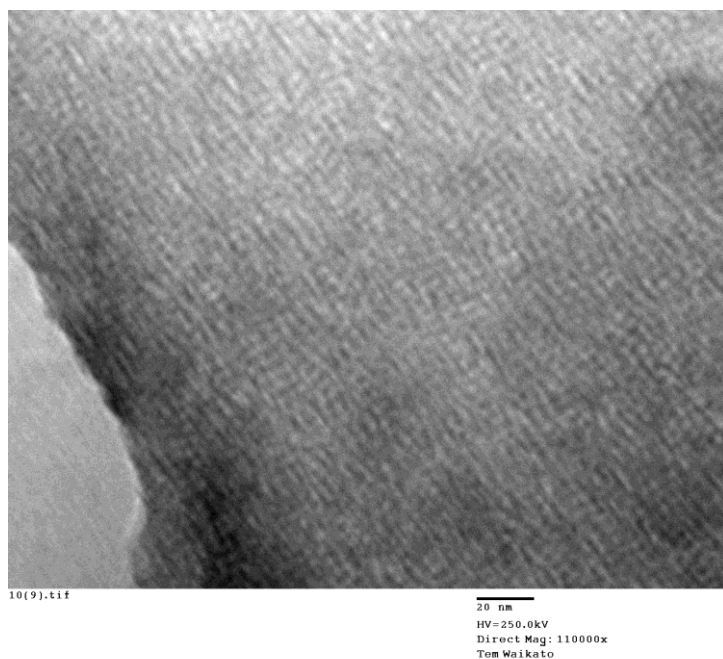


Figure 6.18 TEM image of Mo-Fe (T). The pore structure is clearly resolved. There is no evidence of particles greater than the pore size.

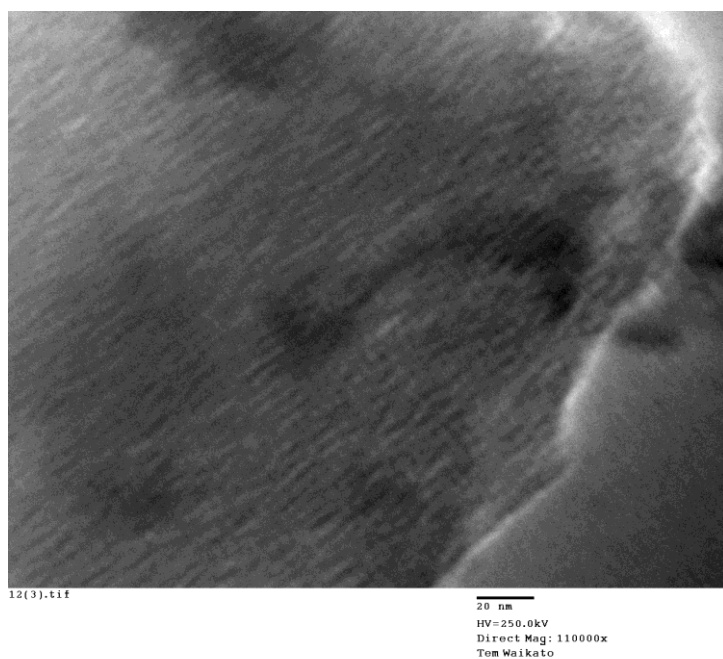


Figure 6.19 TEM image of Mo-Fe (M). The pore structure is resolved and there is no evidence of particles larger than the pore size.

The appearance of large and non porous particles of between 40 and 60 nm diameter

in the micrograph for the sample prepared by the I method is possible evidence that large aggregates of the metal species were formed by this loading method. The pore structure also appears to be less well defined which is consistent with the lower surface area and porosity of I method samples.

6.7 XRD evidence for the absence of crystalline iron oxide in the calcined iron loaded phases

XRD data for the calcined MCM-41 phases loaded by the mixed metal complexes over the 2θ range from 32 to 37 degrees are shown in Figure 4.26 along with data for a physical 2% mixture of iron oxide in pure silica.

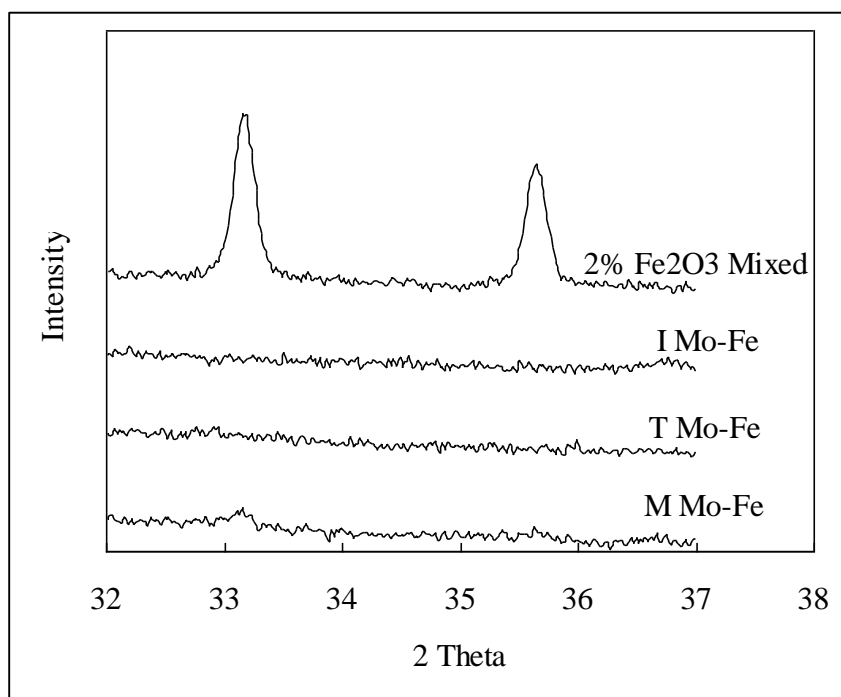


Figure 6.20 XRD powder patterns of the iron oxide physical mixture with pure silica and calcined MCM-41 loaded with Fy by three methods.

Although the iron oxide content of the loaded MCM-41 phases is lower than iron content of the physical mixture, the intensity at 33.2 and 35.5° 2θ for the 2% mixture is sufficiently high that peaks should be easily detected for the loaded samples if

crystalline iron oxide was present. The absence of peaks is thus evidence that any iron oxide present is of very small particle size or amorphous.

6.8 Discussion and conclusions

The synthetic methods used to prepare monometallic phases can be extended to prepare mixed metal systems. However different complexes have different affinities for sites within the structures and when loaded from simple physical mixtures will load in ratios different from the ratio in the mixture. Thus it is not easy to load the metals in predetermined compositions by this approach. The problem can be overcome by loading a single bimetallic complex of defined composition (e.g. Mo-Fe and Mo-Co) into the structures. It has been confirmed that the metal ratio of the loaded product is the same as the metal ratio in the complex.

The ability to load MCM-41 phases with highly dispersed mixed metal particles of predetermined composition has relevance to much current work on heterogeneous catalysis where size-, shape-, structure- and composition dependent behavior of catalyst nanoparticles are employed in alkylation, dehydrogenation, hydrogenation, and selective oxidation reactions for the conversion of hydrocarbons to commodity chemicals. Innovation in these areas is largely driven by novel synthesis of nanoporous and nanostructured catalytic materials. Noble metal nanoparticles such as Pt, Pd, Rh, Au and their alloys with other metals have been extensively employed to catalyze a wide range of dehydrogenation, hydrogenation, and selective oxidation reactions of organic molecules. Novel approaches are still required to synthesize and characterize stable gold and other metal nanoparticles with tightly controlled sizes to further advance the knowledge of their unique size-dependent catalytic behavior. The bulk mixed metal oxides of vanadium, molybdenum, and other transition metals have shown great promise as highly active and selective oxidation catalysts. [1, 2]

6.9 Reference for Chapter 6

1. Che, S.; Li, H.C.; Lim, S.H.; Sakamoto, Y.; Terasaki, O.; Tatsumi, T. *Chem. Mater.* **17**, **2005**, 4103-4113
2. Shiju, N.R.; Guliants, V.V. *Applied Catalysis A: General* **356**, **2009**, 1–1

Chapter 7 Discussion

Addressing the specific research questions posed at the beginning of this thesis has led to the gaining of new information about the preparation of mesoporous silicas and their loading with single and mixed metal particles. In particular it has been found that:

1. An optimised acid route provides a suitable method for the preparation of MCM-41 mesoporous silica systems compatible for use as catalysts and which also provides routes for loading with metals during synthesis. Detailed studies of reaction conditions have allowed mesoporous silicas to be synthesised at room temperature that have thicker walls and larger surface areas than usually reported.
2. A modified imbibing method has been developed to allow the preparation of metal loaded systems containing metal and mixtures of metal of defined composition from preformed calcined phases and appropriate organometallic complexes. The method has advantages over previously reported work in that by rigorous rinsing after imbibing, only adsorbed metal complexes remain. Less sintering and smaller particles should thus be favoured.
3. Two new general methods for loading mesoporous silicas with metal nanoparticles by incorporating the metal, in the form of an organometallic compound, into the structures during the synthesis step have been developed. The M method incorporates the metal complex into the micellar phase and the T method incorporated the complex into the TEOS solution. Other workers [1] have now adopted the M method but none have yet reported the T method.
4. The loading methods have been extended to prepare mixed metal systems of defined composition by using single-source mixed metal (e.g. Mo-Fe and Mo-Co) organometallic compounds such as $\text{Cp}(\text{CO})_3\text{MoFe}(\text{CO})_2\text{Cp}$, or $[\text{Cp}(\text{CO})_2\text{Mo}]_2\text{Co}(\text{CO})_3\text{CMe}$.

5. Microscopic and other methods of characterisation have provided evidence that upon calcining the loaded metal complexes from particles that are smaller than the resolving power of the microscope (1.5 nm) and consistent with being formed within the regular mesoporous structure.

7.1 Optimisation of the acid route for the preparation of stable MCM-41

A very large number of different synthesis approaches for the preparation of mesoporous materials has been reported in literature since the first development of ordered mesoporous materials in the 1990s. The synthesis methods and parameters that influence the final material will allow pore size engineering and control of the morphology and structural properties of the obtained material [2]. Of particular relevance to the present studies is the work that has reported for synthesis under acid conditions. Acid conditions provide a much more favourable environment for metal loading during synthesis because many of the metal complexes of interest as proposed as metal carriers are stable in acid but unstable in alkaline solution.

A new room temperature synthetic route using acid conditions, cationic surfactants (CTAB and PD), and an organic Si source (TEOS) has been developed and optimised. It has many advantages over other commonly reported procedures in the acidic conditions are favorable to the loading of metal salts and organometallic complex during synthesis. The compounds are generally not stable in basic conditions. Room temperature preparation is convenient and is an advantage from a complex stability perspective. The organic TEOS phase also provides a solvent for loading organometallic compounds during synthesis.

The optimum conditions were found to be: 2.5 mol/L HCL, 5 hrs, 500 rpm, 20°C, 2.0 wt% CTAB, mole ratio of CTAB/TEOS = 0.12. Under these conditions, MCM-41 with specific surface area of 1500 m²/g and greater and with high degree of structural

order can be routinely prepared.

During the optimization of the synthetic method, numerous small but useful effects of preparation parameters on the characteristics of the MCM-41 mesoporous silica were observed. The synthesis of mesoporous MCM-41 under strongly acidic conditions can be performed at lower temperatures, within shorter synthesis times and with lower surfactant concentrations than is possible for synthesis under basic conditions. Acid concentration had great influence on the structure of the product. With increasing acid concentration, the d_{100} spacing decreased, the pore size decreased and the wall thickness increased. The results (Section 3.2) also showed that extremes of high and low acid concentration favoured the formation of disordered amorphous phases. It has been determined that the optimum HCl acid concentration to obtain high quality MCM-41 material was 2.5 mol L^{-1} .

While it has been found that highly ordered MCM-41 can be successfully prepared at an extremely low surfactant concentration (0.035 mol L^{-1}), the optimum surfactant concentration determined for the synthesis of MCM-41 in this work was found to be 0.05 mol L^{-1} . The ordered mesophases were synthesised at reaction times ranging from 3 to 72 h. The most ordered MCM-41 materials, as indicated by the XRD intensities, were formed at 5 h, and the quality decreased with increasing reaction time.

It has been demonstrated (Section 3.5) that stirring rate can be used as a convenient tool for controlling not only the size and shape of particles but also their mesostructure. SEM images of the exterior surfaces of the samples prepared at the lowest stirring speed showed relatively smooth small particles. At the higher stirring speeds the particles tended to have rougher outlines and in most cases appeared to consist of inter grown particles made up of flake-like layers approximately 300 nm thick. Surfaces were generally rough and covered by small particles.

High stirring rates favoured a narrow pore size distribution, thick walls and high density products. These materials contracted less upon calcining and formed products that had higher thermal stability. The specific surface areas of MCM-41 formed in this way were amongst the highest that have been reported in the literature reaching areas as large as $1830 \text{ m}^2 \text{ g}^{-1}$ prepared at a stirring rate of 500 rpm. Che and co-workers have reported MCM-41 phases with surface areas of up to $1500 \text{ m}^2 \text{ g}^{-1}$ prepared under similar conditions but with less vigorous stirring [3].

The as-synthesized MCM-41 materials were very stable and showed no detectable change in structure after long term (>4 years) ambient storage. The product calcined at 500°C had high-thermal stability, withstanding temperatures of 700°C for 24h. Calcined materials were stable for at least 6 months when stored dry. However, when treated with neutral aqueous solution at 100°C , structural collapse occurred after between 5 and 8 hours. The material will have limited usefulness in neutral and alkaline solutions.

Post synthesis treatment with 4 mol/L HCl solution at 75°C for 2 hours led to an improvement of the ordering, and adsorption measurements revealed a limited pore size enlargement, the d_{100} spacing. Thus while the systems are not appropriate for use in neutral or basic solutions they should be usable in acid solution.

Removal of the templating molecules by calcination in air resulted in further ordering of the mesostructure as indicated by the improved sharpness of XRD lines. It has been confirmed (Section 3.2) that the products from acid synthesis have smaller pore diameters, thicker walls, higher surface areas and larger mesopore volumes than the products hydrothermally synthesized in basic media.

The materials produced under optimum conditions were well ordered, hexagonally arranged structures, giving (211) and (220) as well as the characteristic (100) XRD reflections, regular hexagonal pores as shown by TEM images, and BET surface area

of 1500 m² g⁻¹ and greater.

The refined reaction conditions including high stirring speeds, low surfactant concentration, high acid concentrations and short reactions times developed in the present work represent important improvements in the synthetic methodology giving stable, well ordered and high surface area products. The method is very simple and the morphology is easy to control compared to the alkaline synthesis route. The small scale laboratory preparation of the as-synthesized product and the calcined product could easily be scaled up for large-scale production should the product or any of its modifications become important for industrial applications.

7.2 Loading of Preformed Calcined MCM-41 with transition metals by imbibing organmetallic complexes (I method)

While several methods [4] have been developed for introducing metals, metal ions, metal oxides or metal complexes into MCM-41 or other mesoporous materials, the usual route [5] to metal loaded MCM-41 materials depends on immersing the calcined material in an appropriate aqueous salt solution containing the desired, metal atom. No reference is made to measure taken to ensure that the mesopores are filled with treatment solution. Also the treated materials were not rinsed. Thus although imbibing method has been widely used, it is characterized by producing metal particles much larger than the pore size indicating likely agglomeration on the exterior surfaces. Access of treatment solution to the channels of mesopores can only occur if air is displaced but no reference is made to applying vacuum to achieve this.

In the present work two innovations were adopted in an attempt to have better control of the loading and to ensure that uptake of the metal species was limited to the pores. Firstly the after the MCM-41 was immersed in the treatment solution, a vacuum was

applied to withdraw all the air and force the solution into the pores. Secondly after such treatment the sample was thoroughly rinsed with dichloromethane to ensure that treatment solution adhering to external surface was removed and free solution within the pores was also had a chance to diffuse out and be removed. The purpose of this procedure was to ensure that the solute remaining was strongly adsorbed to pore walls. Further the use of organometallic compounds dissolved in a suitable organic solvent avoiding the possibility of the simultaneous loading with the atom of the anions when metal salts are used [6].

Toluene and THF are commonly used organic solvents for organometallic compounds. The effect of the solvent on the MCM-41 structure seems to have been largely neglected. The results of this investigation have demonstrated that solvents used in the imbibing of organometallic compounds into MCM-41 can have a significant effect on the mesoporous structure. For example, THF treatment decreases the d_{100} spacing, pore size and specific surface area, but ethyl acetate treatment results in a minor increase in the d_{100} spacing and pore sizes without appreciable effect on specific surface area. While the use of appropriate organic solvents might be used as tool for modifying the structure of MCM-41, in most cases solvent treatment causes deterioration of structural features. The solvent chosen for the imbibing work was toluene because it had modest effect on MCM structure, has good solvent properties for organometallic compounds and has a relatively high vapour pressure.

Loading of organometallic compounds using the I method produced structural changes over and above the effects of the toluene solvent after loading and further effects after calcining to decompose the complexes and deposit the metal species usually as the oxide. The changes resulted in lower ordering and less well resolved XRD patterns. The pore sizes and the surface areas were significantly decreased upon loading of organometallic complexes but increased after calcining. This may have been due to unblocking of pores and releasing of space occupied by the bulky

organometallic complexes. However pore volumes and surface areas were still significantly reduced relative to the starting materials.

Loading of the complexes varied with the nature of the complex. Although in each case the same amount of organometallic solution was imbibed under vacuum, the amount of complex remaining in the structure after rinsing excess varied dramatically. The rinsing was to ensure complex was dispersed at a molecular level and that aggregates did not precipitate from the free complex remaining dissolved in solution filling the pores as the solvent evaporated. The amount of organometallic complex retained within the structure appeared to correlate with the polar surface area of the complex which generally reflected the carbonyl content and was a measure of the polar nature of the molecule. The different organometallic complexes have different ability to react with Si–OH groups of the pore walls. In a pure silica MCM-41 both internal and external surfaces terminate in a layer of silanol groups (Si–OH) pointing into the mesopores. These silanol groups provide adsorption sites for hydrogen bonding with polar organometallic complexes. The adsorbed complexes can be expected to be retained during rinsing of excess imbibed solution from the structures. The amount of complex retained should reflect the strength of the adsorption interaction. The metal content retained in MCM-41 phases loaded by the I method was in the order:



This is also the order of the number of C=O groups in the respective compound groups. Fc has no C=O; Fac, Ft and Fb have one C=O; Fd has two C=Os; Fa and O-Mn have three C=Os and Fy and O-Mo have more than three C=Os. The number of C=O groups also reflects the polar surface areas (See Section 4.3).

The absence in the XRD results of the calcined materials of peaks characteristic of the metal oxides provides evidence that the metal after calcining remains well dispersed in particles too small to give diffraction signals.

Although the organometallic complexes can be effectively incorporated into MCM-41 in a highly dispersed state by the I method, invariably it was found that the structure of MCM-41 was significantly destroyed and the pore size and the surface area was significantly decreased. Other workers have also observed these effects [7] which tend to be greater as loading increases. These changes are likely to compromise the usefulness of the metal loaded phases in catalytic applications. These problems are avoided when the metal is incorporated into the pores during synthesis.

7.3 Loading during synthesis

Much of the new work described in this thesis was concerned establishing two novel routes for introducing metal species as isolated metal atoms or small particles into the pores of the MCM-41 structure during synthesis. These are the M method, where the complex is incorporated into the surfactant micelle and the T method where the complex is dissolved in the TEOS of the synthesis mixture. The amount of metal that can be incorporated into MCM-41 is controlled by the solubility of the organometallic compounds in the micellar solution or the TEOS. The location of the metal species in the structure is also likely to be controlled by the choice of the synthetic method.

The two synthetic routes are illustrated diagrammatically in Fig 7.1 for the M method and Figure 7.2 for the T method.

According to the M method metal complex loaded micelles are first formed by adding a dry mixture of the metal complex and surfactant (formed from evaporating a solution of the two components in a mixed solvent of dichloromethane/methanol) to the acid synthesis solution. Upon the addition of TEOS the micelles become coated with silica. The silica coated rods condense into the hexagonal array of a metal loaded precursor phase. Upon calcining, the surfactant is removed and the metal complex decomposed. Because the loading of metal into the micelles is quite low, aggregation and sintering can be expected to be limited favouring the formation of surface atoms

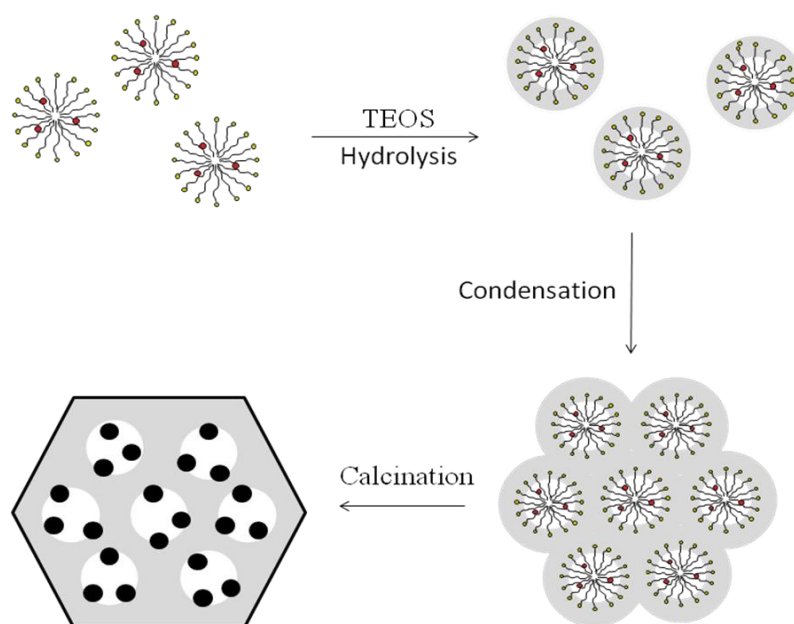


Fig 7.1. Schematic of loading by the M method.

or small metal aggregates easily accommodated within the pore structure. This procedure, which was first published in 2006 [8,9,10] differs from the micelle loading route used by Xue who used an ambient temperature alkaline route based upon TEOS as the silica source and also from work done more recently [12] where the metal complex dissolved in non polar solvent was loaded into aqueous micelles and the MCM-41 was produced by the hydrothermal route in alkaline solution at elevated temperature using silica fume as the silica source. For example, Ohtaki et al. [13] prepared small Fe particles located in mesopores of MCM-41 using a chloroform solution of ferrocene as the source of metal. In contrast, when $[\text{Pd}(\text{acac})_2]$ was employed as another inorganic precursor the process was less successful. This has been attributed to the low decomposition temperature of precursor (ca. 130°C) which caused severe decrease of pore ordering as compared to the ferrocene system. In a similar manner, Kaskel and coworkers [14] incorporated platinum and palladium particles into channels of MCM-41 using a toluene solution of $[\text{Pt}(\text{acac})_2]$ and $[\text{Pd}(\text{acac})_2]$, respectively.

The clear advantage of the M method used in the present work is that a greater range of metal complexes are stable in acid conditions used and the reaction can be carried

out at ambient temperatures allowing incorporation of less thermally stable complexes.

The second synthetic route for loading metal into the MCM-41 structure that has been explored in the present work and does not appear to have been attempted elsewhere, is the T method. This is illustrated diagrammatically in Fig 7.2.

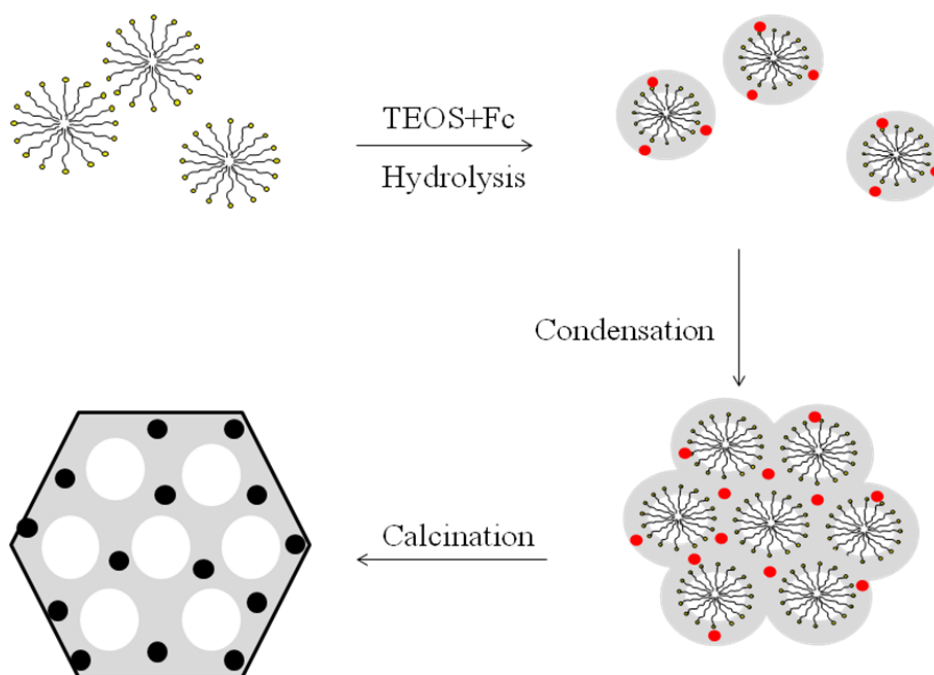


Fig 7.2. Schematic of loading by the T method.

According to this method the metal complex is added to the liquid TEOS before it in turn is added to the acid micellar solution. As the diagram suggests, loading by the T method is likely to incorporate metal atoms into the walls of the product. While this may be of advantage to inhibit sintering during calcining, it may also isolate the metal from the pores. Alternatively it is possible that the metal species could migrate from the walls into the pores at any stage of the synthesis and/or calcining processes. A further synthetic strategy analogous to the T method, that also does not seem to have been investigated, is to add the metal species to the acid micellar solution. This method might be called an A method where a metal salt is added to the acid solution

of an anionic surfactant. The metal cations might be expected to associate with the negative anionic head groups of the surfactant and thus be fixed in the walls on the surfaces of the pores. This is a possible area for further investigation.

The amount of metal that can be incorporated into MCM-41 by the M and T method is controlled by the solubility of the organometallic compounds in the micellar solution or the TEOS. The location of the metal species in the structure is also likely to be controlled by the choice of the synthetic method.

The XRD patterns of all samples exhibited an intense low angle reflection. The excellent regular mesostructure of MCM-41 was sustained and the materials possessed high surface area, large pore volume and uniform pore size. The intensity was not significantly changed with the increasing amounts of the metal incorporated. One inherent advantage of the loading during synthesis strategy is the likelihood that the organometallic complex can be selectively loaded into the channels (M method) or walls (T method). Since loading during synthesis is a one-step loading method, better control of the amounts and location of the loaded materials can in principle be maintained. In addition, the metal will be uniformly distributed as molecular entities due to the molecular level dissolution of the loading compounds in the hydrophobic core of the surfactant template (for the M method) or the TEOS liquid (for the T method). The loading during synthesis routes offer the further advantage that they offer general routes for any loading compound, the only requirement being that the compound is either soluble in the core of the micelle or soluble in TEOS. No post synthesis exposure to solvents is involved so the solvent induced structural changes inherent with the I method should be absent.

For the T and M methods, large variations in the amounts of the different organometallic complexes loaded were observed. The mesoporous structure and amount of metal complex loaded at a given complex to surfactant mole ratio was affected by molecular structure and correlated with topological polar surface area.

Molecular structure affects the ability of the molecule to pack into the micelle core and thus the amount of organometallic complex loaded.

The topological polar surface area (see section 5.4) of a molecular is an inverse measure of its hydrophobicity, and thus lower topological polar surface areas indicate greater hydrophobicity. More hydrophobic compounds will tend to be preferentially partitioned into the initial hydrophobic organic phases (micelle core in the M method) and hydrophobic polymeric silica phases formed during synthesis (T method). This reasoning can account for the greater loading by both synthetic routes of those complexes with lower topological polar surface areas.

Evidence to support the expectation that the metal complexes and their decomposition products will be widely and uniformly dispersed throughout the structures came from TEM which indicated that particles were smaller than the 1 nm resolving power of the instrument used. The absence of XRD lines characteristic of the oxides after calcining was also evidence that particles formed by calcining were sufficiently small to be X-ray amorphous.

7.4 Preparation of MCM-41 with encapsulated mixed metal phases

The synthetic methods used to prepare monometallic phases can be extended to prepare mixed metal systems. However, different complexes have different affinities for sites within the structures and when loaded from simple physical mixtures of mono-metallic compounds, will load in ratios different from the ratio in the mixture. Thus it is not easy to load the metals in predetermined compositions by this approach. The problem can be overcome by synthetic loading single source bimetallic complexes of defined composition (e.g. Mo-Fe and Mo-Co) into the structures. It has been confirmed that the loaded metal ratio is the same as the metal ratio in the complex.

The capability to load MCM-41 phases with highly dispersed mixed metal particles of predetermined composition has relevance to much current work on heterogeneous catalysis where size-, shape-, structure- and composition dependent behavior of catalyst nanoparticles are employed in alkylation, dehydrogenation, hydrogenation, and selective oxidation reactions for the conversion of hydrocarbons to commodity chemicals. Innovation in these areas is largely driven by the need to synthesise novel nanoporous and nanostructured catalytic materials with encapsulated metal and noble metal nanoparticles and their alloys. Noble metals in particular have been extensively employed to catalyze a wide range of dehydrogenation, hydrogenation, and selective oxidation reactions of organic molecules [15]. Novel approaches are still required to synthesize and characterize stable metal nanoparticles with tightly controlled sizes to further advance the knowledge of their unique size-dependent catalytic behavior. Metal and mixed metal oxides of vanadium, molybdenum, and other transition metals have shown great promise as highly active and selective oxidation catalysts [3,16]. Their activities may be both enhanced and made more selective by encapsulation as nanoparticles using the procedures developed in the present study.

7.5 Catalysis by MCM-41 with encapsulated mixed metal nanoparticles

There are many strategies [17] for the design and the preparation of mesoporous catalysts. The well ordered mesoporous materials synthesized by the T and M method with extremely high surface area hold much promise for the development of novel solid catalysts.

One example one reaction where the systems studied might find application is the ammonia synthesis reaction. Kojima and Aika [18] have found that Co/Mo nanoparticles provide an optimum ammonia synthesis catalyst. They determined that a 1:1 mixed metal cobalt/ molybdenum compound provided catalytic activity for low pressure ammonia synthesis comparable to the much more expensive rhodium and

much better than the iron catalyst used industrially. The possibility exists that 1:1 cobalt-molybdenum nanoparticles encapsulated in MCM-41 could provide an effective ammonia synthesis catalyst. In the case of ammonia synthesis, the chemical form of the mixed metal system was $\text{Co}_3\text{Mo}_3\text{N}$. Formation of $\text{Co}_3\text{Mo}_3\text{N}$ from the Co/Mo mixed metal MCM-41 system by reaction of the calcined material with ammonia at approximately 900 K should lead to $\text{Co}_3\text{Mo}_3\text{N}$ nanoparticles of much smaller size and greater activity than those produced by the conventional cobalt molybdate route [19].

The gold system provides [20] another example where the procedures developed in the current work might find application. Systems loaded with mixed metal complexes containing Au could be expected, upon calcining, to produce Au metal/metal oxide systems of the type that have been the centre of much interest for reactions such as the low temperature oxidation of carbon monoxide. If the mixed metal complexes of the required stability cannot be obtained for loading by a one step process, a combination of the I, T and/or M methods could be used. For example, one metallic substrate could be loaded during synthesis using the M or T method with a stable monometal complexes and other metal loaded subsequent to calcination by post synthesis treatment using the I method followed by a second calcination.

7.6 Reference for Chapter 7

1. Viđes, S.G.; Schweyer, F. T.; Rabu, P.; Paillaud, J.L.; Braunstein, P.; Lebeau, B.; Estournès, C.; Guille, J.L.; Rueff, J.M. *Microporous and Mesoporous Materials* 106, **2007**, 17–27
2. Meynen, V.; Cool, P.; Vansant, E.F.; *Microporous and Mesoporous Materials* 125, **2009**, 170–223
3. Che, S.N.; Li, H.C.; Lim, S.; Sakamoto, Y.; Terasaki, O.; Tatsumi, T. *Chem. Mater.* 17, **2005**, 4103–4113
4. Taguchi, A.; Schüth, F. *Microporous and Mesoporous Materials* 77, **2005**, 1–45
5. Trejda, M.; Ziolek, M. *Catalysis Today* 101, **2005**, 109–116
6. Schweyer, F.; Braunstein, P.; Estournès, C.; Guille, J.; Kessler, H.; Paillaud, J.L.; Rosé J. *Chem. Commun.*, **2000**, 1271–1272
7. Decyk, P.; Trejda, M.; Ziolek, M. *C. R. Chimie* 8, **2005**, 635–654
8. Xu, S.; Langdon, A.G; Nicholson, B.K. The synthesis of ferrocene containing mesoporous materials, Proceedings 5th International Mesostructured Materials Conference, August 5-7 **2006** Shanghai, China, (poster and paper)
9. Xu, S.; Langdon, A.G; Nicholson, B.K. A comparison of methods for dispersing metals onto mesoporous silica, Proceedings of the NZIC **2006** Conference, Vol II Posters (abstract and poster)
10. Xu, S.; Langdon, A.G; Nicholson, B.K. The synthesis of mesoporous materials (MCM41 containing encapsulated organometallic compounds, Proceedings supramolecular chemistry and nanoscience – towards functional nanostructures. (abstract and poster) 3 March, **2007**, University of Otago, Dunedin.
11. Xue, P.; Lu, G.; Guo, Y.; Wang, Y.; Guo, Y. *J. Mol. Catal. B* 30, **2004**, 75.
12. Yuan, Y.Z.; Ma, H.T.; Luo, Q.; Zhou, W. *Mater. Chem. Phys.* 77, **2003**, 299.
13. Ohtaki, M.; Inata, K.; Eguchi, K. *Chem. Mater.* 10, **1998**, 2582–2584
14. Krawiec, P.; Kockrick, E.; Simon, Paul.; Auffermann, G.; Kaskel, S. *Chem. Mater.* 18, **2006**, 2663–2669
15. Jibril, B.Y.; Ahmed, S. *Catalysis Communications* 7, **2006**, 990–996
16. Shiju, N.R.; Gulianti, V.V. *Applied Catalysis A: General* 356, **2009**, 1–117. Yuan,

17. Z.Y.; Ma, H.T.; Luo, Q.; Zhou, W. *Materials Chemistry and Physics* 77, **2002**, 299–303
18. Kojima, R. Aika, K. *Chem. Lett.* **2000**, 514
19. Wang, X, H; Zhang, M, H; Li,W; Tao, K,Y. *Catalysis Today*. 131,**2008**, 111–117
20. Haruta, M.; Dat é M. *Applied Catalysis A: General* 222, **2001**, 427–437

Chapter 8 Conclusion and further work

8.1 Summary and conclusions

The studies presented in the current thesis have contributed to our understanding of the synthesis of mesoporous solids and how they can be loaded metal with potential catalytic activity. The following general conclusion have been drawn:

1. The acid synthetic route has been proven to be a suitable route for synthesis of MCM-41 systems. The refined reaction conditions including high stirring speeds, low surfactant concentration, high acid concentrations and short reactions times developed in the present work represent important improvements in the synthetic methodology giving stable, well ordered, small pore diameters, thick walls and high surface area products.
2. Mesoporous MCM-41 prepared by calcining precursor products prepared by the acid route are good candidates for support materials for the preparation by an imbibing method (I method), of metal and mixed metal nanoparticles catalyst systems for dry gas reactions. New information about the role of the solvent in the imbibing process has been discovered. Solvents with low polar surface areas and complexity (more hydrophobic) such as THF interact strongly with the silica lattice and cause structural breakdown. Toluene on the other hand, having a higher polar surface area (less hydrophobic) has much less effect on the lattice and is thus a better solvent for imbibing metals
3. Single metal (Mo, Co, Mn and Fe, with differing sizes, stabilities, polarities) and mixed metal (Mo/Fe, Mo/Co) organometallic complexes can be effectively loaded into the preformed mesoporous supports by the I method and then decomposed to prepare metal and mixed metal nanoparticles within the structures. It has been found that filling pores with metal or/or metal oxide species by this

method causes disordering and destruction of the MCM-41 porous supports, broadening of the XRD diffraction lines, and a significant reduction of pore size, pore volume and specific surface area.

4. A major contribution of the current work has been the development of methods for controlling the loading of metals into the structures during synthesis. In the M method, single and mixed metal organometallic complexes are loaded into the micellar phase of the synthetic solution and could favour the uptake of the metal into the pores. In a second synthetic loading route, the T method, the organometallic complexes are dissolved into the TEOS the synthesis system which could favour uptake of the metal species into the silica framework. The M and T methods allow loading without significant disruption of the lattice or reduction of surface area.
5. All loading methods can be used to prepare mixed metal systems of defined composition where the metals are introduced as single-source mixed metal (e.g. $\text{Cp}(\text{CO})_3\text{MoFe}(\text{CO})_2\text{Cp}$ and $[\text{Cp}(\text{CO})_2\text{Mo}]_2\text{Co}(\text{CO})_3\text{CMe}$) organometallic compounds. Encapsulated metal compositions after calcining were determined by the stoichiometry of the initial mixed metal complex. The way has been made possible to load mixed metal nanoparticles designed to have synergistic catalytic effects.
6. The metal loading obtained according to the three methods typically ranged up to 4%. At these levels, crystalline metal and metal oxide phases can be routinely determined by XRD. The absence of XRD peaks characteristic of the metal or metal oxides in any of the samples provides evidence that the metals after calcining were well dispersed in particles of size less than a few nm, and too small to give diffraction signals. TEM evidence also supports the conclusion that the encapsulated particles formed after calcining were smaller than the nanometer

resolution of the instrument.

8.2 Suggestions for further work

8.2.1 Characterizations of encapsulated nanoparticles

The metal or metal oxide MCM-41 systems prepared according to the three methods were characterized with XRD, nitrogen sorption, TEM and FTIR. Differences in the XRD data before and after calcining and in the FTIR data before calcining for the products formed by the T and M methods point to different mechanisms of encapsulation and point to the likelihood that the metal species were loaded into the pores (for the M method) and the walls (for the T method). Although during the synthesis and calcining agglomeration of the particles did not take place, no direct evidence for the location or of the size of the nanoparticles has been obtained. It is possible that X-ray absorption spectroscopy (XANES/EXAFS) determination of the local structure around the metal atom will be of use. XANES/EXAFS has recently been used to provide a powerful technique to study the coordination structure of hetero-atoms introduced to MCM-41 [1]. For iron loaded MCM-41, the use of bright field TEM high resolution has been used to infer the presence of the iron nanoparticles from changes in the contrast of the images [2].

8.2.2 Chemistry of encapsulated complexes

In all the work presented in this thesis, the organometallic complexes loaded into MCM-41 were decomposed by calcining in the air. For the metals involved this would lead to the formation of nanoparticles of oxides. Many catalytic systems are based upon other chemical forms of metals, either the metals themselves or in combination with other elements. Studies of calcining under reducing or reactive atmospheres to produce pure metal particles and metal compound particles are thus of interest. For

example, the thermal stability of the MCM-41 matrix offers the possibility of reaction with ammonia at elevated temperatures to produce metal nitride catalysts (see below).

8.2.3 Catalysts based upon Co/Mo MCM-41 systems

In chapter 7 the activity of Co/Mo mixed metal systems in the ammonia synthesis reaction was discussed as a possible application of MCM-41 systems loaded with Co and Mo mixed metal nanoparticles. This is suggested as an area for further studies.

8.2.4 Catalysts based upon mixed metal Au MCM-41 systems

Another catalytic system of continuing interest is the metal/metal oxide supported gold nanoparticle systems. While the stabilities of available gold complexes may be inadequate to allow direct mixed metal loading, the two step strategy discussed in section 7.5 would be worthy of investigation.

8.2.5 Improvement of hydrothermal stability

While the synthetic method developed in this work has produced materials of excellent thermal stability, their hydrothermal stability is quite poor. Pore walls of 1 to 2 nm thickness are obtained. Microporosity and low wall density is believed to be a major reason for low hydrothermal stability. Post calcining acid treatment was observed to cause increased pore size, decreased cell parameter and reduced wall thickness implying a tighter packing of the silica chains in the framework consistent with a decrease in microporosity and increase in wall density. This should be investigated further. The fact that it was shown that the systems were stable in acid environments and acid treatment was shown to improve resistance to hydrolytic structural collapse means that providing an acid environment can be maintained, stability in aqueous systems should not be a problem. Whether volatile acid can impart similar stability in gas applications needs to be investigated.

Others have attempted to improve the stability of these materials by a variety of techniques. Some of these methods include in-situ techniques like the addition of various salts. Other methods are post-modification methods such as ion exchange, grafting of organosilane functional groups to produce hydrophobic organic chains on the surface [3].

8.3 Reference for Chapter 8

1. Zhu, H; Lee, B; Dai, S; Overbury, S.H. *Langmuir*. 19, **2003**, 3974
2. Haruta, M. *Studies Surf. Sci. Catalysis.*, 145, **2003**, 31
3. Ryong, R and Shinae, J. *J. Phys. Chem. B* 10,**1997**, 317-320